Circuit design for biomedical laboratories based on impedance measurement

Pablo Pérez García

Instituto de Microelectrónica de Sevilla
Departamento de Tecnología Electrónica
Universidad de Sevilla

Supervised by:

Dr. Alberto Yúfera García

Dra. Gloria Huertas Sánchez

June 2019

I would like to dedicate this thesis to my loving parents, my sister and my family.
To my dearest friends and everyone who walked with me at any time during the process.
To my colleagues from the Seville Institute of Microelectronics (IMSE-CNM).
To my colleagues from the Electronic Technology Department from University of Seville.

Acknowledgements

There are many people who participated in the creation of this work. Some were involved in the technical details while others have enriched my life in other ways. If I neglect to mention your name, you know who you are and how you have helped me through this process, and I thank you.

This work would have not been possible without funding provided by the University of Seville (US) and the Spanish government (Mixcell project, REF: TEC2013-46242-C3-1-P). The Ph.D. scholarship awarded to me in 2015 by the University of Seville made possible to fulfill the research project exposed on dissertation pages.

First of all, I would like to thank my advisers Prof. Alberto Yúfera and Prof. Gloria Huertas, for their friendship, enthusiasm and positive attitude. They have been great mentors, cultivating scientific curiosity and providing me with valuable light on harsh times. I appreciate their guidance on several aspects, and I feel truly grateful for helping me develop my scientific career.

I would like to thank Andrés, his advice and help in the laboratory greatly contributed to the development of the work contained in this thesis. I am truly thankful and I consider him a mentor too. Likewise, all my colleagues from IMSE-CNM (Seville Institute of Microelectronics) and Electronic Technology Department (DTE), whose friendship, kindness and advice contributed to the result presented.

Prof. Paula Daza and Prof. María Martín, for the huge amount of time devoted to perform the cell culture assays always with positive attitude, kindness and willing to help. The work presented here would not be possible without you. Prof. Pablo Huertas for the guiding on cell culture assays and the initial testing on CABIMER which helped develop a reliable prototype to perform cell culture measurements. Prof. Esther Rodríguez-Villegas, for her friendship and all the positive vibes I received from her and everyone around while performing two academic internships under her supervision at the wearable technologies lab on Imperial College London. It was really fun collaborating with the team, and I consider you all my friends.

I want to thank my loving parents Manuel and Matilde, and my sister Irene, for teaching me the value of hard work, honesty and integrity. For their endless love and support which led me from a curiosity-driven kid to writing this thesis. Thank you very much, for everything.

Finally, I would like to thank Andreea, for being supportive with all the process involved in the writing of this dissertation, especially thank you for caring about me during the harsh times.

Abstract

This dissertation presents a contribution to the biomedical circuits and systems field. The development of a system capable of performing real-time monitoring and characterization of cell culture assays, which are useful in many biomedical environments and disciplines. The biological electrical impedance (Bio-impedance) of cells is the selected sensing parameter or biomarker. This is due to biological matter electrical properties, and the potential to acquire the information from an electrical sensor using electronic circuits. Bio-impedance is an excellent candidate technique to enable Lab-on-a-Chip (LoC) systems in biomedical and health applications. Regarding the development of a Bio-impedance system from the Internet-of-Things (IoT) paradigm, this thesis proposes a structure based on three blocks; sensors, gateway and services.

A full electronic system is proposed, implementing the electrical sensor measurements, which consists of an analog front-end based on the Oscillation Based Technique (OBT), a current source for cell culture excitation, signal processing circuits devoted to parameter extraction from measurements, and the communication system for real-time signal acquisition and continuous recording. The proposed OBT avoids some critical circuits in bioimpedance test systems, as sinusoidal excitation sources and lock-in-amplifiers, neglecting the influence of mismatching between real and imaginary circuit paths. Additionally a micro-processor is selected for sensor control and task management.

The Electrical Cell-substrate Impedance Spectroscopy (ECIS) technique is as a popular and reliable measurement technique for cell culture experiments. A special mention is devoted to electrodes, as interface elements between the sample under test and the measurement circuits. A model for the electrodes is analyzed and tested for our application. The electrode model is a fundamental part for circuit design, and provides useful insight to better understand the experimental results. Design equations and graphics are reported including the proposed model for the electrode and cells electrical performance. Circuit design specification were selected following those guidelines. In order to improve accuracy in frequency and amplitude extraction, an optimized signal-processing algorithm was directly implemented on the micro-controller. Furthermore, since the computational workload is reduced, power consumption is also improved.

The gateway is a device located on the biomedical laboratory with a direct link to the remote web server, providing the service layer. The gateway device is implemented by a commercial Linux based system on a chip, Intel Edison. This device includes a Yocto Linux version as the Operating System and implements both WiFi (link to services) and Bluetooth (sensor link) communication.

The service layer provides secure access, storage and real-time visualization for the potential user of the system; the biomedical researchers. All the information related to services is stored on a MySQL database. The database is designed to provide scalability and comply with the functional requirements of the system. The remote control and real-time visualization of the system are performed via a custom web application prototype, developed for this purpose, which allows biomedical researchers to monitor cell cultures in real-time.

Experimental results over four different cell lines are described, for cell growth, cell differentiation and cell toxicity assays. Circuit performance agrees with the expected frequency and amplitude ranges. Exponential and confluent phases in cell growth assays are correctly observed and measured, validating the feasibility of the proposed technique for the correct characterization of this type of biological assays. On the other hand experimental results for stem cell differentiation prove that muscle cell evolution toward complex structures (myotubes) can be detected using the proposed system. Finally, cell toxicity assays are also reported, confirming the potential cell-counting method with a cyto-toxicity experiment, where cells will not reach maximum growth levels.

Table of contents

List of figures

List of tables

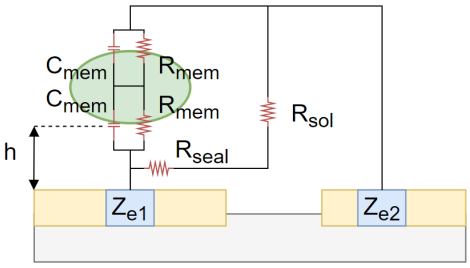

Chapter 1

Introduction

This dissertation develops a contribution to the circuits and systems required for the real-time monitoring and characterization of cell culture assays, useful in many biomedical environments and disciplines. The selected sensing parameter is the biological impedance (Bio-impedance) of cells due to the electrical properties of the biological matter, and the potential to measure it using electronic circuits. A special mention is devoted to electrodes, as elements of interface between the sample under test and the circuits for measurement. A model for the electrodes will be analyzed and tested for our application, being this of great interest for circuit design and to understand the research results. A full electronic system is proposed to implement the electrical measurements, consisting of an analog front-end based on the Oscillation Based Technique (OBT), a current source for cell culture excitation, signal processing circuits devoted to parameter extraction from measurements, and the communication system for real-time signal acquisition and continuous recording. A microprocessor-based approach has been selected for system control and task management. Experimental results for the electronic systems performing measurements over several cell cultures will be described in the text, validating the feasibility of the proposed technique for the correct characterization of this type of biological assays.

Biomedical engineering is a multidisciplinary field covering many areas which form an extraordinarily wide and complex set of scientific research and applications, requiring the cooperation of many experts from different fields: biology, physics, chemical, medical, electronics, etc. The cooperation between different expert teams is fundamental for the success of the work. In our case, we have collaborated with several researchers of different groups and institutions. Dra. Daza Navarro and Dra. Martin Rubio from the Cell Biology department, Faculty of Biology (Universidad de Sevilla, US). Dr. de la Portilla from the Surgery department, Faculty of Medicine (Universidad de Sevilla) and also Instituto de Biomedicina de Sevilla (IBIS-US). Dr. Pablo Huertas from the Andalusian Molecular

Biology and Regenerative Medicine Centre (CABIMER, Universidad de Sevilla, US, Consejo Superior de Investigaciones Científicas, CSIC). Dra. Esther Rodríguez-Villegas, head of the Wearable Technologies Lab at Imperial College London, provided deep knowledge on data communication and low power design. Biomedical researchers from these teams provided valuable advise and supervision for the cell culture assays, the design of the experiments and the validation of the results obtained.

The document is structured in several chapters and the work is developed across them. Chapter 1 will introduce and define the problem, explaining the motivation, objectives and structure of the work. First, different approaches to biomedical sensors will be analyzed, specially those of reduced dimensions. The reason to select the electrical bioimpedance as a biomarker in this work will also be discussed. Second, a short introduction to bioimpedance analysis is presented, beginning with a review of the circuit techniques employed up to date, describing its main problems and solutions. Third, the electrode's role and the limitations associated to the proposed cell culture test will be analyzed. Fourth, the proposed work is centered on the application environment (cell-culture) and the main contributions, discussing their advantages and disadvantages. Finally, the objectives of the thesis project will be defined and the dissertation structure described.

1.1 Biomedical sensors

In 1993, Andreas Manz [1] initiated a brand new discipline. The development of a device capable of performing capillary electrophoresis on a single chip, first of its kind. The chip, generated using the know-how from microelectronic fabrication was part of a set of devices named Micro Total Analysis Systems (μTAS), a term coined by Andreas Manz himself. Soon, after the initial development, scientist realized that the original concept was applicable on a larger scale than previously thought. The functionality provided by the downscaling of many macro world machines; reactors, separators, fluid-handling devices, etc. could possibly lead to a LoC (Lab-on-a-Chip) based experimental science in the related fields of knowledge, to know; medicine, biology, chemistry, etc. [2].

LoC devices are currently developed as an alternative to acquire biological parameters, mimicking the protocols or alternatively enabling new assays techniques to substitute the heavy and huge classical biomedical laboratory systems. These devices allow a certain cost reduction in both expensive materials and human activities associated to bio-medical protocols [3]. The LoC paradigm aims to benefit from mature technology existing in several fields: biology, medical, chemical, engineering (electrical, mechanical, etc.), microelectronics, computer science, etc., to solve a measurement problem in the bio-medical domain,

but also looks for test samples at biological scale and dimensions, which open perspectives for new assays and scientific approaches since now biological samples could be measured individually, in contrast with the classical statistic approaches [4].

In a LoC system, the input is defined from a biological signal transduction initiated in a physical sensor device. This acquiring sensors can be classified according to their unique nature: optical, mechanical, acoustic, chemical or electrical.

The signal transduced corresponds to a real world variable under observation. Depending on the type of biological sample to be applied or entity, it is possible to create also an additional classification for the bio-medical sensors ranging from biological markers (bio-markers), cell-level processes, living tissue analysis, organs, up to body study. Another possible classification can be stablished in term of the type of biomedical instruments for sensing [5], defined in terms of:

1. The sensor: Optical, pressure, temperature, pH, etc...
2. The transducer: Ultrasound, capacitive, resistive, etc...
3. The organ or system: Heart, lung, skin, brain etc...
4. Medical field: Pediatric, cardiovascular, radiology, cell biology, oncology, etc...

Any criterion leads to a complex classification. Many systems may employ two or more physical principles, or combine a functional bio-sensing part with other physical or chemical part [6, 7]. Considering our problem approach: the conception of a small system for cell-culture test in general environments and applications, the magnitude (sensor) to be measured (used) has been selected to obtain a first and concise classification of reduced size (when possible) biomedical sensors summarized in Table 1.1. In this table are related only some examples of the multiple biomedical sensors of reduced dimensions that can be found in the literature. An analysis of these literature contributions will aid us to define the magnitude (sensor) to be employed in our system.

Many biological assays employ **optical** techniques to visualize and analyze the results. These type of assays are under further research to being implemented as LoC systems since optical sensors technology has proven itself reliable in the microelectronic technology [8]. As a consequence, large number of optical assays is being carried out on biomedical labs.

In [9], a fully integrated CMOS system is reported for optical detection and manipulation of cells. A 320x320 pixel array, with 20x20 $\mu m \times \mu m$ size is integrated along with the readout circuits.

In [10], a portable cell fluorometer is described, the system is oriented to bio-assays for metabolic activity and cell viability. This kind of studies are useful in cytotoxicity and

pathogen detection applications. Optical sensing is performed with CMOS photodetectors of 33.6 x 33.6 $\mu m \times \mu m$ size, and differential readout circuits.

Additionally, optical based methods can be combined with electrochemical sensing for water composition analysis. In [11], herbicide concentration is analyzed through analysis of both micro-algae fluorescence and oxygen production.

Discrete pulse-oximetry based on optical fiber is useful to measure the PhotoPlethysmoGraphy (PPG) and pulse oximetry in several organs such as as liver, stomach, brain, etc. [12], also in spinal cord [13].

There are some **Mechanical** approaches reported in the literature for biomedical applications. Micro cantilever arrays; for cancer cell sensing and monitoring [14]; and DNA test [15] applied to Hepatitis B virus detection. Furthermore, in combination with optical sensors, cantilever may be employed to perform DNA tests [16] or to evaluate thrombin concentration. On [17] an aptamer type or biosensor that exhibit superior sensitivity than classical inmunosensors for this parameter is presented. (Micro-Electro-Mechanical System) MEMs technologies can also be combined with capacitive modeling in [18], for blood pressure sensing from implanted stents.

Some approaches employ sound or **acoustic** signal processing to make predictions on apnea disease [19]. This work proposes a 3.74×2.4×2.1 cm weighed 17 gr. device that was fixed to the skin on the neck, implemented and tested in clinical trials. Furthermore, ultrasound based microscopy can be applied to detect single cells [20]. The results of this system are combined with images from an inverted optical microscope, which helps to understand the undergoing process although resulting in a big a heavy system. A surface acoustic wave microsystem is employed on [21] to perform food analysis which detects salmonella cells. Classical application to hearing aids devices are also reported, on [22] an implantable system implementing optic fiber vibrometer, following the interferometer principle is described.

Classical **chemical** sensor application has been applied to measure solution pHs. Initially, sensors were designed for single measurements, however, surface measurements are introduced recently thanks to the fabrication of 2D ISFET (Ion-Sensitive Field Effect Transistors) arrays to measure cell environment and cell activity [23] or improving DNA sequencing [24]. Furthermore, recent work illustrates applications on *eColi* detection [25]. In [26], an implant capable of measuring during 120 days a person's glucose level is described. This device analyzes immobilized glucose oxidase and catalase coupled to oxygen electrodes for long term glucose sensing. Biosensor implementation represents one of the main drawbacks for high specificity biological sensing techniques. Antibody binding is employed as biomarker in

[27], for sepsis analysis in pathology, combining micro-electrodes in a needle and biomarkers interleukin-6 (IL-6) involved in immune response to infections.

Electric sensing approach is the most prevalent of all existing techniques found in the literature. Several examples can be mentioned: Coulter principle allows to measures changes in electrical impedance produced by particles [28, 29]. A LoC is implemented including microfluidic parts to evaluate the number of bio-particles in a solution, more specifically blood particles. These are detected by voltage pulse generated in a voltage amplifier as a consequence of the increasing impedance due to the path followed by the blood particles. In [8], a two dimensional (2D) capacitive sensor array system is proposed for bio-particles location. Several cells are cultured and sensed with a voltage capacitive amplifier to obtain a cell location image map. Authors also employed bioimpedance to locate and manipulate suspended cells (3D) in a microfluidic system [30].

Tissue impedance can provide some information on the cell status or tissue damage [31]. In this case, the system proposed can detect heart ischemia during surgery or organ transplantation, by measuring wide heart bioimpedance changes in time.

ElectroEncephaloGraphy (EEG) studies report portable systems, which are under development, to perform continuous-time EEG signal recording [32] as a procedure to predict epilepsy episodes. This system includes hardware to perform EEG classification on chip. In addition, some bioimpedance approaches try to find an image description of cell cultures for cell count, toxicity analysis or cell motility assays [33]. Optimization can be performed to select the best frequency range for the sensor and to design a suitable analog front end. Moreover, some 3D systems for cell viability analysis under drug assays are reported in [34].

Fully integrated interdigital electrodes with a size of $4\mu m$, separated $3\mu m$ (on the same range of bacterial dimensions) are proposed in [35], to measure bacterial concentrations by sensing bioimpedance changes.

Electrical stimulation of cells can be applied to promote some cell properties, such as the cell growth rate. Furthermore, this technique can be useful to improve stem cell differentiation processes. In [36] a microsystem for DC and AC electrical stimulation of various cell cultures is reported.

Point-of-Care (PoC) systems might be developed from the enabling technology described through this section. Cell counting technology is a good example for this [29], similarly, physiology-stress evaluation through skin measurements [37] could be applied to diagnose certain conditions directly in the physician office.

To extend sensing applications, biomedical engineers can take advantage of existing technologies in microelectronic devices. Further application of MEMs devices include micro-actuators which, for instance, can store and deliver drug when needed [38], or even apply a certain amount of current to stimulate an organ or tissue [39].

From the overview in Table 1.1, optical and electrical sensing seems to be the most popular for cells studies. Mechanical techniques are usually based on very sensitive, micro-machined systems, with good selectivity, but expensive and fragile. Furthermore, a different set of popular approaches include those based on ISFET, but there is a limited amount of information which can be potentially acquired from cell cultures. Chemical biosensors achieve very high sensing specificity when based on a biosensor functionalization [15]. A specific problem found on this type of sensors is to maintain stable the biosensor properties. Despite difficulties arising due to degradation over long periods of time, certain techniques can achieve great performance as the glucose measurement technique described in the literature. Some acoustic approaches are also described. They need a sound excitation source and the use of complex acoustic models to decode the echoes received from samples under test.

Classical optical techniques, which have been widely employed in cell culture and biomedical assays, are recently being adapted to small laboratories using CMOS technologies. Despite this, like in most classical techniques, biomarkers are required (no free-label) during the assay protocol for cell targeting and later detection. Real time monitoring, require CMOS cameras which must be introduced on the incubator chambers. This chamber is at 95% relative humidity and water condensation might be an issue. This requires a special setup for a correct test. In any case, light passes easily through the cells and is valid for structural description studies.

Electrical techniques employ the bioimpedance property of cells to analyze the biological properties on the assays. Despite the fact that this techniques do not require any other help (biomarker or a secondary sensor) to obtain a representative measure of the cell culture status, the electrical performance or model for the full system must be known for a correct interpretation of the acquired data Low frequency test conditions are widely employed in most electrical impedance measurements [40]. As a direct consequence, the electrical path of the current flowing through the biological sample is drawing a path outside the cell, over the membrane but not considering the cytoplasm. Due to this, electrical techniques can be considered as good candidates for morphological cell studies (number and size).

Table 1.1 Biomedical sensors focused toward small or LoC systems

Sensor	Entity measure	Description	Reference
Optical	cell	cell location and count	[9]
	cell biomarker	handheld fluorometer	[10]
	water	algae detection	[11]
	tissue, organ	PPG, pulse oximetry	[12, 13]
Mechanical	cancer cell	cantilever	[14]
	DNA / virus	virus detection	[15]
	biomarker	cantilever	[17]
	DNA	DNA test	[16]
	blood	arterial pressure	[18]
Acoustic	body	sleep apnoea diagnosis	[19]
	cell	cell location	[20]
	cell	food analysis (salmonella)	[21]
	body	hearing aid	[22]
Chemical	cell	pH / cell activity	[23]
	DNA	ph / DNA sequence	[24]
	bacteria	eColi detection	[25]
	biomarker	glucose concentration	[26]
	biomarker	Interleukin (sepsis)	[27]
Electrical	cell / bio-particles	blood cell counting	[28, 29]
	cell	bio-particles location	[8]
	cell	cell location / manipulation	[30]
	tissue / organ	tissue impedance evolution	[31]
	brain	sleep analysis / EEG	[32]
	cell	cell-growth rate / motility	[33]
	cell	toxicological analysis	[34]
	bacteria	bacterial detection / concentration	[35]
	cell	electrostimulation	[36]

1.2 Bio-impedance

Biological Electrical Impedance or Bio-Impedance (BI) can be referred as an intrinsic electrical property of biological matter. It is possible to visualize it as the ability expressed by a biological tissue or sample to oppose (impede) electric current flow [40]. As mater property, electrical impedance represents a valid parameter to express actual status of any entity, in particular, those referred to biological matter. This fact opens the possibility to study biological systems from its nominal or expected bioimpedance value, and evaluate the changes from this nominal value as symptom of a process evolution, damage or assays in course. To positively evaluate any bioimpedance, two steps must be followed: First, correctly measuring using a precise technique and the corresponding electronic circuits to implement it. Second, evaluate the biological status of the bio-sample under test from the acquired measurements. The latest requires the application of the correct electrical model that emulates the electrical performance of the bio-sample. This dissertation will focus on both steps.

1.2.1 Electrical impedance

The electrical resistance, R, of an entity or component is a physical property accounting for the relation between a voltage applied, V, and a current through, I , occurring in an electrical circuit. Impedance represents the generalization of the Ohm's law which is capable of accounting for electrical behavior of resistors, capacitors and inductors [41] in generic electrical circuits (Figure 1.1).

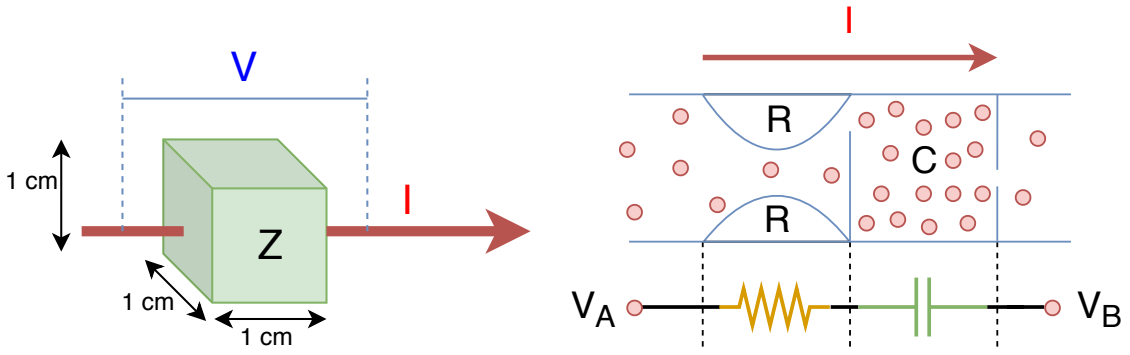

Fig. 1.1 (a) Voltage and current through an element of 1cm x 1cm x 1cm dimensions. (b) resistance (R) and capacitive reactance (C) current flow on any element.

Impedance (Z) is the general frequency dependent relation between Voltage (V) and Current (I):

$$Z = \frac{V}{I} \tag{1.1}$$

Z is represented as a complex magnitude, named impedance. It is a magnitude dependant on the whole frequency spectrum. R is the value of Z at zero frequency, or commonly named Direct Current or *DC*. As a complex property, real component comes from resistances (R), whereas inductors and capacitors contribute to reactance (X), which forms the imaginary component of the complex number.

$$Z = R + jX \tag{1.2}$$

And the inverse, the admitance, defined as $Y = 1/Z$, with its components:

$$Y = G + jB = G + j\omega C = K(\sigma + j\omega \cdot \varepsilon_r \cdot \varepsilon_0) \tag{1.3}$$

Being:

- G the real part of the admittance, called conductance, expressed in Siemens, $(S) = \Omega^{-1}$.
- B is the imaginary part of the admittance, called susceptance, expressed in Siemens, $(S) = \Omega^{-1}$.
- C is the capacitance, expressed in Farads (F).
- K is the geometry scale factor for the $cell = area/length$, expressed in centimeters (cm).
- σ is the material conductivity, expressed in Siemens, $(S) = \Omega^{-1}$.
- $\varepsilon = \varepsilon_r \cdot \varepsilon_0$ is the material permittivity, expressed in F/cm.
- ε_r is the relative permittivity of the material.
- ε_0 is the permittivity of the vacuum, $8.8 \cdot 10^{-14} F/cm$.

To represent the frequency dependence, the bioimpedance is usually named as Z(f) or Z(ω), where f and ω are the linear and angular frequencies respectively. Material properties are introduced on impedance equation (1.3) using its conductivity (σ) and relative permittivity (ε_r). In the specific case of study of this dissertation, a biological sample under test will have certain values of conductivity and permittivity characteristics, leading to a bioimpedance

which value provides insight on the physical characteristics of the sample under test, which is the reason to measure such bioimpedance.

1.2.2 Bioimpedance

Around 1957, Schwan noticed for the very first time, the dielectric properties of biological matter [42]. He reported that both dielectric constant (ε) and conductivity (σ) were varying as a function of the signal frequency, this experience was illustrated on the original article using Figure 1.2. These variations could be treated as if the biological sample was a discrete circuit at a given frequency, and it is possible to measure the electrical response or impedance associated to it, thus converting the biological sample in an electrical transducer. Furthermore, biological electrical impedance or simply BI (Bio-Impedance) represents the electrical response of biological matter to electric fields. This response, if analyzed, can provide some insight on several physical properties or status of the biological entity.

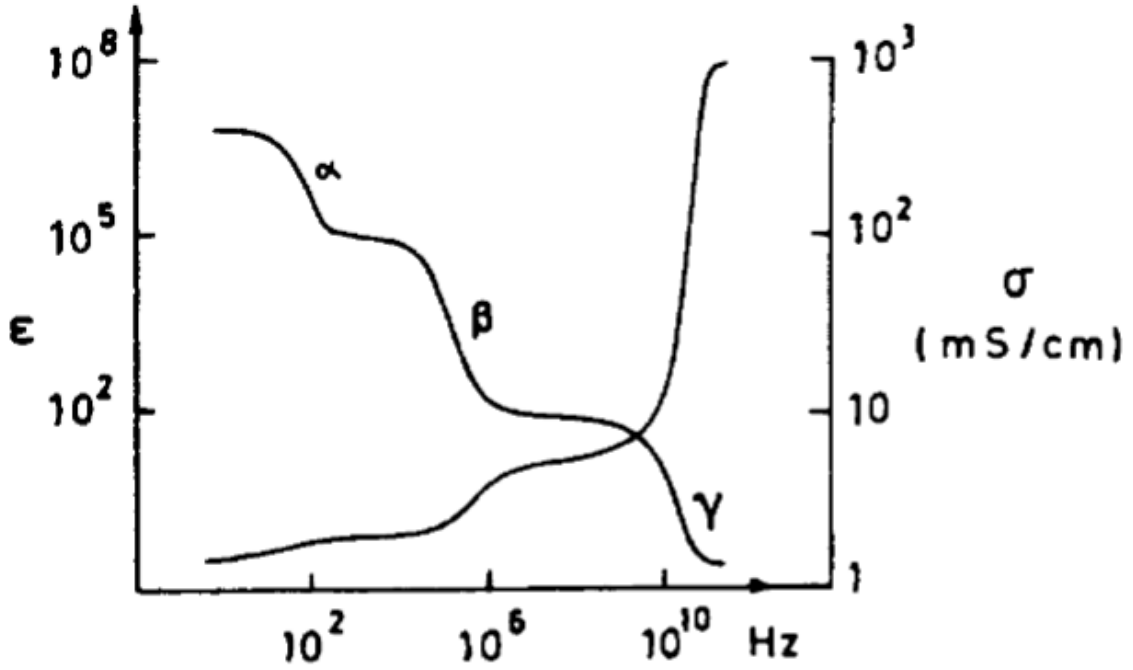

Fig. 1.2 Dielectric constant (ε) and conductivity (σ) variation over frequency spectrum for a biological sample. Introduced on original Schwan article.

From Figure 1.2, a large dielectric dispersion appears between 10 Hz and 10 MHz (α and β dispersion regions). They are generally considered to be associated with the diffusion processes of the ionic species (α dispersion), and the dielectric properties of the cell

membranes and their interactions with the extra and intra-cellular electrolytes (β dispersion). The dielectric properties at the γ region are mostly attributed by the aqueous content of the biological species and the presence of small molecules. There is a fourth main dispersion called δ, between the β and γ dispersion, around 100 MHz, that would be caused by the dipolar moments of big molecules such as proteins [43]. For cell culture impedance changes observed between 100 Hz and 100 kHz, the so called β dispersion is the region to consider. In each application, it must be evaluated the type of biological sample to be tested and the electrical model that better fit the sample.

For cells in culture, the model considered is based on the double lipid layer membrane (BLM: Bilayer Lipid Membrane). Such membrane forms a capacitive structure that isolates the intra- from the extra-cellular medium. The value of this membrane capacitance, C_{mem}, is around $1\mu F\ /\mu m^2$ for almost all types of cells. Also, the membrane is composed by ion-channels (Na/K), ions pump, embedded proteins, organelles in parallel [44], represented by a membrane resistance, R_{mem} (Figure 1.3). Moreover, the cell is attached to the substrate at a distance h, introducing the R_{seal} resistance over the small medium channel created from the attachment. Finally R_{sol} is representing the spreading resistance of the current flowing through the medium solution. Electrical values of the membrane resistance in the frequency range of 100 Hz to 1 MHz are very large (very low conductivity), so it is well accepted that C_{mem} represents correctly the electrical performance of cells in the β-dispersion region.

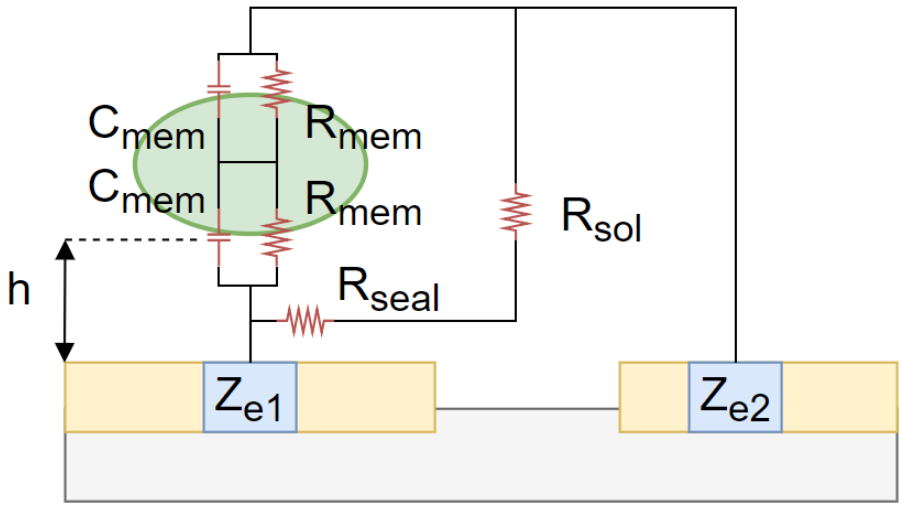

Fig. 1.3 Electrical cell model for the cell over the substrate at a adhesion distance h.

Different biological materials, such as tissue in organs, do actually need a far more complex model. This models will be affected by the inter-cellular gap regions, like myocardium or muscle tissues. For this kind of application, a Constant-Phase-Element (CPE) model it is accepted [45]:

$$Z_{CPE} = \frac{1}{T(j \cdot \omega)^{\beta}} \tag{1.4}$$

Where T corresponds to the impedance magnitude of the constant phase element, β is a parameter whose value affects the resulting behaviour of the system. Linear capacitor behaviour is found on $\beta = 1$ and resistive behaviour when $\beta = 0$. Typical values are on the range [0.5, 1.0].

Currently, many research goals are focused on measuring the impedance of biological samples. Several are the major benefits of measuring impedance in medical and biological environment. Firstly, most biological parameters and processes can be monitored using its impedance as marker. Secondly, it is important to remark that in most situations, the bio-impedance measurement is a non-invasive technique. Finally, it represents a cheap alternative technique to labs; compared to classical biological laboratories assays, which are based on signaling and labeling. For our proposal, BI represents an excellent candidate for real-time cell culture monitoring.

This initial chapter will describe and discuss the research and state-of-the art found on the literature and reference books. Such topics include a survey over different measurement techniques (section 1.3), an analysis of the electrodes for bio-impedance measurements (section 1.4) and application of both to cell culture measurements (section 1.5).

1.3 Bio-impedance measurement techniques

Transduction occurring in a biological sample is the physical effect leading by the specific parameters of the sample under test, the physical interface and the measurement circuits. To address the measurement problem of any bioimpedance, Z_x, with magnitude Z_{xo} and phase φ, a general test can be performed using an *AC* current source, I_x, as provided in Figure 1.4. When current source is applied to the sample under test, Z_x, a voltage level proportional to Z_x is generated, measured by a high input impedance Instrumentation Amplifier (IA). Contact points for interface represented as e_1 and e_2, are named "electrodes" generally fabricated from metal (platinum, gold, etc.). Electrodes not represent only the contact point between bio-samples and circuits; they transduce electrical current from electronic circuits supported by electrons into ionic current inside the bio-samples (or biological medium, in general) thanks to oxidation-reduction reactions (redox) over the metallic surface of the electrode [46]. Z_s corresponds to the electrical model of any impedance in the signal path and/or the source output voltage resistance.

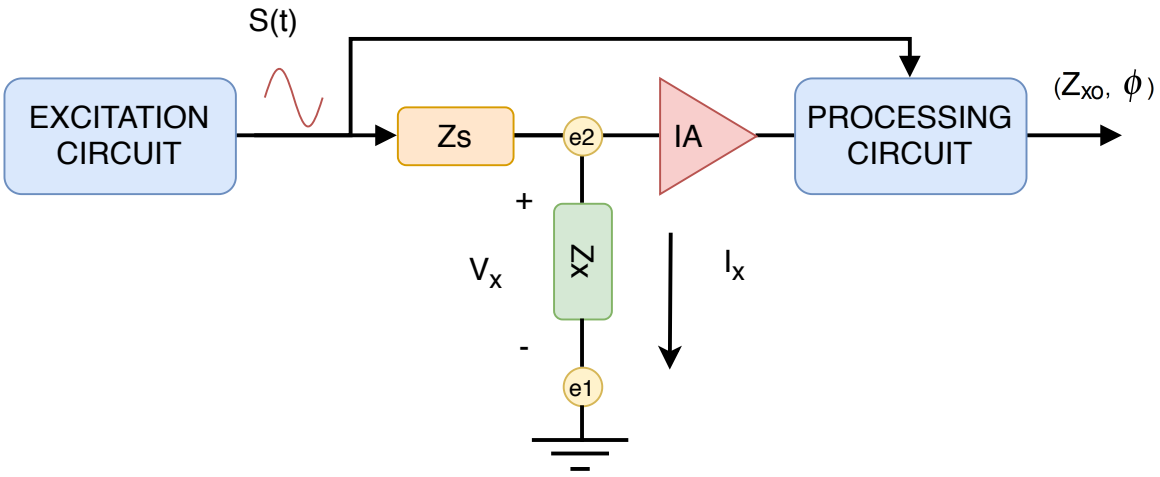

Fig. 1.4 Impedance measurement acquisition circuit.

As described before, the acquisition process usually requires the injection of an *AC* signal (voltage or current):

$$S(t) = A_0 \cot sin(\omega t + \varphi_0) \tag{1.5}$$

Where ω is the angular frequency, in rad/seg, A_0 the signal amplitude (current or voltage), and φ_0 would denote the signal phase, in rad. This signal is used to excite the sample under test, Z_x, and then, the response, voltage or current, is picked-up by a voltage amplifier or trans-impedance amplifier. Processing circuits must extract the useful information (Z_{x0}, φ) from measurement. In most of cases, it is necessary to establish a synchronization path with the *AC* excitation circuits to guarantee the accuracy of the technique. When the signal $S(t)$ travels across the biological sample by the electrodes, these operate as transducers converting electronic charge, at circuits, into ionic charge (at biological environment) and vice-versa. The excitation and processing circuits will be influenced by electrode impedance response. Hence, understanding the electrode-electrical model is a requirement for an adequate circuit design (excitation and measurement circuits). In general, for impedance measurement process based on electrodes, one of the first specifications to be considered is the electrical model employed for both: the electrodes and the biology systems [47].

Biological interface

Electrode influence is a major design factor on the excitation / measurement circuit design due to its electrical response. This is frequency dependent, with a wide range of impedance values depending on the working range, which can spread from several Ω to values in the MΩ range for very small micro-electrodes (patch-clamp). Furthermore, applied voltage to

electrodes must be limited in amplitude to guarantee its correct linear biasing region and assure bio-compatibility behavior, generally some tens of mV. For impedance measurement, the electrodes are usually on the *AC* signal path applied, so electrode response will influence eventually on the measurement. This behaviour will be analyzed in section 1.4.

Bio-impedance measurement techniques

A second major factor to be addressed in the system design for a BI measurement is the measurement technique selection. There are many BI systems reported in the literature [40]. Most of these techniques require adequate excitation and processing circuit design. Usually, including an *AC* signal generator, to provide a signal $S(t)$, which will be injected to the sample. Then, the processing circuits need to perform algorithmic tasks to derive the information generated over the sample under test. These are known as feed-forward techniques since the signal flows directly from the excitation circuits to the sample, and require signal synchronization between the processing and the excitation circuits. However, not all systems are implemented this way. There exists a second group of measurement techniques, which relies on a closed loop design. This approach establishes the operation point on the linear region for the electrode, which can limit the current flowing through the sample, and aims at solving some of the design constrains imposed by the electrodes. The former are known as feedback techniques.

1.3.1 Feed-forward techniques

Coherent Demodulation (CD)

A classical approach for measuring impedance is based on the coherent demodulation principle. In Figure 1.5 a system implementing this principle is presented. An excitation circuit is required to generate the AC input signal which is injected on the sample; Z_x. This signal is captured by a Lock-In Amplifier (LIA) to acquire and process the impedance value of the sample.

The setup presented in Figure 1.5 is reported on [48] and it enables bio-Impedance using a four electrode setup. This technique requires a precise amplifier and signal generation source to perform the measurement. Excitation circuits are affected by the electrode impedance response; however this technique takes advantage of a 4-electrode topology and removes the electrode contribution to the electrical response.

The lock-in amplifier implements a demodulation algorithm, which requires an accurate matching of two signals: in-phase and in-quadrature, generated guided by a reference from the excitation circuit; a square signal synchronized in phase with the reference acquired

from the excitation circuit, and a second signal, in-quadrature, shifted 90 degrees. The main drawback of this technique is that both separated channels for in-phase and quadrature components must be matched to avoid large phase errors. The principle is based on the fact that every biological impedance, $Z_x(t)$, has a resistive (R) and a reactive (X) components.

$$Z_x = R + jX \tag{1.6}$$

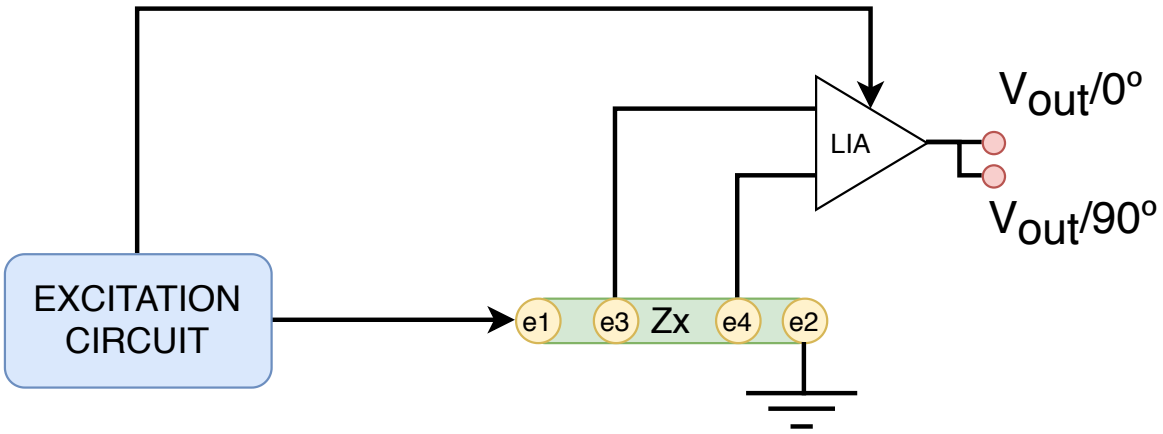

Fig. 1.5 Impedance measurement acquisition circuit.

Hence, using the Lock-In Amplifier is sufficient to acquire the magnitude and phase of the signal and hence derive the impedance of the sample since:

$$V_{out}|0 = Z_{x0} \cdot cos(\varphi) \sim R \tag{1.7}$$

$$V_{out}|90 = Z_{x0} \cdot sin(\varphi) \sim X \tag{1.8}$$

$$\varphi = atan^{-1}(\frac{V_{out}|90}{V_{out}|0}) \tag{1.9}$$

$$Z_{x0} = \sqrt{(V_{out}|0)^2 + (V_{out}|90)^2} \tag{1.10}$$

This technique requires very precise synchronization logic between the two paths created for the input signal (in-phase and quadrature). Otherwise, the resulting value is affected by the differences and errors may arise. A variation of this technique [49], proposes to perform signal amplification and then shift it to intermediate frequencies (IF) to process (LPF, ADC). Finally, the two components are demodulated in the digital domain.

Also, in reference [50] two-electrode bioimpedance measurement of myocardium tissue has been reported. This work employs iridium electrodes, already used on routine surgical

procedures, to monitor the evolution of ischemia on a tissue. Main design efforts should be set on reducing the low frequency bioimpedance of electrodes, since these are on the signal path. Liver tissue ischemia and necrosis status has also been measured and characterized in [51], using four-electrodes and a commercial Impedance Analyzer. A correlation between the cole-cole cell model and the cell damage under test is demonstrated on such article.

In reference [45], an AC signal is applied to study the long term response over a two-electrodes system implanted in the brain. Evaluation of the electrode response allows to analyze the degradation of response as consequence of the new tissue formed on the electrodes.

Some researchers describe in [52], a system based on first works on bioimpedance characterization [53] of cell culture and its performance on two-dimensional (2D) performance during laboratory assays. A direct measurement based on a voltage divider and two-electrode voltage response acquisition is implemented, obtaining the magnitude response in the range of 100 Ω to 2000 $k\Omega$. In addition, a direct voltage of 50 mV is applied in a similar system in [54]. Electrical models for cell-electrode system are proposed on [55].

A Trans-Impedance Amplifier (TIA) can also be implemented for current to voltage conversion of intensity delivered by cell-cultures when support *AC* voltages of 100 mV of amplitudes [44]. Programmable circuits in several frequency ranges and Automatic Gain Control (AGC) enable the circuit to compensate the wide range of electrical performance of microelectrodes over the frequency spectrum.

Also, in [56] the Agilent 4194A Impedance Analyzer can serve to characterize breast cancer cells in suspension. Here, two- and four-electrodes are employed as setups to identify several cell cancer lines in suspension (3D). The bioimpedance circuit employed is inside the equipment device.

In [57], a commercial system is employed to analyze the bioimpedance of skin to detect melanomas. Two electrodes are employed and the measurement circuitry is implemented on the commercial system. AC signals on the range [1 kHz, 1 MHz] are injected to analyze the electrical response.

Micro-motion of mammalian cancer cells are studied in [58] by the author of the Electrical Cell substrate Impedance Spectroscopy (ECIS). A model for attached cells is reported to analyze cell motility. A two-electrode system is employed in the spectroscopy.

Cell migration and cell motility is analyzed in [59], employing a tetra-polar (four-electrode system) along with a commercial impedance analyzer (Agilent 4294A). Speed of cells is measured on wound healing assays [60], and it is also proposed image tomography method for individual cell imaging.

In [61], a glucose sensor is implemented using two and three electrodes. In this case, a DC test is performed and a third electrode is employed for voltage control of the solution under test, avoiding the influence of half-cell potential developed by the electrodes in contact with the solution.

Aditionally, in [62, 63], a biosensor was developed to perform DNA detection using bioimpedance for label-free detection of DNA and proteins. A full LoC CMOS based system is designed using a 10x10 gold electrode-pixel array as the sensing area. An Electrochemical biosensor has been recently reported on [64] to perform DNA detection of Zika virus which employs a novel phase modulation for bioimpedance test.

Body water and fat composition are also potential candidates for bio-impedance analysis. In [65], a system based on a wearable prototype is proposed, using coherent demodulation. Intra-thoracic fluid measurement based on the in-phase and quadrature signals are implemented on [66], with low-power wearable circuits. Furthermore, extraction of the QRS and RA segment evolution in real time is performed.

In [67], active four-wire electrodes are employed to perform EEG recording and evaluation of bioimpedance for brain tomography (Electrical Impedance Tomography, EIT).

In [68], defibrillators performance is improved by increasing the measurement interface from two to four electrodes applied to respiration analysis. As a conclusion of the work, more sensitive respiration characterization can be obtained at low frequencies using two extra electrodes setups and commercial defibrillators.

Non-electrical signal as Pulse Wave Velocity (PWV) and respiration may be acquired as well using bioimpedance. On [69] a fully CMOS system prototype using two four-wire setups are proposed to test the bioimpedance at the wrist and thorax. A similar approach is reported in [70], with a PCB based system for PW Analysis that incorporates the possibility of frequency programming.

Synchronous Sampling (SS)

A second approach is proposed in reference [71]. In Figure 1.6 a 4-electrode diagram is depicted. Signal across the electrodes e_1 and e_4 would be:

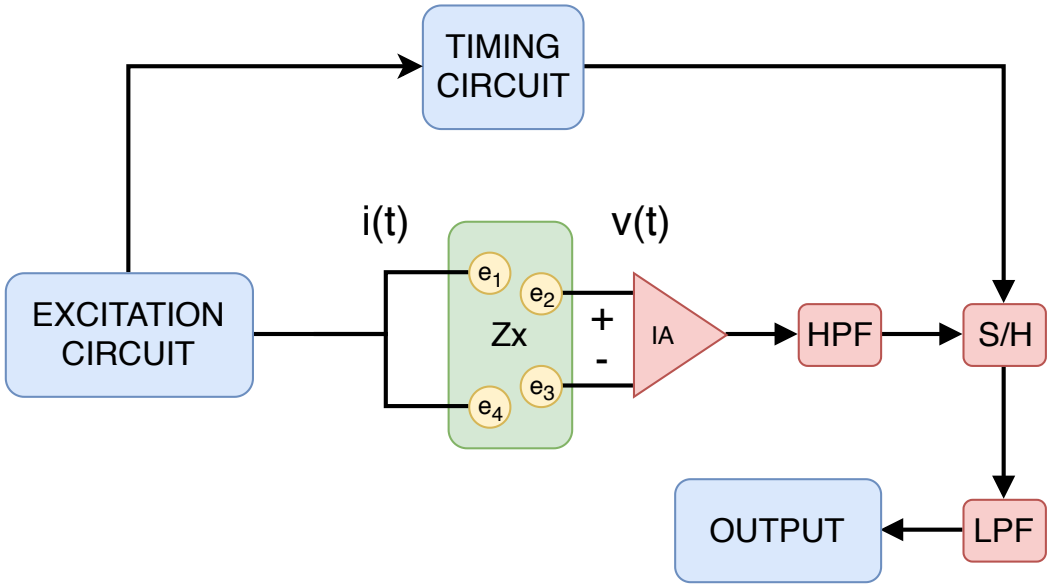

Fig. 1.6 Electrical diagram for a synchronous sampling bio-impedance measurement system.

$$i(t) = I \cdot cos(\omega t) \tag{1.11}$$

Whereas, the voltage drop over the electrodes e_2 and e_3 is denoted by:

$$v(t) = V(t) \cdot cos(\omega t + \varphi(t)) \tag{1.12}$$

Voltage can be also described as:

$$v(t) = V(t) \cdot cos(\varphi(t)) \cdot cos(\omega t) - V(t) \cdot sin(\varphi(t)) \cdot sin(\omega t) \tag{1.13}$$

From the previous equations $R(t)$ and $X(t)$ would be defined as:

$$R(t) = V(t) \cdot cos(\varphi(t))/I \tag{1.14}$$

$$X(t) = V(t) \cdot sin(\varphi(t))/I \tag{1.15}$$

Where $I \cdot R(t)$ and $I \cdot X(t)$ are the in-phase and quadrature components of $v(t)$ (resistive and reactive responses). The equations presented are valid for signals band-limited to the following frequency interval $[\omega_c - \frac{B}{2}, \omega_c + \frac{B}{2}]$. Such kind of signals permit interpolation of in-phase and quadrature components from samples acquired from $v(t)$. The system relies on the principle that implementing precise synchronization on the acquisition process makes possible to recover quadrature and in-phase components; corresponding to resistance and reactance components respectively. For each period of sampling time (T), two samples must be taken, separated a quarter of period (T/4). From such recovered values it is possible

to perform an impedance measurement without the need of implementing two channels demodulation as in the Lock-In Amplifier observed in the previous approach. Finally, the addition of a LPF in the signal path selects the final signal impedance (phase or quadrature) and prevents low-frequency noise and sampler interference.

Microprocessor based methods (μP)

In [72], several techniques are presented based on a microprocessor. The device acquires the bio-impedance signals (Figure 1.7) and performs different signal processing tasks employing the high computational power resources of nowadays micro-controllers and digital signal processors.

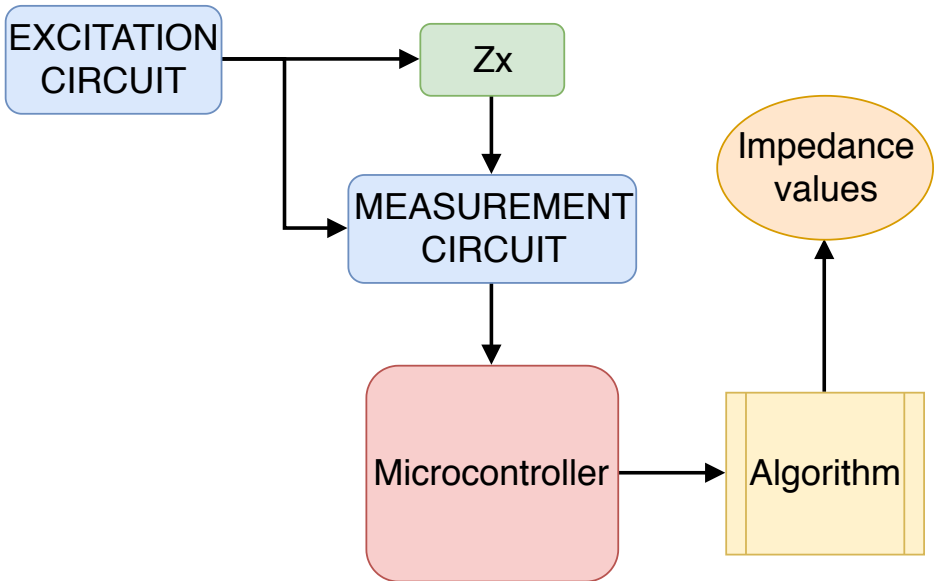

Fig. 1.7 Electrical diagram for a micro-controller based measurement system.

Signal processing techniques allow the estimation of impedance values by implementing an algorithmic method on the microcontroller. Some of the methods reported by the author include; Sine-Fitting, Multi-Harmonic Fitting, Complex Nonlinear Least Squares, Genetic Algorithms for Component Value Estimation, Gene-Expression Programming and Vector Fitting. Furthermore, on [73], an impedance spectrometer analyzer is proposed, which is based on a microcontroller platform that generates the excitation signal and performs the coherent demodulation employing a single microcontroller. This approach reduces the electronic component number and is capable of operating up to 10 kHz. All of these are algorithmic approaches which can be implemented on current devices available on the market.

Specific application integrated circuits as the ADAS1000 from Analog Devices can also be employed for signal acquisition. Such device, combined with an off-the-shelf network

analyzer AD5933 can be implemented for performing ECG signal acquisition and processing along with a Raspberry Pi 3 (RPi3) [74]. While the signal is generated on the analog frontends RPi3 the micro-processor transform the acquired samples to valuable information. A similar approach is followed on [75] to monitor body fluid composition.

Ramp Excitation (RE)

Recently, a new approach has been developed on [76], consisting of a two-electrode system that avoid sinusoidal excitation circuitry and substitutes it by semi-ramp excitation signals for cardiac pacemaker applications. This approach requires programmable gain amplifier with excellent CMRR and synchronization between the reference and measurement channels. Magnitude and phase signals are taken from Pulse Width Modulation (PWM) signals, generated from a voltage-to-time conversion.

Polar Modulation (PM)

A Zika virus test based on DNA identification is proposed on [64]. DNA identification is performed detecting changes of capacitance due to a hybridization process occurring on the device. Due to this, the authors focus on performing impedance phase-shift only analysis, avoiding the magnitude response. On the article a phase detector is implemented, employing low cost circuitry and a fast analog to digital conversion.

1.3.2 Feedback techniques

Closed Loop (CLoop)

The first feedback method analyzed is the closed loop technique for bio-impedance measurement presented on [33]. Authors designed an electronic circuit capable of performing impedance spectroscopy and single frequency measurement using CMOS technology. The closed loop allows to control the voltage injected to the electrode-sample complex, which provides greater control over the operation region of the system and permits to measure without requiring complex synchronization circuitry. This technique requires external AC stimuli to perform the measurement. The signals to build the magnitude and phase of the sample, Z_x, are acquired from the voltages V_m and V_φ, in Figure 1.8

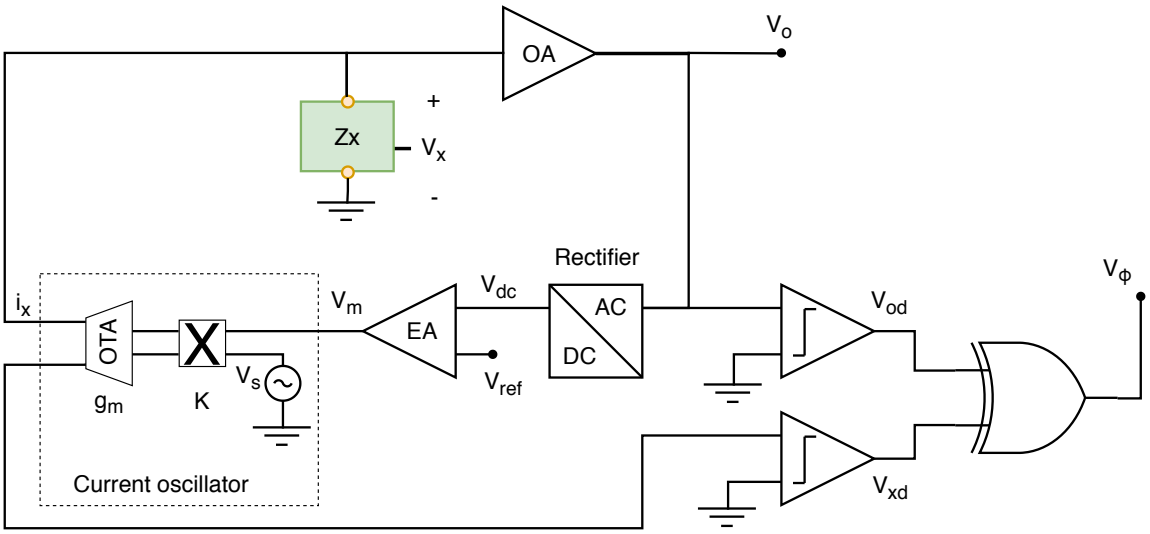

Fig. 1.8 Electrical diagram for a Closed Loop (CLoop) measurement system.

Oscillation Based Test (OBT)

Authors on [77] propose a different feedback sensing technique for bio-impedance analysis. The schema proposed is presented in Figure 1.9. This method enables a control of the voltage applied to the electrode thanks to the closed loop implementation (similar to the previous one). The main advantage of the technique lies on the self-oscillation generated by the oscillator. The oscillation signal is directed through the biological sample before reentering the loop and hence the sample affects the oscillation parameters, which are directly related to the impedance values of the sample under test. Hence, acquiring the oscillation parameters value (frequency and amplitude) would be enough to analyze the physical properties of the sample under test.

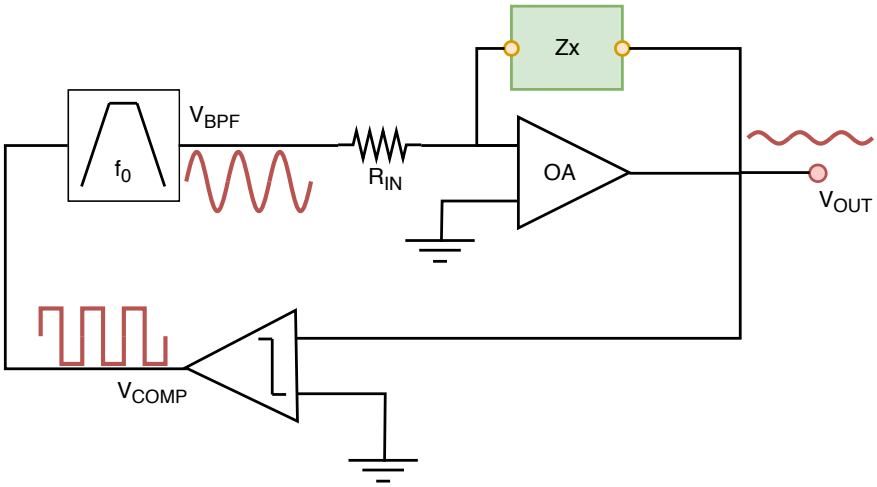

Fig. 1.9 Electrical diagram for an Oscillation Based Test (OBT) measurement system.

Following the analysis of several techniques for BI measurements, we can summarize that:

- Most of them need a sinusoidal current/voltage sources for sample excitation, which demand good and specific circuit design constraints [78], as low harmonic distortion, adequate output resistance and output compliance, the possibility to be frequency programmable for wide frequency ranges.
- Synchronization between the excitation signal and the measurement circuits is mandatory in feed-forward techniques. This makes necessary to have accurate timing circuits (SS) and/or excellent matched designs for in-phase and in-quadrature physical paths to preserve good precision.
- The Instrumentation Amplifier selected must be differential to reduce noise, with a wide band-pass frequency response for spectrometry applications, and good common-mode rejection ratio (CMMR). Usual CMRR values for topology in [79] are of 100 dB.
- Any technique must consider the influence of the electrodes, so setup choice and the impact on the circuit design should be evaluated when selecting the technique to be implemented. Electrode frequency influence should be evaluated within the range of interest.

Table 1.2 Bioimpedance techniques: applications and methods.

Bio-sample	Application	BI Method	Reference
Biomarker / assay	Toxicological analysis	HP 4192A, 2e	[35]
	Glucose concentration	Magnitude (DC), 2-3e	[61]
	DNA detection	CD, 4e	[62, 63]
	DNA, Zika virus	PM, 2e	[64]
Cell level	Cellular growth	Voltage divider, 2e	[52]
		CD, 2e	[44]
		Agilent 4294A, 2e	[80]
		CD, 2e	[54]
		OBT, 2e	[77]
		CLoop, 2e	[33]
	Impedance Spectroscopy	CD, voltage divider, 2e	[53]
		Agilent 4294A, 2e	[55]
	Bacterial Detection	HP 4192A, 2e	[35]
		CD, 2e	[44]
	Cancer	HP 4194A, 2-4e	[56]
		Scibase AB, 4e	[57]
		CD, voltage divider, 2e	[81]
		CD, Agilent 4294A, 4e	[59]
Tissue	Myocardial Ischemia	CD, 4e	[31]
		CD, 2e BI analyzer PPB 100	[50]
	Tissue Degradation	CD, 2e	[45]
	Tissue excitation	CD, 4e	[78]
	Liver ischemia / necrosis	CD, 4e, (Microtest-6379)	[51]
	Cardiac tissue	RE, 2e, CMOS	[76]
Body	EIT	–	[82]
	Body water & fat comp.	CD, R_s as reference, 4e	[65]
		CD, 4e	[75]
	Spinal Cord Stim. (SCS)	2e	[39]
	ECG	CD, 4e	[66]
		CD, 2e	[83]
		SS, 4e	[71]
		CD, 4e	[74]
	EEG	CD, 4e	[67]
	Respiration Monitoring	CD, 4e	[68]
		CD, 4e	[69, 70]

1.4 Bio-electrode electrical models

The influence of electrodes as interface elements on impedance measurement of biological samples (cells, tissues, etc...), is one of the major factors in any biomedical BI sensing system design. Bio-electrodes performing impedance acquisition can affect the voltage and current involved in test, due to their electrical response associated in consonance with their electrical model [84]. These models can change depending on the sensor type: resistive or capacitive, and the load involved in the application: saline solution, medium, cells, tissues, etc.

Two- and four-electrode represent the majority of existing setups used to acquire BI signals (Table 1.3). In Two-wire approaches, signal path incorporates the electrode response, while in four-wires this influence is cancelled or minimized [85]. Three electrodes approaches have also been reported, implementing a RE (Reference Electrode), along with the CE (Counting Electrode) to perform measurements, and the WE (Working Electrode) for excitation. The impact of skin electrodes on BI measurements was analyzed in some references, for instance, to evaluate the effect over ECG test, due to electrode electric model [83]. In all cases, the effect of electrode on BI must be evaluated and, if required, removed or compensated on the final measurement.

Electrode Interface model

The electrical electrode model definition is a preliminary design concern on any Bio-Impedance LoC. The impedance of electrodes immersed in ionic solutions is extensively described [84, 86–88]. When a solid (including metals, semiconductors, and insulators) is immersed in an ionic solution, ions in the solution can react with the electrode and the solid ions from the electrode can enter the solution. This leads to a complex reaction at the interface. An electrified double layer develops at the interface of the two phases. Eventually, electrochemical equilibrium is established at the interface: the current flowing into the electrode is equal but opposite in sign to that flowing out from the electrode. The net result is the development of a charge distribution at the interface with an associated electric potential distribution. The Helmholtz-Gouy-Chapman-Stern model is the commonly accepted model for describing the charge distribution at the electrode interface [46]. The negatively charged electrode attracts hydrated ions with positive charges to the surface but repels negatively charged ions away from the surface, yielding the profiles of cation and anion concentration C+ and C-, respectively. The water dipoles are also reoriented under the electric fields. Some ionic species that are not obstructed by their primary hydration sheath, such as some anions, can make their way to and come into the electrode. The charge distribution extends to the bulk solution thanks to thermal motion, forming an ion cloud-like diffusion layer and a

charge spatial distribution. The profile of the diffuse zone depends on the Debye length, which in turn depends on the fluid constant, the temperature, the ion charge number and the ion concentration of the bulk solution.

The electrical model found on the literature [44, 89] is presented in Figure 1.10. The interface develops the double layer yielding a C_I capacitance. Besides this capacitive behaviour there is a parallel effect modelled as the joint contributions of the R_t (Transfer Resistance) and Z_w (Warburg Impedance); represented as R_w in parallel with C_w. Finally R_s represents the spreading resistance through the electrolyte.

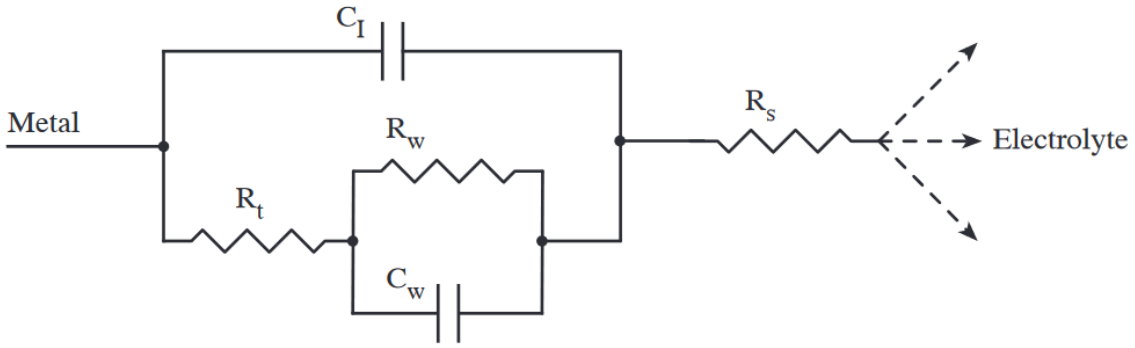

Fig. 1.10 Electrical diagram for the electrode model.

To illustrate electrode effect over the electrical response of the system, a simulation is presented considering the following values (figure 1.11). $C_I = 82\ pF$, $R_t = 27.1\ M\Omega$, $R_w = 91.7\ k\Omega$, $C_w = 1.7\ \mu F$, $R_s = 29.1\ k\Omega$ [44]. A 1 μA AC signal was injected to analyze the voltage drop over the electrode model.

From these figures, it is possible to observe that a typical electrode, presents large changes in magnitude and phase from its electrical model over the frequency range. For magnitude, a 60 dB factor (x1000) is found between low and high frequency values, while phase shift range is 90º. That means that for a given frequency, the circuit design (excitation / measurement) must consider a potentially large electrode resistance range, depending on the AC working frequency, and, which is more problematic, the same must be considered when spectroscopy analysis is done.

The circuit in Figure 1.10 describes, in a general sense, most of electrode performances. In some applications, there is only a capacitive signal path between the electrode-sample, so transfer resistance value can be rejected. Others require the model to match with the biological sample, for instance, tissue impedance measurement [45], cell cultures [77], or cell density in suspension 3D [80], due to particular relations observed between the electrodes and the bio-samples. In the electrode-bio-sample modelling field, alternative setups and methodologies for LoC system are currently being explored [3].

Warburg impedance (R_w, C_w) is associated to ion-charge diffusion at the interface and the greatest influence is located over low frequency ranges [54], in many cases where the operation point is located on higher frequencies its influence over the system can be neglected.

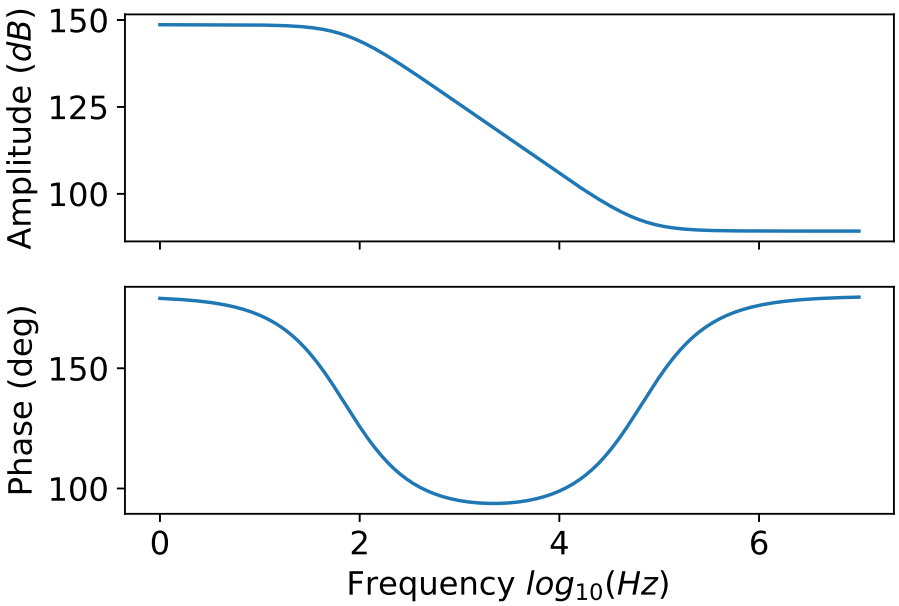

Fig. 1.11 Electrical response for the electrical model reported on the literature.

In the case of implantable and wireless applications, requirements for micropower integrated circuits must consider also the optimum energy efficiency for low power consumption, and low noise influence for very low signal capture and signal processing [47].

1.5 Cell-culture applications

On previous sections the physical parameter was selected (bio-impedance - BI). Most relevant BI techniques were analyzed and the electrode influence was introduced. This section will review the work developed for cell-culture real-time monitoring approaches, towards LoC systems centered on BI that exists on the literature. Next, the objectives of the thesis will be defined, and the dissertation organization will be described in final section.

Cell impedance analysis is accepted as a good method for performing cell assays characterization. It is a label-free and non-invasive technique, which enables a quantitative method that removes the need of performing the “end-point protocols” for cell culture assays. Furthermore, additional consideration is deserved to the efficiency in terms of material reduction and human work associated to cell culture assays. Since all measurements are acquired from the same assay, a deterministic approach would substitute current statistical approaches. A

quantitative method based on electrical sensing can provide several advantages, including real-time and wireless monitoring [90].

Type of cell cultures

Cell culture assays can be performed under several protocols, depending on the interest of the biomedical teams. From a system modelling point of view, different cell culture types are found; suspension cell cultures, attached cells to substrate electrodes, single cells in a flow system or impedance spectroscopy of suspension cells. The cell culture selection will depend on the biologist and medical teams.

Depending on the physical system under test, the modeling of the impedance is different. The ratio between the voltage and current on electrodes will correspond to different physical systems that will depend of the implemented assay and the electrical performance or model of the setup selected. Two major cases are identified: the cell is suspended in the medium or adhered to substrate.

When suspended in a culture or aqueous medium, the biological cells are considered with a membrane composed by a lipid bilayer plasma membrane [91]. The model corresponds to a conducting sphere (the cytoplasm is assumed to be homogeneous) and an insulating thin shell (the plasma membrane), as is illustrated in Figure 1.12 (a) The impedance accepted model for the cell, placed between two electrodes in a fluid is given by its Z_{mix}:

$$Z_{mix} = \frac{1}{j\omega C_{mix}} \tag{1.16}$$

Being C_{mix} the complex capacitance of the whole system which is proportional to ε_{mix}, the equivalent complex permittivity, which depends on the Clausius-Mossoti factor [30] and the electrical and geometry parameters of the system. Average dielectric properties of the particles can be derived using this model. Frequency range employed goes from 1 Hz to 1 GHz (reorientation of water molecules).

In Electrical Cell-substrate Impedance Spectroscopy (ECIS) techniques, the cell is adhered to the electrode substrate, Figure 1.12 (b). Its model can consider a membrane capacitance (C_{mem}), along with a membrane resistance (R_{mem}). The impedance of the cell-medium-electrode can be considered as the contribution of the electrode-medium interface, the medium, the adherent cell, and the cell-to-cell junction. Optimal frequency region for measurements are located in the range of 100 Hz to 100 kHz. The impedance of the electrode-medium interface and medium can be considered as a constant value, and the cell impedance as the increment from these values. ECIS is widely accepted as a morphological bio-sensor useful for long term monitoring assays.

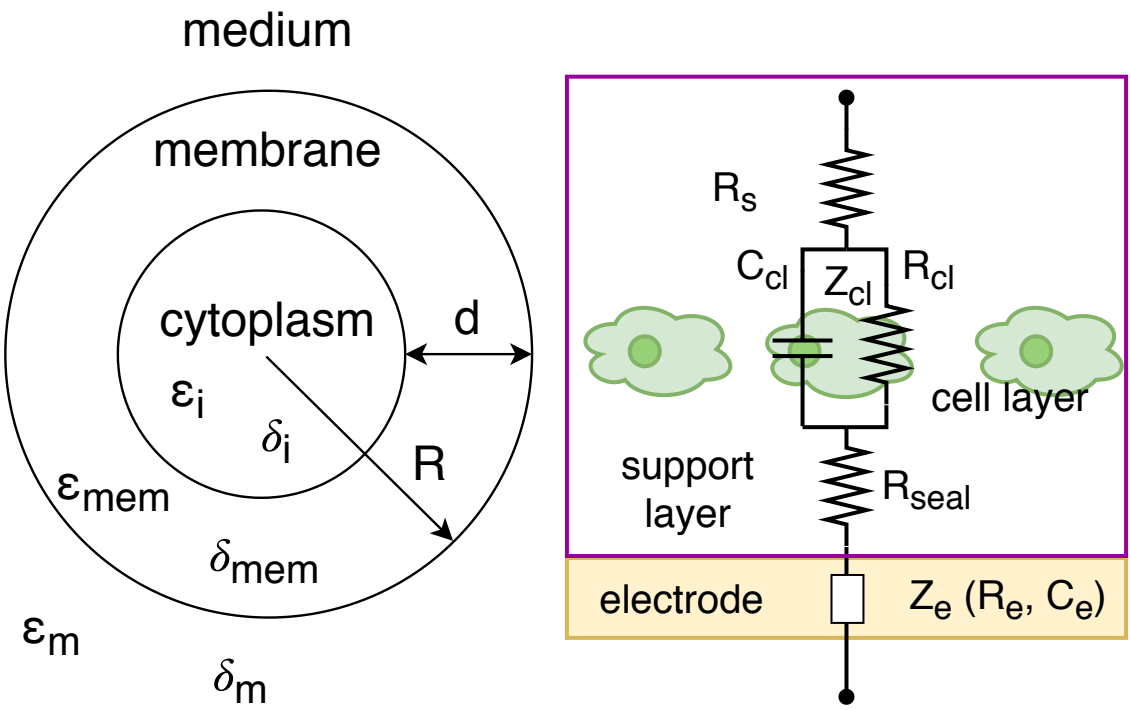

(a) (b)

Fig. 1.12 (a) Cell suspended in a medium. (b) Cell attached to substrate.

This dissertation selects **ECIS approach** since is the most common cell culture technique for biological and biomedical protocols, covering a wide range of useful application for biomedical researchers and clinics.

Type of electrodes

To measure the impedance values of cells, the measurement system requires the physical sensors to acquire the information of interest. Cells are located on the medium, the design of the sensor depends on the electrodes to apply the electric field to the cell-medium system as the interface elements. To measure biological cells with sizes of $10\mu m$ in diameter, the electrode size must be comparable to cell size. Microelectronic technologies represent a good candidate for electrode fabrication [62]. The electrodes must be built upon a substrate. Materials often employed for substrate are glass [92], which is transparent and compatible with microscopy systems, and silicon [93], which is non-transparent, but more compatible with electronic circuits [94] and other sensing structures in the same bulk [95]. For the electrode material, good electrochemical and biocompatible performances must be achieved. Gold (Au) is usually the ideal candidate for electrodes fabrication, which is also compatible

with microelectronic fabrication techniques [96]. Other material includes Ag/AgCl, Pt, Indium Tin Oxide (ITO), and others. Fabrication process includes classical metal deposition, lithography, and reactive ion-etching [97].

The final electrode shape will affect the electric field distribution of the sensing system and the sensitivity of the detection. Inter-Digital Electrode (IDE) arrays, circular electrodes optimizing the sensitive area are common topologies for electrodes [44] [98].

ECIS Applications

Any biological process associated with the cellular morphology or membrane impedance can be monitored by an ECIS system. Cell apoptosis [97] and cell proliferation [99] are examples of assays where the results are directly related with the area of cells adhered to the electrode surface, producing an impedance change. In addition, ECIS has been applied to drug screening [100], toxicity test [52], cancer research [101], cell cycle [102], cell adhesion [103], motility [58], stem cell differentiation [104] and others. Two-electrode setups are employed in all these works, placing the sensing electrode under the cells to be measured, in the signal path of the current. Most of realization employs this resistive sensing principle, being possible to approach to ECIS concept by capacitive coupled electrodes [94]. Table 1.3 summarizes the most relevant realizations of ECIS systems.

Table 1.3 Main BI cell-culture based works and characteristics (ECIS)

Application	BI Method	Electrodes[1][2]	C[3]	W[4]	Freq.	Ref.
Cell growth	Voltage Divider	Au AB[5]. 250 μm (d)	Y	N	1k, 2k	[52]
	CD	Au-Pt 4.4-27.4 μm (d)	Y	N	0.1k-100k	[44]
	Agilent 4294A	Au AB[5]. 250 μm (d)	N	N	0.1k-3M	[80]
	CD, HP 4192A	Au, 2μm (l) 2D	N	N	0.1k-1M	[54]
	OBT	Au AB[5]. 250 μm (d)	Y	N	8k	[77]
	CLoop	-, 50 μm (l)	Y	N	10k-100k	[33]
	Capacitive sensors, CMOS 0.35μm	Al+PDMS, IDE, 50μm (l), 8x8 2D	Y	N	-	[105]
Cell growth and motion	CD voltage divider, LIA	2e 130 μm (l)	Y	N	4k	[53]
Bacterial Detection	HP4192A	Au, IDE 4 μm	N	N	10-10M	[35]
Cancer	HP4194A	Pt, needles	N	N	3k-3M	[56]
Micromotion	CD voltage divider	Au, 1000 μm (l)	N	N	22-90k	[81]
Motility/EIT	CD Agilent 4294A	Pt, 5-4000 μm	N	N	0.1k-1M	[59]
Electrostimulation	CD μm CMOS 0.13 μm	Au, 28 μm (l), 1024x1024	Y	N	<100k	[95]
Cell growth Neointimal tissue	Autolab PGSTAT302N	Au+Pt	N	N	0.1k-100k	[96]
Cell adhesion viability motility	Capacitive coupling CMOS 0.35μm	Al+PDMS, IDE, 50 μm (l), 8x8 2D	Y	N	-	[94]

[1] 10μm (d) means, circular electrode with 10um diameter.
[2] 10μm (l) means, squared electrode with 10um side.
[3] Circuit implementation: yes (Y), no (N)
[4] Wireless communication: yes (Y), no (N)
[5] AB: Applied Biophysics electrodes.

1.6 Objectives

Description

Traditional techniques for cell culture assays involve vast amount of human, material and time resources to perform and analyze a single cell culture experiment. The design of a system capable of performing this task in an automated way while reducing the variability of the measurements is of great interest to the biomedical researchers involved in cell culture experiments.

The proposal presented in this thesis project is oriented towards the design, implementation and validation of an automated system which will sense and analyze the cell cultures experiment in real time. The prototype will be based on the Internet of Things (IoT) [106] paradigm. The project contemplates three different scenarios where the different devices involved in this system will interact; Sensors, Gateway and Services. A global schema is depicted in Figure 1.13

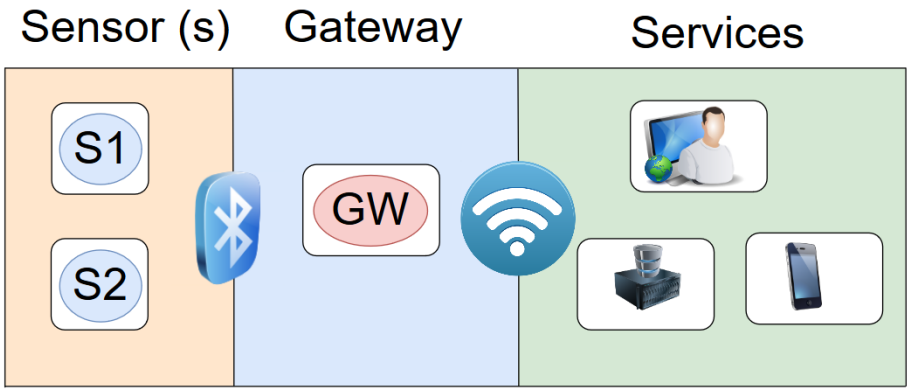

Fig. 1.13 Internet-of-Things (IoT) architecture. Cell culture sensor(s) are connected to the gateway using a Bluetooth link. The whole process will be guided using a gateway device which connects to the internet by an Ethernet link. The gateway uses this link to access the experiment configuration and store information on a remote database. The biomedical researcher finally can access the services provided by the system using a web application on either a personal computer or a smartphone.

Internet of things paradigm establishes a three layer structure formed by the sensors, a gateway and the service layer. On this project, a sensor is the physical device performing the cell count estimation. The device must perform accurate sensing of the sample under test and consider low power consumption requirements. It will be located inside of the cell culture reactor and will be powered by a battery. The communication between this device and the corresponding gateway will be performed via a Bluetooth link.

The second design layer is formed by the gateway. This device acts as a bridge between the sensors and the services. It will be physically located on the biomedical laboratory on a nearby position to the cell culture incubator and will communicate with the sensor to perform measurement specific tasks applying the established measurement protocol. Once the measures are acquired, the gateway will use the storage service to store the information on the remote database. The link between the gateway and the service layer is created via a TCP/IP connection.

Finally, the third layer is formed by all the services the system will expose to both; biomedical researchers as users of the system, and the gateway as the sensor controlling device. The services will be provided by a remote server and are summarized below:

- MySQL database as a storage service.
- Backend services to provide access to experiment management and data.
- Web interface providing the user interface.

The user will perform its interaction with the system by the means provided by a web application, accessible from a personal computer or a smartphone. This web application will provide a secure access to create experiments, edit experiment constraints in real time or visualize the information gathered by the sensors. The gateway will be connected to the MySQL database to acquire the experiment parameters and to store the information sensed from the sensor device.

Sensors, Gateway and Services will be implemented in this work for real-time monitoring of cell culture assays. Every component of the IoT system and the solution proposed in any case are described through the present dissertation.

Objectives

The general objective of this thesis is to contribute with new circuits and systems for the real-time monitoring and characterization of cell culture assays. To fulfill this objective, the dissertation will be divided in several tasks or sub-objectives, which are:

- **To apply the bioimpedance as the main electrical parameter for sensing** in the proposed system, due to several reasons: first, the electrical properties of the biological matter, in our case cells, that enables its electrical sensing. Second, the compatibility with the development of electronic systems for “reading” the response signals. Third, the projection, as an excellent candidate, for LoC implementations.

- **To model the electrodes and the electrode-medium-cells**, as a key point for system design. From circuit design point of view, these electrical models will be part of the working specifications, mainly, magnitude and phase ranges, and frequency range. From response point of view, electrical model will affect the reading of signal and help to decode the results.

- **To propose new circuit designs for ECIS test**. The circuit will include the signal excitation circuits and the analog front-end required for picking-up signal responses. Circuit design should be adapted to cell-culture standard assays, both in long-term assays (power consumption), as in physical conditions compatibility in culture chamber (humidity, temperature and CO_2).

- **To build a full system for cell culture experimentation**, including the electrode sensors, circuits for signal processing, digital test control, and wireless communication required for test. Signal processing will be done in real-time in the system and information acquired send to a web server for assays monitoring.

Document's structure

The following structure describes the work developed in this dissertation.

The electrode-medium theory is described in **Chapter 2**.The main accepted electrical model for a micro-electrode of metal immersed into a liquid solution is defined, and the equivalent circuit together with the design equations for each component. This will be extended to electrode-medium-cell introducing a new resistive parameter (R_{gap}) and a geometrical parameter, fill-factor (ff), for cell-to-electrode area coverage description. An experimental proof will be done to validate the correctness of the model. Finally, time simulations for cell growth processes are implemented, incorporating the presented electrical model. Simulations will be applied to commercial electrodes employed in this work, to evaluate the performance of the model and approximate the errors.

Chapter 3 explains the main concept for Oscillation Based Test technique applied to ECIS assays. Fundamental equations for OBT are described, and design constrains highlighted. An OBT system for cell-culture monitoring is proposed, incorporating the electrical model described in chapter 2 for electrode-medium-cell systems. Functional and electrical simulations are reported, predicting the viability for cell culture growth characterization thanks to the oscillation parameters: f_0, the oscillation frequency, and A_0, oscillation amplitude, and the electrical model proposed for the bio-system. The final prototype will be presented in Chapter 4.

The analog front-end circuit for the sensor, together with the circuit for bio-sample excitations are described in **Chapter 4**. Main circuit blocks are reported: a band-pass filter, a comparator, a current source excitation and some LP/HP filters. Operational amplifier based design solutions are described and the experimental results demonstrating its correct performance are given. Furthermore, an start-up circuit has been included to initialize the circuit oscillations. Digital control and communication system are described in this chapter as well. A microprocessor-based approach was selected for this purpose. The μP will govern all system actions and sequentially execute them in time. In our case, eight wells or cell cultures will be tested for each assay, being multiplexed in time. Furthermore, sample time will be set by the μP. Analog-to-Digital conversion will be done thanks to the embedded ADCs of the μP. Finally, the full system is presented including the power system, electrode cage and isolation, web server, remote database, etc.

Chapter 5 will describe how signal processing is done, for extracting amplitude and frequency from the obtained oscillation. Algorithms are described and tested along the chapter, illustrating the estimation process for frequency and amplitude. Optimization of the process is fundamental for performing the signal processing on the μP. The resulting implementation improves the FFT results reducing computational workload, and hence optimizing power consumption.

Experimental results obtained from five cell culture assays are described in **Chapter 6**. Four different cell lines were employed, and three different experiments set: cell growth, cell differentiation and cell toxicity. An analysis of the obtained data confirms the correct system design, and the potential to quantitatively estimate the cell density in time by applying the reported electrical models for electrodes and cell in this thesis.

Finally, conclusions of the work will be highlighted at the end of the dissertation, and some lines of the future work given.

Summary and conclusions

- The main objective of this thesis was defined, including the design, fabrication and test of circuits and systems required for the real time monitoring and characterization of cell culture assays, useful in many biomedical environments and disciplines. The selected sensing parameter is the biological impedance (Bio-impedance) of cells due to the electrical properties of the biological matter.

- Electrical sensing approach has been selected among other physical alternatives for sensing due on biological properties, and the direct feasibility for electronic circuits testing: use of voltage/currents for BI sensing, potential low-power consumption and low voltage operation, small size, and in general, maturity of the microelectronic technology for practical LoC implementations.

- Cell-culture electrical performance has been introduced by means of the electrical model of both: electrodes and cells, highlighting the relevance of these electrical performances for the correct circuit and system design required for testing.

- An introduction to the cell-culture applications, types of assays, electrical model for cell in cultures, electrode fabrication has been done, concluding that the Electrical Cell-Substrate Impedance Spectroscopy (ECIS) technique is a widely employed and reliable technique for cell-culture characterization. It has been selected in this thesis for cell culture assays.

- The system proposed in this thesis has been defined in the context of the Internet of Things (IoT) paradigm, in which, sensors, gateway and services are the three main actors. In this sense, the Oscillation Based Test approach has been selected as the sensor avoiding the need of any voltage/current sinusoidal excitation circuit and complex instrumentation amplifiers. Moreover, it does not require specific design for signal synchronization. Finally, the OBT feedback approach allows us to control and set the voltage/current flowing along the electrode-medium-cell system, mandatory for optimal electrical electrode model validation and biological constrains.

The state of the art for Bio-Impedance (BI) measurements circuits techniques has been reviewed, finding out that:

- Most of these techniques employ feed-forward circuits, based on Lock-In Amplifiers (LIA) and four-electrodes setups, leading to synchronization problems related with the matching of magnitude and phase circuits paths, requiring accurate AC excitation circuits, and instrumentation amplifiers with good CMRR figure of merit.

- Most of them need a sinusoidal current/voltage source for sample excitation, which requires complex and specific circuit design constraints [78], such as low harmonic distortion, adequate output resistance and output compliance and the possibility to be frequency programmable for wide frequency ranges.
- Synchronization between the excitation signal and the measurement circuits is mandatory in feed-forward techniques. This makes necessary to have accurate timing circuits and/or excellent matched designs for in-phase and in-quadrature physical paths to achieve high precision.
- The selected Instrumentation Amplifier must be differential to reduce noise, with a wide band-pass frequency response for spectrometry applications, and good common-mode rejection ratio (CMMR). Usual CMRR values for topology in [79] are 100 dB.
- Any technique must consider the influence of the electrodes, so the choice of the set-up technique and its impact over the circuit design should be analyzed. The influence of the electrode frequency response should be evaluated within the range of interest.

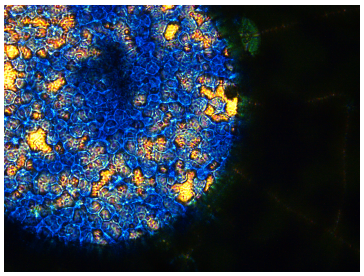

Chapter 2

Electrode modelling for cell culture assays

2.1 Cell culture assays

Cells conform the basic unit of life, where all biological functions are performed. Living organisms on earth are divided in either prokaryotes (single cell organism) or eukaryotes (multi-cellular organism). In eukaryotic organisms cells act in cooperation forming up organs and tissues to achieve a higher order of functionality (and complexity).

Biomedical researchers can reproduce the cell cycles from eukaryotic cells on the laboratory. This kind of assays provide a valuable deep insight into cell dynamics, growth and behaviour. Furthermore, it is employed to test for environmental variations applied to the cells, such as nutrient provision, amount of radiation tolerated, toxicity assays and drug response. All of them illustrate the cell reaction to the external stimuli provided to the cell culture in a controlled environment and can be used among many other applications to identify and analyze medical candidates to treat certain conditions which can affect the human population [107].

Cell culture assays require a controlled environment in terms of external conditions. The former need to be performed on a cell culture reactor with a fixed temperature of around 37º C, high relative humidity and 5% CO_2 atmosphere. These assays have been performed in biomedical laboratories since mid-20th century [108, 109].

Cell culture protocol

Cell cultures assays are accepted as the major tool to observe the cell behaviour under controlled conditions. This observation requires an important amount of human effort and material costs which are associated to the protocol involved on any cell culture assay [4].

Biomedical researchers perform this kind of assays using a controlled environment and cell culture plates. Cells are seeded on the plates to let them grow on the reactor. Whenever the experiment requires an observation (cell amount determination) cells will undergo a process involving several steps. Firstly, the cells need to be fixed to the substrate, a task which is performed by adding trypsine to the sample. Secondly, the fixed cells need to be marked using a specific color additive which will allow the optical analysis of the sample. The final stage of the measurement process involves either cell counting in specific laboratory equipment or the visual inspection on the microscope to count the cells. This protocol is depicted in Figure 2.1 for a number of cells versus time.

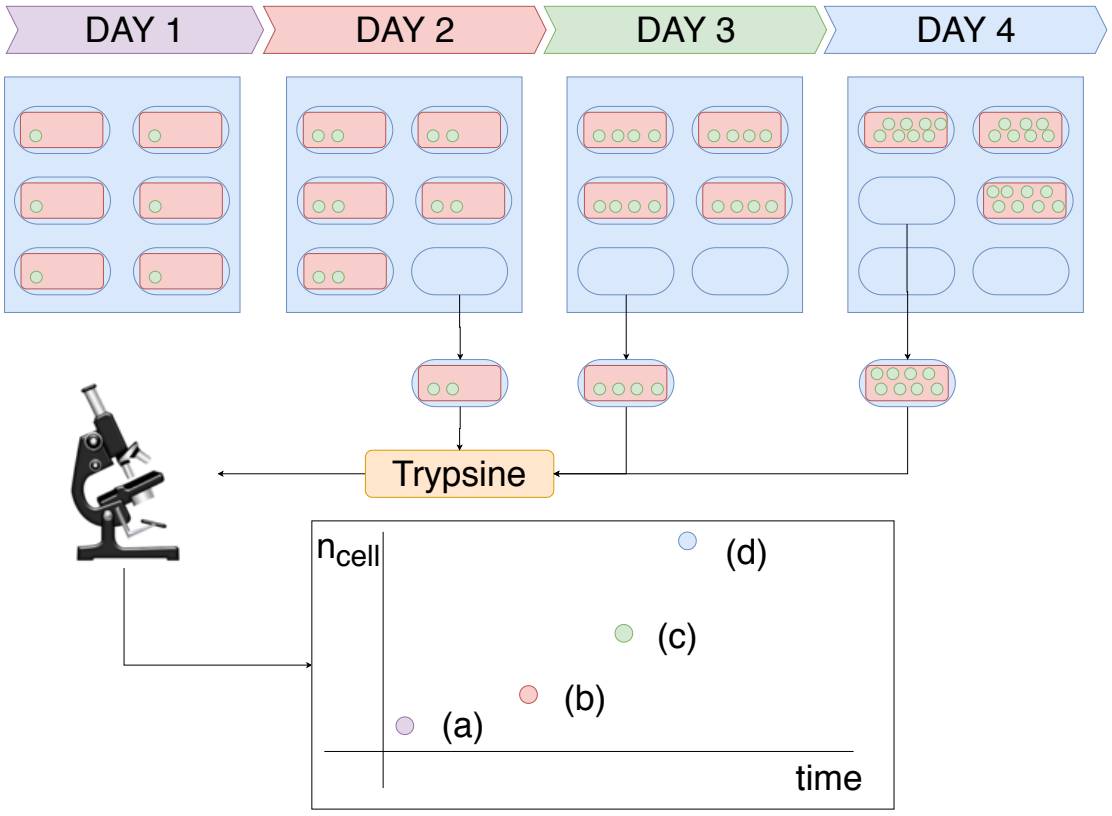

Fig. 2.1 Generic cell culture protocol. Cells are seeded on day 1. Each consecutive day a sample will be trypsinized and observed under the microscope. The information gathered corresponds to days 1 (a), 2 (b), 3 (c) and 4 (d).

The process, as was mentioned, is costly in terms of human effort devoted to analyzing the sample. Moreover, the sample observation requires a single cell culture plate each time a sample is counted (end-point protocol). Even though the cell culture assays protocols are very strict, a certain amount of uncertainty arises from the parallel sample preparation, which is necessary to obtain the cell number on intermediate steps. These protocols have a large variability due to the fact that information is acquired from similar, but different cultures, leading to a potential source of result dispersion. The procedure requires the preparation of three biological assays in parallel to validate a significant result from any experiment.

2.2 Electrode Cell-Substrate Impedance Sensing (ECIS)

Classical methods can be improved with technological advances such as Electrode Cell-Substrate Impedance Sensing (ECIS). The physical principle for measurements using this technique is based on electrodes, usually fabricated with metals (platinum, gold, etc). Cells are deposited on top of electrodes as part of the sensors (S1, S2), which increases the resistance observed between both electrodes (Figure 2.2). From the analysis of the resulting bio-impedance it is possible to infer the cell number. However, to reliably interpret the measurement it is necessary to characterize the physical properties of the electrode.

An electrode immersed in an ionic solution generates an electro-chemical equilibrium reaction leading to a complex inter-phase region on the contact space between the solution and the solid metal [46, 44]. Consider an experiment where an electrode substrate immersed on an ionic solution a certain amount of cells are seeded. The natural behaviour of cells in substrates is to reach the bottom of the substrate and adhere to it, hence, developing a small layer of cells over the substrate.

Electrode Cell-Substrate Impedance Sensing or ECIS is a well documented technique with plenty of results reported on the literature [81, 110, 111]. This technique consists on the analysis of the impedance response evolution of seeded electrodes. This setup allows for the definition of many different types of experiments; cellular growth analysis, cell motility, cell line identification, cytotoxicity, and more [101, 103, 112].

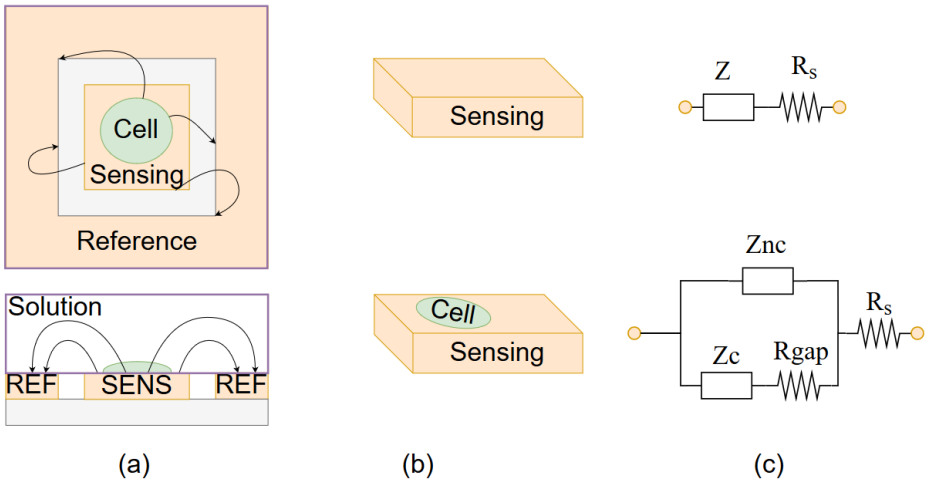

Fig. 2.2 (a): Top and cross view of the cell-electrode immersed on an ionic solution. (b), (c): Differences between electrical models when the electrode is empty (top) or partially covered by cells (bottom). The reference electrode is assumed to be greater than the sensing electrode.

The basic system is formed by a set of electrodes immersed in an electrolyte solution (Figure 2.2). The electrical impedance equivalent circuit model (c) for the empty electrode (b) is depicted on TOP whereas in BOTTOM the impedance model (c) describes the effect when cells are laying over the electrode. Electrical response contribution varies from the empty electrode as an effect of the current partially flowing through the second path containing R_{gap}. From the illustration above Z_{nc} describes the impedance of the non-covered electrode signal path, whereas Z_c defines the impedance of the cell covered electrode.

The analysis of any measurement taken over a two-electrode system such as the one depicted on the igure requires the knowledge of the electrical performance of electrodes and cells. Both of them contribute to the electrical response of the system since they are located on the signal path [54].

2.2.1 Double-layer inter-phase

The physical immersion of a solid into an electrolyte involves the development of an electrified interface at the electrode surface. Since the electrolyte (A) is an ionic solution dissolved in water there exist a certain ion dissociation effect of the ions contained on the solution. This is modelled by the following oxidation reaction:

$$A \rightarrow A^{+} + e^{-} \tag{2.1}$$

This process is lead by the ionic reactions between the electrolyte and the metal electrode which can be described by the following reduction reaction:

$$A^+ + e^- \rightarrow A \tag{2.2}$$

This effect influences the undergoing chemical reaction by the generation of an electrical field which inhibits the reduction reaction while favouring the oxidation one. The complex behaviour on the formed interface will eventually reach an equilibrium condition where net current flow to/from the electrode is equal to zero. The equilibrium leads the formation of a charge distribution formed by the ions solvated in water, specific adsorpted ions on the electrode and the water molecules on the solution. Figure 2.3, adapted from [44], illustrates the whole process depicting two involved layers. The Inner Helmholtz plane (IHP) is formed by water dipoles forming a hydration sheath on the electrode surface. The IHP may include adsorpted ions too, in a sparse distribution along with water dipoles. Next to the IHP there is a second layer formed by the solvated ions under polarization in the near space. This second layer is denoted as Outer Helmholtz Plane (OHP) [44].

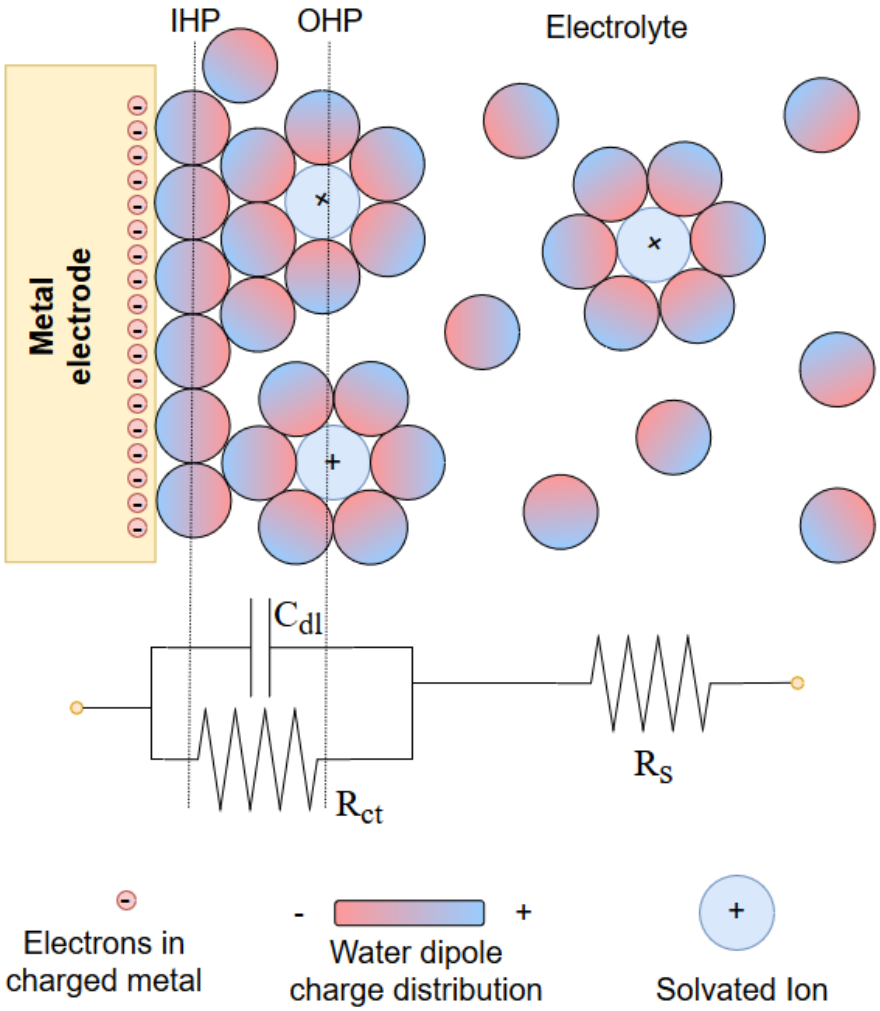

Fig. 2.3 Double layer interphase. Both Helmholtz planes are depicted as IHP and OHP, located nearby the electrode and contributing both to the double layer capacitance (C_{dl}) and the transfer resistance (R_{ct}).

This effect induces the development of an impedance at the double layer inter-phase generated on the electrode-solution contact region (Figure 2.3). The impedance is modelled by a resistor and a capacitor in parallel. A theoretical approximation to the values of such parameters can be obtained following the method and equations described on [44, 113]. The following pages illustrate such approximation based on the aforementioned literature. The model exposed is valid for small values (AC) of voltages applied on the electrode due to the exponential nature of the current density function. Small voltage values ($< 100\ mV$) assure correct behaviour of the electrode on the linear region [44].

Charge transfer resistance (R_{ct})

The effect described on previous pages accounts for the static picture of the electrode immersed in an ionic solution. A question yet to be answered is what will happen on the electrode if an electrical current is injected through it. After the electrode reaches the equilibrium status a polarization across the interface by setting a potential difference on the electrodes would deviate the system from the equilibrium and hence enabling the interface current via charge transfer at the complex.

The exchange current density (J_0) is an intrinsic property of the electrochemical reaction specific to the electrode and the solution involved on the reaction. A range of values is presented on [44] for different materials. The J_0 value is affected by the material and the solution involved in the process. On the above reference, the author established a range of values for gold micro-electrodes ($2 \cdot 10^{-9}\ A/cm^2$ to $3.98 \cdot 10^{-6}\ A/cm^2$). This theoretical value greatly depends on the solution where the electrode is immersed. To approximate the gold electrode immersed in saline solution, the lower selected value is: $J_0 = 3.98 \cdot 10^{-6}\ A/cm^2$. The Charge transfer resistance (R_{ct}) depending on the area exposed to the solution would be:

$$R'_{ct} = 100 \cdot \frac{V_t}{J_0} \tag{2.3}$$

where V_t corresponds to the thermal voltage:

$$V_t = \frac{k \cdot T}{q} = 25.9\ mV \tag{2.4}$$

with $q = 1.6 \cdot 10^{-19}\ C$, $k = 1.38 \cdot 10^{-23}\ J/K$ and $T = 300\ K$.
obtaining:

$$R'_{ct} = 650\ G\Omega \cdot \mu m^2 \tag{2.5}$$

$$R_{ct} = \frac{R'_{ct}}{A}\ \Omega \tag{2.6}$$

for an electrode of area A.

Interfacial capacitance (C_{dl})

The double layer generated at the interface develops a capacitance behaviour created by the space charge region formed in the electrolyte near the electrode surface. First approach to

attempt the determination of this capacitance was elicited by Helmholtz [114] and defined the capacity per unit area as:

$$C_H = \frac{\varepsilon_0 \varepsilon_r}{d_{OHP}} \, F/m^2 \tag{2.7}$$

where $\varepsilon_0 = 8.85419 \cdot 10^{-12} \, F/m$ is the vacuum permittivity, ε_r is the relative permittivity of the solution and $d_{OHP} = 8.25 \cdot 10^{-10} \, m$ corresponds to the distance value of the OHP from the electrode surface [115].

A second capacitance term [46], corresponding to Gouy model, is defined by:

$$C_G = \frac{\varepsilon_0 \varepsilon_r}{L_D} \cdot cosh(\frac{z \cdot V_0}{2 \cdot V_t}) \, F/m^2 \tag{2.8}$$

$$L_D = \sqrt{\frac{\varepsilon_0 \cdot \varepsilon_r \cdot V_t}{2 \cdot n^0 \cdot z^2 \cdot q}} \, m \tag{2.9}$$

Using $V_0 = 100 \, mV$ as the potential at the electrode and $V_t = 26 \, mV$. L_D is known as Debye Length which models the spatial of electrical potential. The value $q = 1.60217662 \cdot 10^{-19} \, C$ corresponds to electron charge, and ε_r value is fitted to a range between $[6 - 78.5]$ as suggested by [44]. For our simulations we will employ $\varepsilon_r = 6.8$. The value z is the valence number for the reaction involved on the double layer formation and n^0 is the ionic concentration of the solution expressed in $mols/m^3$.

The solution involved in the cell culture process is culture media. This saline solution is composed of several biochemical nutrients necessary for cells growth. However the major component is sodium chloride (Minimum Essential Medium Eagle - MEM) preparations [116]. The concentration of [NaCl] on this solution is $n^0 = 0.14 \, mols/l$ and $z = 1$. The chemical dissociation is defined by:

$$NaCl \leftrightarrow Na^+ + Cl^- \tag{2.10}$$

All of the above leads to:

$$L_D = \sqrt{\frac{\varepsilon_0 \varepsilon_r V_t}{2 \cdot 140 \cdot 6.022 \cdot 10^{23} \cdot q}} = 8.1631 \cdot 10^{-8} \, m \tag{2.11}$$

obtaining:

$$C_H = \frac{\varepsilon_0 \varepsilon_r}{d_{OHP}} = 0.073 \, F/m^2 \tag{2.12}$$

$$C_G = \frac{\varepsilon_0 \varepsilon_r}{L_D} \cdot cosh(\frac{zV_0}{2V_t}) = 0.882 \, F/m^2 \tag{2.13}$$

The C_{dl} per area unit (C'_{dl}) is defined as the series contribution of C_H and C_G.

$$\frac{1}{C'_{dl}} = \frac{1}{C_H} + \frac{1}{C_G} \tag{2.14}$$

Finally:

$$C'_{dl} = 6.7402 \cdot 10^{-14}\ F/m^2 \tag{2.15}$$

$$C_{dl} = A \cdot C'_{dl}\ F \tag{2.16}$$

Spreading resistance (R_s)

The spreading resistance represents the opposition of the solution to the net charge flow and is characterized by the solution in contact with the electrodes. For a circular electrode immersed in an ionic solution, its value is governed by the following equation [44]:

$$R_s = \frac{\rho \cdot \sqrt{\pi}}{4 \cdot \sqrt{A}}\ \Omega \tag{2.17}$$

Where A corresponds to the electrode area and ρ is the solution resistivity. The conductivity of a saline solution of NaCl at 0.14% is approximately:

$$\sigma = 2 \cdot 10^{-6}\ S/\mu m \tag{2.18}$$

$$\rho = \frac{1}{\sigma} = 5 \cdot 10^{5}\ \Omega \cdot \mu m \tag{2.19}$$

Finally:

$$R'_s = 2.2156 \cdot 10^{5}\ \Omega \cdot \mu m \tag{2.20}$$

$$R_s = \frac{R'_s}{\sqrt{A}}\ \Omega \tag{2.21}$$

being A the electrode area.

Cell-electrode interface model

This parameter is introduced to model the effect of cells attached to electrodes immersed in an ionic solution. Authors in [58] discuss the physics for electrical behaviour of cells adhered to micro-electrodes. They theoretically approximate the problem to describe a model for the cells adhered to electrodes on a cell culture assay. The parameters considered to model the effect are the resistance between cell, and both impedances through the electrode and cell layer for a specific cell line.

On [54] the R_{gap} value is modelled following a finite element analysis approach. The analysis returns a value of 75 $k\Omega$. The parameter R_{gap} is modelling the current flowing laterally through the electrode-cell interface which is dependant on the adhesion distance of the cell to the electrode. This distance varies between 15-150 nm [117] and is dependent on the specific cell line under test and the solution involved. In [118], lower values were obtained for this parameter; $R_s = 1\ k\Omega$.

2.2.2 Bio-electrical system model

ECIS technique depends on the double layer generated on the electrode-solution complex. The electrical properties of the model depend on the electrode surface exposed to the solution. The electrical stimuli injected through the two-electrode system finds a double path; one through the adhered cells (A_{cell}) to the sensing electrode and a second one through flowing directly through the solution. This effect is illustrated in Figure 2.4.

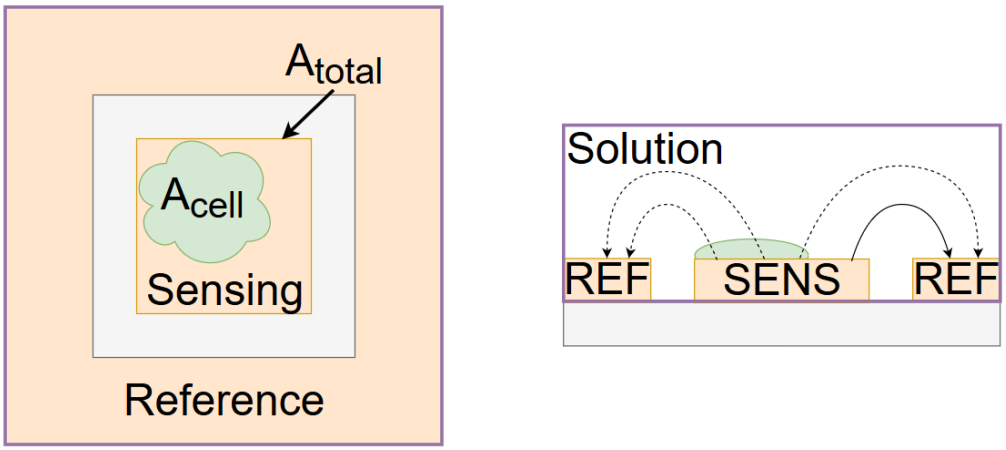

Fig. 2.4 Fill factor (ff) is the relation between the area covered by cells (A_{cell}) and the total electrode area (A_{total}). Two electrical paths are generated on the electrode after cells adhere to it, the electrical properties of those paths are different, which will produce electrical current flowing at different rates through the solution and through the cell depending on the frequency of the signal injected.

Definition 1 *A_{cell}: Area covered by cells over the sensing electrode.*

Definition 2 *A_{total}: Total area for the sensing electrode.*

Definition 3 *ff: Fill-factor is $\frac{A_{cell}}{A_{total}}$.*

From the bio-impedance model described previously in Figure 2.2 it is possible to define two electrical paths corresponding to the empty electrode ($Z_{nc}(ff)$) and the cells growing on the electrode ($Z_c(ff)$).

$$Z_{nc}(ff) = (\frac{Z}{1-ff}) \tag{2.22}$$

$$Z_c(ff) = (\frac{Z}{ff}) \tag{2.23}$$

Let $Z_{bio}(ff)$ be the combined impedance resulting from the contributions of both possible paths, as a function of the area covered by cells in the sensing electrode [44, 52].

$$Z_{bio}(ff) = (Z_{nc}(ff) \| (Z_c(ff) + R_{gap})) + R_s \tag{2.24}$$

From the model presented in Figure 2.3 the capacity (C_{dl}) and resistance (R_{ct}) as:

$$C_{nc} = C_{dl} \cdot (1-ff) \tag{2.25}$$

$$R_{nc} = R_{ct}/(1-ff) \tag{2.26}$$

similarly the electrical values for the cell branch would be:

$$C_c = C_{dl} \cdot ff \tag{2.27}$$

$$R_c = R_{ct}/ff \tag{2.28}$$

where R_{ct} and C_{dl} corresponds to the nominal capacitive and resistive values of the double layer inter-phase developed on the electrode.

$$Z_{nc} = (C_{nc}||R_{nc}) = \frac{1}{\frac{1}{R_{nc}} + \frac{1}{\frac{1}{s \cdot C_{nc}}}} = \frac{R_{nc}}{1 + s \cdot C_{nc} \cdot R_{nc}} \tag{2.29}$$

$$Z_c = (C_c||R_c) = \frac{1}{\frac{1}{R_c} + \frac{1}{\frac{1}{s \cdot C_c}}} = \frac{R_c}{1 + s \cdot C_c \cdot R_c} \tag{2.30}$$

Cell branch accounts for the gap resistance formed on the cell adhesion process:

$$Z_c + R_{gap} = \frac{R_c}{1 + s \cdot C_c \cdot R_c} + R_{gap} = \frac{R_{gap} \cdot C_c \cdot R_c \cdot s + R_c + R_{gap}}{1 + s \cdot C_c \cdot R_c} \tag{2.31}$$

Note that both impedances share the form:

$$Z = \frac{n_1 s + n_0}{d_1 s + d_0} \tag{2.32}$$

where, for $Z_c + R_{gap}$:

$$n_{1c} = R_{gap} \cdot R_c \cdot C_c \tag{2.33}$$

$$n_{0c} = R_c + R_{gap} \tag{2.34}$$

$$d_{1c} = C_c \cdot R_c \tag{2.35}$$

$$d_{0c} = 1 \tag{2.36}$$

and Z_{nc}:

$$n_{1nc} = 0 \tag{2.37}$$

$$n_{0nc} = R_{nc} \tag{2.38}$$

$$d_{1nc} = C_{nc} \cdot R_{nc} \tag{2.39}$$

$$d_{0nc} = 1 \tag{2.40}$$

Equation (2.32) corresponds to a one-pole, one-zero system. Bare electrodes have this behaviour. The Z_{bio} expression can be expressed as:

$$Z_{bio}(ff) = \frac{1}{\frac{1}{Z_{nc}} + \frac{1}{Z_c + R_{gap}}} + R_s = \frac{1}{\frac{(n_{1c} \cdot s + n_{0c}) \cdot (d_{1nc} \cdot s + d_{0nc}) + (n_{0nc}) \cdot (d_{1c} \cdot s + d_{0c})}{(n_{0nc}) \cdot (n_{1c} \cdot s + n_{0c})}} + R_s \tag{2.41}$$

reformatting and rewriting a bit:

$$Z_{bio}(ff) = \frac{(n_{0nc}) \cdot (n_{1c} \cdot s + n_{0c})}{(n_{1c} \cdot s + n_{0c}) \cdot (d_{1nc} \cdot s + d_{0nc}) + (n_{0nc}) \cdot (d_{1c} \cdot s + d_{0c})} + R_s \tag{2.42}$$

and finally:

$$Z_{bio}(ff) = \frac{n_{0nc} n_{1c} s + n_{0nc} n_{0c}}{n_{1c} d_{1nc} s^2 + (n_{1c} d_{0nc} + n_{0c} d_{1nc} + n_{0nc} d_{1c}) s + n_{0c} d_{0nc} + n_{0nc} d_{0c}} + R_s \tag{2.43}$$

Which again can be written on the form expressed by equation (2.32):

$$n_1 = n_{0nc} n_{1c} \tag{2.44}$$

$$n_0 = n_{0nc} n_{0c} \tag{2.45}$$

$$d_2 = n_{1c} d_{1nc} \tag{2.46}$$

$$d_1 = n_{1c} d_{0nc} + n_{0c} d_{1nc} + n_{0nc} d_{1c} \tag{2.47}$$

$$d_0 = n_{0c} d_{0nc} + n_{0nc} d_{0c} \tag{2.48}$$

Recalling equation (2.24) the resulting impedance would be:

$$Z_{bio}(ff) = \frac{n_1 s + n_0}{d_2 s^2 + d_1 s + d_0} + R_s = \frac{R_s d_2 s^2 + (R_s d_1 + n_1) s + n_0 + R_s d_0}{d_2 s^2 + d_1 s + d_0} \tag{2.49}$$

This result represents the final equation for the Bio-Impedance formed by the electrodes and the cell adhered to the electrode surface with respect to the amount of cells covering the sensing electrode. The coverage is modeled as a fill-factor which is the relation between the area covered and the total electrode area. In equation (2.49) a two-pole, two-zero system is encountered derived from the electrodes immersed in the cell culture medium. Adhesion of cells to electrode generates a new pole-zero pair, which is illustrated in Figure 2.5.

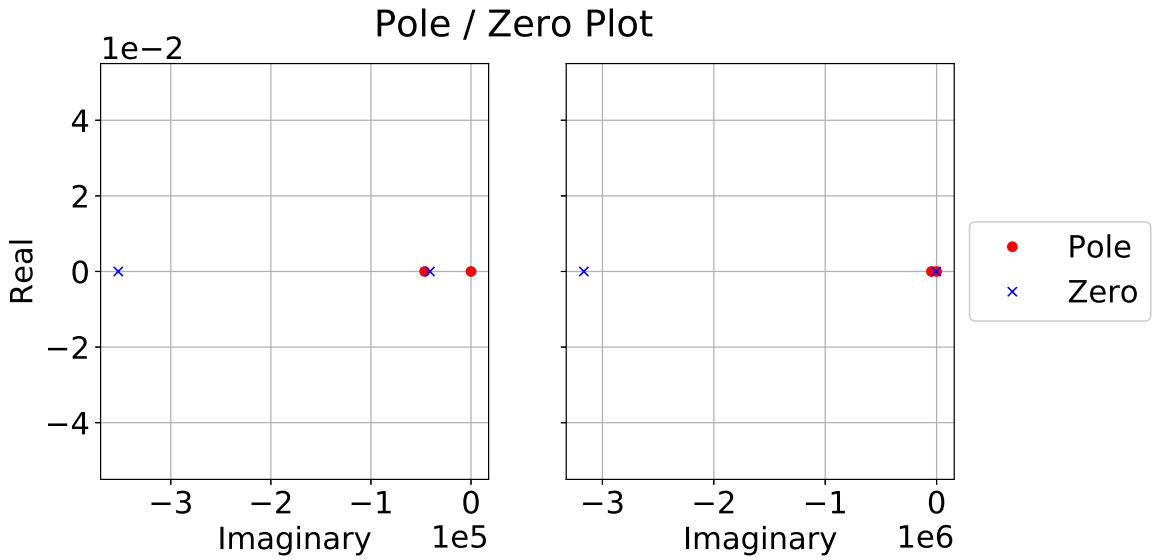

Fig. 2.5 Pole-Zero diagram for the electrical models in two cases: Empty electrode ($ff = 0$) is showed on the left, whereas full electrode ($ff = 1$) is depicted on the right.

Single electrode covered by cells

Consider an alternating current source circulating through a terminal of the $Z_{bio}(ff)$. The impedance is formed by the biological sample under test and two electrodes (e_1,e_2). With e_2 much greater in size than e_1 and tied to ground. A simulation has been prepared using pspice and the models exposed in this chapter to evaluate the impedance of the system. For the sake of simplicity let us consider a single circular electrode with a radius of 125 μm. From the results exposed in equations (2.49), (2.6), (2.16) and (2.21). Therefore, theoretical electrical parameters value would be defined as:

$$R_{ct} = \frac{R'}{125^2\pi} = 13.25\ M\Omega \tag{2.50}$$

$$C_{dl} = 125^2\pi \cdot C' = 4\ nF \tag{2.51}$$

$$R_s = \frac{R'_s}{125^2\pi} = 1\ k\Omega \tag{2.52}$$

The electrical simulation setup is depicted on Figure 2.6. *AC* stimuli is injected through an electrode and the second is tied to ground. The voltage drop is considered across the whole system to analyze the electrical response.

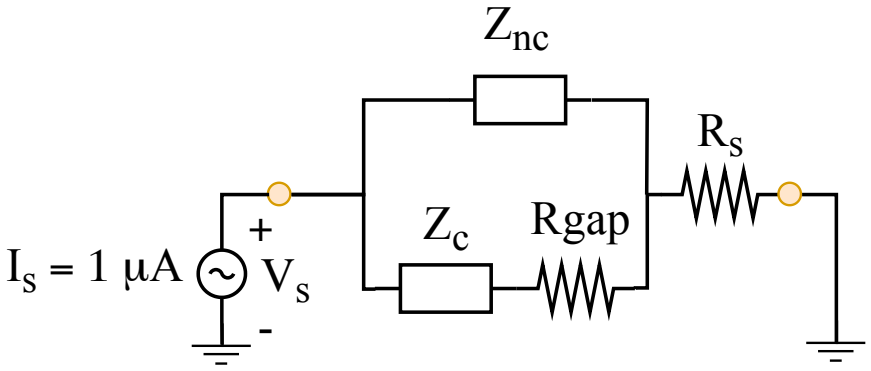

Fig. 2.6 Circuit simulation schematic. One electrode is tied to ground and the other is connected to an alternating current supply set at 1 μA. Z_c and Z_{nc} both depend on the fill-factor value as previously exposed. These values are obtained from the R_{ct} and C_{dl} values depicted above.

The electrical impedance of the whole biological complex was modeled according to the results previously exposed. A simulation was implemented and run to acquire the electrical response. Several variations in fill-factor were performed to analyze the sensitivity of the system modeled. Identically, variations on the R_{gap} value (according to literature [54, 118]) were introduced too, since this parameter is dependent on the cell properties on the sample. Simulations consist in AC simulation in a frequency range of $[0.1, 10^7]\ Hz$. Voltage response, V_s, correspond to Z_{bio} magnitude expressed in $M\Omega$. ($1\ V/1\ \mu A$).

This analysis was implemented and the result is presented in Figure 2.7 and Figure 2.8. Initial value for R_{gap} was 75 $k\Omega$. The variation of the ff value introduces variations on the impedance response of the sample due to cell growth. The fill factor variation generates different electrical responses on the modeled electrode. The absolute and normalized curve depict different variations on different operation points. To perform reliable acquisition the system must operate on a point where the variation is maximized. The phase variation range is maximum near 1 kHz region, whereas magnitude is located on 10 kHz. Despite this, the 10 kHz point depicts a really bad sensitivity on phase response since there is a polarity change around 10 kHz, which makes the phase response unsuitable for sensing on that operation point.

This result is greatly affected by the electrical parameters of the system (electrode area and the R_{gap}). On figures 2.9 and 2.10 several values of R_{gap} are tested to analyze the electrical response. The curve illustrates the influence of the R_{gap} value, affecting both magnitude and phase and altering notoriously the obtained result. Smaller values of R_{gap} suggest lesser sensitivity on the system to fill-factor changes than those exposed on greater values.

Finally, electrode area value influences the electrical response of the whole system. To consider and analyze this response the simulation was adapted to modify radius of the single micro-electrode considered and observe the alterations exposed on the electrical response. These variations on the electrode area presented on figures 2.11 and 2.12. Both illustrate a displacement of the ideal operation point depending on this value. Electrodes with small area values would require higher operation frequency than those with a greater area.

As a conclusion both parameters (R_{gap} and A_{total}) will influence the resulting performance of the sensor, to summarize a bit:

- R_{gap} value affects the electrical response of the system. A lower R_{gap} value leads to a decreasing sensitivity. Experimental determination of the R_{gap} for different cell lines may be employed as a potential bio-marker for cell identification on a controlled environment.

- A_{total} value affects the electrical response as well. Larger electrode area means lower optimal frequencies for sensing. This size can be adapted to reach different sensitivity levels and cell sizes.

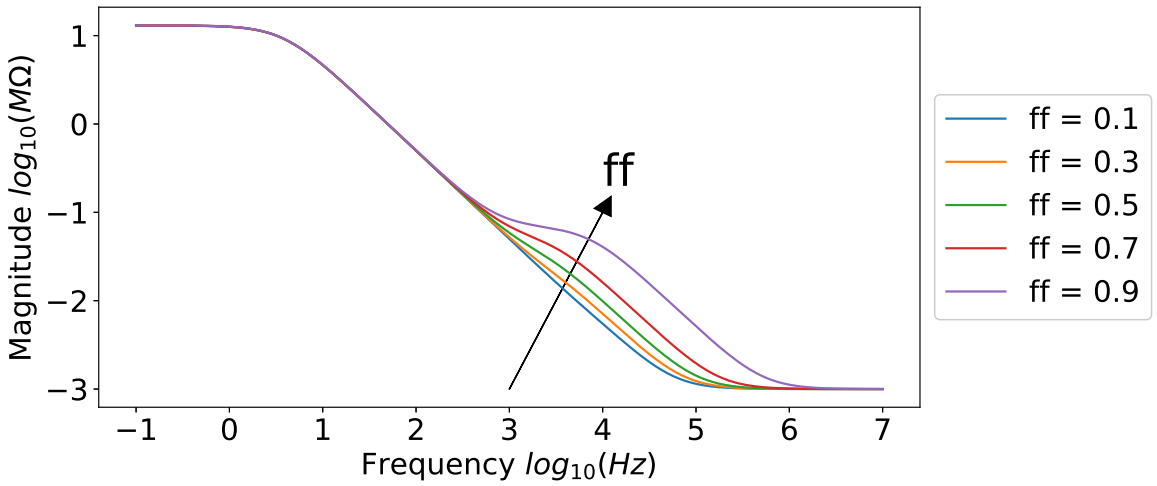

(a) Magnitude

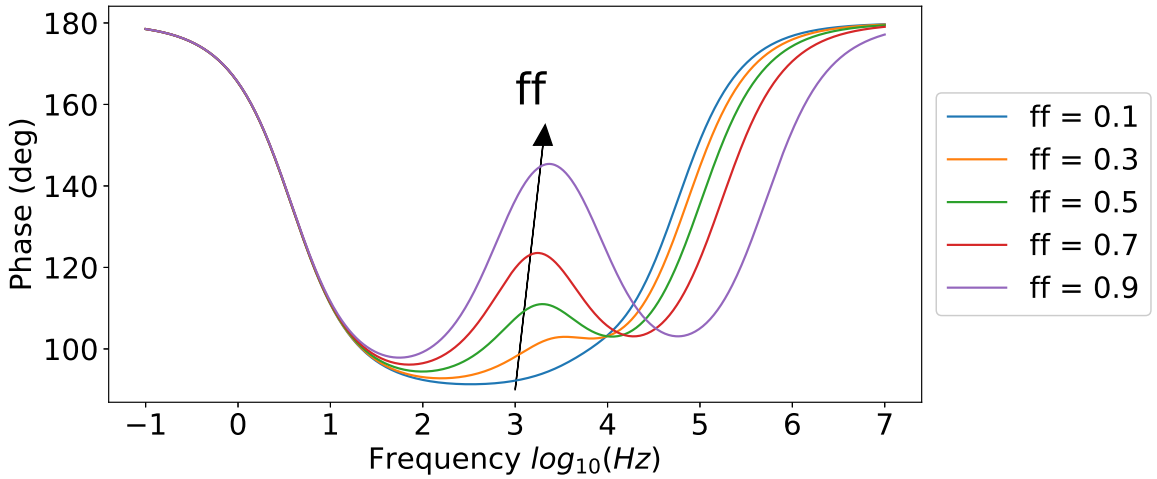

(b) Phase

Fig. 2.7 Electrical impedance response of the electrical model exposed previously using the parameters: $R_{ct} = 13.25\ M\Omega$, $C_{dl} = 4\ nF$, $R_s = 1\ k\Omega$ and $R_{gap} = 75\ k\Omega$. (a) magnitude, (b) phase.

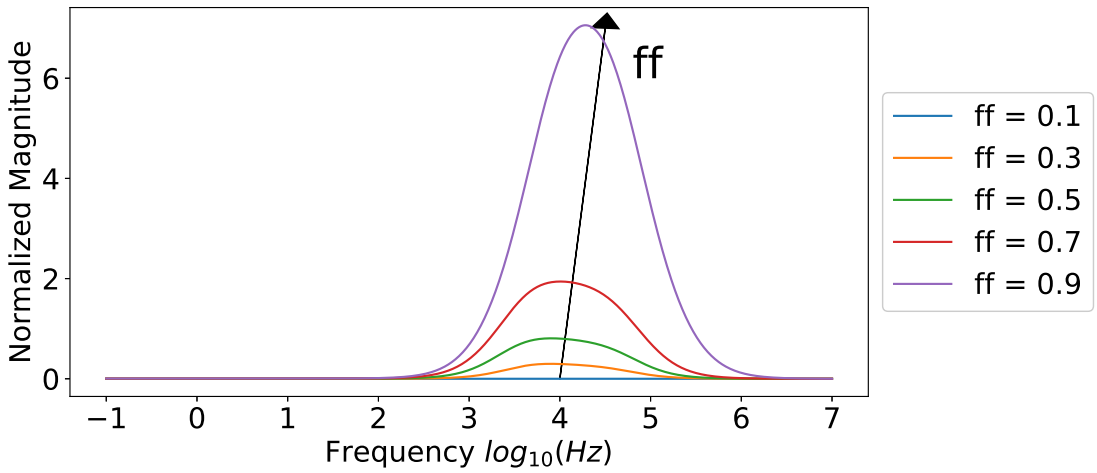

(a) Magnitude

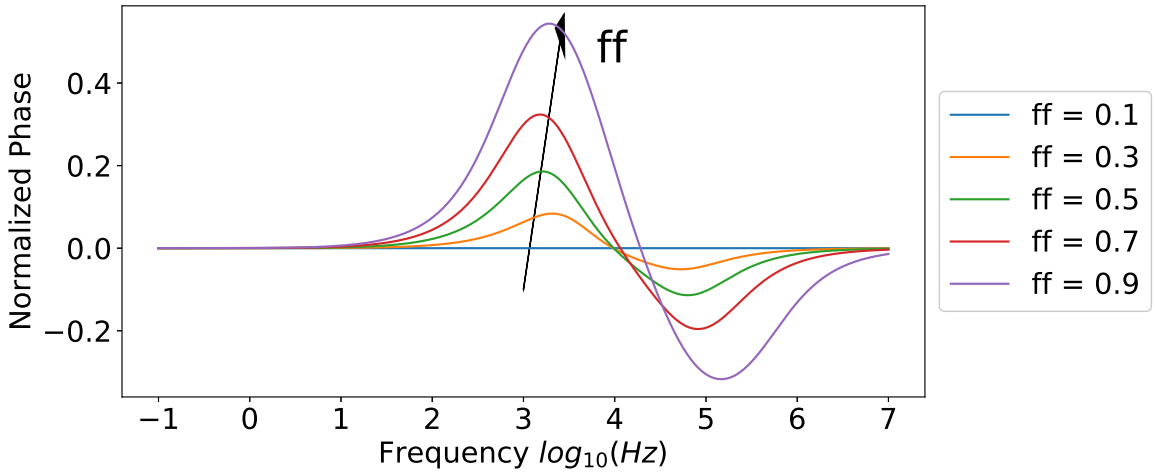

(b) Phase

Fig. 2.8 Normalized electrical impedance response as $\frac{Z_{bio}(ff)-Z_{bio}(0)}{Z_{bio}(0)}$. Values obtained from the electrical model exposed previously using the parameters: $R_{ct} = 13.25\ M\Omega$, $C_{dl} = 4\ nF$, $R_s = 1\ k\Omega$ and $R_{gap} = 75\ k\Omega$. (a) magnitude, (b) phase.

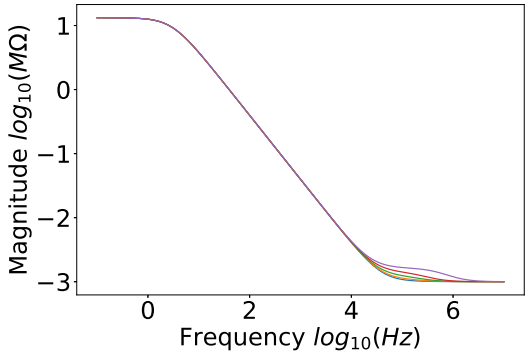

(a) Magnitude, $R_{gap} = 750\ \Omega$

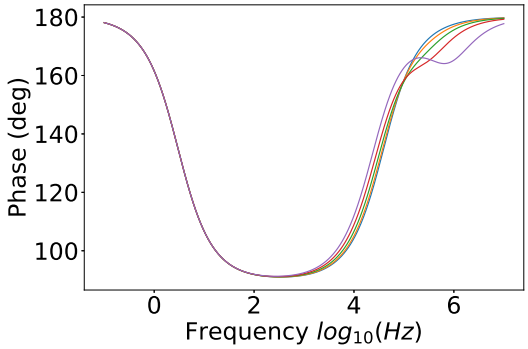

(b) Phase, $R_{gap} = 750\ \Omega$

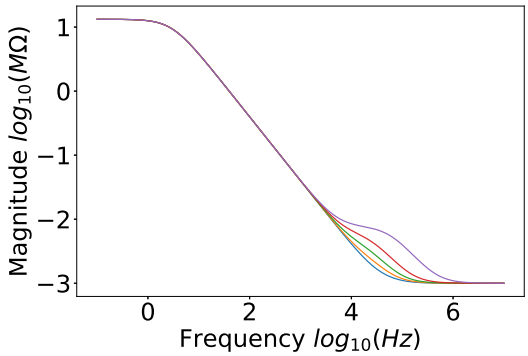

(c) Magnitude, $R_{gap} = 7.5\ k\Omega$

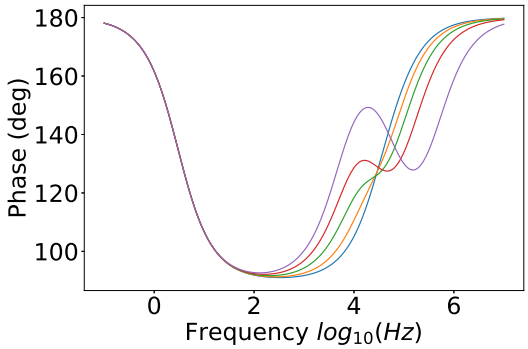

(d) Phase, $R_{gap} = 7.5\ k\Omega$

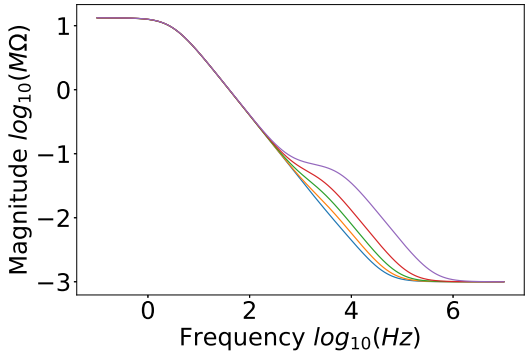

(e) Magnitude, $R_{gap} = 75\ k\Omega$

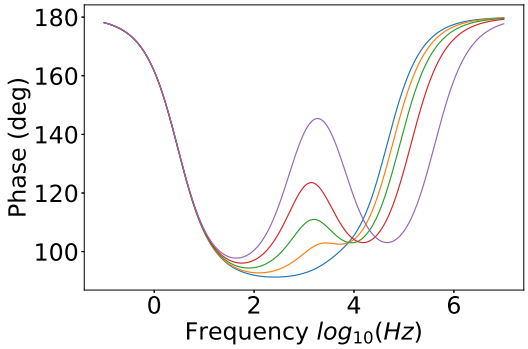

(f) Phase, $R_{gap} = 75\ k\Omega$

Fig. 2.9 Variations on R_{gap} value using a single $125\mu\ m$ radius circular micro-electrode. The result depicts both magnitude (1st column) and phase (2nd column) responses.

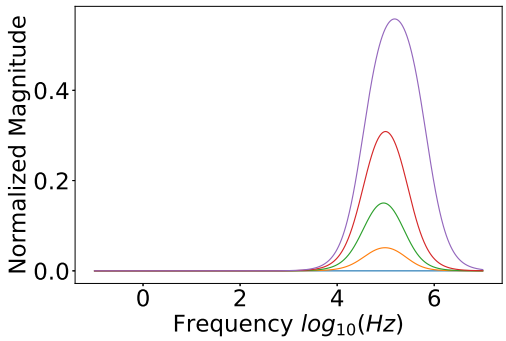

(a) Nomalized magnitude, $R_{gap} = 750\ \Omega$

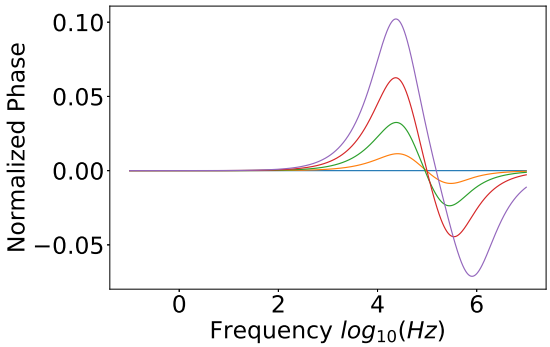

(b) Nomalized phase, $R_{gap} = 750\ \Omega$

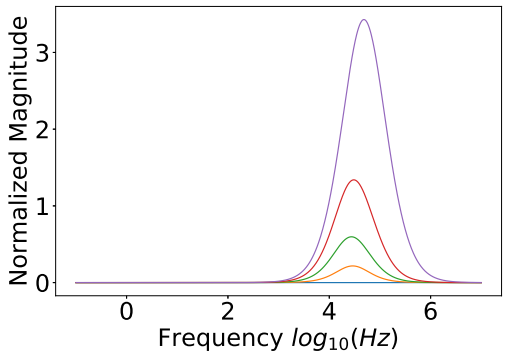

(c) Nomalized magnitude, $R_{gap} = 7.5\ k\Omega$

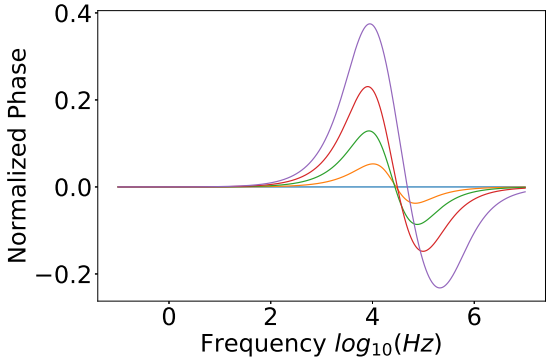

(d) Nomalized phase, $R_{gap} = 7.5\ k\Omega$

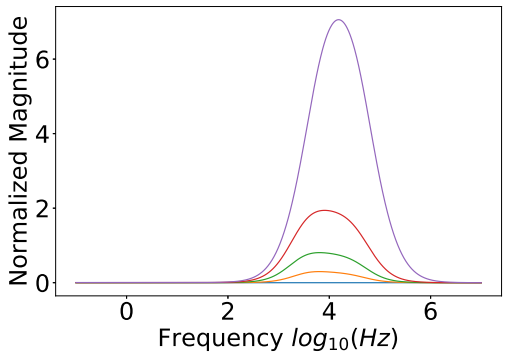

(e) Nomalized magnitude, $R_{gap} = 75\ k\Omega$

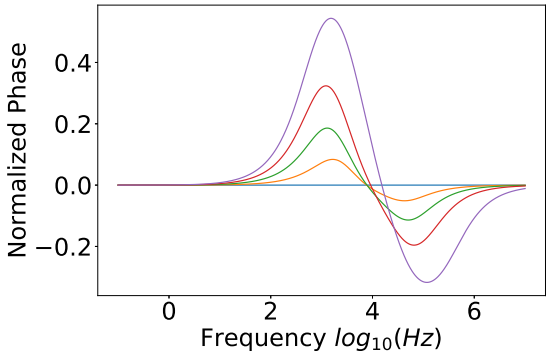

(f) Nomalized phase, $R_{gap} = 75\ k\Omega$

Fig. 2.10 Variations on R_{gap} value using a single $125\mu\ m$ radius circular micro-electrode. The result depicts both magnitude (1st column) and phase (2nd column) normalized responses.

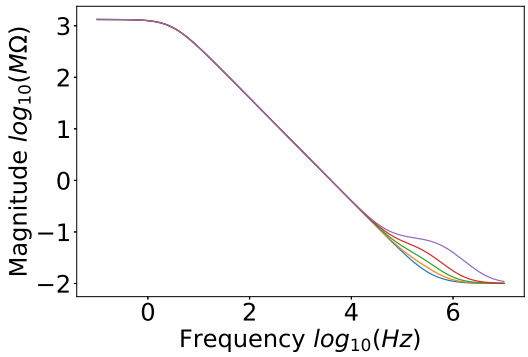

(a) Magnitude, $r = 12.5\ \mu m$

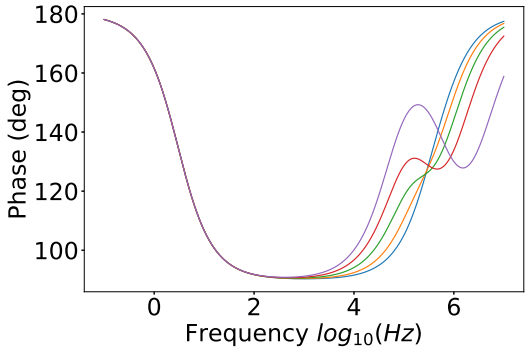

(b) Phase, $r = 12.5\ \mu m$

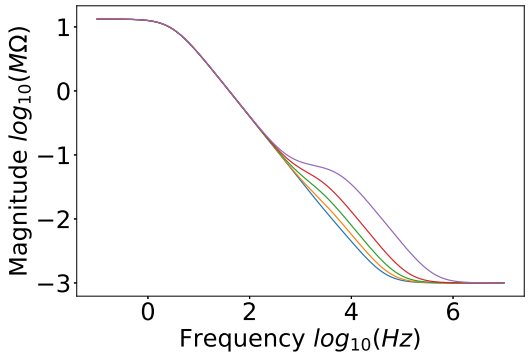

(c) Magnitude, $r = 125\ \mu m$

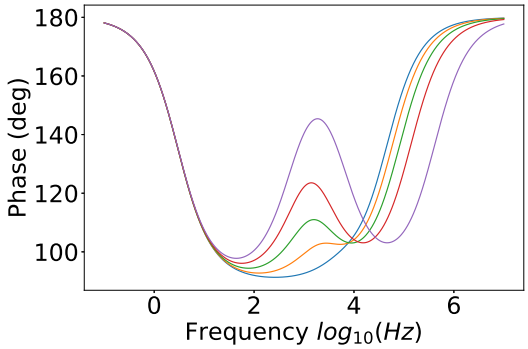

(d) Phase, $r = 125\ \mu m$

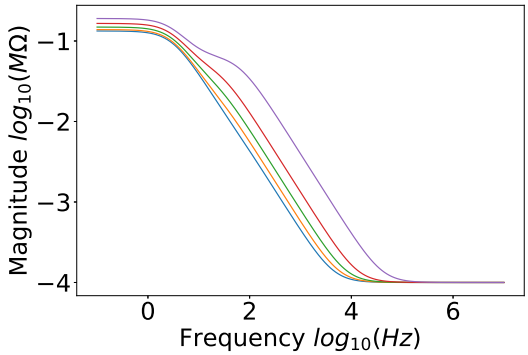

(e) Magnitude, $r = 1250\ \mu m$

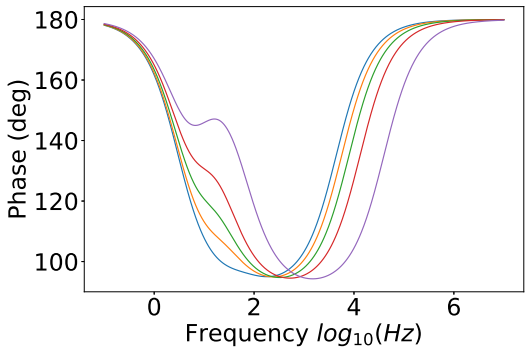

(f) Phase, $r = 1250\ \mu m$

Fig. 2.11 Variations on electrode area (A) induced by different radius on the micro-electrode area. $R_{gap} = 75\ k\Omega$. The result depicts both magnitude (1st column) and phase (2nd column) response.

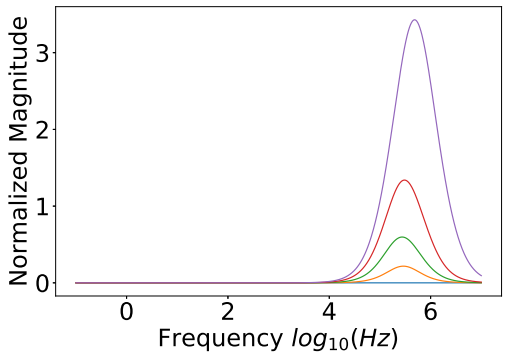

(a) Nomalized magnitude, $r = 12.5\ \mu m$

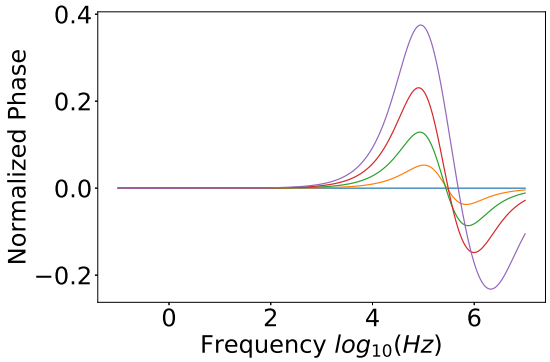

(b) Nomalized phase, $r = 12.5\ \mu m$

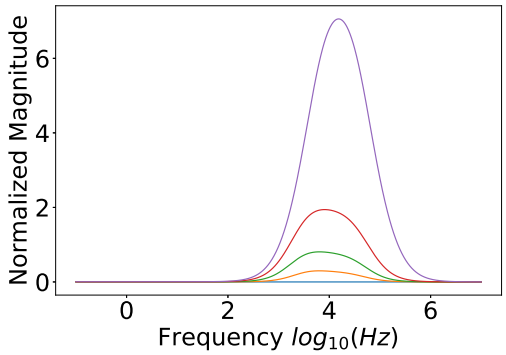

(c) Normalized magnitude, $r = 125\ \mu m$

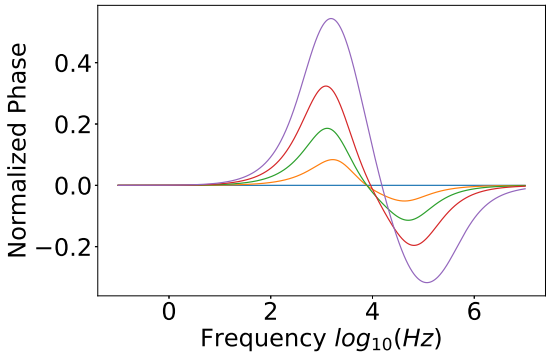

(d) Normalized phase, $r = 125\ \mu m$

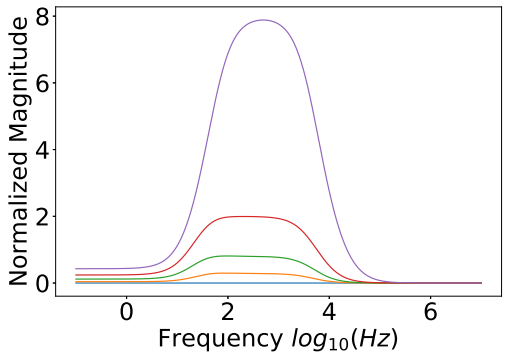

(e) Normalized magnitude, $r = 1250\ \mu m$

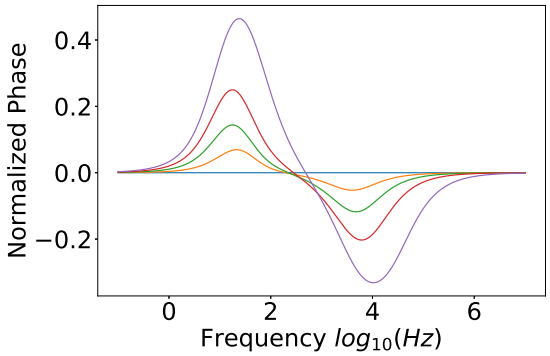

(f) Normalized phase, $r = 1250\ \mu m$

Fig. 2.12 Variations on electrode area (A) induced by different radius on the micro-electrode area. $R_{gap} = 75\ k\Omega$. The result depicts both magnitude (1st column) and phase (2nd column) normalized response.

2.3 Cell-growth simulations

The commercially available electrodes for ECIS technique, usually differ on micro-electrode number, geometry and materials. Additionally, cell dynamics will influence the system response. These two concepts will be explored in this section to further illustrate the electrical response of the system considering the cells adhered to the electrode surface and different growing patterns.

Electrode selection

Previous section exposed the electrode model calculations for a simple circular electrode immersed in an ionic solution and the physical effect of cell adhering to it was studied and analyzed for a wide ranges of cell growth levels. The experimental application will analyze two commercially available electrodes. These electrodes are provided by Applied Biophysics [98] and contain several circular micro-electrodes ($r = 125\ \mu m$) where the cells can be sensed. Following Figure 2.13 depicts the commercial electrode and a model for each of the different versions.

These electrodes are off-the-shelf solutions for culturing cells on a cell culture reactor and provides an electrical interface to the cell culture which can be used to analyze the biological sample under test and infer the cell culture number from the electrical response.

Random growth

To model the cell growth, an algorithmic method which emulates this biological process was developed. Cell culture behaviour under controlled conditions is extensively documented on the literature [119, 120]. The cell culture growth experiences different stages as depicted in Figure 2.14 adapted from [121]. Phase identified as three is known as exponential phase and is the region of interest for the application described through this chapter. The cell amount (X_t) on this phase is characterized as:

$$X_t = X_{t-1} \cdot e^{\mu(\Delta t)} \tag{2.53}$$

where μ $[seg^{-1}]$ is defined from the mean doubling time or generation time (g) as:

$$\mu = \frac{ln\,2}{g} \tag{2.54}$$

(a) 8W10E

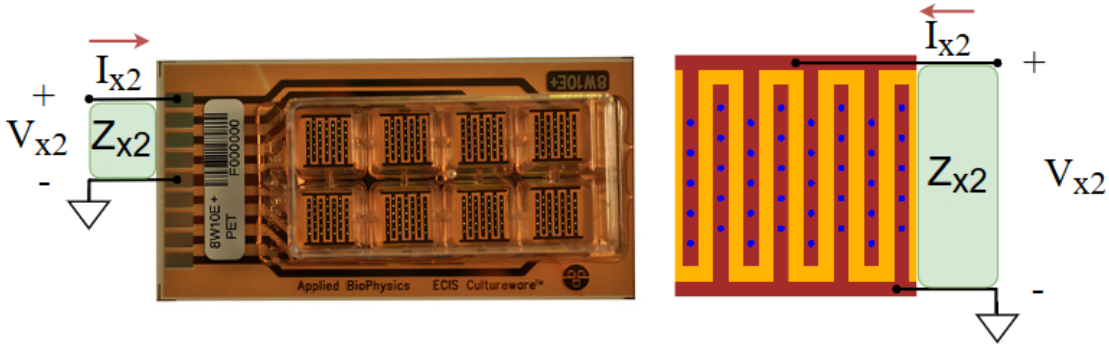

(b) 8W10E+

Fig. 2.13 Applied biophysics commercial electrodes. (a) circular multi-array and (b) interdigital electrodes.

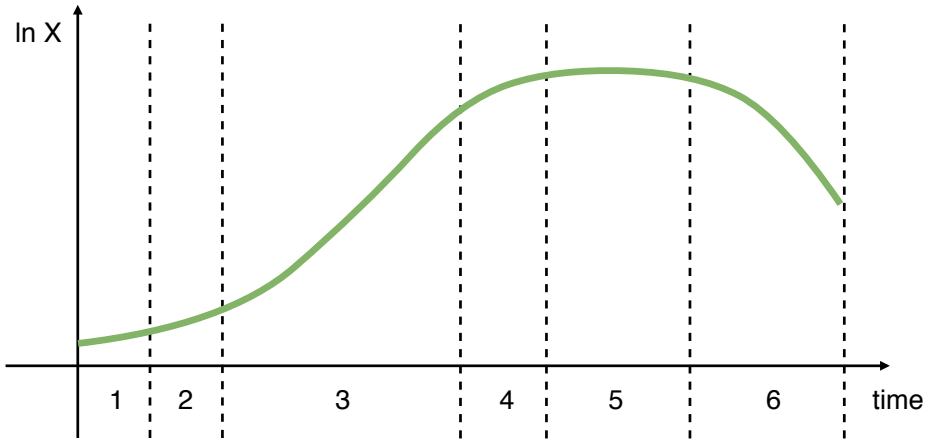

Fig. 2.14 Cell amount (X) as a function of time. Different growth phases for a cell culture. 1 (lag), 2 (acceleration), 3 (exponential), 4 (deceleration), 5 (stationary) and 6 (apoptosis).

Most of the cell amount variation while growing in cell culture is happening on the third stage of the growth phases, the exponential stage. Figure 2.15 illustrates the cell cycle of the cells adhered to the substrate on this stage, the process illustrated is corresponding to a full

cell cycle characterized by $g = t_4 - t_0$. Any cell on the substrate is assumed to be adhered to it while not performing cell division (a). Before the mitosis occurs the cell will detach from the substrate (b) and initiate the biological process, which will eventually lead to a duplication (c). Finally, both cells will land again (d) adhering to the substrate at a certain distance (d) from the original position (e). This distance or new cells position is modeled as a random distribution function around the original position. This model will be employed on several approaches to analyze potential differences on the electrical response derived from variations on cell growing on the electrode surface.

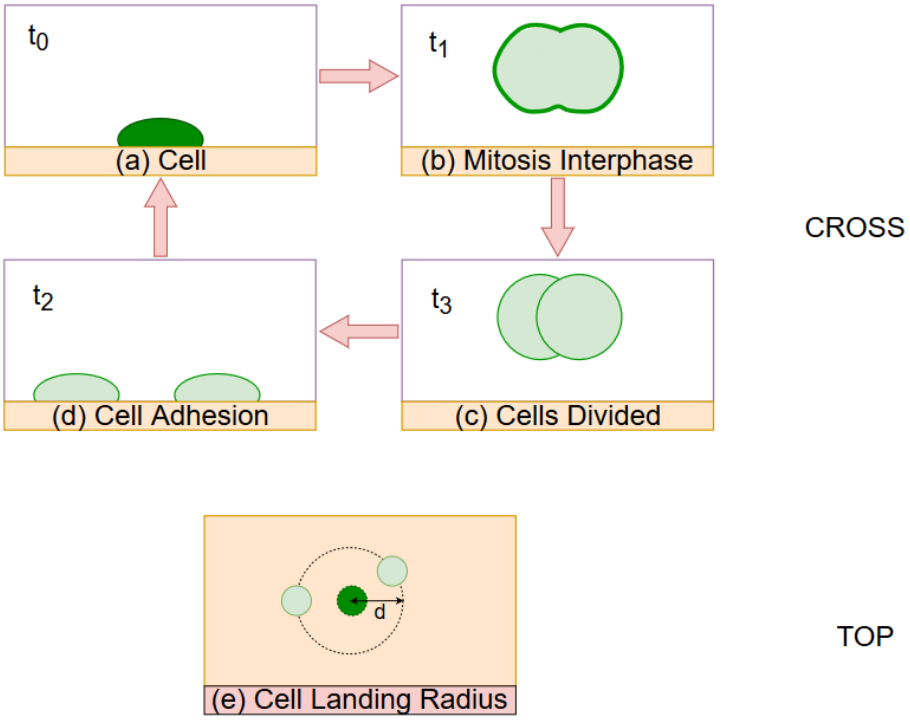

Fig. 2.15 Cell division cycle. A cell is adhered to the electrode surface on (a). To perform the mitosis, the cell detaches and starts to divide (b), (c). After the division was performed, both cells land on the electrode surface (d) at a certain distance from the initial point (e).

Simulation process

A growth model and an electrode model (both geometrical and electrical) were defined on the previous sections. It is possible to design a simulation environment considering the cellular growth at different stages using such models. This simulation illustrates the cell growing process on the electrode surface and provides insight on the electrical response variations associated to such process using electrical simulations.

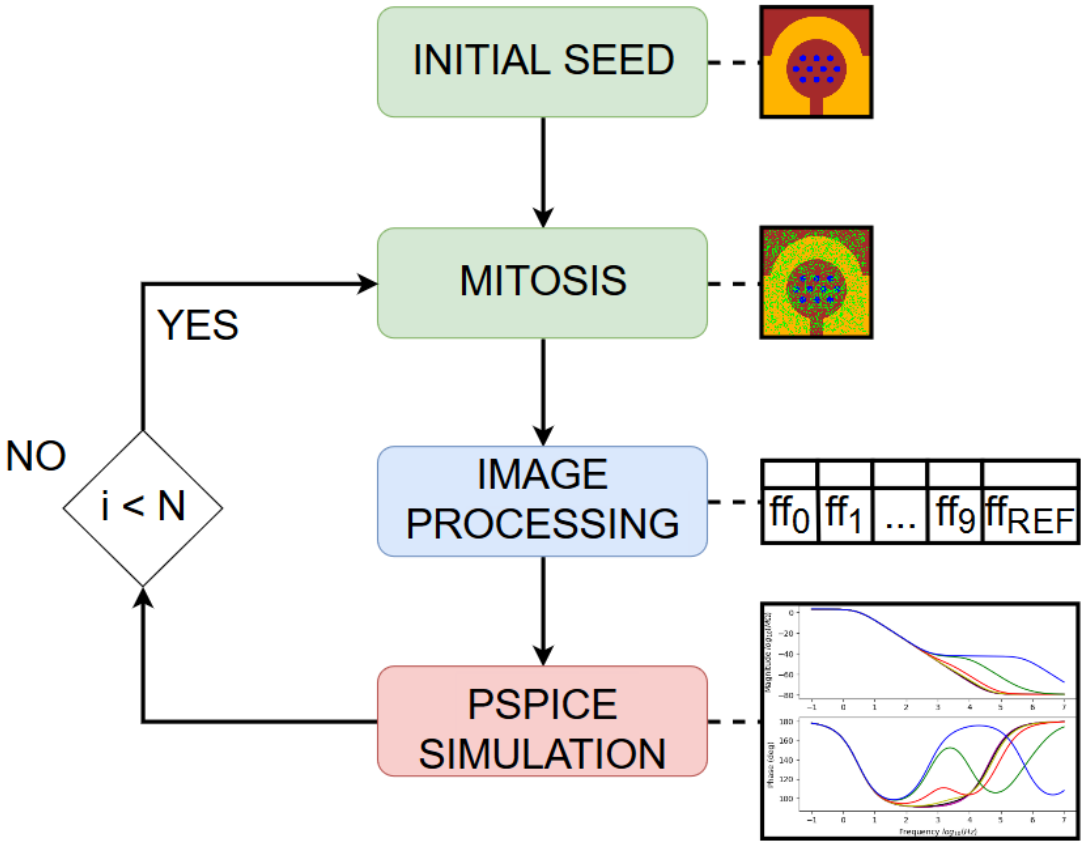

Fig. 2.16 Simulation algorithm. The model images are generated using the cell growth model. The fill-factor is estimated using image processing analysis. Finally, electrical response is obtained running a pspice simulation parametrized with the fill factor calculated by the image processing analysis.

Using the aforementioned approach, two different topologies were considered. Along with the two topologies, three cell growth patterns were analyzed to obtain further insight on the differences across electrodes. Electrical simulations using pspice were run on all of them. The following pages will illustrate the results obtained.

2.3.1 Simulation results

Both commercial electrode versions (Figure 2.13) are formed up by eight wells each one containing a distribution of micro-electrodes inside. The wells are square shaped with an area of 0.8 mm^2. Three simulations are proposed based on different cell growth patterns (random, central and border):

→ Random simulation analyzes the dynamics of cells growing evenly distributed across the electrode surface.

→ Central simulation performs a study on the cell sensitivity for cell growing in a cluster near the electrode center.

→ Border simulation represents a third option with two clusters growing from the corners.

All simulations apply similar parameters to model the cell growth behaviour:

- Cell radius: $r_{cell} = 25\ \mu m$.
- Time: On every iteration the algorithm will duplicate existing cell population. Hence each step represents $\Delta t = g$.
- Landing distance: $d = 36\ \mu m$ for random/border and $d = 16\ \mu m$ for central.

Random analysis

Results for the random simulation using 8W10E are depicted in Figure 2.17 describing exponential growth over the electrode in terms of fill-factor from (a) to (i). Identically, Figure 2.20 illustrates the same analysis over 8W10E+ electrode. The bode diagram for each of the different growth stages on 8W10E is depicted on figures 2.18 and 2.19. Similarly, the electrical response for 8W10E+ is presented on figures 2.21 and 2.22. This simulation results illustrates the fact that sensitivity to the number of cells over the electrode is observed in the form of a variation on the electrical response of the system due to the different values of bio-impedance of the complex. Slight differences are observed over the higher range of frequencies derived from the differences in electrode surfaces exposed to the cells and ionic solution; 8W10E expose 10 micro-electrodes vs a reference electrode, whereas 8W10E+ implements 20 micro-electrodes vs 20 micro-electrodes on the second terminal.

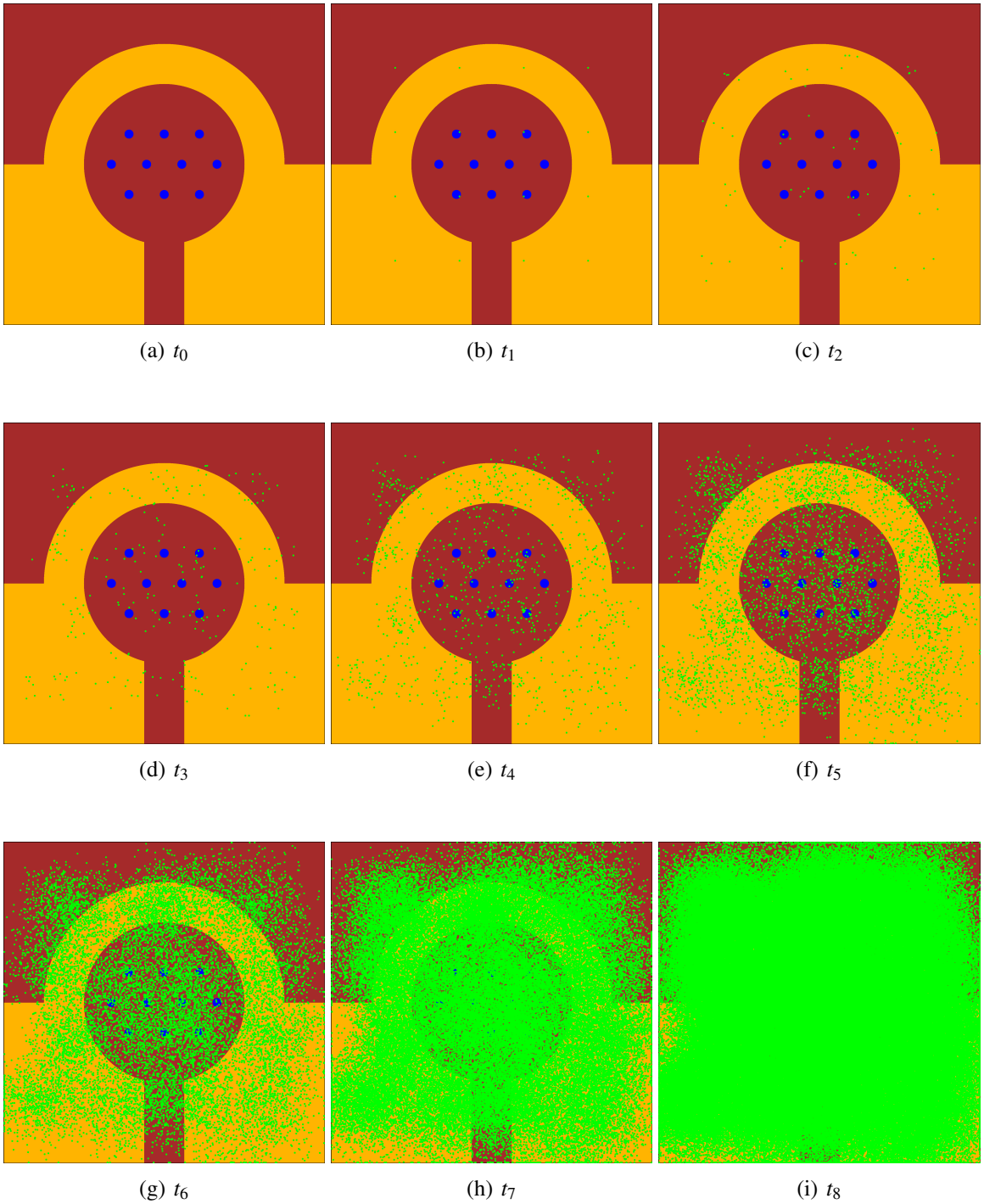

(a) t_0 (b) t_1 (c) t_2

(d) t_3 (e) t_4 (f) t_5

(g) t_6 (h) t_7 (i) t_8

Fig. 2.17 Random simulation on 8W10E. The algorithm calculates the cell population based on an exponential growth. Different time steps are depicted on the figure ($t_0 - t_8$). Timeshift ($t_i - t_{i-1} = g$ which is the cell division cycle for a cell line.

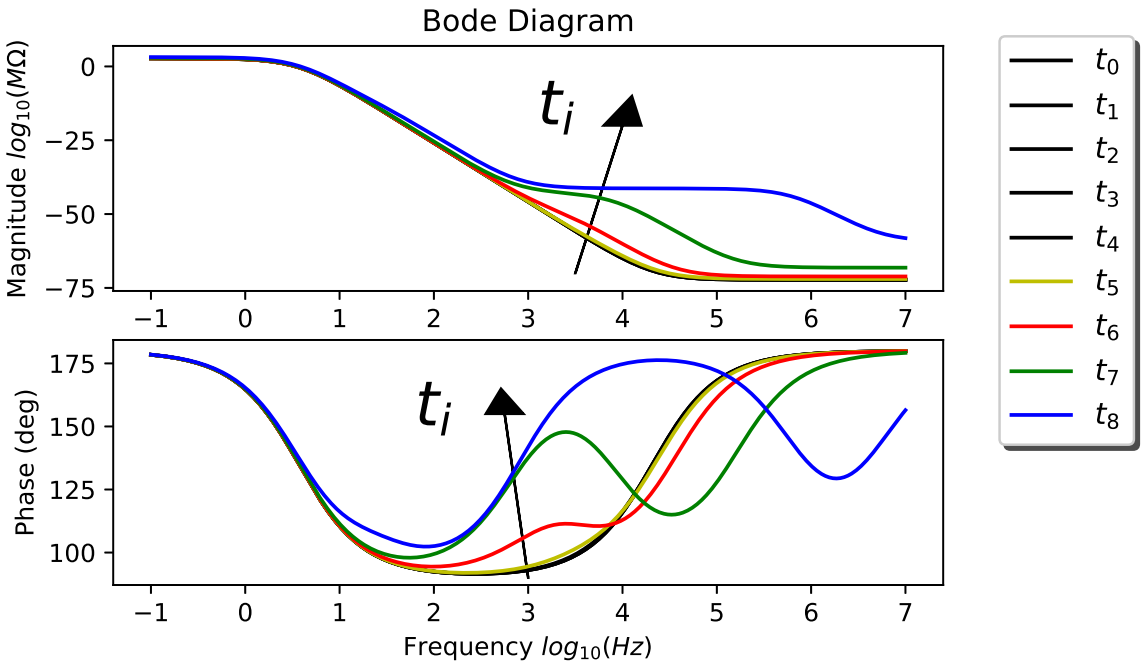

Fig. 2.18 Bode diagram for (a)-(i) images corresponding to the 8W10E electrode.

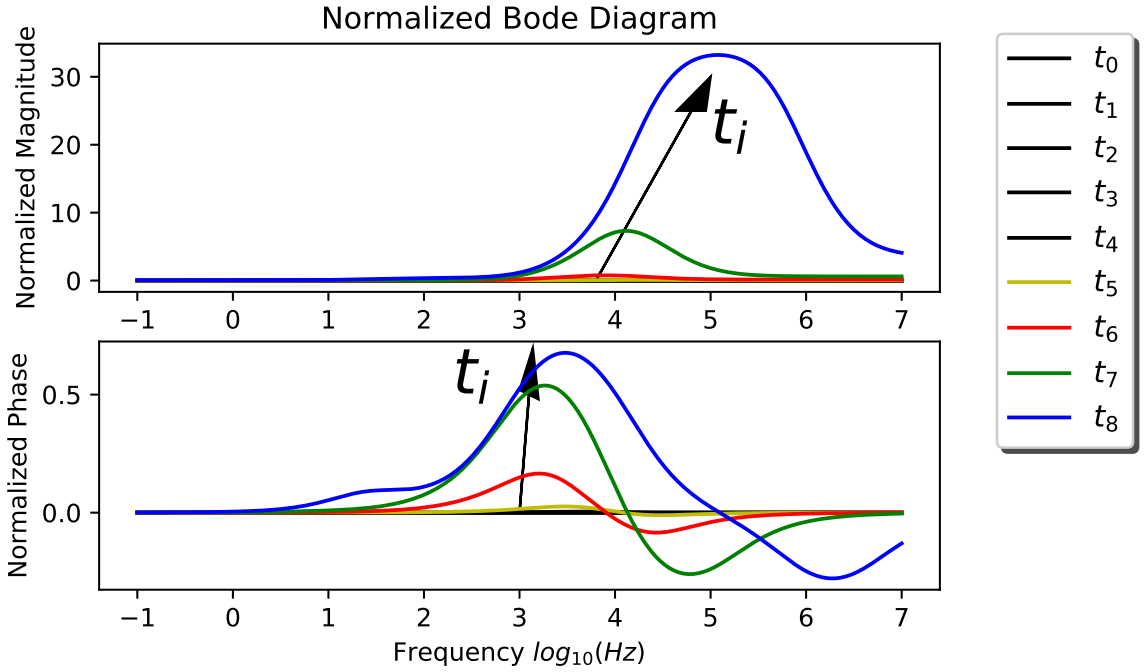

Fig. 2.19 Normalized bode diagram for (a)-(i) images corresponding to the 8W10E electrode.

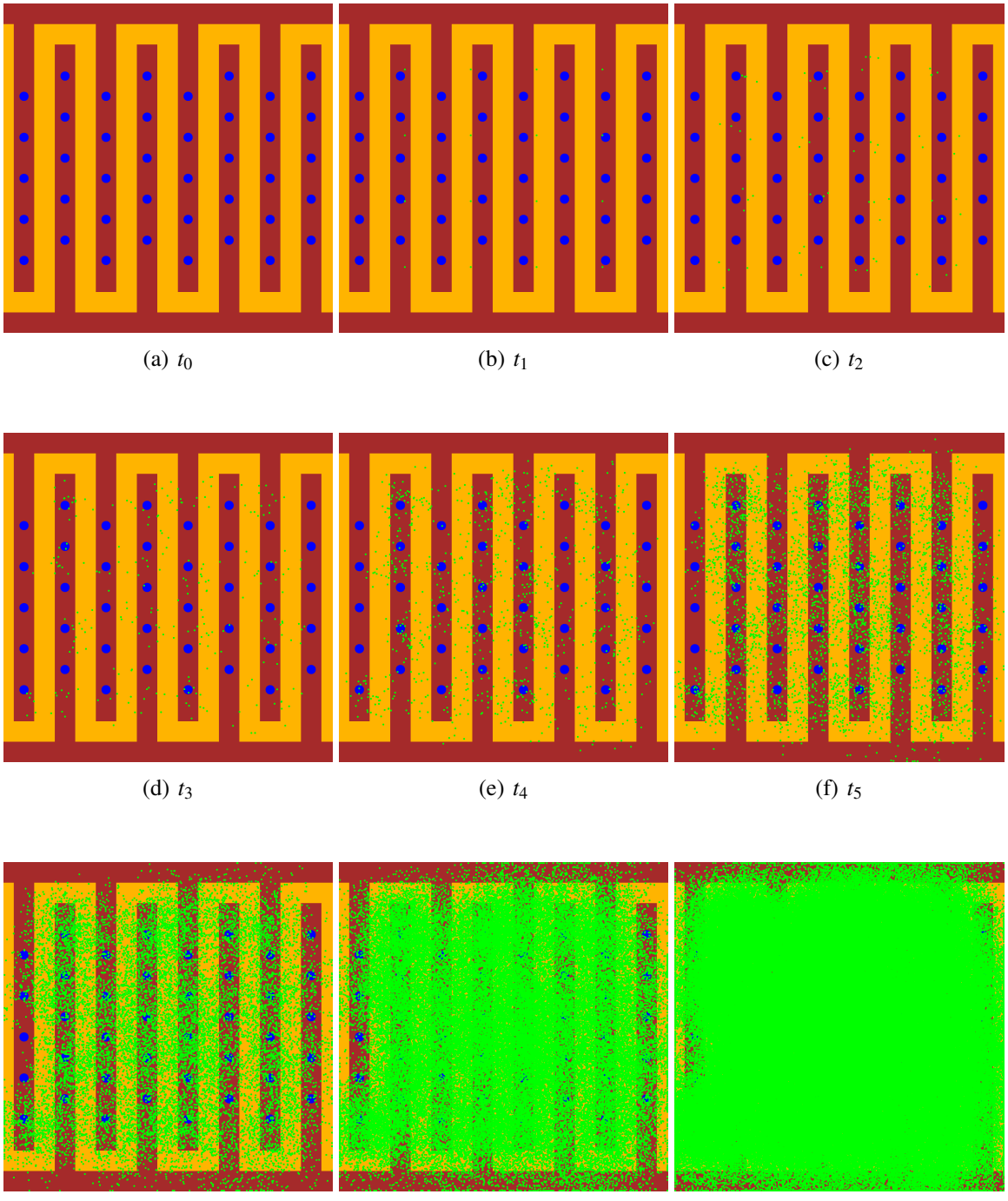

(a) t_0 (b) t_1 (c) t_2

(d) t_3 (e) t_4 (f) t_5

(g) t_6 (h) t_7 (i) t_8

Fig. 2.20 Random simulation on 8W10E+. The algorithm calculates the cell population based on an exponential growth. Different time steps are depicted on the figure ($t_0 - t_8$). Timeshift ($t_i - t_{i-1} = g$ which is the cell division cycle for a cell line.

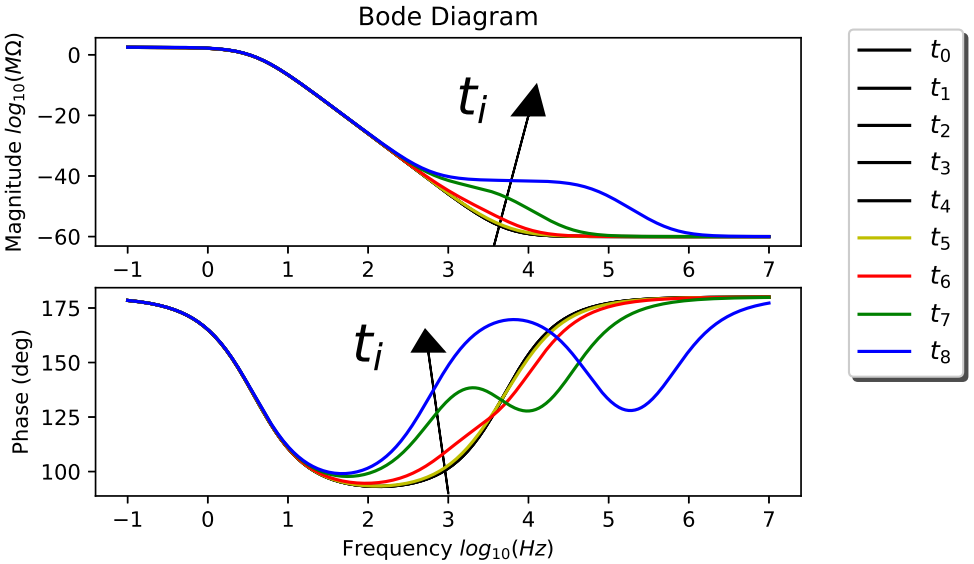

Fig. 2.21 Bode diagram for (a)-(i) images corresponding to the 8W10E+ electrode.

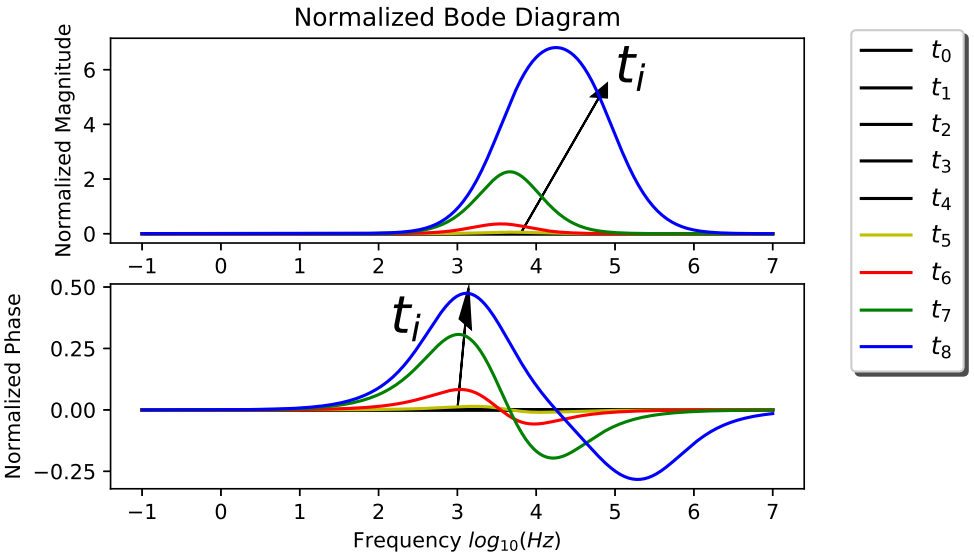

Fig. 2.22 Normalized bode diagram for (a)-(i) images corresponding to the 8W10E+ electrode.

The ff_{REAL} corresponds to the amount of cell-covered area on the well surface, where as ff_{SENSED} refers to the same relation but related to the sensible area; such area defined by the micro-electrodes in both devices. On figures 2.23 both curves depict a similar model for the random growth.

Hence considering a random growth model, it is possible to conclude that the values are similar in absolute terms in both topologies. According to the scientific references and

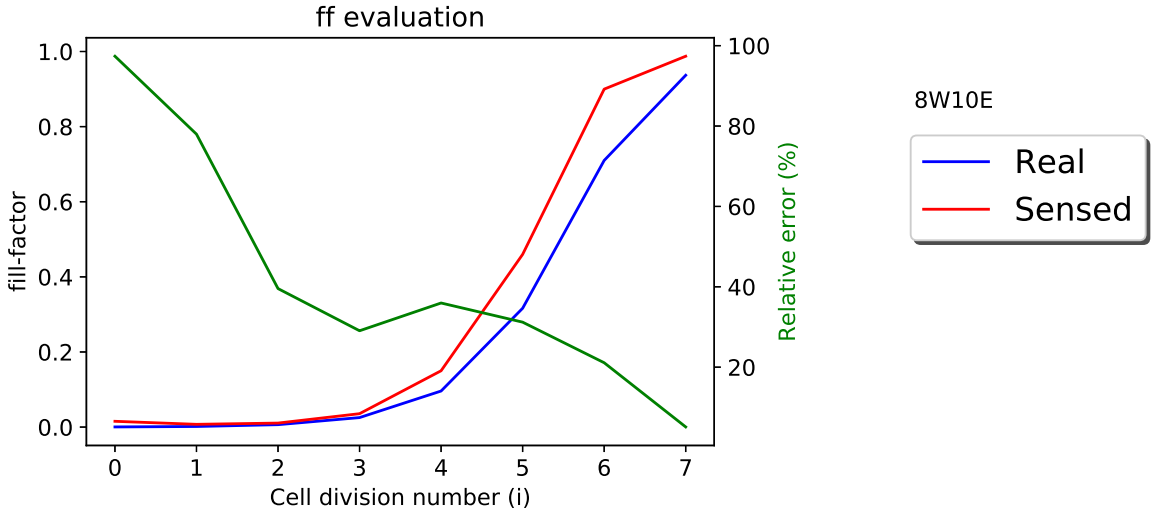

(a)

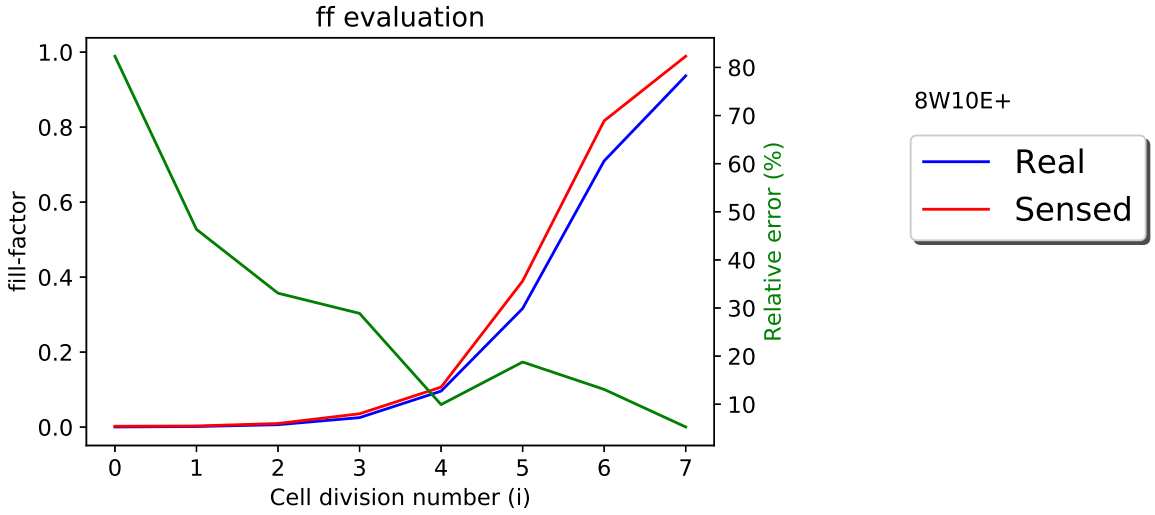

(b)

Fig. 2.23 Real and sensed ff versus the number of cell division cycles for (a) 10 micro-electrodes (8W10E) (b) 40 micro-electrodes (8W10E+).

existing knowledge on cells cultures growth dynamics, cell may grow forming up clusters on the substrate (rather than following up a random pattern). To tackle this issue using the existing simulation, it is enough to adapt the grow model by reducing the cell landing radius and establishing a lower number for initial seeding.

Central and border analysis

The second example assumes an unique central cluster growing on the electrode. Different stages are illustrated in Figure 2.24, not all the images are provided since those are similar to the ones exposed before. The sensed area is significantly lower using the 10 micro-electrodes topology compared to the 40 micro-electrodes topology as it is exposed in Figure 2.25. Furthermore, a third growing model is proposed herein; in the Figure 2.26 cells are forming two external cluster, thus avoiding the sensing area in 8W10E. The resulting value for the simulation is presented in Figure 2.27. The results obtained on this analysis expose the fact that both topologies do not sense equally when cell distribution is not constant across the sample substrate.

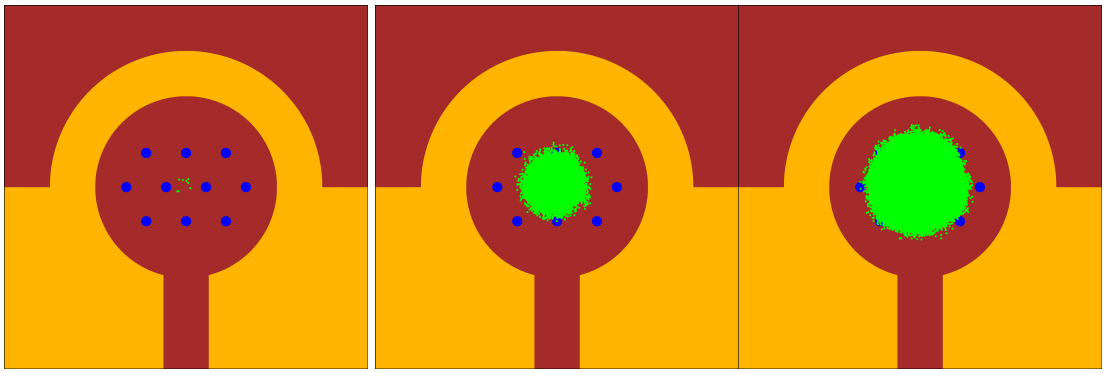

(a) t_2 (b) t_6 (c) t_8

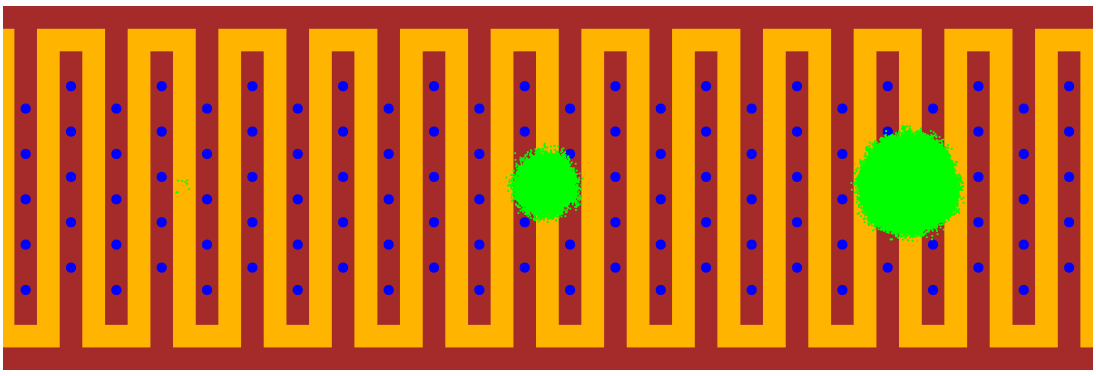

(d) t_2 (e) t_6 (f) t_8

Fig. 2.24 Border simulation on 8W10E. Different growth simulations for the 40 electrodes. Different time steps are depicted on the figure ($t_2 - t_8$). Timeshift ($t_i - t_{i-1} = g$ which is the cell division cycle for a cell line. Images illustrate 8W10E (a) i = 2, (b) i = 6, (c) i = 8 and for 8W10E+ (d) i = 2, (e) i = 6 and (f) i = 8.

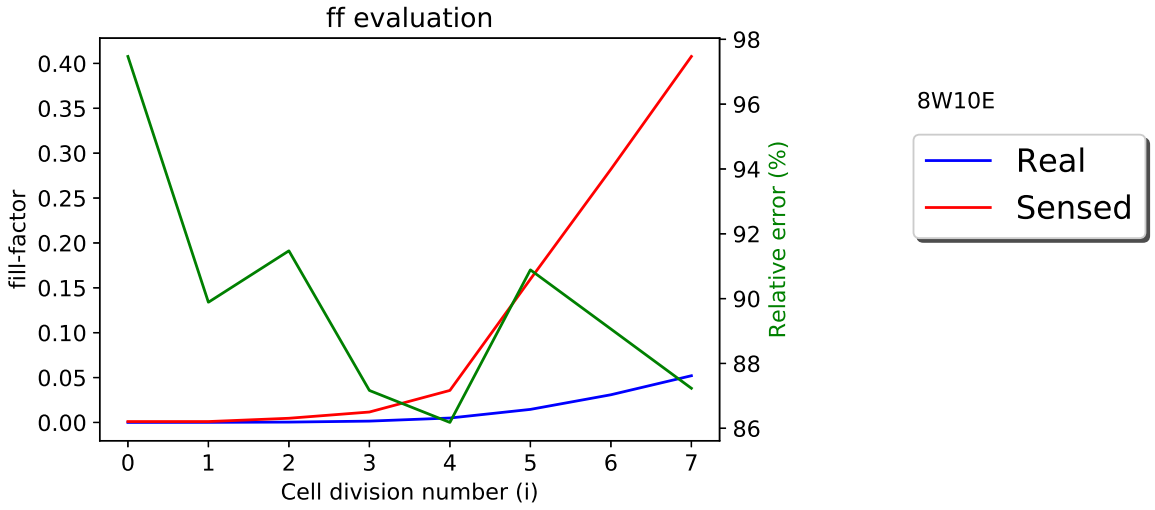

(a)

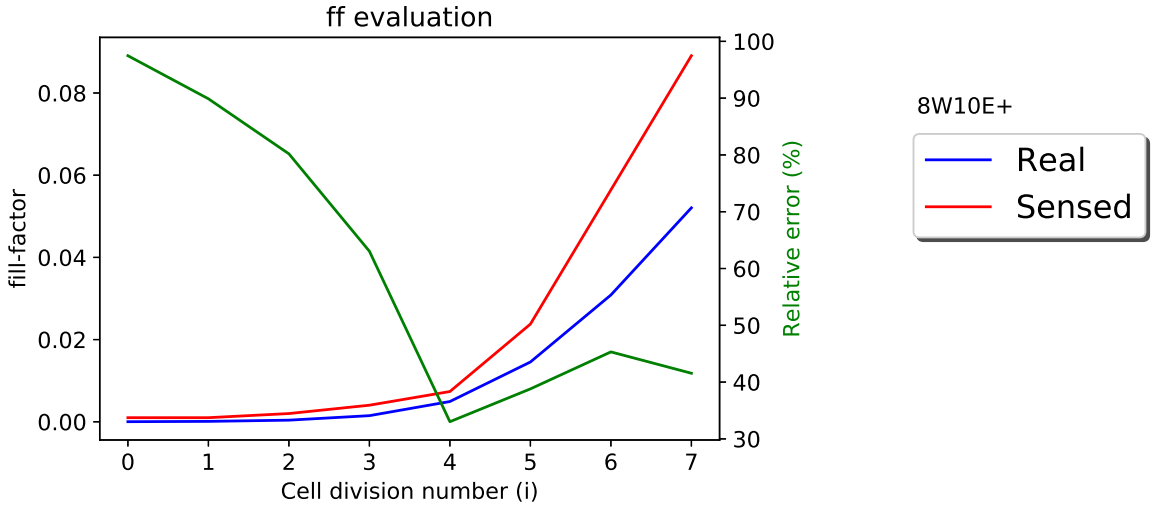

(b)

Fig. 2.25 Real and sensed ff versus the number of cell division cycles for (a) 10 micro-electrodes (8W10E) (b) 40 micro-electrodes (8W10E+).

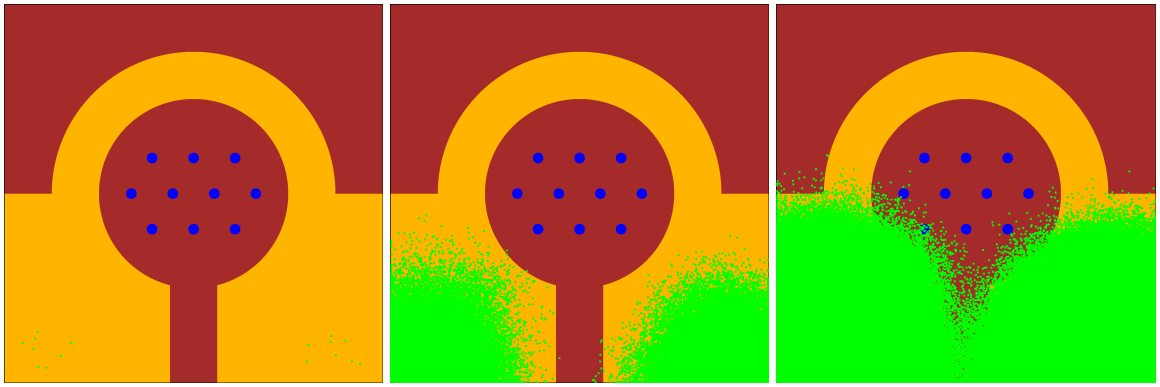

(a) t_2 (b) t_6 (c) t_8

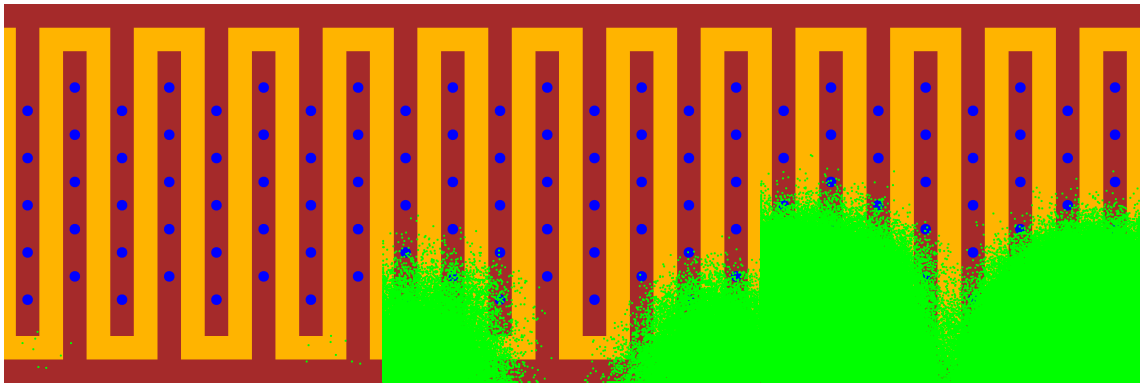

(d) t_2 (e) t_6 (f) t_8

Fig. 2.26 Central simulation on 8W10E+. Different growth simulations for the 40 electrodes. Different time steps are depicted on the figure ($t_2 - t_8$). Timeshift ($t_i - t_{i-1} = g$ which is the cell division cycle for a cell line. Images illustrate 8W10E (a) i = 2, (b) i = 6, (c) i = 8 and for 8W10E+ (d) i = 2, (e) i = 6 and (f) i = 8.

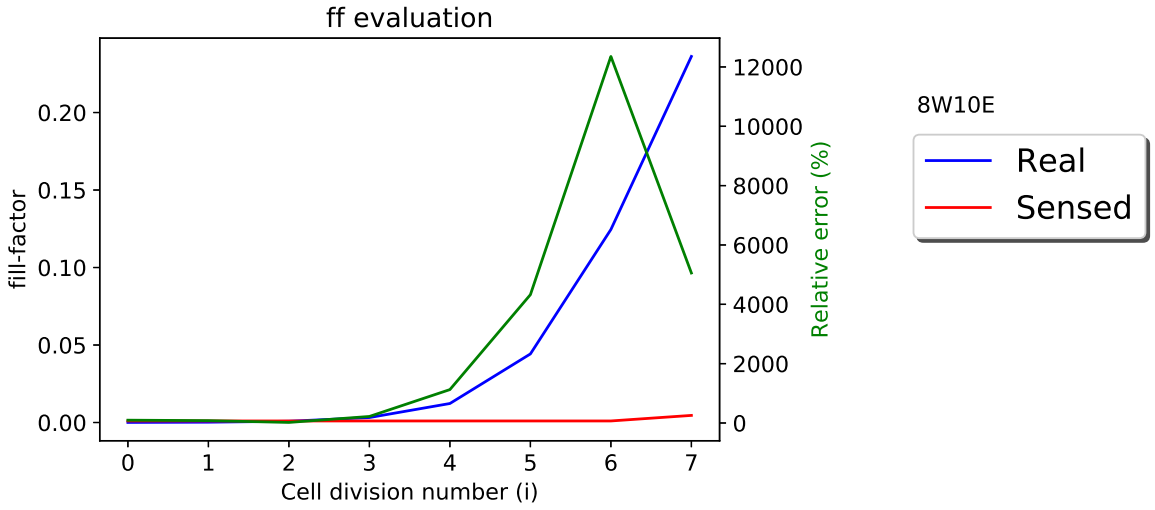

(a)

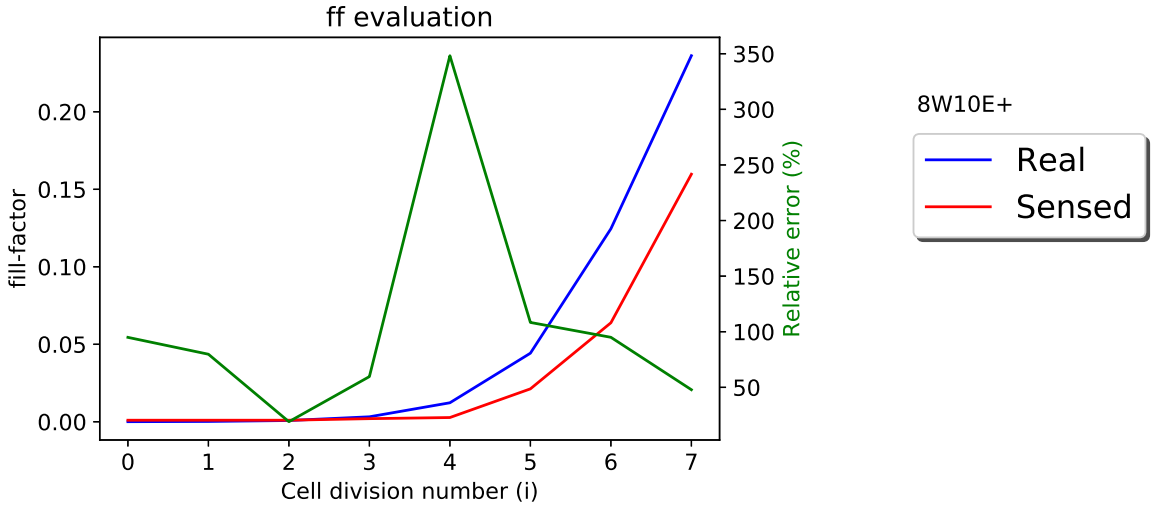

(b)

Fig. 2.27 Real and sensed ff versus the number of cell division cycles for (a) 10 micro-electrodes (8W10E) (b) 40 micro-electrodes (8W10E+).

2.4 Experimental analysis

The simulations exposed on the previous pages depict the relation between the fill-factor variation on the electrodes and the electrical response due to the electrode impedance related value. To validate those theoretical models, an experiment is designed to acquire empirical data. To obtain such measure, the interface depicted in Figure 2.28 (a) with tunnable R_{in} values was implemented and connected to an Analog Discovery 2 device capable of performing network analysis [122]. The full system capturing data is depicted in Figure 2.29

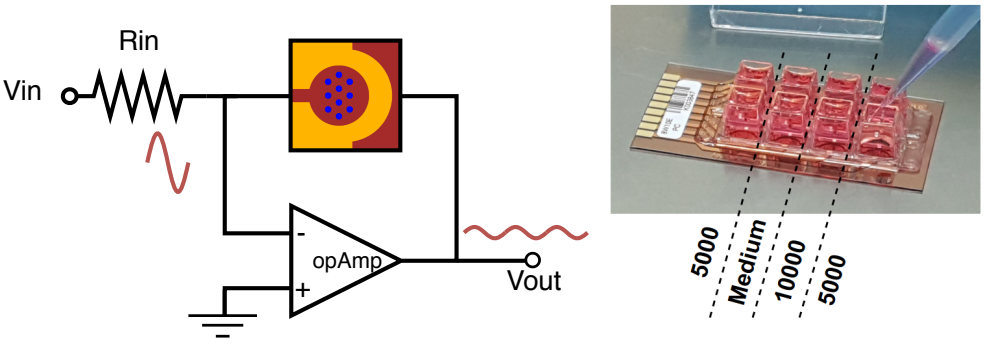

(a) Electrical interface (b) Cell culture

Fig. 2.28 (a) Circuit schematic for measurement. V_{in} is connected to the network analyzer output. A voltage follower is implemented on V_{out} and then to the Network analyzer input. (b) Cell Seeding process on the biomedical laboratory. Different initial cell values (5 k, None, 10 k, 5 k) are seeded on the wells.

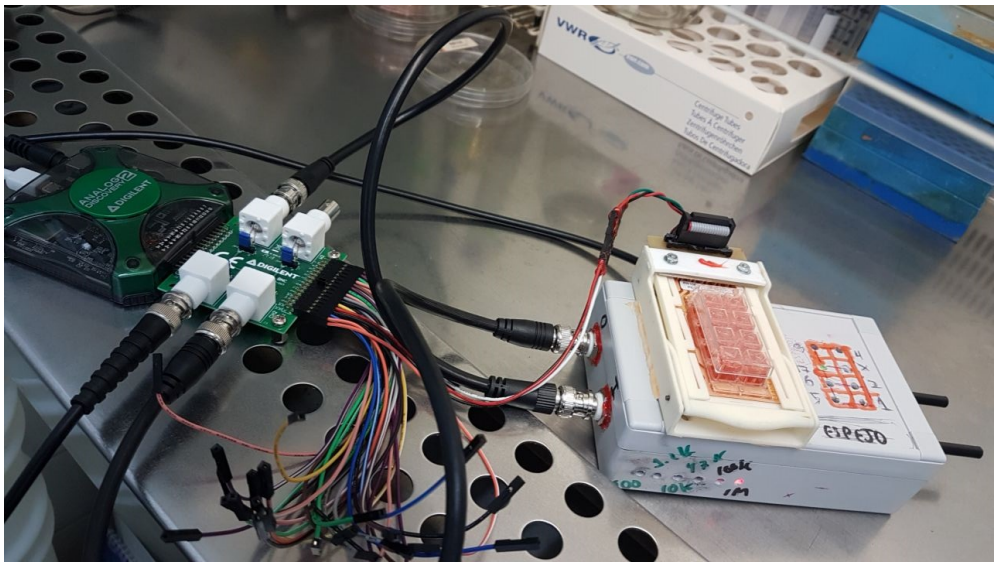

Fig. 2.29 Experimental setup for measuring the electrical response of the sample under test using Analog Discovery 2 device.

2.4.1 Acquisition protocol

The bio-impedance system under test has a dynamic range of around 80dB. The following protocol is proposed and summarized on table 2.1. This protocol assures that the signal recovered from the bio-impedance sample is always under measurable voltage levels. Furthermore, the electrode is kept under 100 mV which guarantees a linear operation point. To visualize the results in a single curve, the magnitude obtained from this set of measurements is related to 1 $M\Omega$ thus representing the value as Magnitude per MegaΩ.

Table 2.1 Measurement protocol

Start	*Stop*	*Amplitude*	R_{in}
$3Hz$	$30Hz$	$100mV$	$1M\Omega$
$30Hz$	$600Hz$	$100mV$	$100k\Omega$
$600Hz$	$1MHz$	$100mV$	$10k\Omega$

2.4.2 Experimental results

Initially, the electrodes are empty and the system must behave as proposed on the previous simulations. To validate the model we compare the simulated output to the experimental value acquired on the well number 6. Figure 2.30 is acquired using an inverted microscope to amplify by a ratio of 5x the sample. This enables the observation of the micro-electrodes under test. In Figure 2.31 the electrical response matches our previous simulations for the 8W10E substrate.

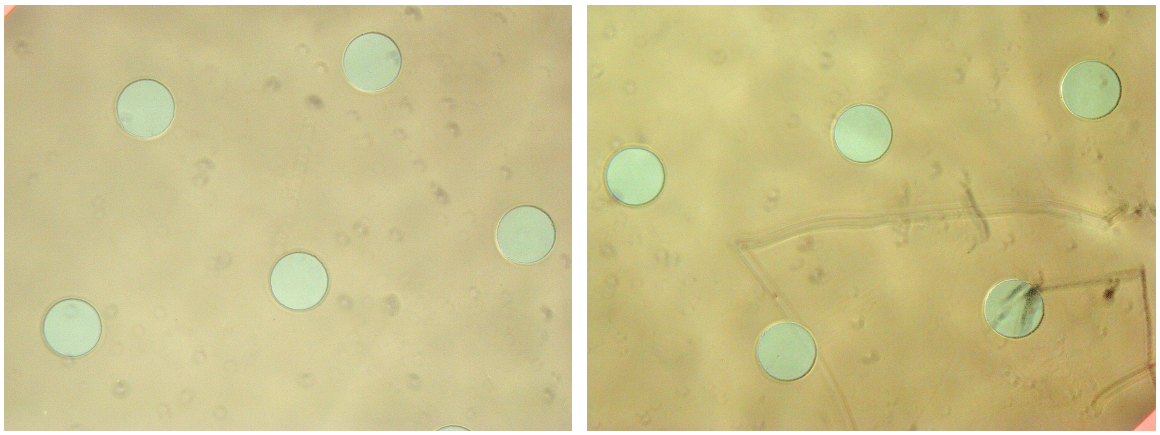

(a) 5x Well 6 (b) 5x Well 6

Fig. 2.30 5x TOP (a) and BOTTOM (b) view of the well number 6, filled with medium.

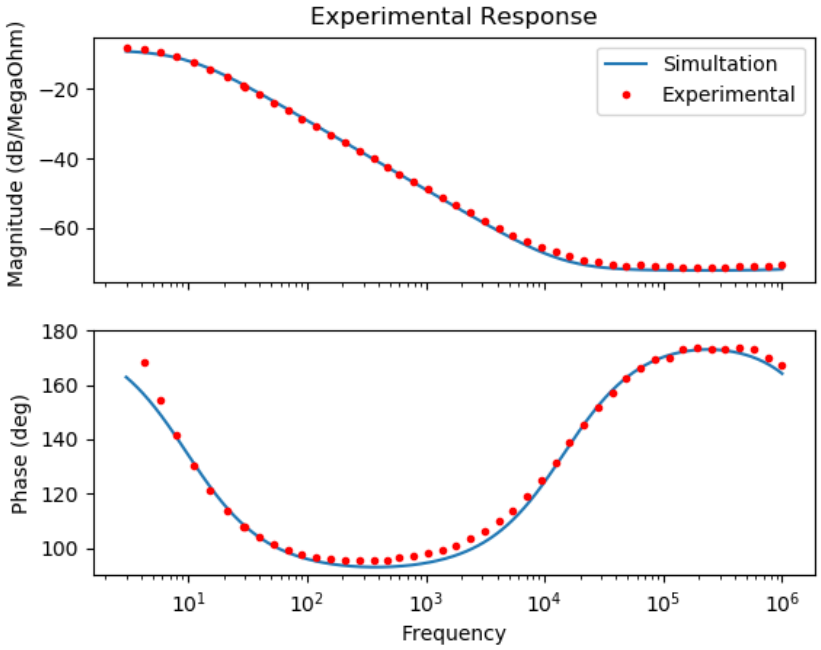

Fig. 2.31 Experimental vs simulated electrical response using $J_0 = 3.98 \cdot 10^{-6}\ A/cm^2$, $d = 5 \cdot 10^{-10}\ m$, $\varepsilon_r = 6$ and $n = 0.14\ mols/l$.

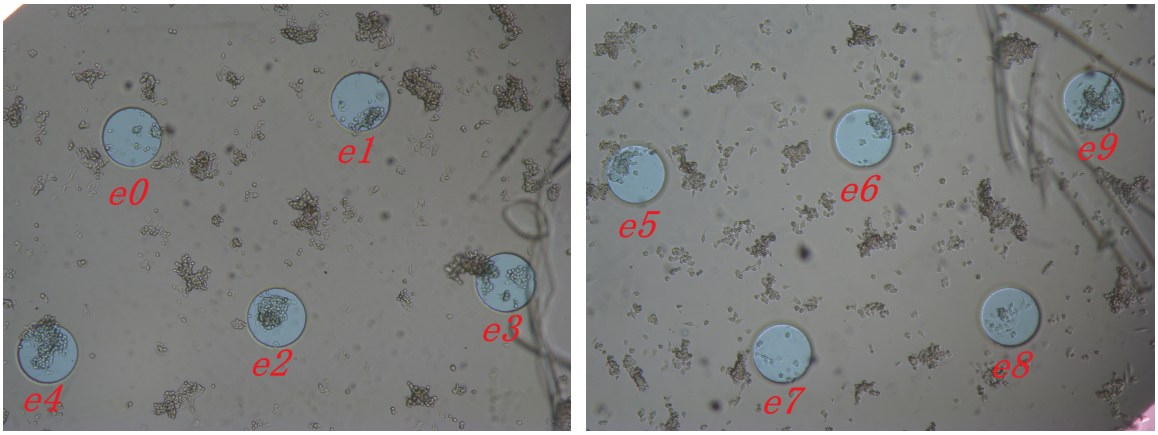

(a) 5x Well 7 TOP (b) 5x Well 7 BOTTOM

Fig. 2.32 5x view of the well number 7 on day 3, (a) TOP and (b) BOTTOM view. This well was initially seeded with 10 k cells. Each of the micro-electrodes is identified with a number ranging 0-9.

The wells depicted on figures 2.32, 2.33 and 2.34 are cropped to form the ten micro-electrode images depicted on figures 2.35 and 2.36 (a) - (j).

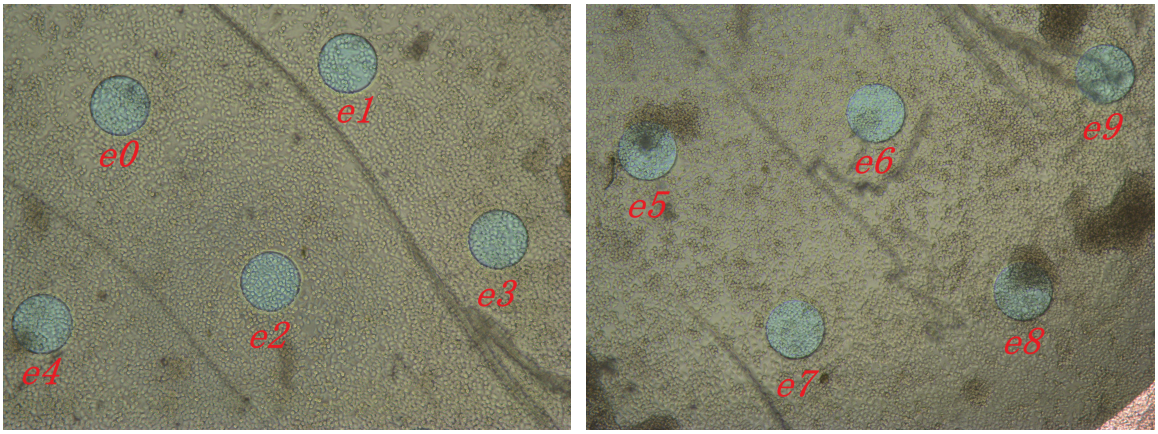

(a) 5x Well 8 TOP (b) 5x Well 8 BOTTOM

Fig. 2.33 5x view of the well number 8 on day 7, (a) TOP and (b) BOTTOM view. This well was initially seeded with 5 k cells. Each of the microelectrodes is identified with a number ranging 0-9.

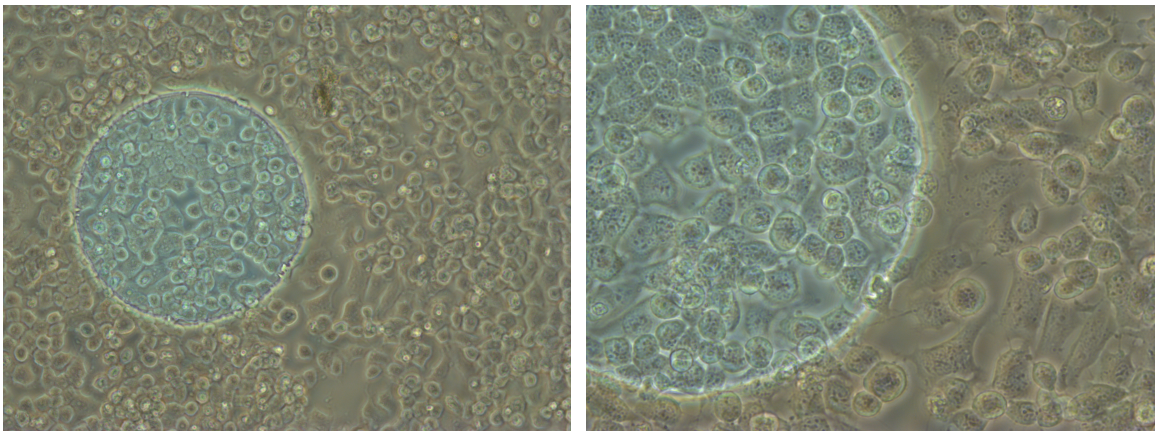

(a) Single micro-electrode 20x (b) Single micro-electrode 40x

Fig. 2.34 Microscopic view of the e_2 electrode on well number 8 on day 7, (a) 20x (b) 40x

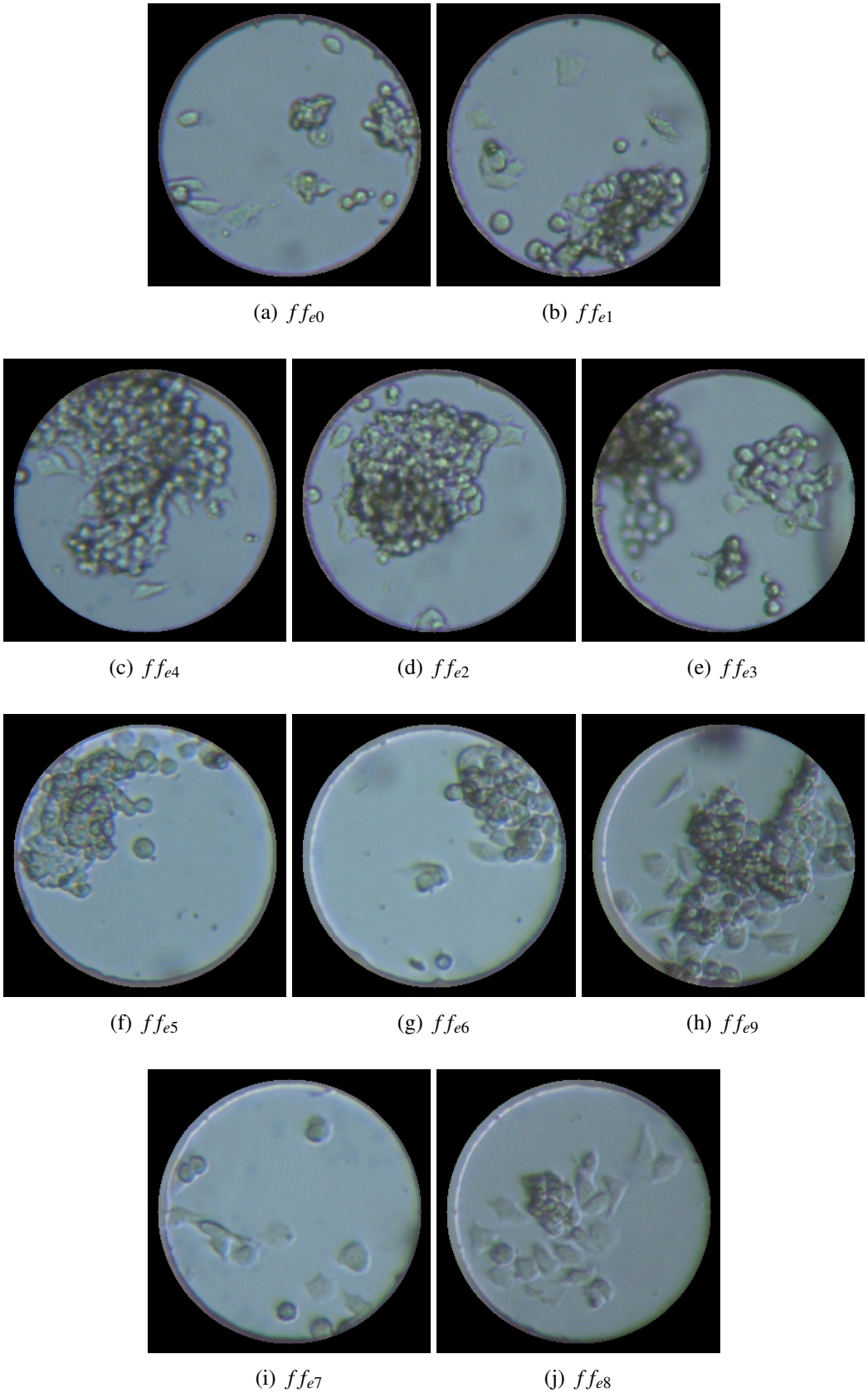

(a) ff_{e0} (b) ff_{e1}

(c) ff_{e4} (d) ff_{e2} (e) ff_{e3}

(f) ff_{e5} (g) ff_{e6} (h) ff_{e9}

(i) ff_{e7} (j) ff_{e8}

Fig. 2.35 Image crops (a)-(j) from the microscopic image for well 7 to compute ff_{0-9} values.

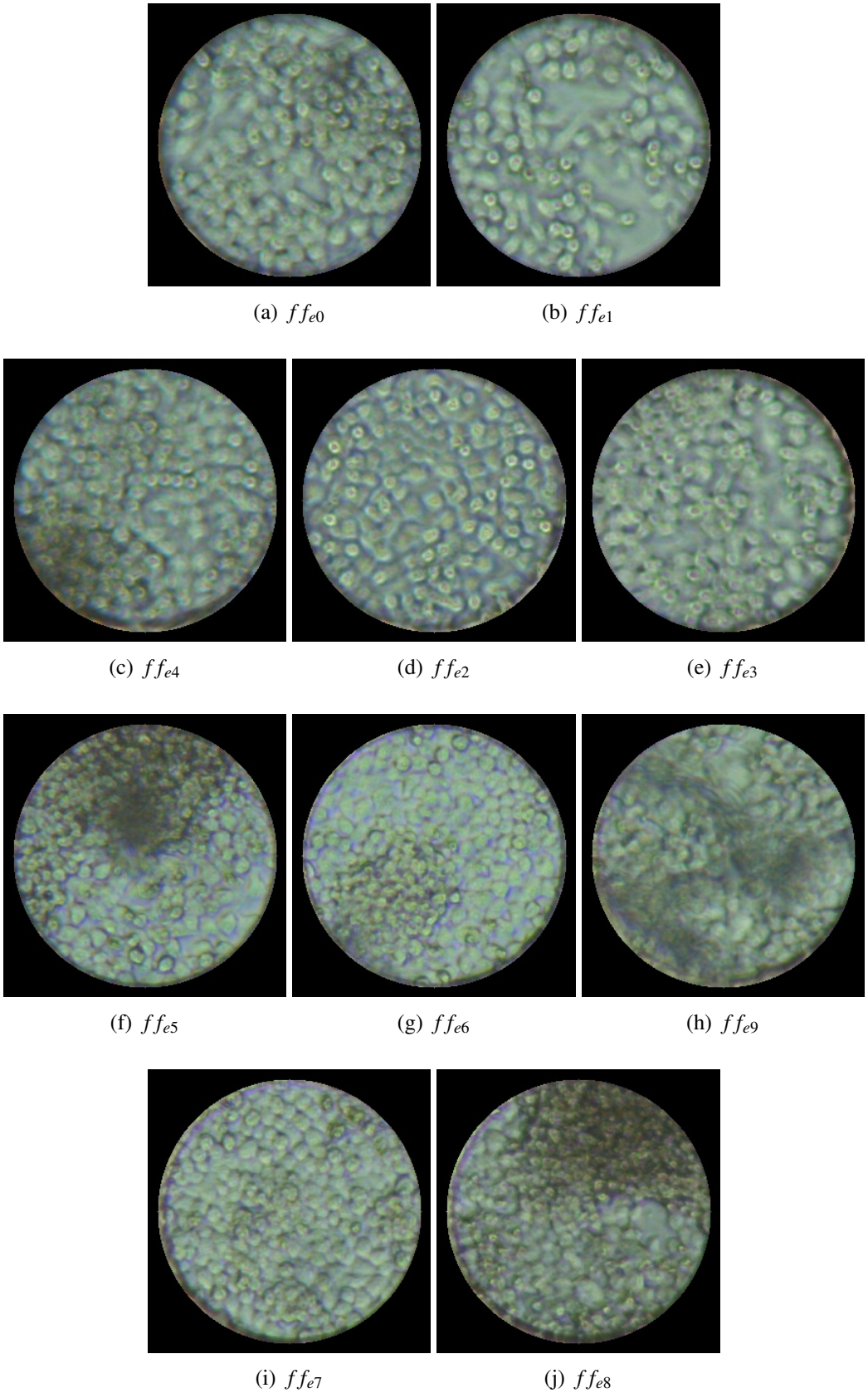

(a) ff_{e0} (b) ff_{e1}

(c) ff_{e4} (d) ff_{e2} (e) ff_{e3}

(f) ff_{e5} (g) ff_{e6} (h) ff_{e9}

(i) ff_{e7} (j) ff_{e8}

Fig. 2.36 Image crops (a)-(j) from the microscopic image for well 7 to compute ff_{0-9} values.

A biomedical scientist is then requested to mark in red the cell-attached areas. Further processing is then developed by an Open-CV algorithm implemented on Python which will estimate the fill-factors value for each of the micro-electrodes from the marked images. The resulting estimation for fill-factors is presented on table 2.2. The fill-factor value for the reference electrode is denoted as ff_{Ref} and it is obtained by computing the mean value across the 10 micro-electrodes.

Table 2.2 Computed fill-factor values

f_i	**Well 7 - Day 3**	**Figure 2.35**	**Well 8 - Day 7**	**Figure 2.36**
ff_0	0.28	(a)	0.85	(a)
ff_1	0.38	(b)	0.70	(b)
ff_2	0.47	(d)	0.85	(d)
ff_3	0.49	(e)	0.90	(e)
ff_4	0.60	(c)	0.75	(c)
ff_5	0.33	(f)	0.70	(f)
ff_6	0.21	(g)	0.94	(g)
ff_7	0.17	(i)	0.95	(i)
ff_8	0.40	(j)	0.99	(j)
ff_9	0.62	(h)	0.70	(h)
ff_{Ref}	$\sum_{i=0}^{N} \frac{f_i}{N+1}$	-	$\sum_{i=0}^{N} \frac{f_i}{N+1}$	-

The electrical response for both days is depicted on the following figure 2.37. The simulation result (blue line) is programmed using the parameters studied on the previous sections of the chapter for the electrodes and the fill-factor estimated from the crop images (table 2.2).

Figure 2.38, depicts the electrical response evolution for two wells (8 and 7). Initially, well 7 was seeded with 10 k cells and well 8 with 5 k cells. The cells were seeded on a Monday and the experiment duration was set to one week.

The experimental data gathered illustrates a sensitivity band for the electrode located between 1 kHz and 10 kHz for both phase and magnitude. This information is greatly useful and will allow us to effectively design the cell sensor using the commercially available micro-electrodes from Applied Biophysics [98].

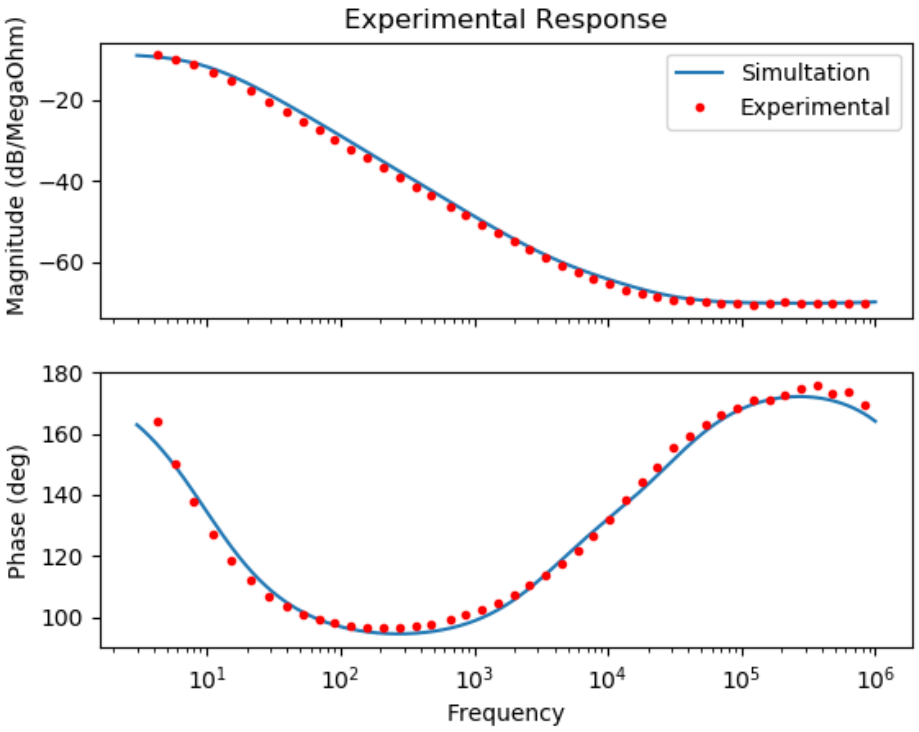

(a) Well 7 / 3rd day

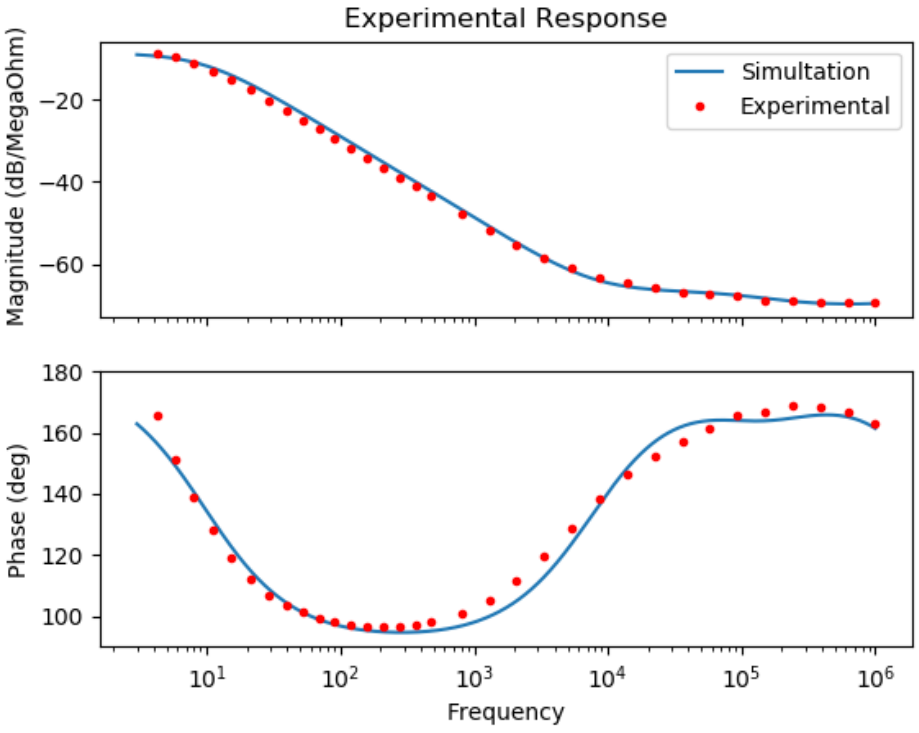

(b) Well 8 / 5th day

Fig. 2.37 Experimental vs simulated electrical response using $J_0 = 3.98 \cdot 10^{-6}\ A/cm^2$, $d = 5 \cdot 10^{-10}\ m$, $\varepsilon_r = 6$ and $n = 0.14\ mols/l$, $R_{gap} = 2\ k\Omega$

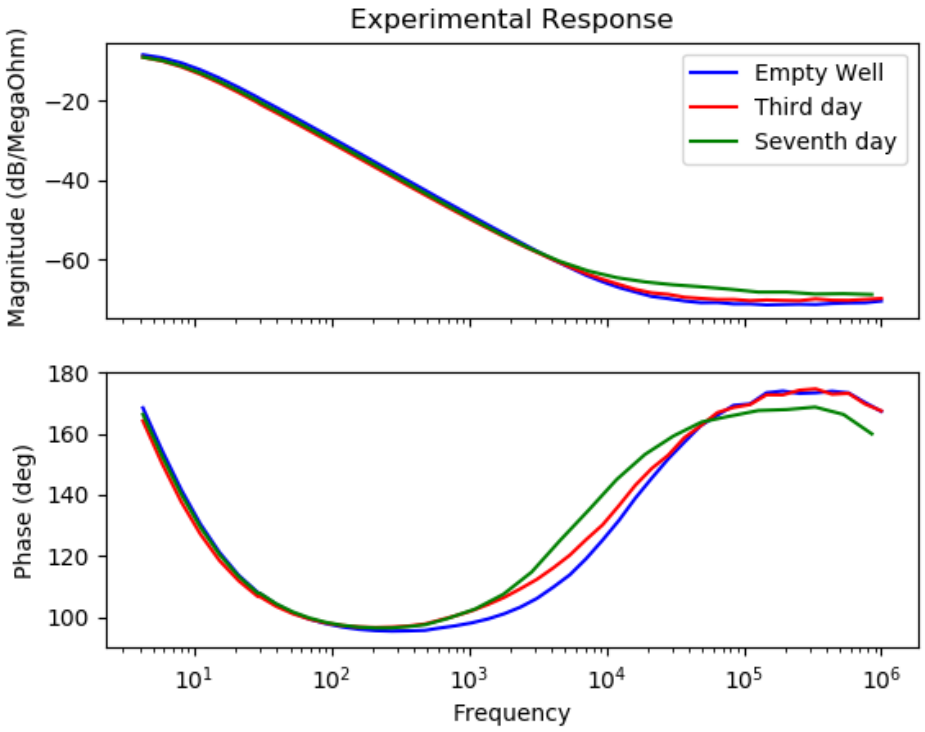

(a) Well 7

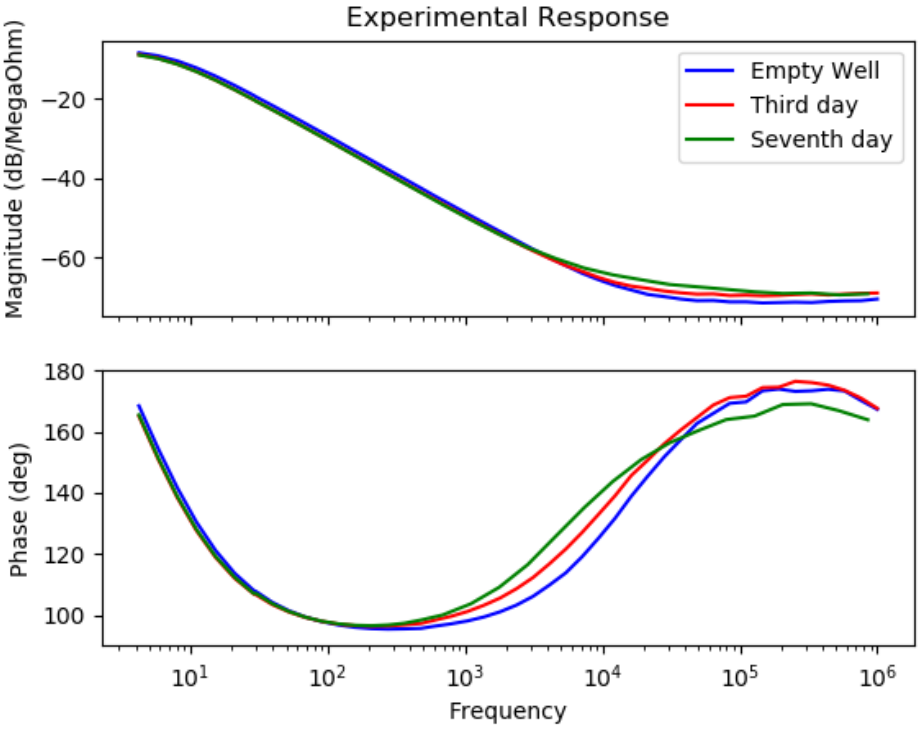

(b) Well 8

Fig. 2.38 Electrical response variation with time evolution of cell culture under growth on well 7 (a) and well 8 (b).

Summary and conclusions

This chapter illustrates the physical background for the cell culture sensing using the ECIS technique. The content develops an engineering approach by providing deep understanding of the underlying physical process.

- The double layer inter-phase generated on the micro-electrodes immersed in saline solution is the guiding process along with the impedance variation generated on the electrode due to cell adherence to the substrate. This process has been described and electrically modelled. This knowledge allowed the description of an equivalent electrical model for the cell electrode interface.

- Several analysis of the geometric variations at the electrode have been performed via computer simulations; including cell-growth dynamic modelling and image processing. This provides additional insight on the cell culture sensing dynamics.

- The influence of both the electrode geometry and the R_{gap} parameter on the electrical response was analyzed. The results show the effect over the reliability of the cell number estimation process. Moreover, three different growth patterns analyzed effectively alter the reading from the sensor and its potential effect is dependant on the electrode geometry.

- The proposed model has been validated by simulation, using a basic circuit and a commercial analyzer system; Analog Discovery 2 from Digilent [122]. A cell culture assay was accordingly planned to evaluate the electrical response variation with a 7-day experiment performing acquisition on the third and the seventh day. Alongside the electrical measurements, optical visualization was performed using an inverted microscope capable of performing digital imaging acquisition. These images were further processed using to obtain an estimation of the fill factor (ff) value for each of the micro-electrodes under test. The goal of it is to match the previous simulations with the experimental results from the assays.

- The experimental results highlight a difference between the simulated model used in the literature and the real cell-culture assay electrical response. The affected electrical parameters are C_{dl} , R_s and R_{gap}. The greatest difference is found out on the R_{gap} value, which depicts a reduction factor of almost one hundred times. This factor provides the reason for the difference in shape on the simulation and the experimental curves. A reasonably good matching was achieved on such curves, by adjusting the electrical

parameters and hence providing a candidate model for the underlying process as a result. This electrical model will be fundamental for performing the sensor analysis and design to measure the cell culture growth on next chapters.

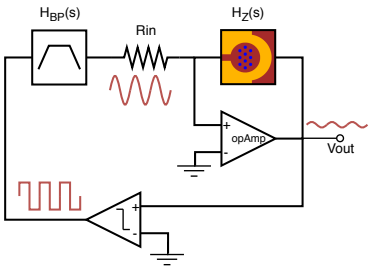

Chapter 3

Oscillation Based Test (OBT) for cell culture measurements

3.1 Oscillation Based Test (OBT) concept

The electrodes and the cell-electrode interaction model have been analyzed on the previous chapter. This chapter will introduce the design of a sensor which can provide accurate insight from the physical effects undergoing on the electrode as a result of the cell attachment to the substrate. There are several different techniques existing on the literature which can perform impedance measurement from a biological sample (chapter 1). The Oscillation Based Test (OBT) approach converts the bio-impedance in a sensing oscillator, where the signal oscillation parameters are related to the biological sample under test.

The OBT technique presents several advantages; avoids complex synchronization and does not need external stimulation injection therefore reducing the cost of complex extra circuitry. This is the reason to consider it as the selected bio-impedance measurement tool. Furthermore, signal acquisition and processing to analyze frequency and amplitude parameters is also a simple task.

3.1.1 Analytic study

The OBT circuit forms a non-linear feedback loop containing the biological sample under test. This loop will self-oscillate and the generated signal parameters are related to the physical properties of the biological sample, hence transforming the system into a biological oscillatory sensor. Consider the following circuit depicted on Figure 3.1.

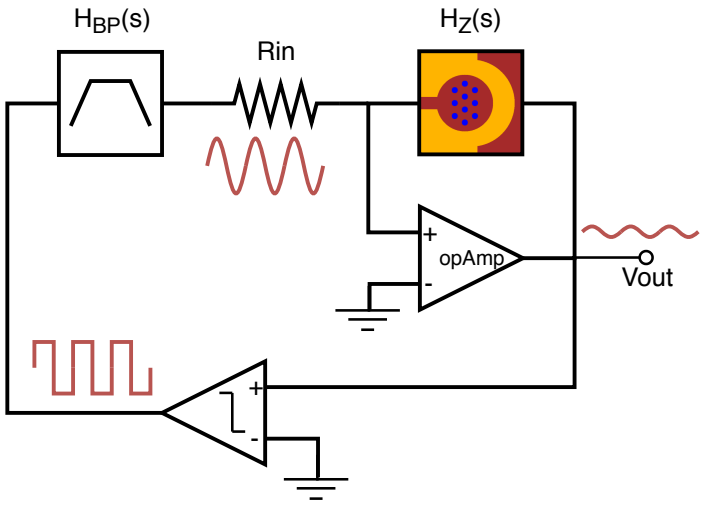

Fig. 3.1 Oscillation based test concept for bio-impedance sensing.

As presented in Figure 3.1, the cell-culture is transformed into a robust oscillator, adding some extra components. In order to force oscillations, a positive feedback loop has to be implemented. It is particularly important to accurately predict the parameters of oscillation (frequency and amplitude), analytically or by means of simulations. It is also necessary to avoid the dependence of these parameters on the saturation characteristics of the active elements, like occurs in common oscillators. A solution to this problem is to use a non-linear element (a simple comparator) closing a feedback loop to guarantee self-maintaining oscillations. This non-linear element also provides a precise control of the oscillation amplitude. On the other hand, we need to guarantee that this system complies with a (relatively) simple set of oscillation conditions, which can provide information on the oscillation parameters. A simple way to achieve this is to use a band-pass filter in the loop, as proposed in the general circuit block. For the sake of simplicity, as a concept proof, let us now set up the case of a second-order band-pass filter and a comparator with saturation levels $[-V_{ref}, V_{ref}]$.

This closed-loop system verifies the required premises: the system is autonomous, the non-linearity is separable and frequency-independent, and the linear transfer function contains enough low-pass filtering to neglect the higher harmonics at the comparator output. Furthermore, the equations ruling the oscillation conditions can be handled easily.

Choosing the band-pass filter adequately, the closed-loop system of Figure 3.1 can be forced to oscillate and its first-order Describing-Function (DF) equation, $N(a) + 1/H(s) = 0$, has an oscillatory solution (ω_{osc}, a_{osc}), being ω_{osc} the oscillation frequency and a_{osc} the oscillation amplitude. The DF function will be, in this case N(a) for the non-linear block (comparator), while H(s) is the transfer function of the open-loop system.

Aiming at validating these results, the proposed biological oscillator was firstly implemented in simulation. A comparison between theoretical predictions and simulation results

led us to confirm that both are very similar. It can be seen that the adopted method predicts the oscillation parameters with enough accuracy for this application [77].

The adequate design of the band pass filter will force the oscillations on the system [123]. As was mentioned before, the oscillator characteristic equation can be expressed as:

$$1 + N(a) \cdot H(s) = 0 \tag{3.1}$$

Where $N(a)$ correspond to the comparator non-linear transfer function and $H(s)$ represents the biological-impedance and the band-pass filter response. As said, this equation will have an oscillatory solution (ω_{osc}, a_{osc}), with ω_{osc} and a_{osc} as the angular frequency and the amplitude of the oscillation generated. Where, as previously stated, $H(s)$ defines the contribution of band pass filter and the biological sample under test:

$$H(s) = H_{BP}(s) \times H_z(s) \tag{3.2}$$

Let H_{BP} be the transfer function for the second order band pass filter defined as follows:

$$H_{BP}(s) = \frac{G_0 \cdot \frac{\omega_f}{Q_f} \cdot s}{s^2 + \frac{\omega_f}{Q_f} \cdot s + \omega_f^2} \tag{3.3}$$

Where G_0 defines the filter gain, Q_f is its quality factor, and ω_f the peak frequency. For illustration, a typical frequency response would be depicted on the following Figure 3.2. The values considered were: $Q_f = 10$, $G_0 = 1$, $\omega_f = 2\pi 10^3$ rad/s for a peak frequency $f_0 = 1$ kHz.

For the sake of simplicity in the exposition presented here, the interface system is accounting for a single electrode interface. To illustrate the approach, an example simulated response of the ideal interface model for a fill-factor of 0.5 is presented in the Figure 3.3. Assuming there is only one micro-electrode under test and recalling equation (2.49), the bio-impedance response is proposed in the form:

$$H_z(s) = \frac{k_2 \cdot s^2 + k_1(\frac{\omega_b}{Q_b})s + k_0 \cdot \omega_b^2}{s^2 + (\frac{\omega_b}{Q_b})s + \omega_b^2} \tag{3.4}$$

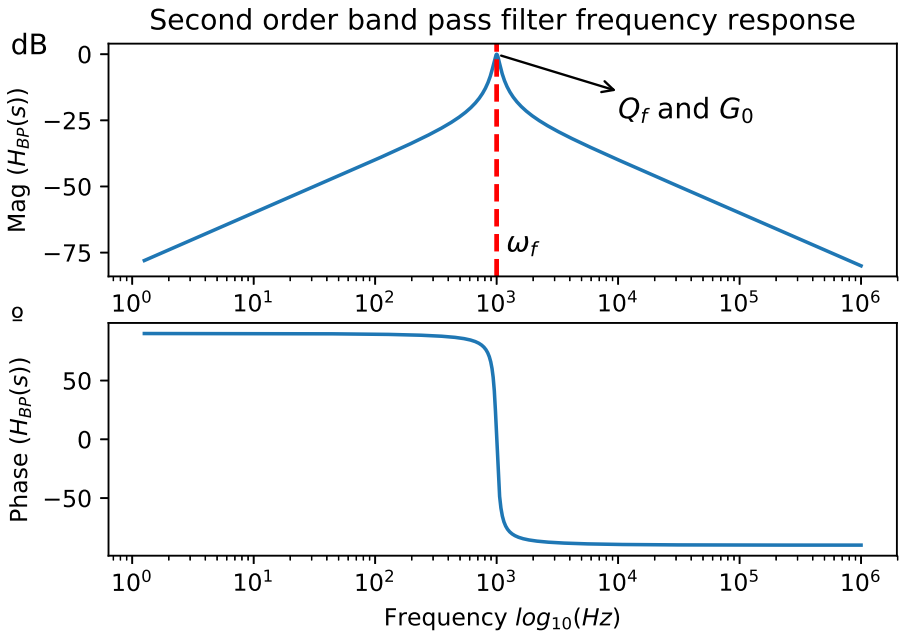

Fig. 3.2 Frequency Response for the Band Pass Filter. Parameters for the filter are $Q = 10$, $G_0 = 1$ and $f_0 = 1\ kHz$

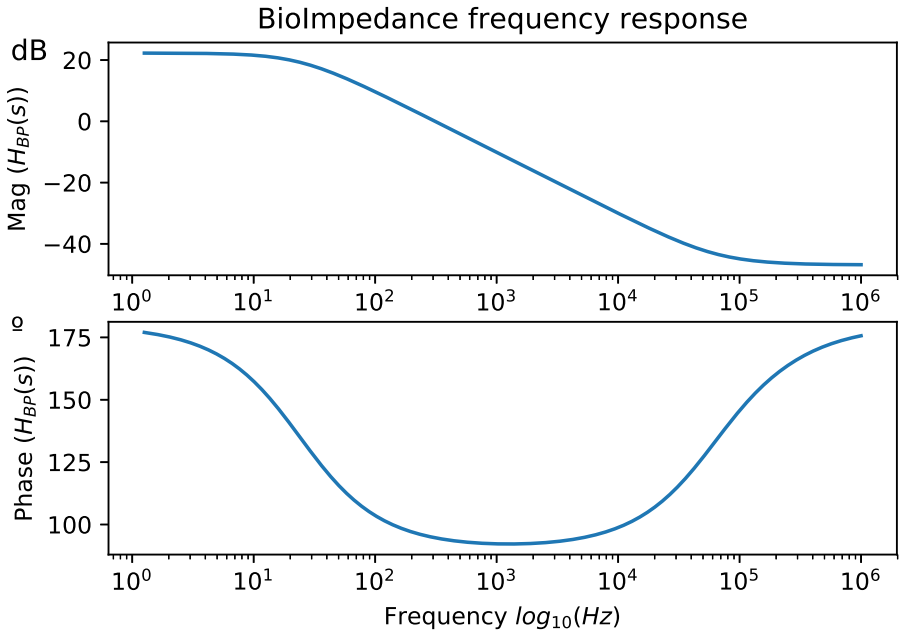

Fig. 3.3 To illustrate the biological single-electrode interface response this simulation is performed. The sample fill-factor entitles a value of $ff = 0.5$. The rest of the parameters for the interface simulation are $R_{in} = 100\ k\Omega$, $R_s = 455\ \Omega$, $R_{ct} = 1.3\ M\Omega$, $C_{dl} = 32\ nF$ and $R_{gap} = 750\ \Omega$.

Biological parameters on equation (3.4) (Q_b, ω_b, k_0,k_1,k_2) are computed from the electrical values (C_{dl}, R_{ct}, R_s and R_{gap}) which depends on the cell culture fill-factor (ff) as described in Chapter 2. Those electrical values are obtained from equation (2.49), performing the amplifier circuit (Figure 3.1) electrical analysis and expressing the result in the form presented in equation (3.4):

$$H_z(s) = \frac{-R_s \cdot d_2 \cdot s^2 - (R_s \cdot d_1 + n_1) \cdot s - (R_s \cdot d_0 + n_0)}{R_{in} \cdot d_2 \cdot s^2 + R_{in} \cdot d_1 \cdot s + R_{in} \cdot d_0} \tag{3.5}$$

Where d_2, d_1 and d_0 represent the denominator coefficients and n_1, n_0 the numerator coefficients involved in the Z_{bio} second-order transfer function from equation (2.49). Those values represent the physical properties of the biological sample under test, by the mathematical model already analyzed on Chapter 2 and conceptualized in equation (2.49). Dividing the equation by the s^2 denominator coefficient term ($R_{in} \cdot d_2$) results:

$$H_z(s) = \frac{\frac{-Rs}{R_{in}} \cdot s^2 - \frac{Rs \cdot d_1 + n_1}{R_{in} \cdot d_2} \cdot s - \frac{R_s \cdot d_0 + n_0}{R_{in} \cdot d_2}}{s^2 + \frac{R_{in} \cdot d_1}{R_{in} \cdot d_2} \cdot s + \frac{d_0}{d_2}} \tag{3.6}$$

Comparing this result to equation 3.4 it is possible to define the following system:

$$\omega_b^2 = \frac{d_0}{d_2} \tag{3.7}$$

$$\frac{\omega_b}{Q_b} = \frac{d_1}{d_2} \tag{3.8}$$

$$k_0 \cdot \omega_b^2 = -\frac{R_s \cdot d_0 + n_0}{R_{in} \cdot d_2} \tag{3.9}$$

$$k_1 \cdot \frac{\omega_b}{Q_b} = -\frac{R_s \cdot d_1 + n_1}{R_{in} \cdot d_2} \tag{3.10}$$

$$k_2 = -\frac{R_s}{R_{in}} \tag{3.11}$$

As previously stated on equation (3.2), the response ($H(s)$) is affected by both contributions; from the band-pass Filter and the sample under test. Hence, a major design concern at this stage is to define the band-pass filter parameters which will promote the oscillatory behaviour on the sensor for an electrode and cell electrical models given. A simulation representing Q variations over the combined response ($H(s)$) is depicted on the next Figure 3.4. Higher Q values provide a greater resonance peak over the tuning frequency, f_0. However,

since the filter bandwidth is narrow in this case, frequency dynamic range will be smaller. The design focus is on achieving a less abrupt phase change at the operation point.

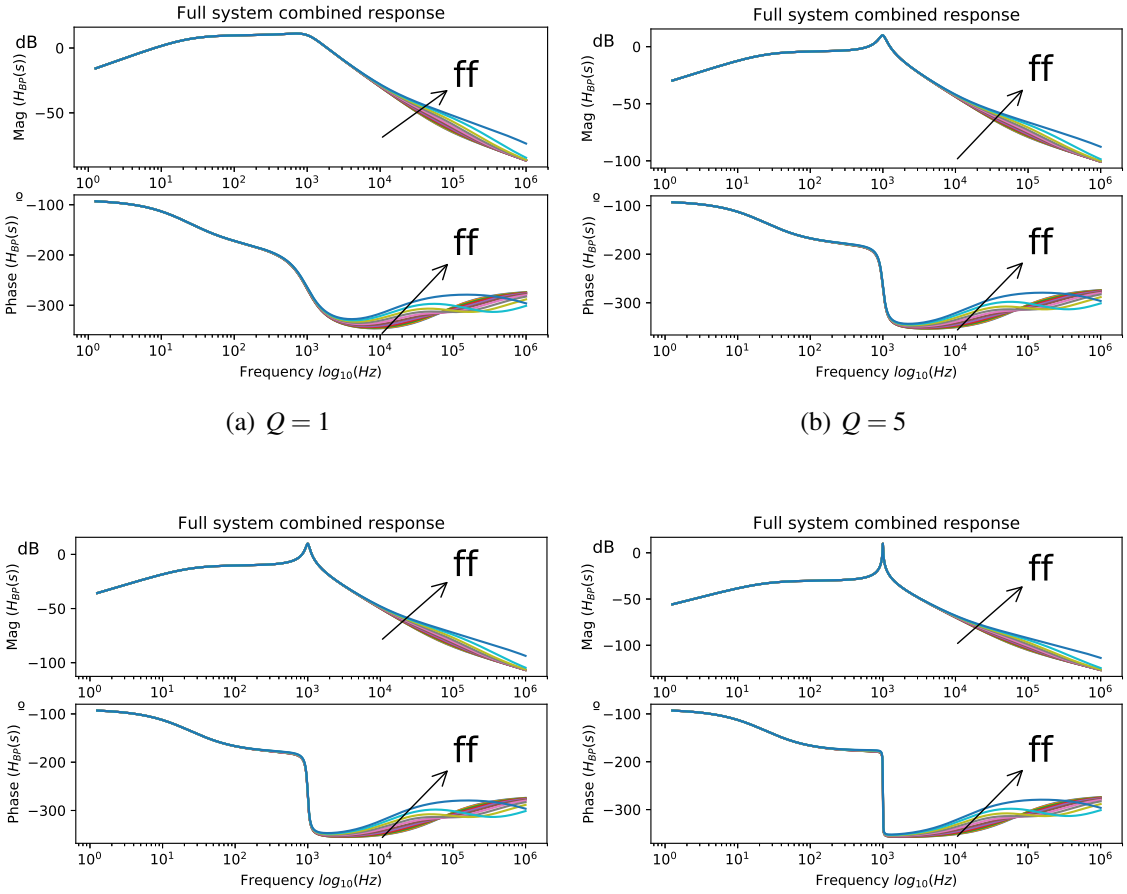

(a) $Q = 1$ (b) $Q = 5$

(c) $Q = 10$ (d) $Q = 100$

Fig. 3.4 Different quality factor (Q) values for the combined response of the filter and the bio-impedance. A sweep is performed on the fill-factor over every simulation. The analysis was performed for $Q = 1$ (a), $Q = 5$ (b), $Q = 10$ (c) and $Q = 100$ (d). $f_0 = 1\ kHz$.

The oscillation conditions require the existence of a complex pole pair in the system. Therefore, oscillation parameters (amplitude, gain, frequency) can be determined by solving equation 3.1. This is equivalent to assume a pair of complex poles on the aforementioned equation:

$$1+N(a)\cdot H(s)=(s^2+\omega_{osc}^2)(s^2+B\cdot s+A)=0 \tag{3.12}$$

where, matching the equations result on the following coefficients:

$$B=\frac{\omega_b}{Q_b}+\frac{\omega_f}{Q_f}+N(a_{osc})\cdot G_0\cdot k_2\cdot\frac{\omega_f}{Q_f} \tag{3.13}$$

$$A+\omega_{osc}^2=\omega_b^2+\frac{\omega_b}{Q_b}\cdot\frac{\omega_f}{Q_f}+\omega_f^2+N(a_{osc})\cdot G_0\cdot\frac{\omega_f}{Q_f}\cdot k_1\cdot\frac{\omega_b}{Q_b} \tag{3.14}$$

$$B\cdot\omega_{osc}^2=\omega_0^2\cdot\frac{\omega_f}{Q_f}+\frac{\omega_f}{Q_f}\omega_f^2+N(a_{osc})\cdot G_0\cdot\frac{\omega_f}{Q_f}\cdot k_0\cdot\omega_b^2 \tag{3.15}$$

$$\omega_{osc}^2\cdot A=\omega_b^2\cdot\omega_f^2 \tag{3.16}$$

Biological system output (which acts as the input to the comparator) is sinusoidal due to the band-pass characteristics of the previous filter. This fact permits the application of the linear approximation in the describing function method [124]. The resulting transfer function for the comparator can be defined as $N(a_{osc})=\frac{4\cdot V_{ref}}{\pi\cdot a_{osc}}$ where V_{ref} is the comparator voltage reference and a_{osc} is the voltage oscillation amplitude. The resulting oscillation parameters (ω_0, a_{osc}) (Figure 3.4) depend entirely on the band-pass filter selected parameters (Q_f, ω_f, G_0) and the biological impedance under test parameters (Q_b, ω_b, k_0,k_1,k_2), which are computed from the electrical model depicted on Chapter 2 and the fill-factor (ff).

To solve the equation system and obtain the oscillation parameters, initially the equations (3.13), (3.14), (3.15) and (3.16) are expressed in the form:

$$\begin{bmatrix} B \\ A+\omega^2 \\ B\cdot\omega^2 \\ A\cdot\omega^2 \end{bmatrix}=\begin{bmatrix} c_1 \\ c_2 \\ c_3 \\ c_4 \end{bmatrix}+\begin{bmatrix} m_1 \\ m_2 \\ m_3 \\ 0 \end{bmatrix}\cdot N(a_{osc})$$

Hence using equations (3.16) and substituting (3.13) into (3.14) and (3.15) the system can be expressed as:

$$\omega_{osc}^2 = \frac{c_4}{A} \tag{3.17}$$

$$A + \omega_{osc}^2 = m_2 \cdot N(a_{osc}) + c_2 \tag{3.18}$$

$$(m_1 \cdot N(a_{osc}) + c_1) \cdot \omega_{osc}^2 = m_3 \cdot N(a_{osc}) + c_3 \tag{3.19}$$

Further substitution of equation (3.17) in (3.19) leads to a definition for A:

$$A = \frac{c_4 \cdot (m_1 \cdot N(a_{osc}) + c_1)}{m_3 \cdot N(a_{osc}) + c_3} \tag{3.20}$$

Using this result the system can be reduced to a two-variable system, being those ω_{osc} and $N(a)$. Solving such system will return a deterministic value for frequency and amplitude of the OBT sensor.

$$\alpha_3 \cdot N(a_{osc})^3 + \alpha_2 \cdot N(a_{osc})^2 + \alpha_1 \cdot N(a_{osc})^1 + \alpha_0 = 0 \tag{3.21}$$

$$\omega_{osc}^2 = \frac{m_3 \cdot N(a_{osc}) + c_3}{m_1 \cdot N(a_{osc}) + c_1} \tag{3.22}$$

where:

$$\alpha_3 = m_1 \cdot m_2 \cdot m_3 \tag{3.23}$$

$$\alpha_2 = m_1 \cdot m_3 \cdot c_2 + m_2 \cdot m_3 \cdot c_1 + m_1 \cdot m_2 \cdot c_3 - c_4 \cdot m_1^2 + m_3^2 \tag{3.24}$$

$$\alpha_1 = m_1 \cdot c_2 \cdot c_3 + m_2 \cdot c_1 \cdot c_3 + m_3 \cdot c_1 \cdot c_2 - 2 \cdot (m_1 \cdot c_1 + m_3 \cdot c_3) \tag{3.25}$$

$$\alpha_0 = c_1 \cdot c_2 \cdot c_3 - c_1^2 + c_3^2 \tag{3.26}$$

The solution of equation 3.21 allows to study the behaviour of the biological OBT sensing system in order to analyze the measurement dynamic ranges and propose an operation point for the sensor.

3.2 Sensor tuning

The solution to the OBT system yields the frequency (ω_0) and the amplitude (a_{osc}) of the oscillations as two dependent variables on the sample-under test fill-factor. However, the sensor design requires to establish certain parameters which greatly affect the measurement process. Those parameters are the filter peak frequency ω_f, the filter gain G_0 and the filter quality factor Q_f. To evaluate the influence of such parameters over the measurements performed using the OBT approach, a full set of simulations was performed and is illustrated in Figure 3.5. An identical electrical model was programmed for all of them using the results obtained in Chapter 2. Since the electrical model is established, the resulting values only depend on fill-factor variations.

The analytic solution and the associated system simulation prove the sensor dynamic ranges are greatly variable, depending on the different filter parameters selected for the sensor design. These parameters configure the sensor operation point and hence greatly affect its performance and potential applicability. The analysis of the sensor parameter is centered exclusively on Q_f and ω_f, since G_0 parameter controls the filter gain and its effect over the operation point results in an amplitude scaling factor.

As presented in the previous section, the quality factor (Q_f) value of the filter has a great influence over the dynamic range of the sensor measurement curves. Lower Q_f values tend to produce greater frequency ranges over the same central frequency ω_f. Amplitude range values remain constant all over the simulations performed. Q_f value does not show any effect over amplitude dynamic range or behaviour.

Central filter frequency (ω_f) correspond to the band-pass peak location over the frequency axis. This parameter affects output ranges and shape of the sensor measurement curves. Frequency response is significantly different depending on the ω_f selected. Moreover, the curve linearity is highly affected by this parameters, exposing great linear behaviour on lower frequencies (800, 1000, 5000 Hz) and non-linear over higher frequencies(10, 54, 100 kHz). Interestingly, for high frequencies, a valley appears once the fill-factor is close to a 0.9 value. This particular value is of special interest to biomedical researchers since they use it as a reference to add drugs or measure growth time. Amplitude ranges remain constant but the linear behaviour is greatly degraded over higher frequencies, exposing a big sensitivity over higher fill-factor values, which again might be interesting for the biomedical researcher on future applications.

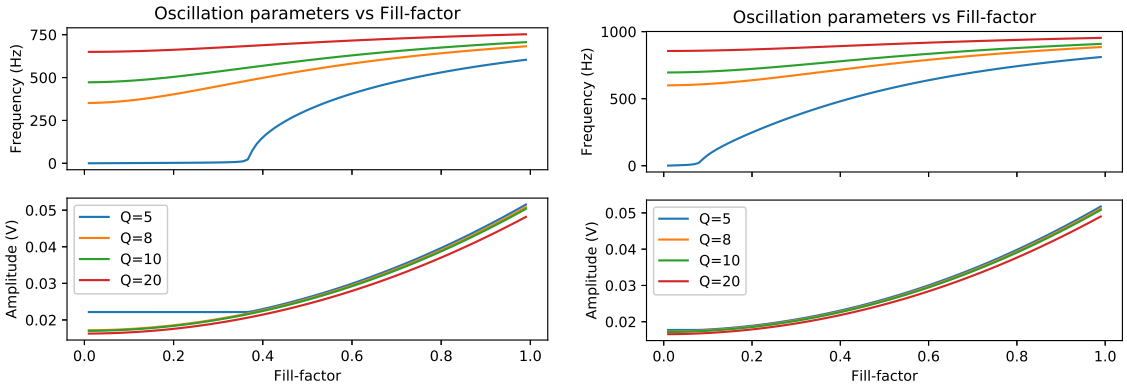

(a) $f_0 = 800\,Hz$

(b) $f_0 = 1000\,Hz$

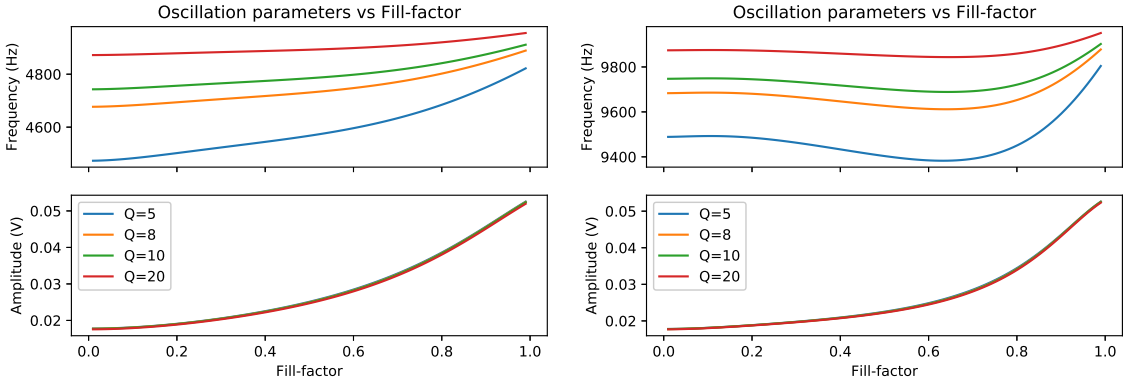

(c) $f_0 = 5000\,Hz$

(d) $f_0 = 10000\,Hz$

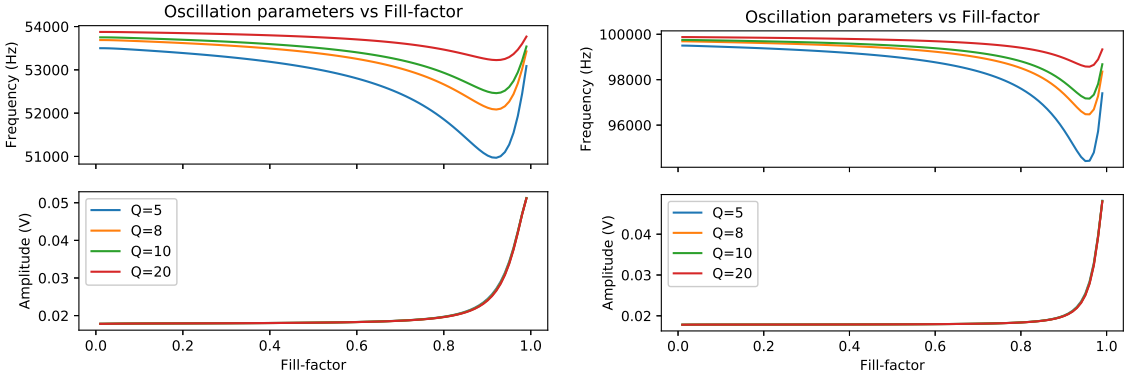

(e) $f_0 = 54000\,Hz$

(f) $f_0 = 100000\,Hz$

Fig. 3.5 Variations on f_0 and Q on the Oscillation Based Test sensor. This analysis depicts the different responses on the band-pass filter, which governs the operation point on the OBT sensor. The selected value for f_0 are 800 Hz (a), 1 kHz (b), 5 kHz (c), 10 kHz (d), 54 kHz (e) and 100 kHz (f). In all of them the analysis performed variations over the quality factor of the band-pass filter using different Q_f values (5, 8, 10, 20).

Previous simulation set illustrated the variations on the design parameter for the OBT sensor. This thesis aims at designing a cell culture sensor which can analyze the cell culture behaviour on any range, and for that reason it seems a good choice to discard greater operating frequency. On the other hand, lower (Q_f) values combined with a low central frequency (ω_f) may never lead to an oscillatory solution. A good compromise seems to exist around the operation point described by $\omega_f = 2\pi f_0\ rad/s$ where $f_0 = 1000\ Hz$ and $Q_f = [5, 10]$.

Figure 3.6 represents a solution for this system over the selected operation point. Frequency ranges obtained for the application using this parameters are $[695 - 930]Hz$ and amplitude range is $[17 - 50]mV$ for $f_0 = 1\ kHz$. Subsequently, Figure 3.7 illustrates the variations on the impedance components ($Z_{\angle\phi}$) across the fill-factor values.

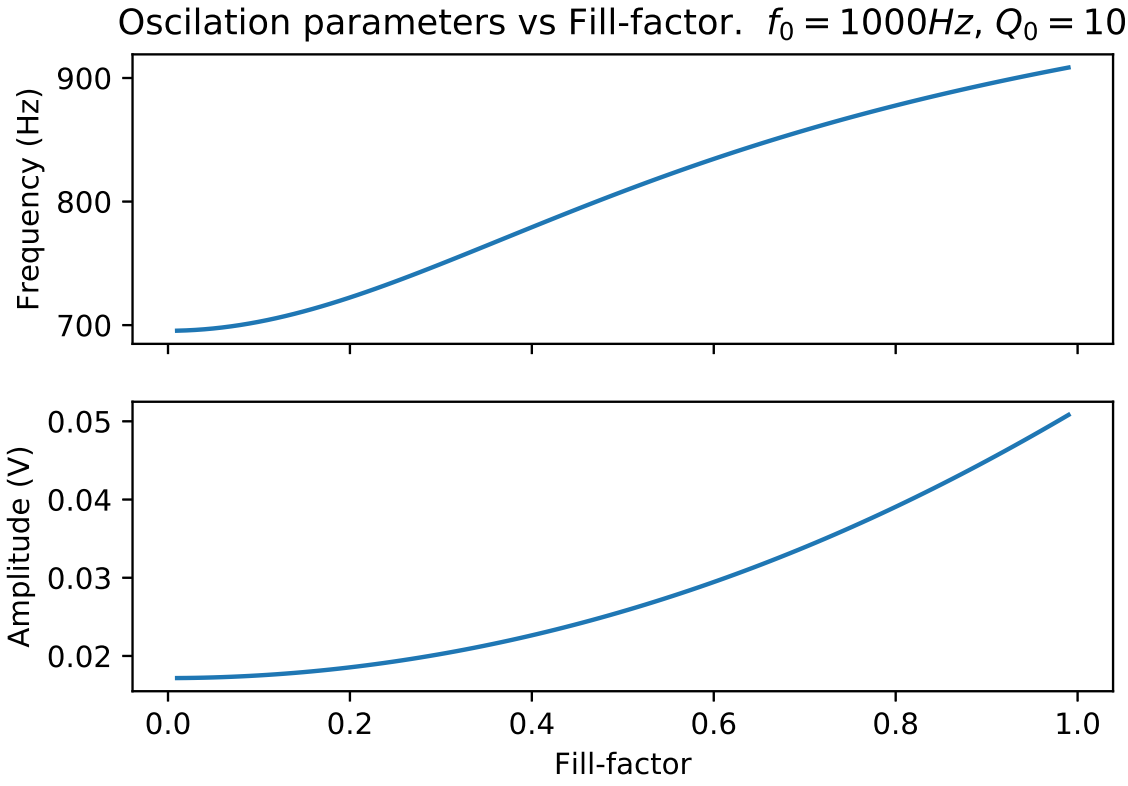

Fig. 3.6 Frequency, Amplitude evolution of the system considering $C_{dl} = 32\ nF$, $R_{ct} = 1.3\ M\Omega$, $R_s = 1000\ \Omega$, $R_{gap} = 2000\ \Omega$, $Q = 10$ and $\omega_0 = 2 \cdot \pi \cdot 1000\ rad/s$.

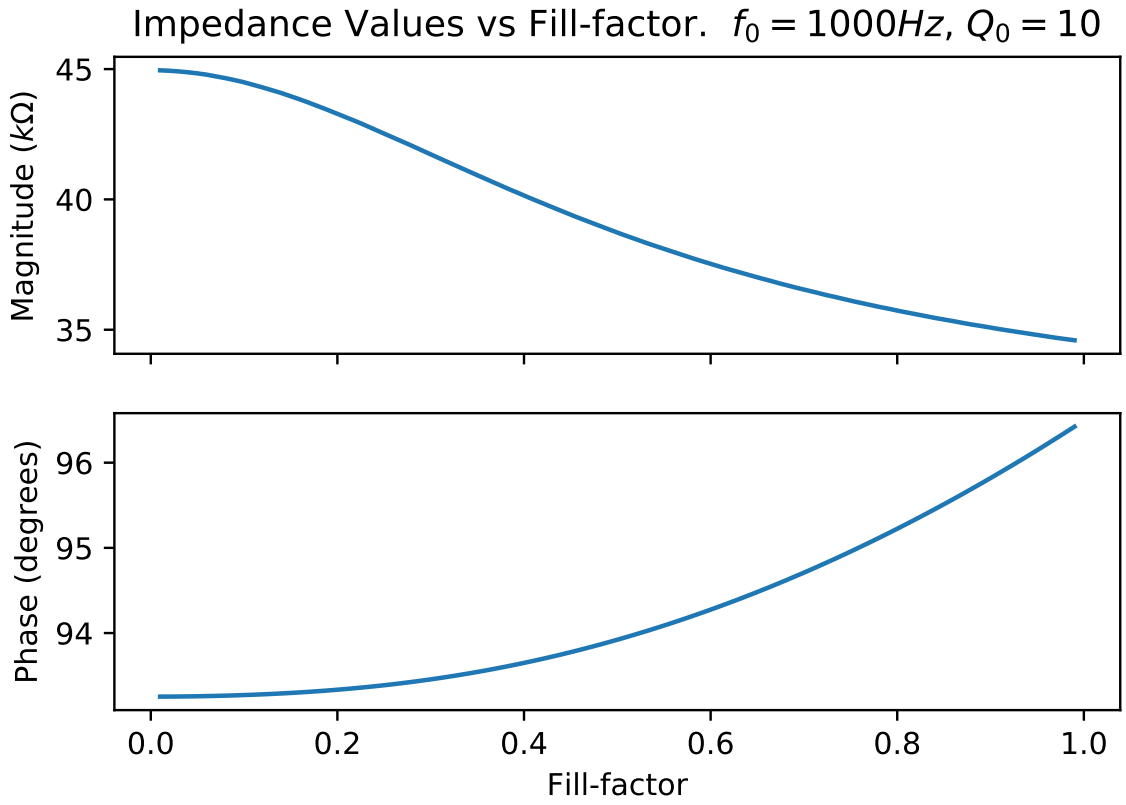

Fig. 3.7 Frequency, Amplitude evolution of the system considering typical values: $C_{dl} = 32\ nF$, $R_{ct} = 1.3\ M\Omega$, $R_s = 1000\ \Omega$, $R_{gap} = 2000\ \Omega$, $Q = 10$ and $\omega_0 = 2 \cdot \pi \cdot 1000\ rad/s$.

The dynamic ranges from simulations performed permit to compute the sensor sensitivity with respect to the fill-factor. These values are shown in Table 3.1.

Table 3.1 Biological oscillator dynamic ranges.

	Frequency (Hz)	**Amplitude (mV)**
ff_0	695	17
ff_{100}	908	50

Considering a simple linear fitting:

$$F_s \approx 2.13\ \frac{Hz}{\%ff} \tag{3.27}$$

$$A_s \approx 0.33\ \frac{mV}{\%ff} \tag{3.28}$$

Where F_s and A_s denote the sensitivity to fill-factor percentage unit of the designed biological OBT sensor.

3.2.1 Cell number estimation

The generated sensor response is dependent on both, the biological sample under test and the OBT design parameters. The former are fixed by design, therefore, oscillation signal parameter are exclusively varying as a function of the cell-culture growing over the electrodes. Since the response is close to linear, an adequate initial estimation for the fill-factor could be extracted from linearly matching the fill-factor to the sensor. From such fill-factor the estimation of the cell number over the electrode requires additional information.

Cell Number The estimation of fill-factor provides a direct relation to the number of cells on the substrate. Consider a cell culture experiment involving a known cell line. The cell number determination is given by the formula:

$$n = ff \cdot \frac{A_{total}}{A_{cell}} \tag{3.29}$$

Where A_{cell} represents a single cell area over the electrode. This parameter is dependant on the specific cell line under test and presents a certain amount of dispersion. For illustration purposes next Figure 3.8 depicts a 250 μm diameter micro-electrode in contrast with the estimated cell diameter ranging between $12.5 - 25.0$ μm for AA8 cell line.

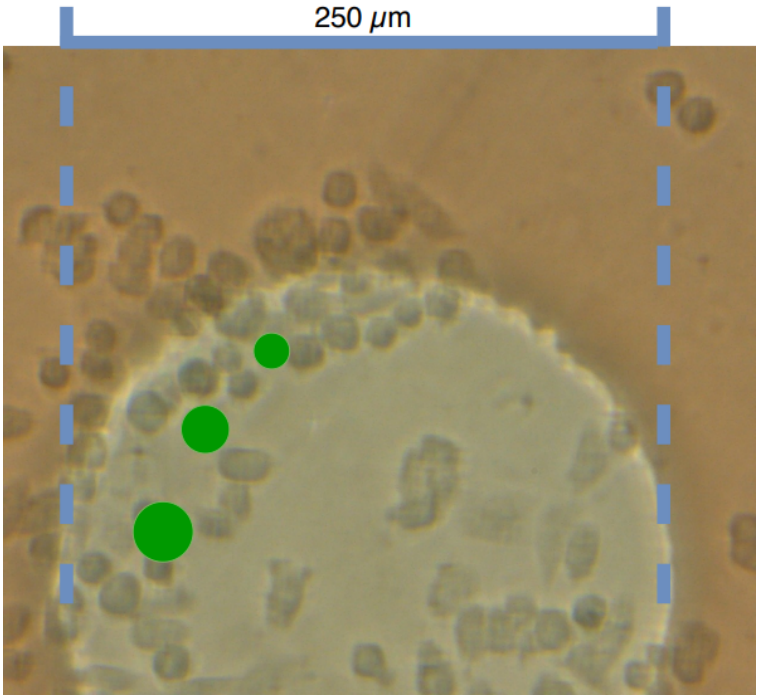

Fig. 3.8 AA8 cells by the microscope over a 250 μm micro-electrode. Green dots represent cells with diameter from 12.5 to 25.0 μm.

Summary and conclusions

The proposed solution; Oscillation Based Test (OBT) sensing is essentially supported by two advantages over other different alternative solutions. OBT does not require external AC stimulation and IA, nor needs complex synchronization to acquire impedance information.

- A proposal for the OBT measurement system has been studied to analytically define its oscillation parameters. These parameters are governed by the electrical response of the cells growing on the assay and the electrical characteristics of the oscillation circuit. A sensor based on the OBT principle will produce a signal which oscillation parameters (frequency and amplitude) are related to the biological sample under test. Hence, obtaining such parameters can effectively provide the biological information.

- The biological OBT is built by closing a non-linear feedback loop around the cell-culture with a band-pass filter and a non-linear element, a comparator. The band-pass filter parameters (Q_f and ω_f) control the operation point of the sensor. From the analytic solution of the system using the oscillation equations, the sensor curves are extracted, this is, the frequency and amplitude response for variations on the cell culture under test fill-factor (ff).

- Several simulations using the analytic equations have been presented to provide further insight over the differences between the potential operation points. Despite the fact amplitude ranges remain constant in all the analyzed operation points, a monotonously increasing behaviour is only observed on relatively low frequencies (1 kHz). On the other hand, the variation of the frequency range is high in different operation points but similarly, the monotonously increasing behaviour is located on low frequencies (1 kHz). From this analysis, and according to analytic data from the OBT equations a good operation point for the cell culture sensor has to be located near 1 kHz and the Q value should be between 5 and 10.

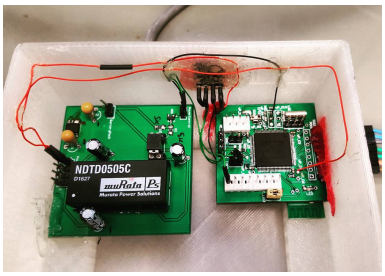

Chapter 4

System design and implementation

4.1 Introduction

On previous chapters the cell-electrode interface model and the associated electrical circuits was studied. Furthermore, the oscillation based test approach for turning an electronic oscillator into a biological sensor by fitting the oscillator with the biological sample was designed by simulation. This chapter deals with the implementation of the full prototype for a biological OBT (bio-OBT) measurement system using discrete electronic components and software programming to automatize the measurement process that allows the real-time visualization of the gathered information. The prototype design is based on the Internet of Things paradigm, previously described, including three different sub-blocks. A sensor device, a gateway and a remote web server.

The system described on this chapter implements the bio-OBT sensor, able to generate an oscillation proportional to the cells adhered to gold micro-electrodes. The signal parameters (amplitude and frequency) provide the sensed information. The system will extract those parameters using an algorithmic approach for oscillation signal processing and send the information over a Bluetooth link to an external device known as gateway device. Moreover, this device will perform experiment control and data management operations from the biomedical laboratory. On this thesis, the selected device is an Intel Edison [125]. This Linux based device implements wireless connectivity (Bluetooth and WiFi) and acts as a bridge between the user interface and the cell culture sensor. Furthermore, the Intel Edison will manage every connection parameters and assure that real-time measurements are stored on the remote database provided by a server computer. The remote server provides the user interface, which can be accessed through the internet to configure and visualize available experiments and works as the main storage unit on the system. A general diagram is presented in Figure 4.1

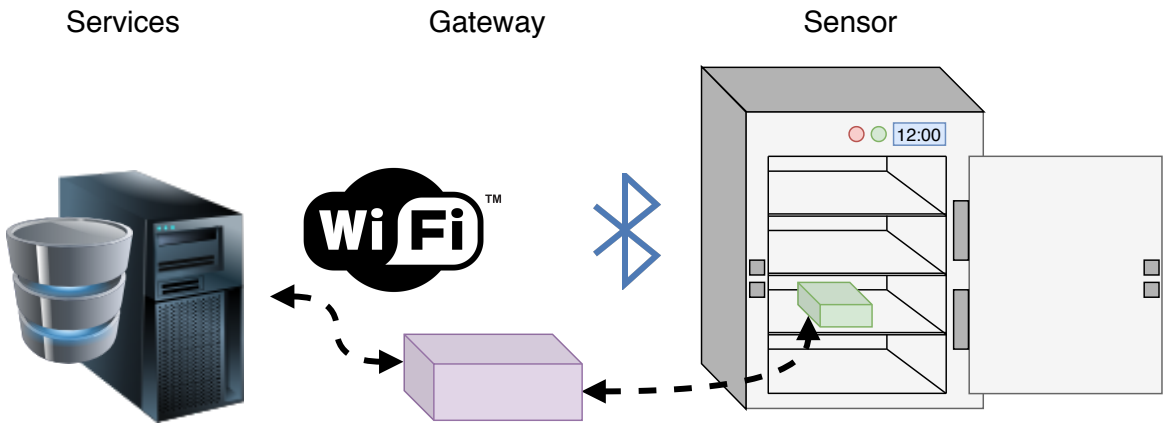

Fig. 4.1 General diagram for the implemented prototype system. Sensor devices are located on the cell culture reactor, gathering information from the cell culture assay. This will be sent to the gateway device (Intel Edison) which manages and control the measurement acquisition process. The gateway device communicates using a WiFi link with the remote server (service provider) and stores information acquired on the remote database.

4.2 Analog circuits

4.2.1 Biological oscillator

The Oscillation-Based Test is the selected approach to effectively design a real-time cell-culture system as it was exposed on the previous chapter. The oscillator will be designed on four stages as depicted in Figure 4.2. The sensor provides two different outputs: the Noise Filter Amplifier voltage output signal (V_a) and the Comparator voltage output signal (V_f).

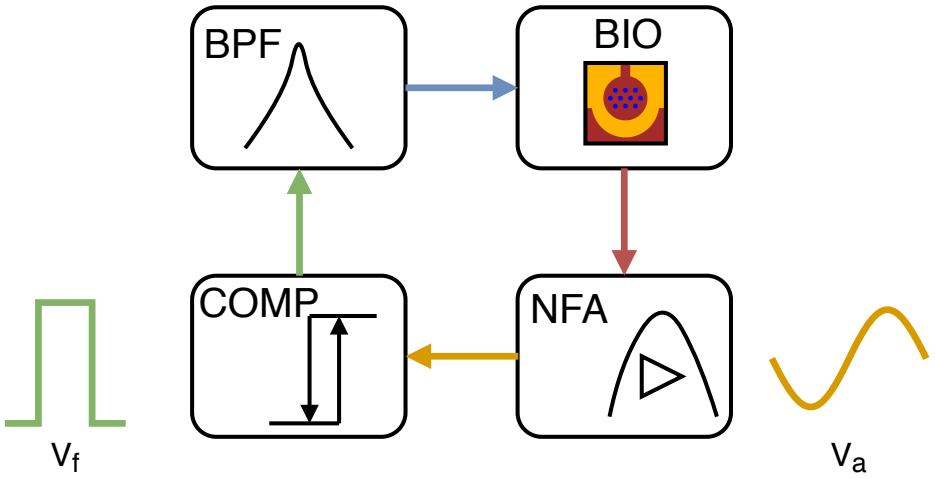

Fig. 4.2 Block diagram scheme depicting the four stages of the oscillator design and the interconnections between them.

The previous chapter illustrated a general approach to a sensor based on oscillation test. The actual design and implementation is based on such approach while taking into consideration issues that could potentially affect the system behaviour. Using the aforementioned division into stages, we will study and evaluate the circuit limitations to provide a solution which will be implemented to analyze the electrical variation on the electrode due to cell growth on the laboratory.

Band-pass filter

The second-order band-pass filter (BPF) will be implemented using discrete components to adjust the Q factor (Q_f) and the peak frequency value (f_0). The filter was implemented following the topology described in [41], which is illustrated in Figure 4.3.

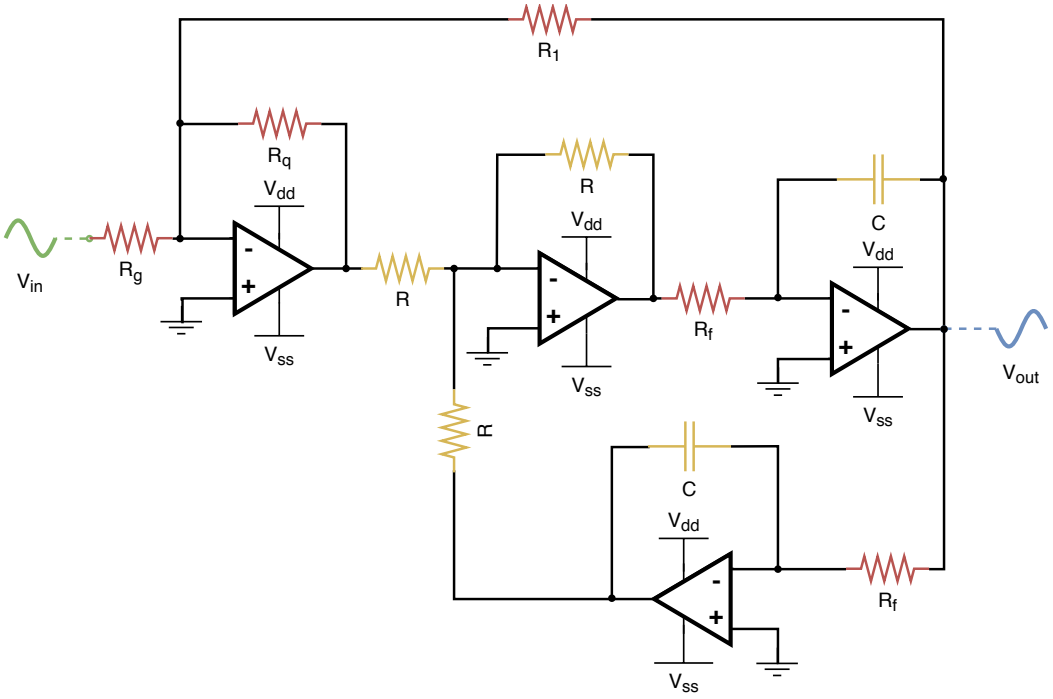

Fig. 4.3 Second order BPF implemented using commercial OPAx227 operational amplifiers. $R_g = R_1 = 5.11\ k\Omega$, $R_q = R = 820\ \Omega$, $R_f = 2.6\ k\Omega$ and $C = 56\ nF$.

This design allows to configure Q_f, f_0 and G_0 values using resistors R_g, R_q, R_1 and R_f:

$$f_0 = \frac{1}{2 \cdot \pi \cdot R_f \cdot C} = 1096\ Hz \tag{4.1}$$

$$Q_f = \frac{R_1}{R_q} = 6.23 \tag{4.2}$$

$$G_0 = \frac{R_1}{R_g} = 1 \tag{4.3}$$

A range proposal for the Q_f and f_0 values ($5 \leq Q_f \leq 10$, and $f_0 \approx 1\ kHz$). Following such guidelines, the implemented filter is tuned to fit such values: $Q = 6.23$, $f_0 = 1096\ Hz$ and $G_0 = 1$. To validate the band-pass filter design, a pspice simulation is configured and executed using commercial devices OPAx227. The electrical response of such design along with a transient analysis operating near the range frequency is provided in Figure 4.4 (a) and (b).

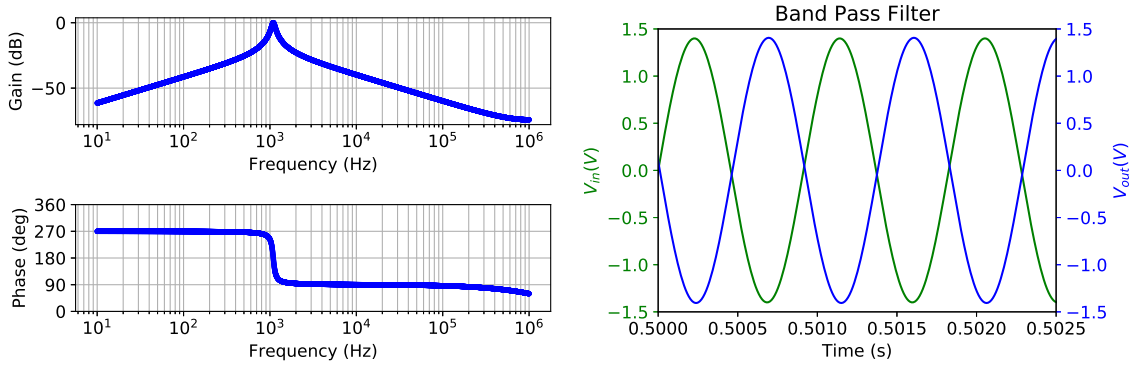

(a) pspice AC Simulation

(b) pspice Transient Simulation

Fig. 4.4 (a) Magnitude and phase bode diagram for $H_{BP}(s)$. (b) transient response for a signal of frequency $f_{in} = f_0 = 1.096\ kHz$.

Cell-culture interface (BIO)

The design of the interface for the biological sample is a critical block on the sensor. On Chapter 2 the electrodes were analyzed under the assumption of the electrode linear behaviour occurring on the electrode at voltages below 100 mV. Furthermore, the voltage level introduced on the electrode must not harmfully affect the growing culture or the measurement system would be worthless. Preliminary tests using the basic interface depicted on Chapter 3 (Figure 3.1) demonstrated an offset generation on the interface which could produce a displacement of the operation point far from the 100 mV limit. This effect is led by the negative feedback connection providing a source for signal integration due to the partially capacitive behaviour of the bio-impedance sample. A different approach to overcome this issue included the implementation of a bipolarity current source-sink [41], depicted in Figure 4.5. This circuit injects a current over the biological load as a function of the V_{in} value and the resistors $R_1 = 50\ k\Omega$, $R_2 = 10\ k\Omega$ and $R_s = 40\ k\Omega$.

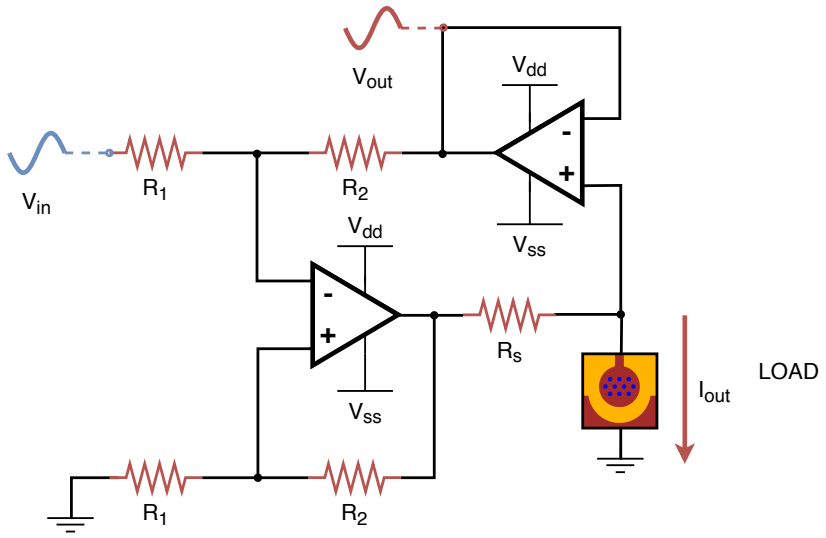

Fig. 4.5 Electrical schematic for the interface implemented using commercial LT1114S operational amplifiers. Resistor values are $R_1 = 50\ k\Omega$, $R_2 = 10\ k\Omega$ and $R_s = 40\ k\Omega$

The candidate circuit was simulated using pspice and the electrical response of such design along with a transient analysis operating near the peak frequency is provided in Figure 4.6. The commercial device for the interface circuit is the LT1112 operational amplifier. For the selected resistor values I_{out} is:

$$I_{out} = \frac{R_2}{R_1} \cdot \frac{V_{in}}{R_s} = 125 \cdot V_{in}\ \mu A \tag{4.4}$$

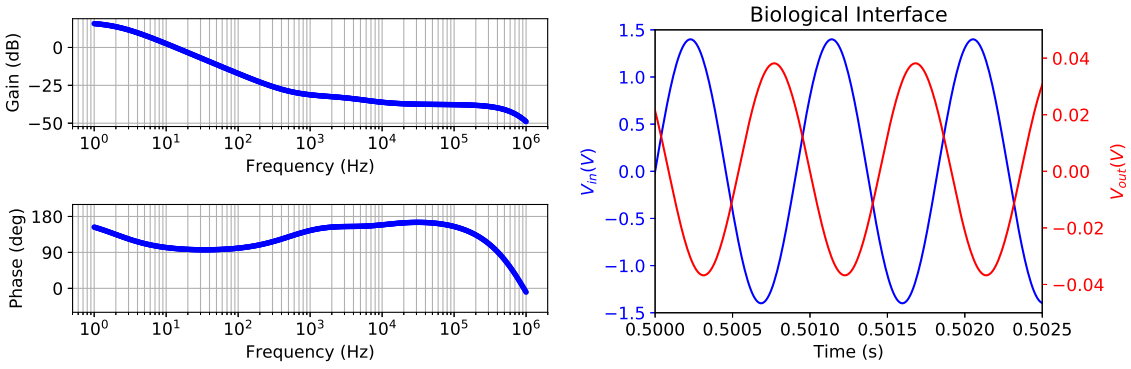

(a) pspice AC analysis

(b) pspice Transient analysis

Fig. 4.6 (a) Magnitude and phase bode diagram for $H_z(s)$. (b) transient response for a signal of frequency $f_{in} = f_0 = 1.096\ kHz$.

The interface circuit described on this section does not modify the equation (3.2) since V_{out} is proportional to V_{in} in a gain factor that can be compensated later on. For an amplitude

of $V_{in} = 100\ mV$, the corresponding I_{out} would be 12.5 μA, which is below the maximum current application limit to cells (20 μA). Amplitude and phase changes in frequency are low around 1 kHz (Figure 4.6 (a)).

Noise filter amplifier

The output of the interface block is a small signal generated by the voltage response to the biological impedance under test. This block receives the V_{out} from the interface block, applies a noise filter to the signal and amplifies the result. The proposed circuit is depicted in Figure 4.7.

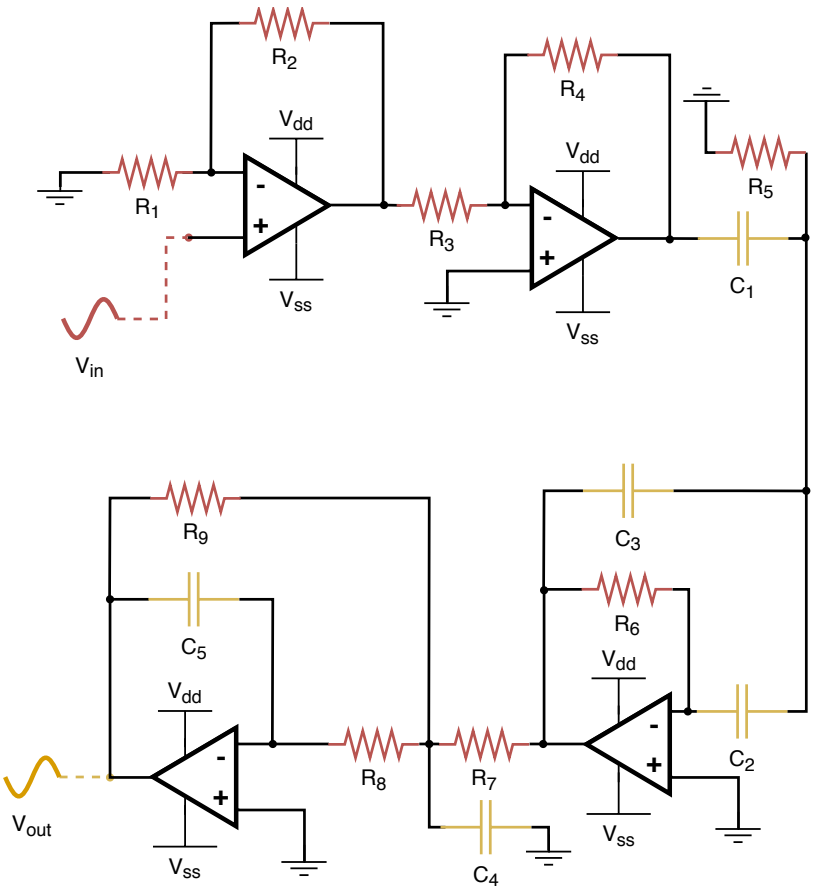

Fig. 4.7 Electrical schematic for the filter amplifier stage implemented using commercial OPAx227 operational amplifiers. Component values are $R_1 = 1\ k\Omega$, $R_2 = 4\ k\Omega$, $R_3 = 10\ k\Omega$, $R_4 = 10\ k\Omega$, $R_5 = 22\ k\Omega$, $C_1 = 84\ nF$, $C_2 = 94.5\ nF$, $C_3 = 14.66\ nF$, $R_6 = 330\ k\Omega$, $R_7 = 910\ \Omega$, $C_4 = 1\ nF$, $R_8 = 1.3\ k\Omega$, $R_9 = 5.6\ k\Omega$, $C_5 = 1\ nF$.

The block is formed by three different parts, the initial part corresponds to an amplification stage formed by two operational amplifiers. Second block is formed by two chained multiple feedback filters: a high pass followed by a low pass. The equations are:

$$G_{Ampl} = \frac{R_2}{R_1} \cdot \frac{R_4}{R_3} = 4 \tag{4.5}$$

$$G_{HPF} = \frac{C_1}{C_3} = 5.73 \tag{4.6}$$

$$G_{LPF} = \frac{R_9}{R_7} = 6.15 \tag{4.7}$$

$$f_{HPF} = \frac{1}{2\pi\sqrt{R_5 R_6 C_2 C_3}} = 50.2\ Hz \tag{4.8}$$

$$f_{LPF} = \frac{1}{2\pi\sqrt{R_8 R_9 C_4 C_5}} = 59.0\ kHz \tag{4.9}$$

where G_{Ampl} corresponds to the amplifier stage gain and G_{HPF}, G_{LPF} to both filter gains. f_{LPF} and f_{HPF} correspond to filter cut-off frequencies. The total gain of the system (G_{NFA}) be 141.0.

The noise filter and amplification circuit was simulated using pspice, and the electrical response of such design along with a transient analysis operating near the peak frequency is provided in Figure 4.8. The commercial device for the interface circuit is the OPAx227 operational amplifier.

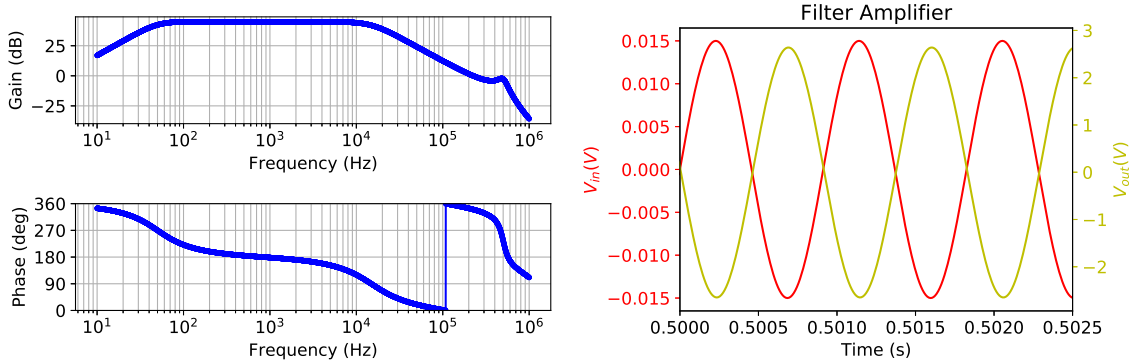

(a) pspice AC analysis

(b) pspice Transient analysis

Fig. 4.8 (a) Magnitude and phase bode diagram for $H_{NFA}(s)$. (b) transient response for a signal of frequency $f_{in} = f_0 = 1.096\ kHz$.

Comparator

The comparator block is the fourth block of the loop system. The input is received from the noise filter amplifier and then connected to a commercial LMC7211 comparator device (Figure 4.9). To prevent unwanted transitions which would affect the oscillatory behaviour and performance of the sensor, a hysteresis system is implemented based on a Schmitt trigger [41]. According to the component data-sheet, the addition of the capacitor C_1 in parallel to R_2 resistor increases switching speed and improves short term hysteresis resulting in better noise immunity.

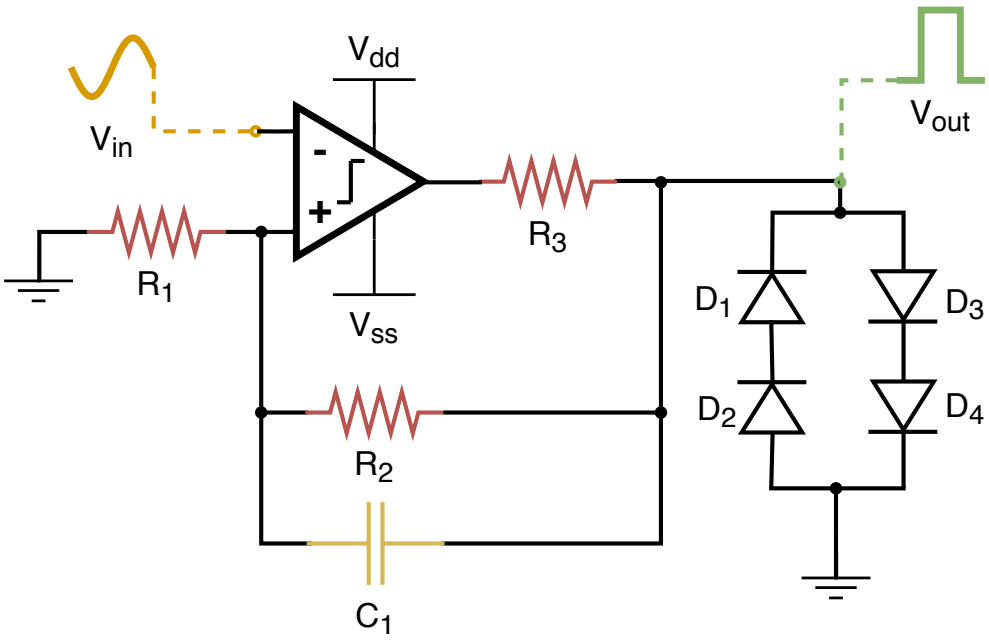

Fig. 4.9 Electrical schematic for the comparator stage implemented using a commercial LMC7211 comparator. Component values are $R_1 = 1\ k\Omega$, $R_2 = 68\ k\Omega$, $R_3 = 240\ \Omega$, $C_1 = 16.6\ nF$.

The hysteresis is calculated considering the voltage divider formed by R_2 and R_1:

$$\beta = \frac{R_1}{R_1 + R_2} = 0.015 \tag{4.10}$$

where β denotes the feedback fraction, which multiplied by the total output swing ($10\ V$) returns the hysteresis window amplitude value. Amplitude of such window would be:

$$H_w = 10 \cdot \beta = 0.150\ V \tag{4.11}$$

Since the window is zero-centered (R_1), the hysteresis window for the circuit depicted above is described by $V_H = 75\ mV$ and $V_L = -75\ mV$ (Figure 4.10). This values avoid the

introduction of multiple phantom transitions which may arise due to signal noise, especially when the voltage from the cell-culture interface block is low. When the cell-culture is on the lower growth ranges, the signal will be on the lower range as we already studied in Chapter 3. Finally, an amplitude control block is added on the output of the block to set the maximum signal range to $[-1.4\ V, 1.4\ V]$.

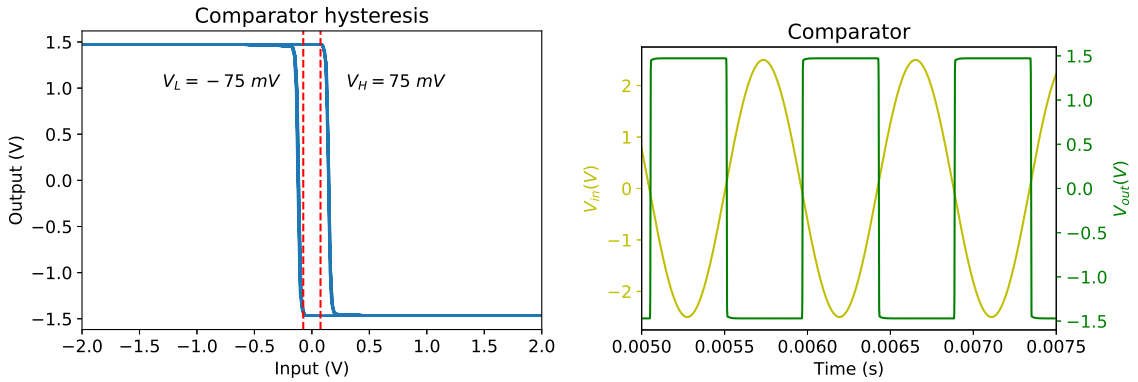

(a) pspice Hysteresis analysis

(b) pspice Transient analysis

Fig. 4.10 pspice simulation for the comparator circuit. Image (a) illustrates hysteresis window associated to the design, while (b) shows a transient simulation.

Closing the loop

The four elements are designed and ready to form the oscillator. All of them are connected following the schema depicted previously in Figure 4.2. The pspice simulation generates a stable oscillation pattern for different fill-factor values (Figure 4.11). However, this result is achieved through thoughtful configuration on the initial parameters of the simulation so that the oscillation is triggered. The real circuit will be triggered by a start-up circuit driven by a microcontroller. This will be described on the following section.

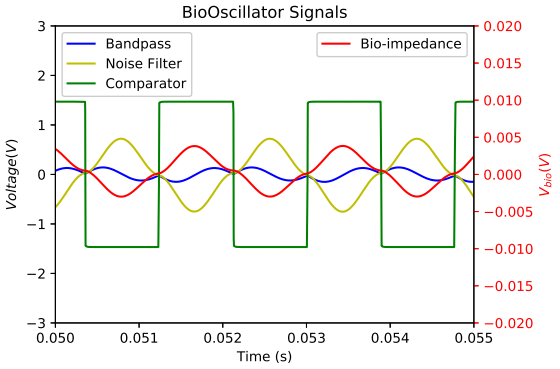

(a) $ff = 0.2$

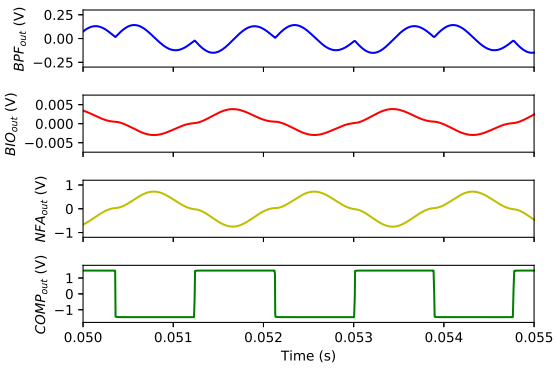

(b) $ff = 0.2$, split view

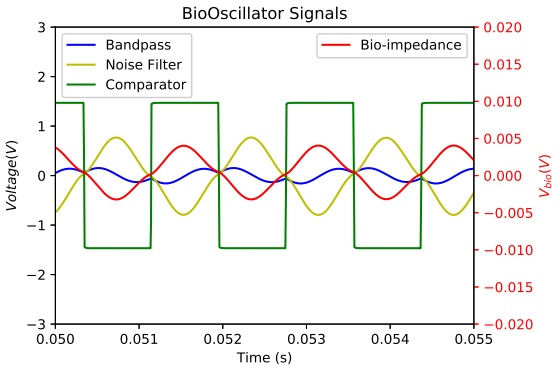

(c) $ff = 0.5$

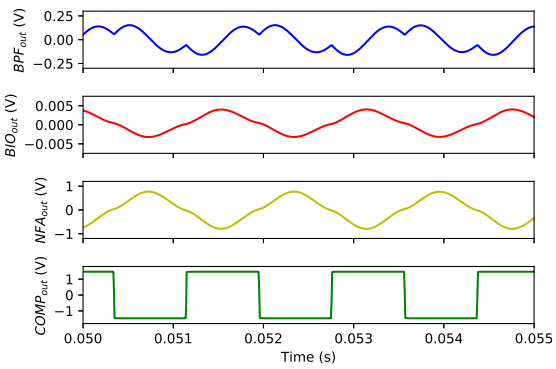

(d) $ff = 0.5$, split view

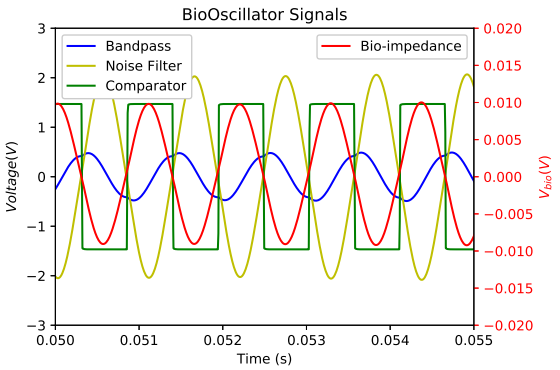

(e) $ff = 0.9$

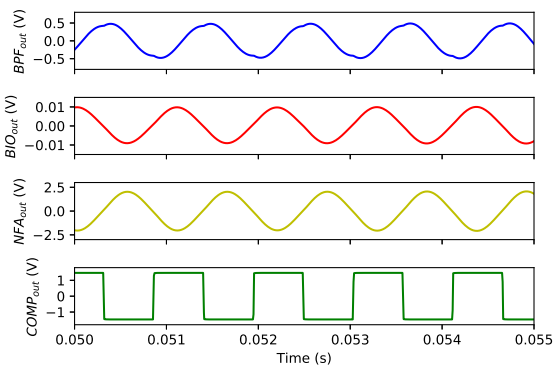

(f) $ff = 0.9$, split view

Fig. 4.11 Oscillation signals over different fill-factors. (a), (b) represent the signals associated to a fill-factor value of 0.2, (c), (d) correspond to a fill-factor of 0.5 and final result (e), (f) represent the signals for a 0.9 fill-factor value.

4.2.2 Control and acquisition circuitry

The Bio-oscillator circuit performs well under specific initial parameters established for the pspice simulation. These parameters are configured so that the system initiates the oscillation by itself. A real system might need start-up circuitry to initiate rapidly, which in any case would improve performance of the sensor by allowing quick oscillation establishment. Additionally, the sensor would require level shifting to accommodate the generated signal to the ADC level in a microcontroller and a multiplexer to measure over different cell culture wells.

Interface multiplexer

The interface switching circuitry was implemented using a discrete analog multiplexer from Texas Instruments. The selected device is a CD4067B. Figure 4.12 depicts the connection between the cell culture wells, the multiplexer and the current source described on section 4.2.1. This device requires an enable signal (E) and four control lines (A, B, C, D) to select the common channel.

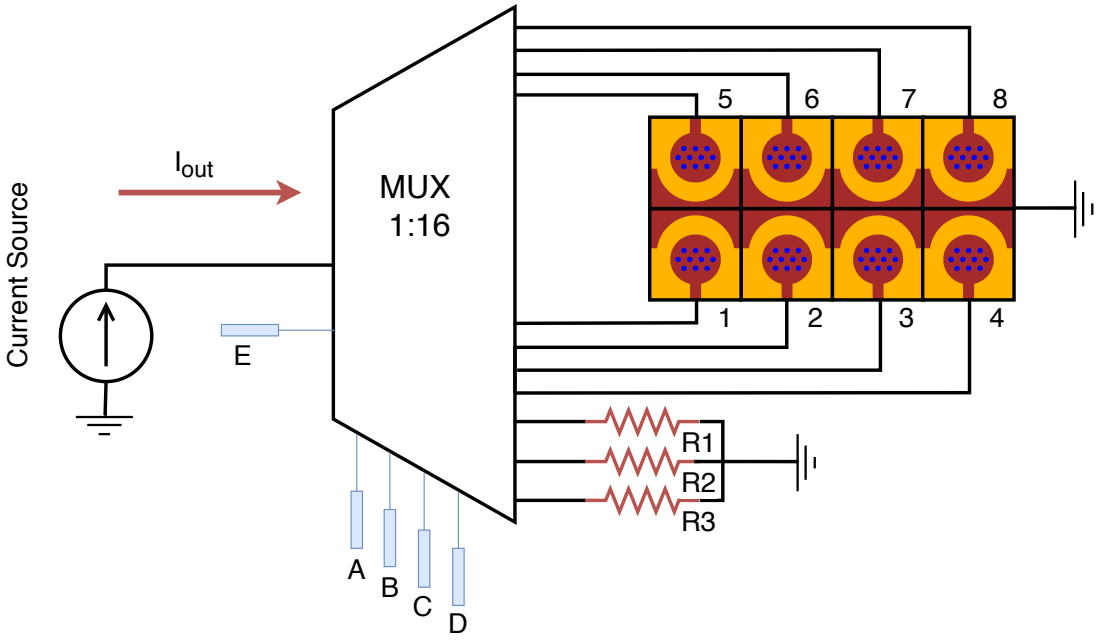

Fig. 4.12 Electrical Schematic for the multiplexer stage implemented using commercial CD4067B 4:16 multiplexer. There are eight electrodes that will be measured sequentially. Resistors R_1, R_2 and R_3 are implemented for functional supervision.

Micro-controller start-up circuit

The start-up circuit will contribute to uniformly initiate the oscillation on every single well under test. The start-up signal is generated on an external micro-controller and will be injected on the sensor between the comparator and the band pass filter blocks. This signal is a square signal, emulating the amplitude values of the circuit (Figure 4.13) is configured as a summing amplifier and hence the output value is fixed to:

$$V_{out} = -(V_{in} \cdot \frac{R_1}{R_2} + V_{ss} \cdot \frac{R_1}{R_3}) \tag{4.12}$$

Where $R_1 = 30\ k\Omega$, $R_2 = 10\ k\Omega$ and $R_3 = 30\ k\Omega$.

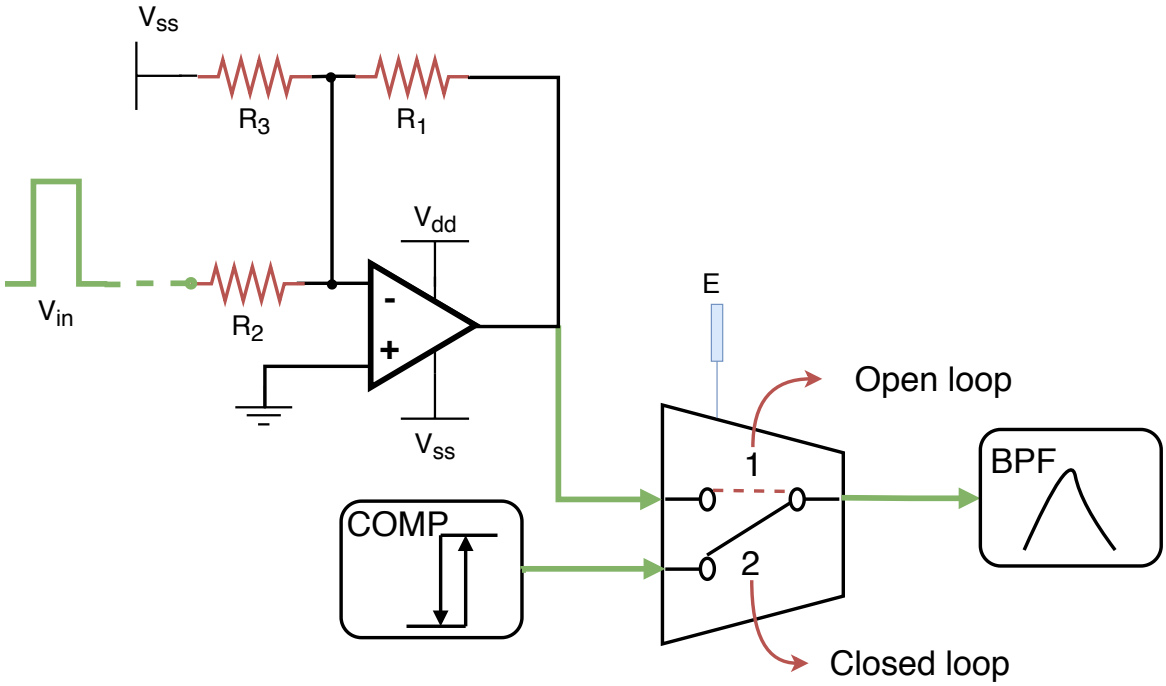

Fig. 4.13 Electrical Schematic the start-up circuit using a commercial OPAx227 operational amplifier and a TS12A analog switch. Component values are $R_1 = 8.5\ k\Omega$, $R_2 = 39\ k\Omega$ and $R_3 = 30\ k\Omega$. On switch position 1, the loop is open and the signal can be injected through the amplifier circuit. Position 2 closes the loop.

Micro-controller ADC interface

The oscillatory signal generated is the physical variable carrying the cell-culture growth information. To acquire such signal it is necessary to adapt the voltage levels to a micro-controller which will then perform the analog to digital conversion to process and store the information. This circuit (Figure 4.14) is implemented using two summing amplifiers (similar to the one on the previous section). The output value is governed by:

$$V_a = -(V_{NFA} \cdot \frac{R_1}{R_2} + V_{dd} \cdot \frac{R_1}{R_3}) \tag{4.13}$$

$$V_f = -(V_{COMP} \cdot \frac{R_1}{R_2} + V_{dd} \cdot \frac{R_1}{R_3}) \tag{4.14}$$

Where $R_1 = 10\ k\Omega$, $R_2 = 39\ k\Omega$ and $R_3 = 30\ k\Omega$.

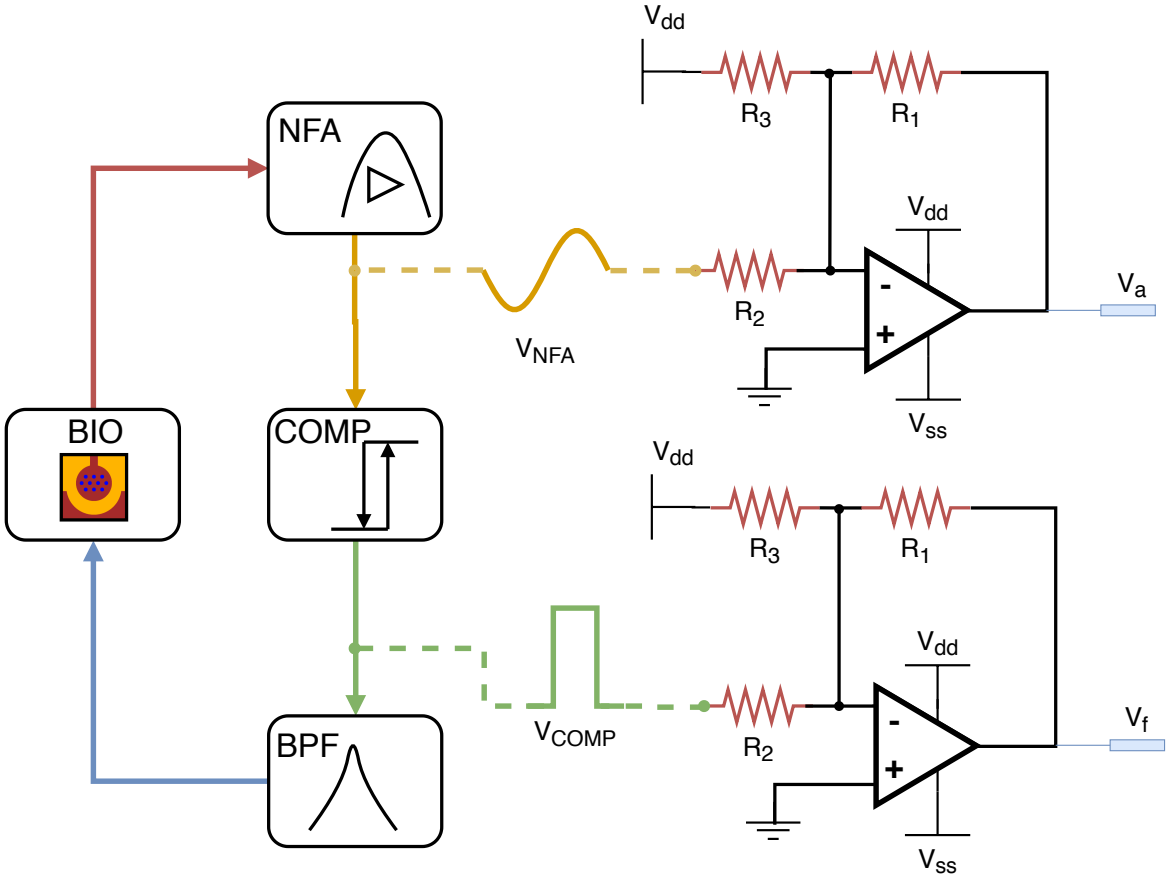

Fig. 4.14 Electrical Schematic for the acquisition circuit using a commercial OPAx227 operational amplifier. Component values are $R_1 = 10\ k\Omega$, $R_2 = 39\ k\Omega$ and $R_3 = 30\ k\Omega$.

Logic level shifters

The analog circuit, and more specifically, the analog multiplexer and the start-up circuit, is implemented using devices operating at a different voltage level than those on the digital board. To accommodate the digital control signals generated on the microcontroller which will govern the analog multiplexer and the start-up switch, a simple circuit using transistors is implemented and depicted in Figure 4.15

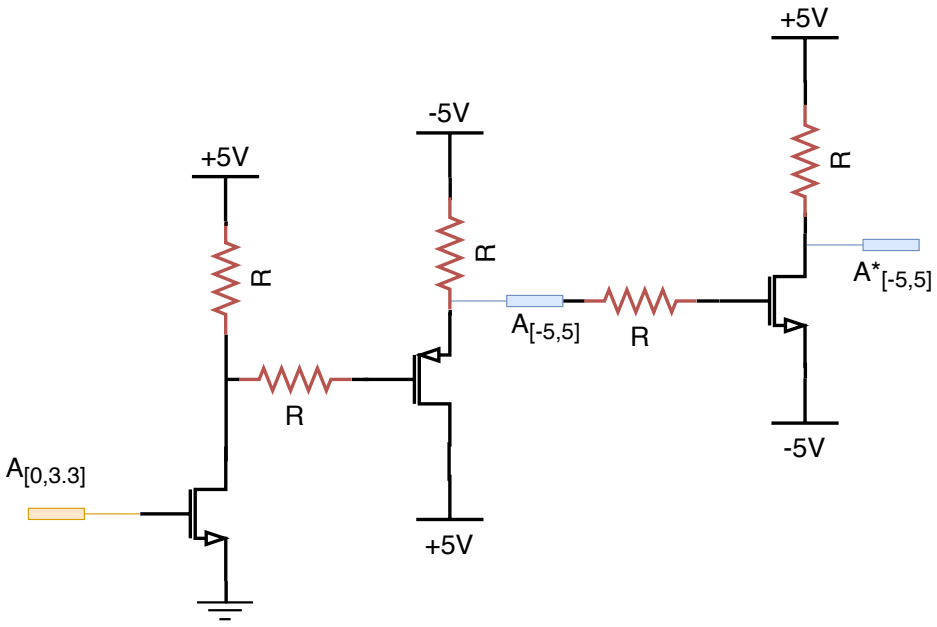

Fig. 4.15 Electrical Schematic for a level shifter circuit using NMOS and PMOS transistors. Component values are $R = 10\ k\Omega$

Analog sensor electrical connections

Finally, at this stage we can consider the analog sensor board as a blackbox depicting a set of input signals and generating two output signals, Figure 4.16 illustrates the electrical connection diagram for future reference. On this diagram, power supply lines are V_{dd}, GND and V_{ss}. Control signals (A, B, C, D, E_1 and E_2)

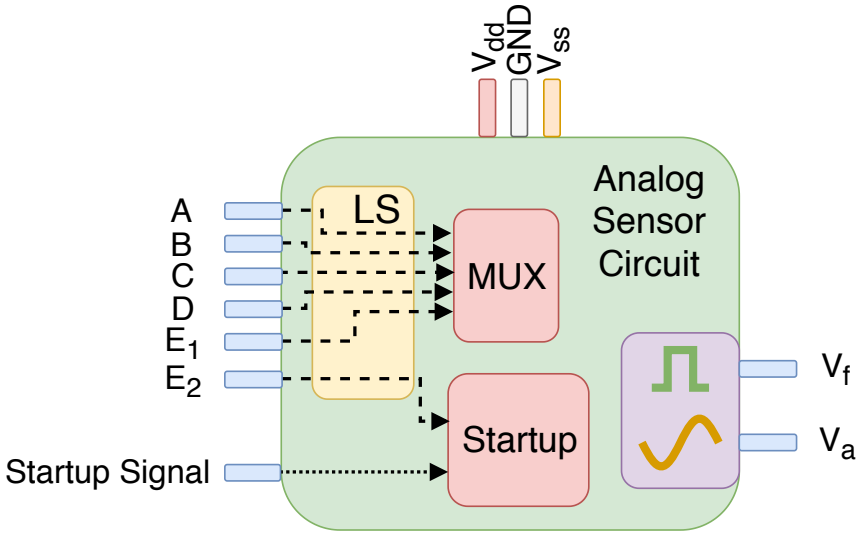

Fig. 4.16 Final connection diagram for the designed analog circuit board.

4.3 Digital circuits

In the previous section the analog electronics which will perform the sensing task were introduced. However, the prototype will require additional functionality to control the analog circuits and perform signal processing computation on the go. This requirement can be fulfilled by a commercial state-of-the-art micro-controller. The full system should comply to a certain set of specifications which will be described below:

- **Computational power** to implement the signal processing algorithms which will extract the information from the sensor output signals.
- **Low power** consumption which will allow long term experiments without requiring battery changes.
- **Precise measurements** of the sensor output signals to provide accurate information to the signal processing algorithm.
- **Manage and control** the analog sensor via the defined control lines and the start-up signal generation.
- **Wireless communication** to send the information over the air without using wires on the cell-culture incubator.
- **Side sensors** to monitor the environmental variables associated to the cell-culture process (relative humidity and temperature).
- **Remote control and data visualization** so that the biomedical researcher can configure experiments and visualize them in real-time.

Among the existing devices, the micro-controller selected is the STM32F7 from STMicroelectronics. This device includes an ARM Cortex-M7 core [126]. These are powerful computing units with several capabilities provided by the embedded peripherals and capable of performing floating point operations, which later will implement the algorithm that processes the acquired signals and obtains the cell-culture information from the bio-OBT. This device can alternate between operation and standby modes, a feature which along with the computational power, suits the needs described above. Furthermore, the STM32F7 embeds several peripherals which can be used directly to perform certain tasks. Among the included peripherals, there are several analog to digital converters (ADCs) with 12-bit resolution level complying with the third requirement elicited before.

The device implements general purpose input/output (GPIO) pins which can effectively control the analog board to operate the sensor function (cell culture multiplexing and open/-close the OBT loop). To generate the startup signal, the micro-controller can employ another peripheral, the digital to analog converter (DAC) with 8-bit resolution. Finally, the micro-controller embeds a set of digital communication ports (*I2C*, *UART*) which will be employed to connect a Bluetooth module (based on Bluetooth 2.0) using the *UART* port and the environmental sensor (vía *I2C*). An schema for the digital design is provided in Figure 4.17.

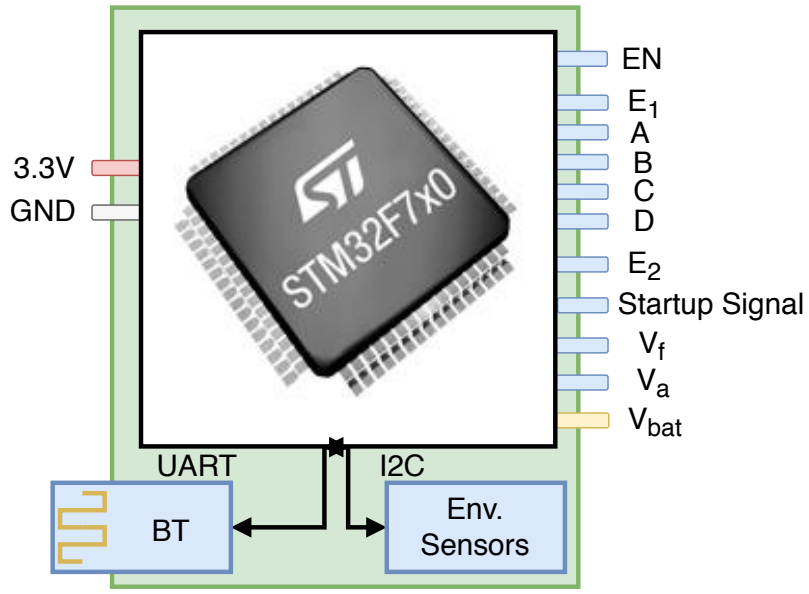

Fig. 4.17 Electrical design for the digital circuit. This circuit provides the control interface to the sensor, the acquisition system, and the Bluetooth link.

4.3.1 Firmware design

The digital prototype system depicted on the previous section will implement the control and processing logic taking advantage of the hardware features provided by the STM32F7 micro-controller. This device embeds a floating-point unit (FPU), thus enabling for advanced algorithmic implementation, which can be tested on a standard computer to assess validity of the proposed solution. The firmware code can be divided into different sections depending on the nature of the hardware resources employed by the design. Different functionalities are identified and summarized on the following table 4.1.

Table 4.1 Firmware functionalities classified by peripheral.

ID	*Description*	*Peripheral*
F01	OBT Parameter Estimator	None
F02	Command Driven Finite State Machine.	None
F03	Signal Acquisition	Analog to Digital Converter (ADC)
F04	Startup Circuit driver	Timers (TIM) & PWM
F05	Synchronization & Low power mode	Real Time Clock (RTC)
F06	Bluetooth Communication	UART
F07	Environmental Sensors	Inter-Integrated Circuit (I2C)

The firmware functionalities were classified according to the different hardware resources to propose a development methodology which can be applied to every code section of the present thesis. All the features defined on the previous table are implemented and tested using the micro-controller development environment except for the signal processing and the finite state machine methods which will follow a different approach.

Peripheral independent methods

From the functionalities in table 4.1, two peripheral independent methods are identified. These methods are formed by the signal processing algorithms (F01) which will perform the signal feature extraction from the captured analog signal using the ADC on the micro-controller and the command driven finite state machine (F02). Both of them will be implemented in C programming language. To implement debug and validate the algorithm without interfering with the complex micro-controller debugging interface, a specific methodology was followed.

Python is a powerful programming language with a huge set of features, allowing engineers, and scientists, to design, simulate, analyze, test, and much more. This tool was employed widely across the present dissertation to design, implement and analyze every simulation presented through the text. On this section, Python capabilities will be employed once more to provide a quick validation method following test driven development approach for the C code. Python allows definition of external extensions which can be compiled and executed from the Python environment. Extending Python with C modules is a tool described through its documentation [127]. This tool permits rapid development and testing of the C algorithms implemented for the thesis. Furthermore, since tests have been performed on the go while developing the algorithm with the same code block, the result has already been validated when flashed on the digital device. This methodology has been followed for testing

both, the feature extraction from the sensor analog signal and the finite state machine. The signal processing algorithm will be described on following chapter.

Finite State Machine (F02)

The state machine flow diagram is depicted in Figure 4.3.1. The illustration represents the behavior of the system in terms of execution steps. The state machine initiates the execution on IDLE state.

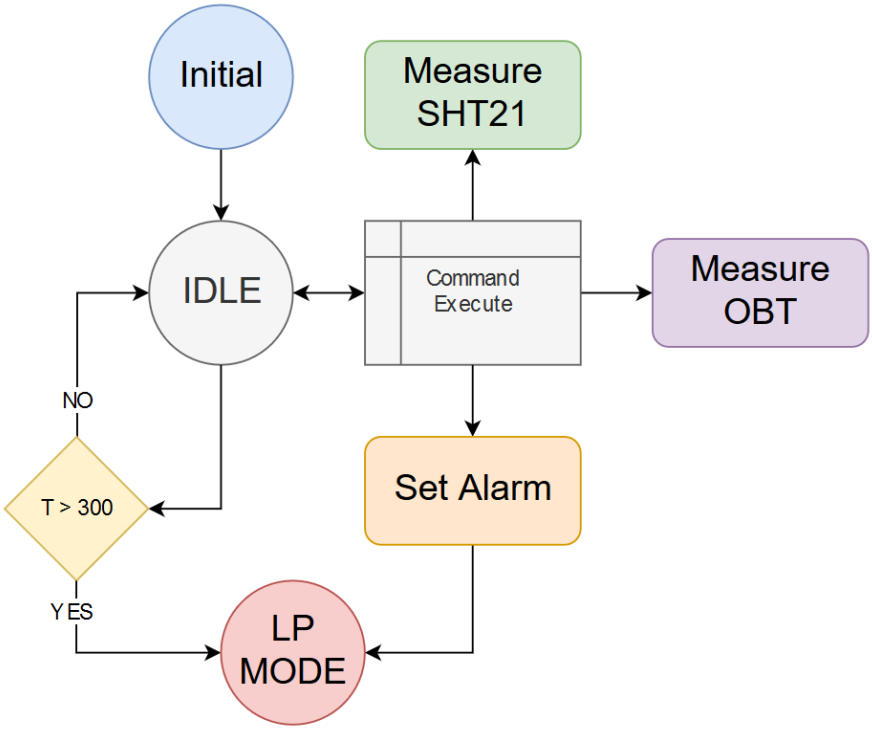

Fig. 4.18 Finite state machime (FSM) flow diagram. Implemented on the STM32F7.

The state machine performs a periodic check while on IDLE state accounting for the online time (T) in seconds. The machine will remain on IDLE state for a maximum of 300 seconds. If the time surpasses that limit ($T > 300$) the system establishes an alarm to 15 minutes in the future and sets the micro-controller to low power mode stopping execution. While the state machine is on IDLE state, the system is waiting for a new command reception. Any command received will generate a transition to execute the associated task, and once finished, returns to IDLE state while resetting the online time ($T = 0$). There are three special states where the system will either send results of the sensing process over Bluetooth (environmental measurement and OBT measurement) or put the system into low power mode to minimize power consumption. After the low power (LP) mode is triggered as a result of

command execution of online time condition, the system will enter into such mode and will resume execution once the configured alarm hits the desired time target established using the appropriate command. A summary of the available commands on the system is depicted on table 4.2.

Table 4.2 Command methods implemented on the micro-controller and peripheral associated.

Command	*Peripherals*	*Description*
SM_ALIVE	–	Returns SM_ALIVE for communication checking.
SM_GETID	–	Returns unique #ID for identification.
A0HHMMSS	RTC	Set the alarm time to HH:MM:SS from last system boot.
A2XXXXXX	RTC	Activates the alarm and send the system to LP mode.
TEMPERAT	I2C	Retrieves temperature from the SHT21 sensor.
HUMIDITY	I2C	Retrieves humidity from the SHT21 sensor.
STARTER0	PWM	Deactivate the starter signal.
STARTER1	PWM	Activate the starter signal.
_C_LOOP_	GPIO	Close the loop.
_O_LOOP_	GPIO	Close the loop.
_MUX1OFF	GPIO	Disable interface mux.
MUX1ON	GPIO	Enable interface mux.
_MUX1CSS	GPIO	Select the channel SS on interface mux.
_FREQCAA	ADC	Calculate frequency over ADC channel AA.
_AMPLCAA	ADC	Calculate amplitude over ADC channel AA.
_SIGNCAA	ADC	Acquire the signal over ADC channel AA.
ANALOG_1	GPIO	Activate the analog power supply.
ANALOG_0	GPIO	Deactivate the analog power supply.

Peripheral dependent methods

Beside the finite state machine and the signal processing algorithm on table 4.1, there are a few methods implementing several functions using the micro-controller hardware peripherals. These peripherals will provide several functionalities to achieve the desired prototype function. The device implements a Hardware Abstraction Layer (HAL) library provided by ARM [128]. This library permits configuration of the selected peripheral for the desired task.

Signal Acquisition (F03)

The signal produced on the OBT analog sensor is acquired using two of the micro-controller ADC configured pins. The information is sampled using direct memory access (DMA) and triggered acquisition at a constant rate of $f_s = 42.683\ kHz$. All samples acquired are stored into an array located on the micro-controller random access memory (RAM) to compute the signal feature using the algorithms depicted on following chapter.

Start-up Driver (F04)

The OBT sensor requires a start-up circuit which will provide an uniform oscillation triggering system and ensures correct operation. The circuit requires the generation of a square signal through the micro-controller connection. The injected signal must have a frequency value within the sensor range of oscillation, hence the proposed value of 1 kHz seems a reasonable selection for this purpose. The generation of the aforementioned signal is produced via a pulse width modulation (PWM) peripheral configuring the duty cycle at 50% and the frequency at the selected value.

Environmental Sensors (F07)

The environmental variables of the experimental procedure involving cell-culture assays include temperature, relative humidity and CO_2 concentration. The cell-culture reactor provides an automated reliable control system for all the variables and the potential disturbances that are mainly due to human effect. Hence, the continuous monitoring of temperature and relative humidity is sufficient to track the status of the cell culture assay growing inside the cell culture reactor. The sensor implemented for this purpose is a digital SHT21 sensor from Sensirion [129]. This cheap module uses I2C communication bus to provide the resulting measurements and control the sensor. I2C communication was implemented on the micro-controller using HAL methods.

General Port Input Output (GPIO)

The general port input/output pins or simply GPIO is the most extended interface existing on any micro-controller. This kind of ports provide a digital source/read pin to either control external devices or read control signals on them. This dissertation will employ the GPIO pins on the micro-controller to control the analog sensor board and the power board. These connections are depicted on the figures 4.16, 4.17 and 4.19.

- Interface Multiplexor (A,B,C,D, En).

- Startup Switch (En)
- Power Supply Switch (En)

Bluetooth Module (F06)

The Bluetooth communication is a major design issue on this platform. It will enable the communication with the external gateway device which will control the micro-controller via the exposed commands programmed on the finite state machine and will send all the information gathered once a measurement is performed. The module selected is the HC-05, which exposes an UART interface to control the Bluetooth link and presents a serial port over the Bluetooth link to easily send commands over any gateway device. The micro-controller implements the Bluetooth module as an UART device with the methods to configure the Bluetooth link initially and then the processing capabilities to select the command from the received bytes through the transmission lines.

Low power mode (F05)

Power consumption is also a major design issue. Since the device will perform its task spending most of the time on IDLE state waiting for the cells to grow over the electrodes a low power mode for the time between measurements, seems a good choice for the sensor device. The micro-controller uses a real time clock (RTC) for controlling the low power mode transitions on the STM32F7. The configuration of the low power mode requires the establishment of an alarm which will wake up the micro-controller from the low power mode. While the device is on low power mode, all the peripherals are disabled except the RTC. Once the RTC reaches the established alarm time, the device will wake up and await for further instructions from the gateway device for 3 minutes. In the event that no message was received from the gateway device during this time the device will again be set to low power mode for 15 minutes to save power from the lithium batteries.

4.4 Prototype

4.4.1 Sensor

On previous sections, the circuits implementing the cell sensing capability was introduced. Both analog and digital circuits were implemented using electronic protoboards and printed circuit boards. The sensor device,as previously depicted on table 4.2, implements an identifier unique to every sensor device. This enables multiple sensor management from a single

gateway on the biomedical laboratory. This feature would enable to parallelize experiments on the biomedical laboratory. Each of the sensor devices can operate a single 8E10E or 8E10E+ substrate from applied biophysics. These substrates contain eight wells where the biomedical researcher can perform the cell culture assays while recording in real-time cell-culture evolution.

Power supply

Beside the analog and digital boards, the system will require a power management circuit which will provide the supply for the analog sensor and the digital board from external lithium ion batteries. Electrical diagram for the power supply board is depicted in Figure 4.19.

On such circuit, the battery pack is formed by two lithium-ion cells operating at a nominal voltage of 7.2 V. This pack provides the power supply for the whole system. To operate the system it is necessary to generate several voltage supply levels. $V_{cc} = 3.3\ V$ for the digital board is generated by an Low Dropout (LDO) regulator with signature TPS7133Q. This device always provides stable supply for the digital board.

The second branch of the power supply system is formed by a second LDO regulator which provides a stable 5 V level on its output. The output is then regulated by a NDTD0505C device which provides a stable dual-rail $V_{dd} = 5\ V$ and $V_{ss} = -5\ V$. The microcontroller operates the activation signal (EN) with a dual purpose, activating this secondary LDO and allowing current flow through a voltage divider formed by two resistors R_1 and R_2. This voltage divider provides a battery level measurement method after acquisition of the V_{bat} signal.

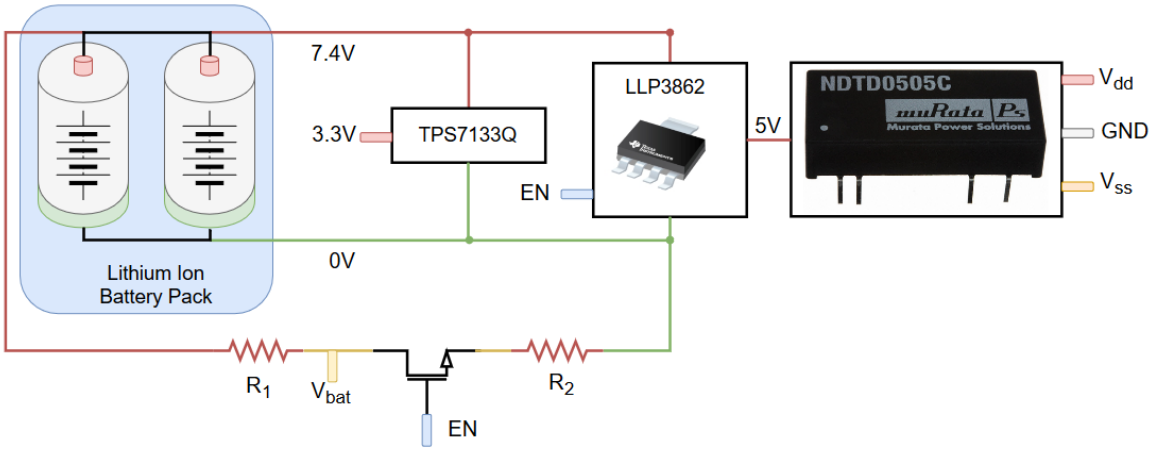

Fig. 4.19 Electrical design for the power supply circuit. This circuit provides reliable feed source to both micro-controller (3.3V) and the analog sensor supplies (V_{dd}, V_{ss})

A preliminary implementation is depicted in Figure 4.20, illustrating the power and digital board of the prototype.

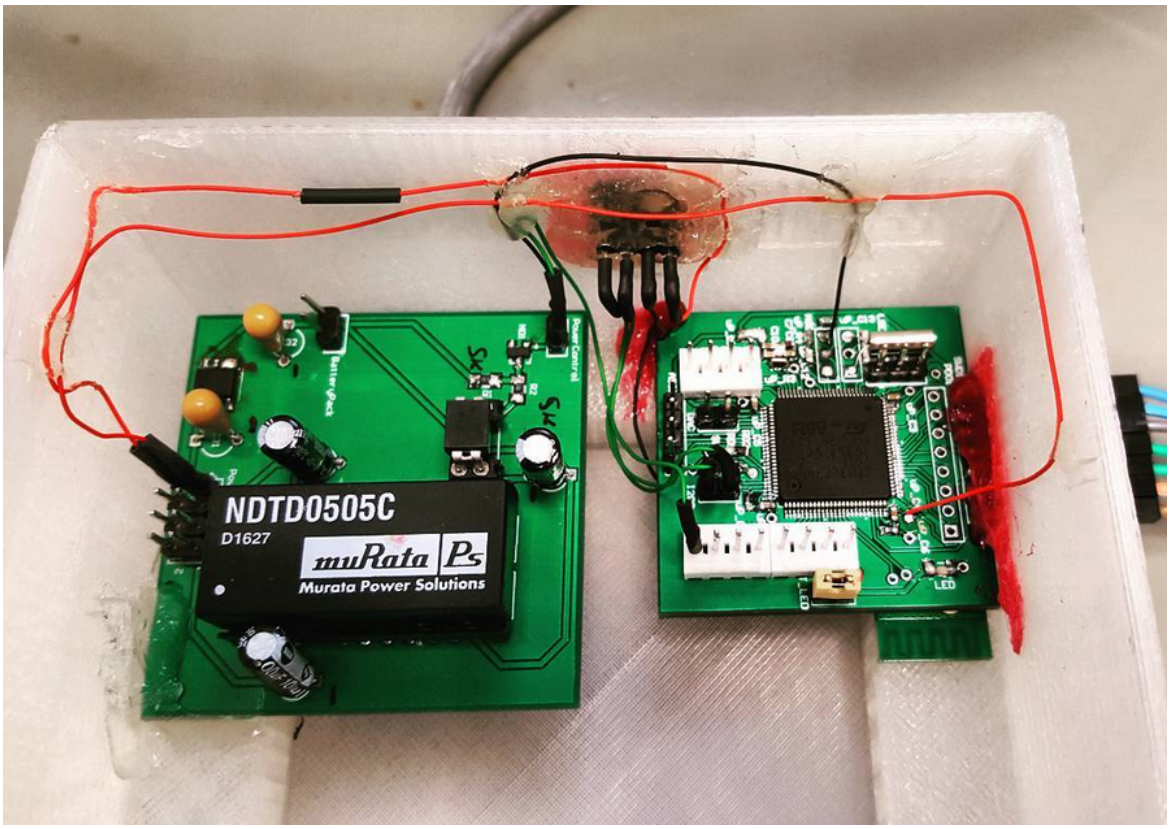

Fig. 4.20 Initial Implementation for the Digital and power boards.

Prototype

Figures 4.21 and 4.22 illustrate the sensor system: analog protoboard is highlighted in red whereas digital board is marked in blue. Finally, the power board appears in yellow. All three of them together conform the desired functionality for the sensor device. The lithium-ion battery pack is depicted on green below the gateway device.

In Figure 4.23, the device is pictured performing a cell-culture assay in the cell-culture reactor. Next to the sensor device, highlighted in yellow is the lithium-ion battery pack.

The cell-culture reactor generates a wet environment at a constant temperature of around 37º C. The prototype enclosure was designed using Autodesk Inventor [130] and fabricated on a 3D printer: Prusa i3 MK3S [131]. To prevent potential damage, the device is properly isolated using hot-melt glue as a gasket on the PLA plastic pieces. A picture captured during one of the experiments is depicted in Figure 4.23

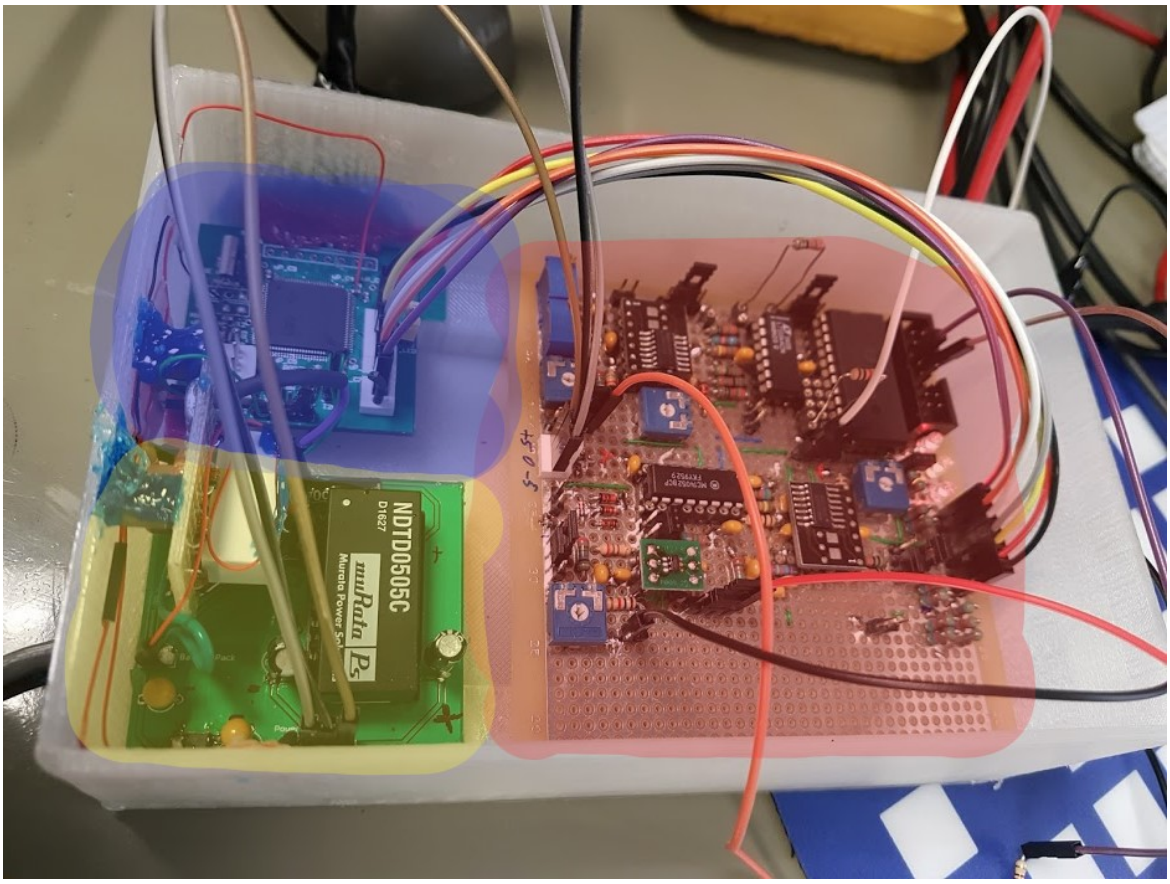

Fig. 4.21 Disassembled sensor device. Three modules are implemented: Digital (blue), Power (yellow) and Analog (red).

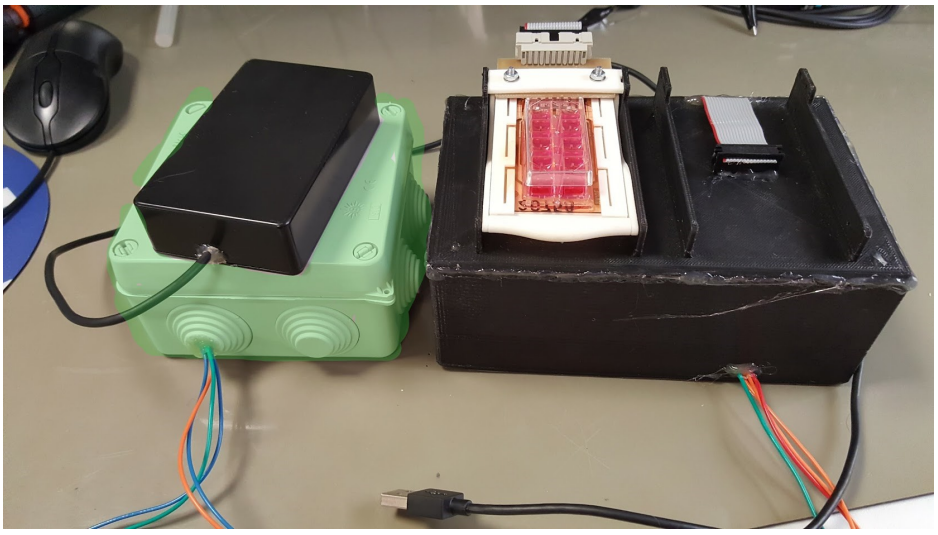

Fig. 4.22 Assembled sensor device. The device is ready to perform a cell-culture assay. Lithium-ion battery pack is highlighted in green. The black box on top the batteries is the gateway device (Intel Edison).

Fig. 4.23 The sensor device is inside the cell-culture reactor. The lithium ion battery pack is placed next to it isolated in a different enclosure. Gateway device is located nearby on the biomedical laboratory.

4.4.2 Gateway

As it was introduced before, the gateway device (Intel Edison) will be located on the biomedical laboratory, in a place nearby to the cell culture reactor in order to assure proper radio signal strenght to develop wireless communication through Bluetooth. The system is designed to be able to manage several sensors by a single gateway device (pictured in Figure 4.22 on top of the battery pack).

The gateway is a 'headless' (non graphical user interface) Linuxcomputer with the control and acquisition driver already configured. The sensor driver is programmed in Python and runs continuously by a daemon which whenever an experiment is active on the database (section 4.4.3), searches for known Bluetooth devices. Once a device is found, the gateway attempts to connect to it and initiates the sampling protocol described on the following subsection.

Sampling protocol

The experiments are guided through the definition inserted on the remote database by the user when using the interface provided. The defined parameters are sensor device and experiment period (T). However, the acquisition process is slightly more complex and involves several steps which the gateway governs without the user supervision. The full process is depicted in Figure 4.24.

Initially, the micro-controller wakes up from low power mode. The device starts a measurement process involving several sequential steps. First of all, the environment variables are acquired (temperature and humidity). Next step involves the activation of the analog power supply and the measurement of the battery voltage for battery tracking purposes. Secondly, a measurement is taken on every of the eight available wells and the three reference channels. To such purpose, for each channel the system needs to activate the starter signal, then close the loop and deactivate the starter signal. Then, a delay is introduced so that the oscillator stabilizes before acquiring the signals. Following, signal is captured and processed to obtain amplitude and frequency values. The loop is opened once again and as soon as the measurements are obtained the wake-up alarm is configured and the system set to standby mode.

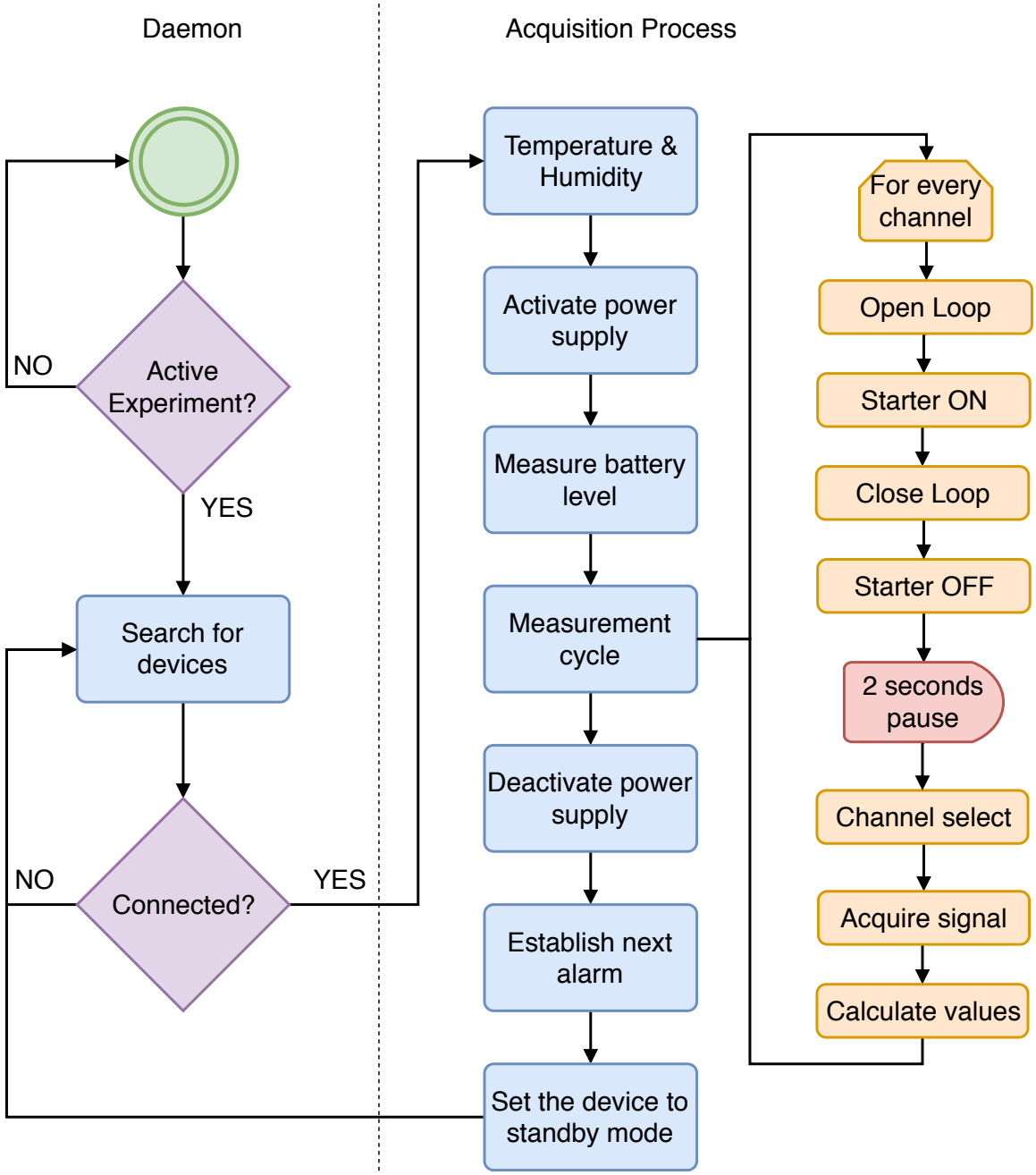

Fig. 4.24 Flow diagram for the acquisition process implemented on gateway device. On the left, the daemon process which is in charge of checking if there are active experiments registered on the database, if positive the process must search and connect to available devices on range. Once the connection is active the system will perform the acquisition process depicted on the right side of the image following all the necessary steps to acquire the frequency and amplitude values from the sensor.

4.4.3 Services

The final component of the system is formed by the set of services implemented on a remote server located at the University of Seville.

Database

The storage service for the data gathered from the sensor and the configuration established by the user is implemented in the form of a MySQL database, running continuously on the remote web server. The database entity-relation scheme is depicted in Figure 4.25. On such diagram it is possible to identify the different entities (illustrated in blue), which correspond to a different table implemented on MySQL. Each entity has a few attributes which store the required information for meeting the design criteria.

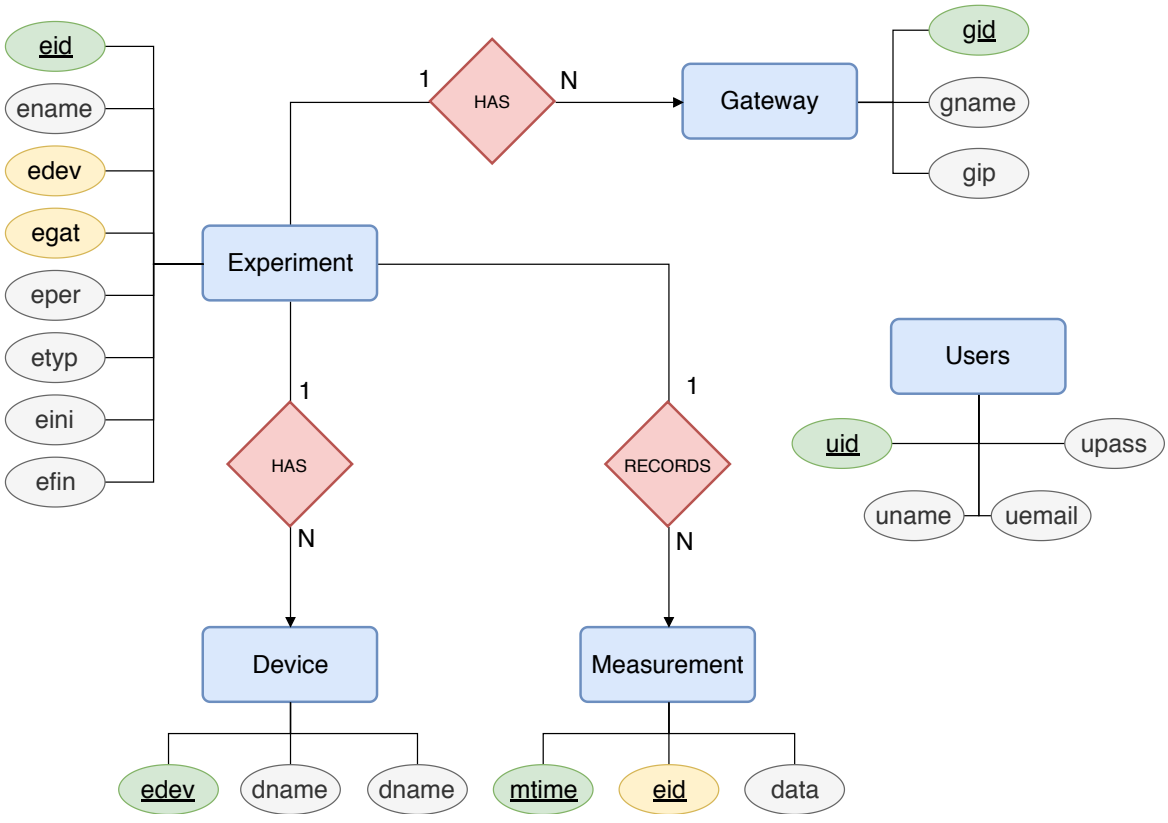

Fig. 4.25 Entity relation diagram for the implemented database.

Users entity provides the secure access parameters for the user interface. The user login information; email and MD5 hashed password are stored in the table representing this entity. Additionally, the user name is stored too on this table.

Two different entities identify the hardware devices involved in the measurement process (gateway and sensor). Both contain an unique identifier and a name. Third attribute is IP

address for the gateway and MAC address for the device. This structure enables the system to manage multiple gateways (different laboratories on the same building) each one with several sensor devices using the same database.

Experiment entities are defined by the user and associated with an unique identifier (*eid*), the name is assigned by the user and, each experiment is referred to a sensor device and a gateway device already present on the database. The user must define measurement period and the experiment begins. Field *etyp* is a boolean value representing the status of the experiment (1 = active, 0 = finished). Dates are configured automatically on creation and whenever the experiment concludes.

User Interface

The user interface service is also located on the remote server. This service is implemented using PHP, Javascript and HTML5 along with CSS. All these technologies conform the web development stack employed during this project. The prototype should be capable of attaining to the following use-case:

1. Biomedical researcher prepares a cell-culture assay and set the system ready insider the cell-culture reactor.
2. The researcher opens the user interface (via web page), logs in, and configures the experiment setting the time period at 60 minutes (Figure 4.26).
3. The researcher evaluates the results several times per day.
4. Once the experiment is finished, the researcher visualizes the resulting experience online or download the results in .xls, .mat, .csv format.

This use case was elicited during pre-development meetings with the biomedical researchers to analyze their needs and the user interface was developed based on it. Data visualization is implemented using Google Graph API library in JavaScript, an image from the application is presented in Figure 4.27, all other functionalities are built from scratch.

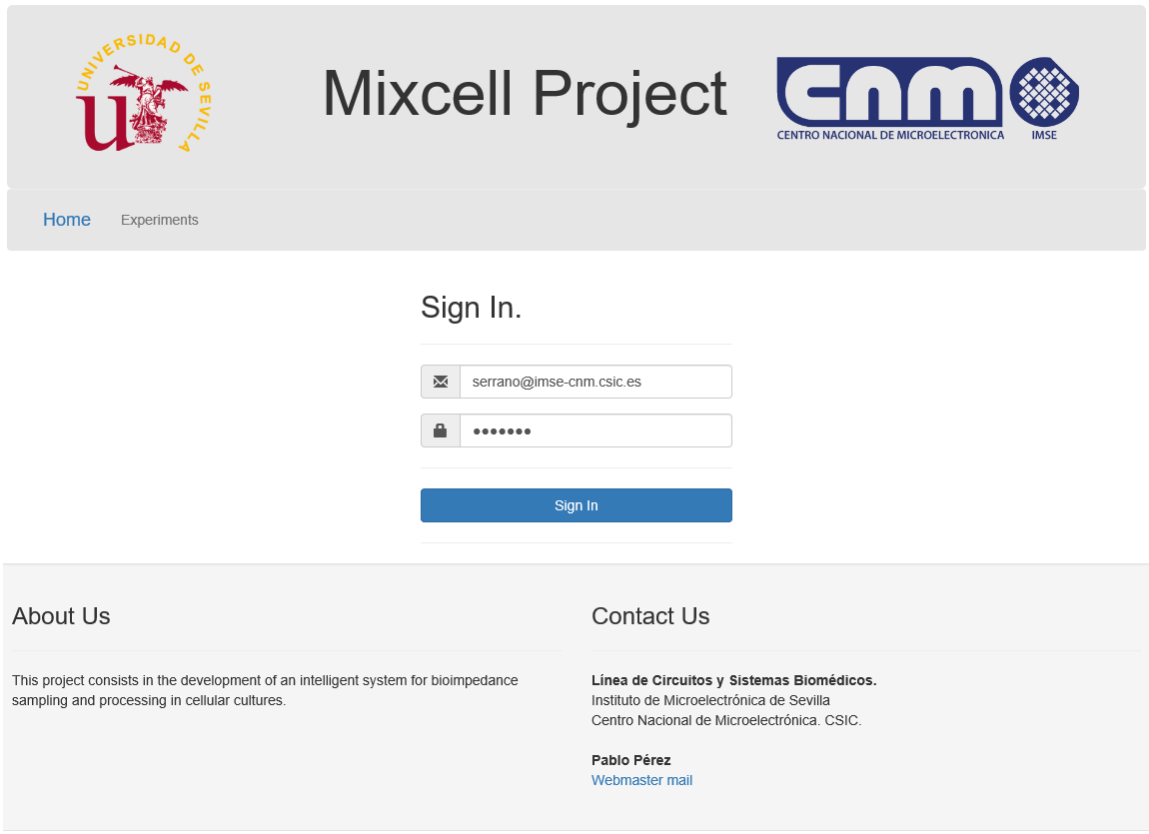

Fig. 4.26 Web Application login page.

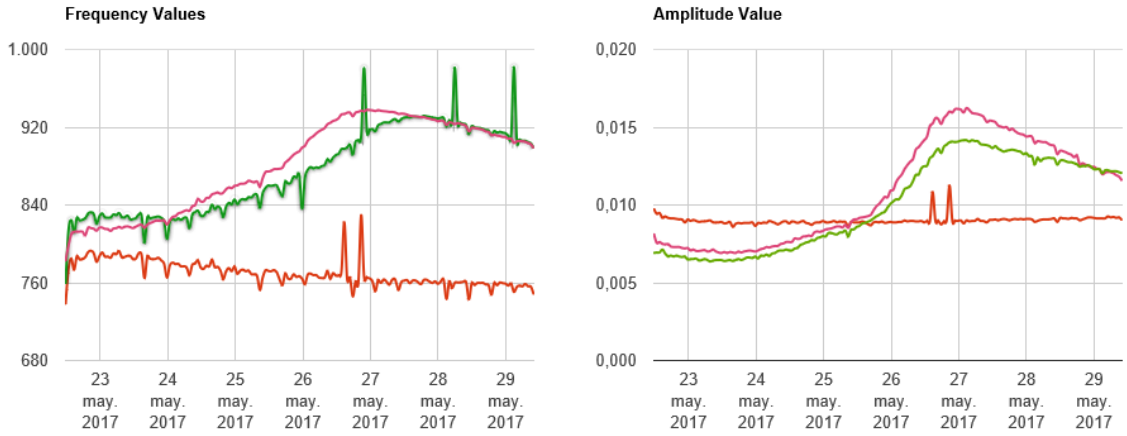

Fig. 4.27 Web Application Data Visualization.

Summary and conclusions

This chapter described the design and implementation of a full IoT system to fulfill the dissertation objectives. The system is divided into several parts ranging from the bio-OBT electronic implementation, the digital micro-controller device, the wireless communication, the data acquisition, the data management, the sensor control and the real-time visualization.

- Firstly, the electrical design for a complete sensing solution based on the Oscillation Based Test (OBT) is described. A band-pass filter was implemented and tuned accordingly so that the frequency and amplitude ranges are monotonously increasing and a good precision is achieved. The biological interface is implemented based on a bipolar current source sink so that appropriate level of current flowing through the cells is assured and the electrodes are operating on the linear region ($< 100\ mV$), implying cell current exciting amplitudes below ($20\ \mu A$). Noise filter and amplification is performed on the following stage and finally the loop is closed by a comparator with a hysteresis and amplitude range control.

- The whole system performed well in pspice simulations and oscillations are formed for different fill-factors values. To control the well under test, acquire the signal, and provide a fast start-up three blocks are added to the design: a multiplexer block enables measuring different wells using a discrete component, driven by the micro-controller, a power supply level shifter required for the specific circuits, and a start-up circuit to initialize the OBT system.

- The digital system and sensor communication link is managed by the firmware implemented on the micro-controller, a STM32F7 chip, which guides the operation by a command driven finite state machine. This implementation is described along the text executing atomic instructions in response to wirelessly received command through the Bluetooth interface. To implement the required functionality set, the device takes advantage of the multiple peripherals included on-chip. This design uses a Real Time clock (RTC) for power efficiency, I2C for the environment digital sensor, pulse width modulation (PWM) for the OBT starter signal, analog to digital converters to acquire the OBT signals and estimate battery levels and general purpose input/output (GPIO) pins to manage the control signals (multiplexer, starter switch) on the analog circuit.

- The final elements for a design complying with the Internet of Things (IoT) architecture are defined (gateway and service layers). The gateway is located on the biomedical laboratory with a direct link to the remote web server, which provides the service

layer. The gateway device is formed by a commercial Linux based system on a chip; Intel Edison. This device includes a Yocto Linux version as the Operating System and implements both WiFi and Bluetooth communication. This makes the device suitable for our application. The sampling protocol for the cell culture experiments, which is implemented on the gateway, is described through the chapter and a flow diagram is provided.

- The service layer provides secure access, storage and real-time visualization for the potential user of the system; biomedical researchers. All the information related to this services are stored on a MySQL database, which structure is described on this chapter. The database is designed to provide scalability and comply to the functional requirements of the system. The remote control and real-time visualization of the system is performed via a custom web application prototype developed for this purpose.

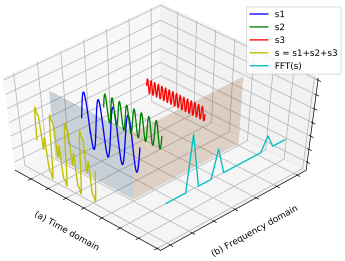

Chapter 5

Signal acquisition and processing system

5.1 Introduction

On previous chapters, the basic electronic circuit and digital device included on the design were presented. This chapter will present the signal processing concepts, and the processing algorithm implemented on the microcontroller which will estimate the frequency and amplitude from the acquisition performed using the microcontroller and sensor already described. The analog front-end generates two signals corresponding to different measurement points in the oscillation circuit (F_{out} and A_{out}). The cell culture status information is included on those two signals, hence to obtain valuable data on the growth state of the cell culture assay, it is necessary to analyze the signals and obtain the parameters which are related to the physical biological sample; signal amplitude and frequency. This calculations will be performed in real-time using the μP resources. A detailed analysis is done in order to optimize the energy consumption or equivalently reducing the computational workload.

On chapter 3 the oscillation based test (OBT) sensor was analyzed and different designs were compared in an attempt to determine the optimal operation point for the sensor. The study concluded with the band pass filter tuning frequency $f_0 = 1.096\ kHz$ and $Q = 6.23$. Developing the full system simulation from those parameters and the experimental model presented on chapter 2 and the implementation circuit provided on chapter 4 the following dynamic ranges are found for the acquired signals the sensor output (V_f, V_a):

$$Frequency(V_f) = [500, 1000]\ Hz \tag{5.1}$$

$$Amplitude(V_a) = [0.2, 3.33]\ V \tag{5.2}$$

Both represent minimum and maximum values on the signal generated by the sensor which is then to be acquired. The main objective of the signal acquisition process is to assure that information can be derived from the sampled signal.

5.1.1 Analog to digital conversion

The information processing relies on the precise determination of amplitude and frequency of both output signals from the analog sensor. To perform this processing it is necessary to acquire the signal in a process denoted as analog to digital conversion. This process is mediated by an Analog to Digital Converter (also known as ADC) which is a device that samples an analog signal and returns the quantized value of the original signal as a packet of bits. The result of the conversion is a binary coded number where the precision depends on the number of bits involved in the conversion. A greater number of bits provides greater precision levels. An ideal signal would be represented by:

$$y = sin(\omega t) \tag{5.3}$$

Where $\omega = 2\pi f$ being f the signal frequency in Hertz. Setting this parameter to 500 Hz would generate the signal depicted on Fig. 5.1.

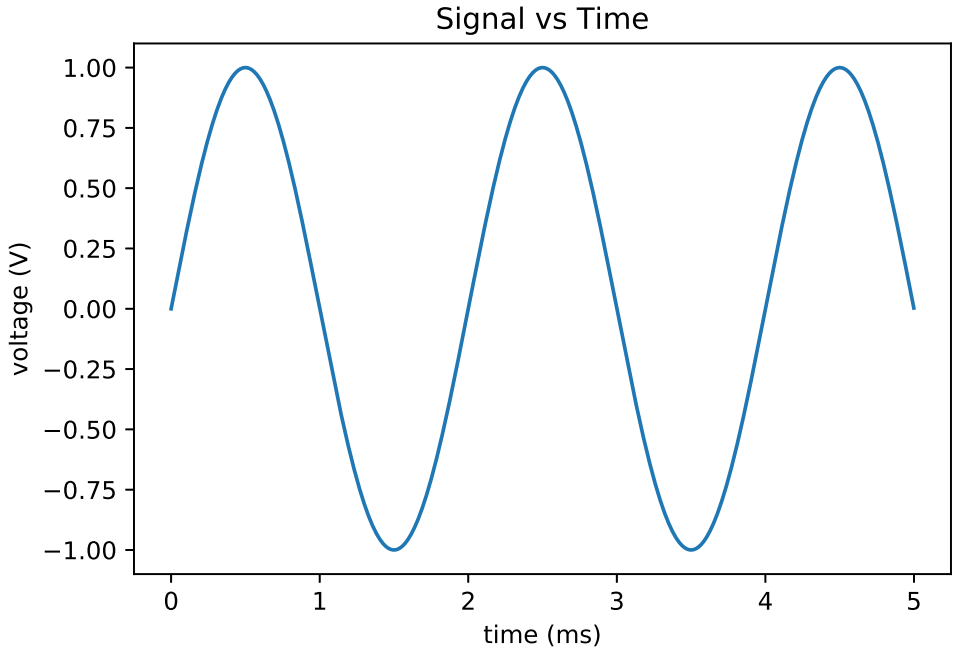

Fig. 5.1 Ideal sinusoidal signal with $A = 1\ V$ and $f = 500\ Hz$

The signal expressed above is a continuous time signal; there's always a voltage value associated to a time instant. Despite this fact, digital converted signals are discrete signals,

meaning that the digital conversion process produces a set of measurements acquired from the signal at regular time intervals. Figure 5.2 illustrates the samples acquired by an ADC in red.

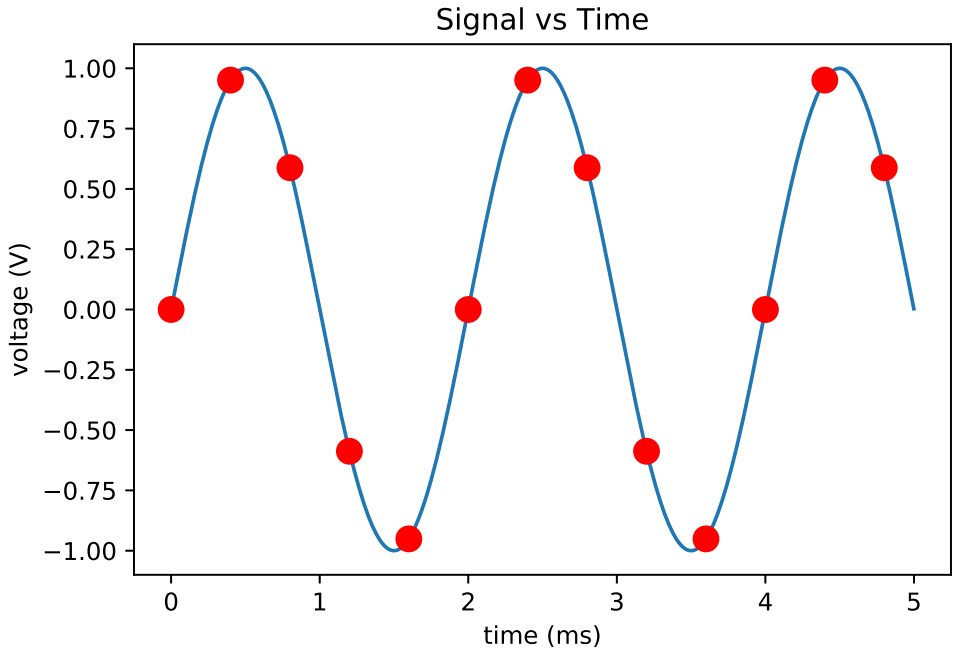

Fig. 5.2 Sampled Ideal Signal

The digitalization process is performed on every single red dot from figure 5.2. The process begins with a sample & hold (S&H) stage where the analog value will be kept steady for some period of time (t_{SH}), allowing the ADC device to perform its conversion to bit information. This process can be identified as a signal level classifier for 2^n levels being n the number of bits involved in the process. Figure 5.3 present a visualization of the different classification levels generated when using different number of bits $(1-4)$ in the conversion process. The quantization error associated to the digitalization conversion process is defined by the following equation:

$$e_r = \frac{V_r}{2^{n+1}} = \frac{LSB}{2} \tag{5.4}$$

Being V_r the amplitude voltage range for the ADC converter and n the number of bits involved in the conversion. By increasing this number of bits the relative error is lower since the classifier level amplitude is becoming smaller. This relative error is presented on Fig. 5.4, from there we realize that for a $e_r < 0.1\%$ on the conversion process a 10 bit ADC it is good enough.

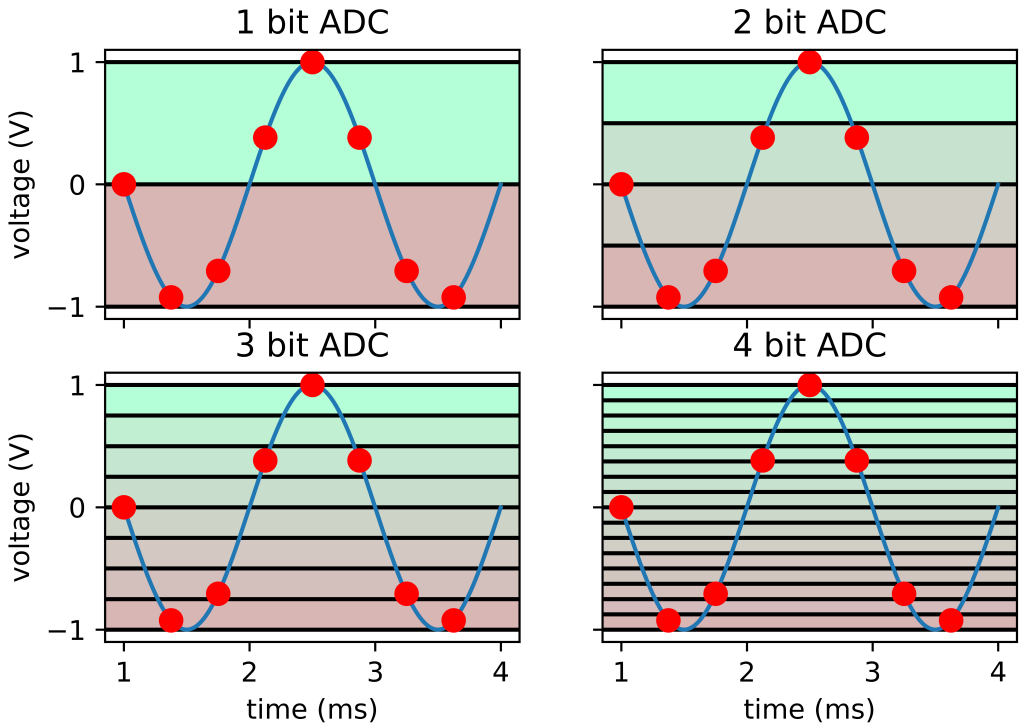

Fig. 5.3 Different classification levels depending on the different resolution bits on an ADC conversion process.

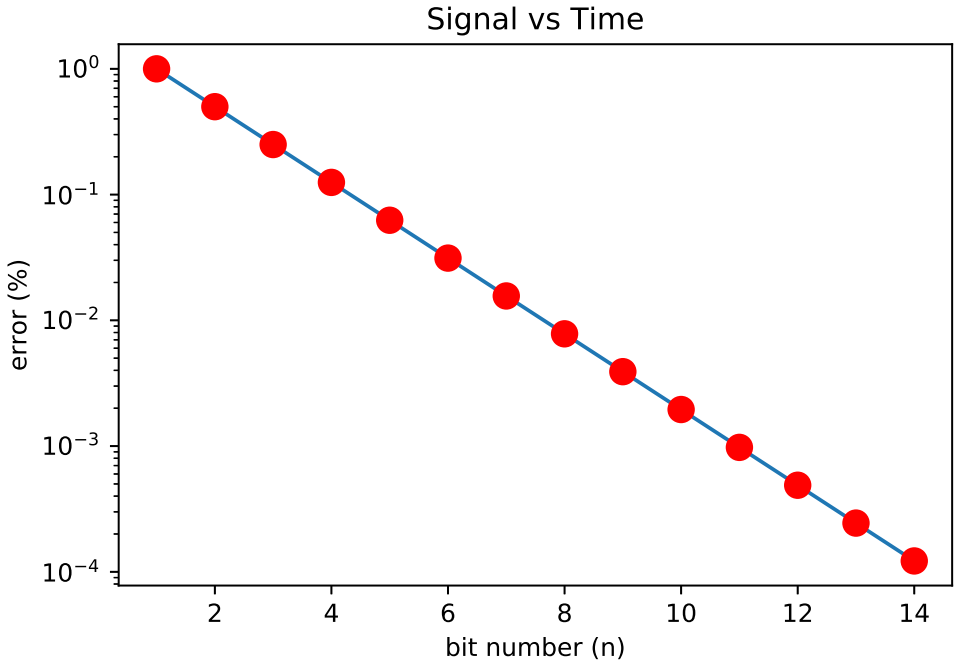

Fig. 5.4 Relative error (e_r) associated to the conversion process (ADC) vs resolution bits number involved in the conversion.

Nyquist-Shannon theorem

The acquisition frequency is a critical design parameter on any analog to digital conversion process. Assume the original input signal depicted on figure 5.1 is sampled by a slow ADC (red points on figure 5.5). An undesired effect known as signal aliasing may arise if the acquisition frequency is not properly selected. This is due to the fact that the points recover may represent more than one signal frequency, and it would be difficult to recover the original signal from the sample due to this non-uniqueness of the signal retrieval process.

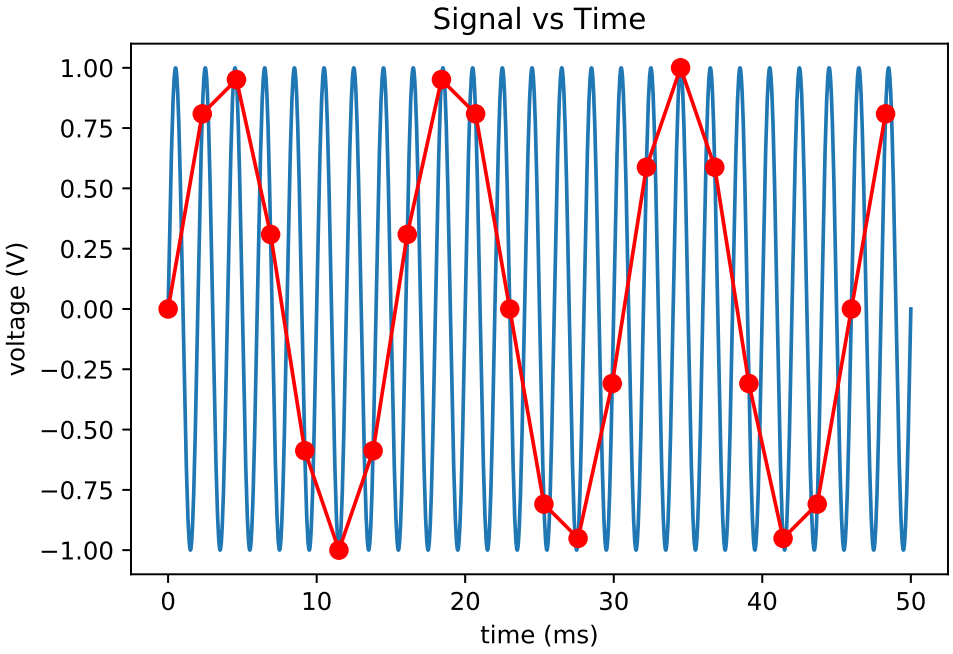

Fig. 5.5 Aliasing effect in time on the original signal

Signal theory introduces a concept known as Nyquist-Shannon theorem or sampling theorem to address the sampling rate determination problem we just presented[132]. Stated as:

> Given a signal S(t), with a bandwidth limited to f_b, the sampling frequency (f_s) should be at least twice the highest frequency contained in the band-limited signal (f_b).

$$f_s \geq 2f_c \tag{5.5}$$

This theorem and equation 5.5 state that in our range application where the signal range is confined to a specific range, the selected sampling frequency should be at least twice the maximum frequency of the sensor signal.

Time and frequency domains

Electrical signals can be analyzed from two domains; time and frequency. In Fig. 5.6 an illustration on both of them is presented. A signal composed of three fundamental frequencies can be described as (a) in the time domain or as (b) in the frequency domain.

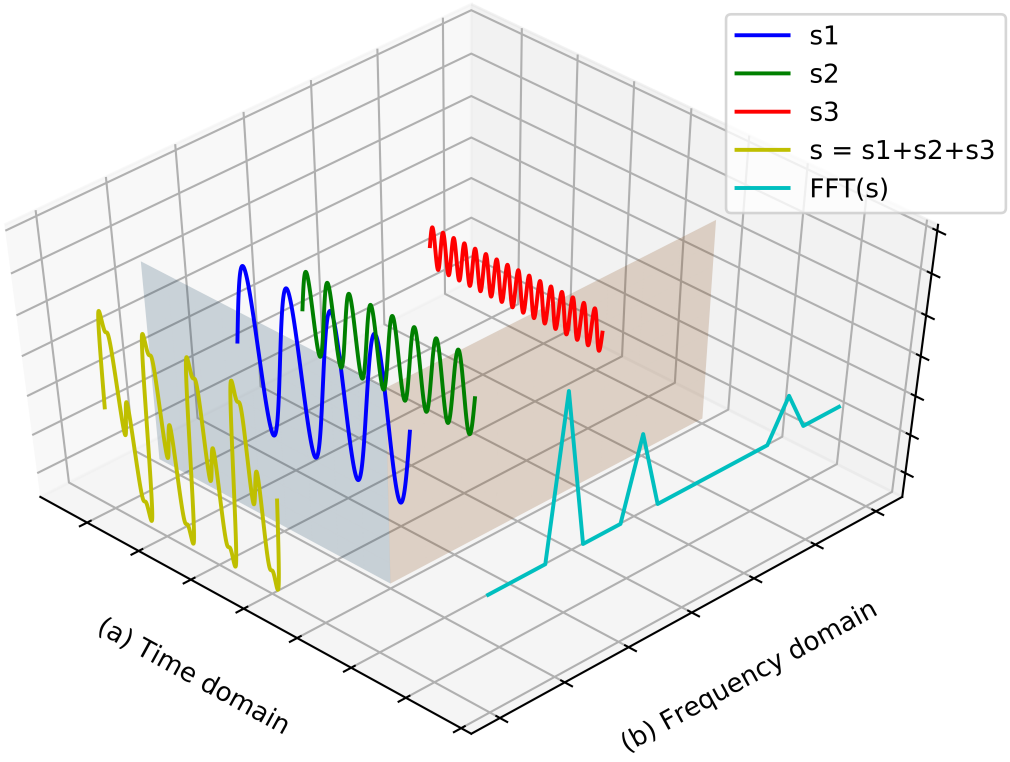

Fig. 5.6 Frequency and time domain for a signal composed of three components ($s1$, $s2$ and $s3$).

Time domain contains temporal representation of the signal and it is useful to perform a transient analysis, whereas frequency domain describes the frequency power spectrum of the signal and illustrates amplitude information as well as signal quality. These concepts will be used along the present chapter to extract precise signal parameters from the OBT sensor signal acquisition.

5.2 Signal processing

On chapters 2 and 3 the simulation and design of a sensor system capable of measuring cell culture assays was introduced. The OBT circuit generates a couple of signals (F_{out}, A_{out}) which encode cell culture status within their physical parameters (frequency and amplitude). To analyze the information provided by the sensor, it will be necessary to obtain the signal parameters. This process is extensively reviewed on the literature [132][133].

This chapter evaluates the design and implementation of the signal processing algorithms which will perform the frequency and amplitude estimation. The process is based on [134]. The authors propose the application of a gaussian window to the signal prior to the discrete fourier transform. This is due to the gaussian window properties which provides a dual benefit. First, it enhances precision on the FFT and second, the peak estimation is improved due to the parabolic shape on the FFT.

The system must acquire the oscillator signal which codes the cell growth information within the self-oscillation. The parameters to measure are the frequency and the amplitude of the signal. Both variables will change depending on the number of cells located over the sensor surface. This variation will be measured by the means provided by the signal processing algorithms and tools depicted on this section.

5.2.1 Gaussian windowing

The estimation process requires the application of a window function to increase the precision on the frequency values estimated. This process greatly improves the performance of the estimation algorithm as it is described on [135]. The window will generate a parabolic-shaped FFT output, allowing for a better estimation of the peak using parabolic interpolation.

Assuming an ADC acquired signal S_{ADC} of lenght L. The gaussian window is described by the following set of equations. The window is valued from $i = 0$ to $i = L$.

$$z(i) = \frac{\pi}{L}\left(\frac{L-1}{2} - i\right) \tag{5.6}$$

$$w(i) = w(L-i+1) = e^{-cz(i)^2} \tag{5.7}$$

Where $c = 4.5$ and L is the window lenght, corresponding to the sample number. Figure 5.7 illustrates the window for $0 \leq i \leq L$ and $L = 4096$. Second equation presents the symmetrical behaviour existing on the window from position $i = L/2$.

To provide an example for the gaussian window effect, consider an ideal signal with 1 kHz frequency and 1 V amplitude, similar to the one depicted on 5.2. The gaussian window would produce the output illustrated on figure 5.8.

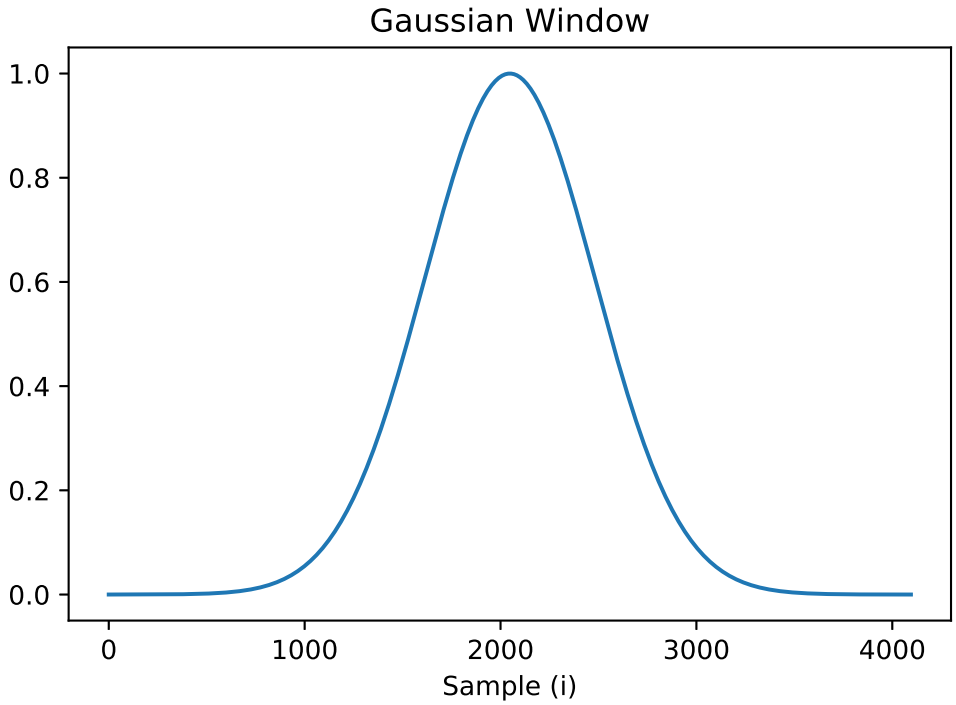

Fig. 5.7 Gaussian Window shape for the frequency estimation process.

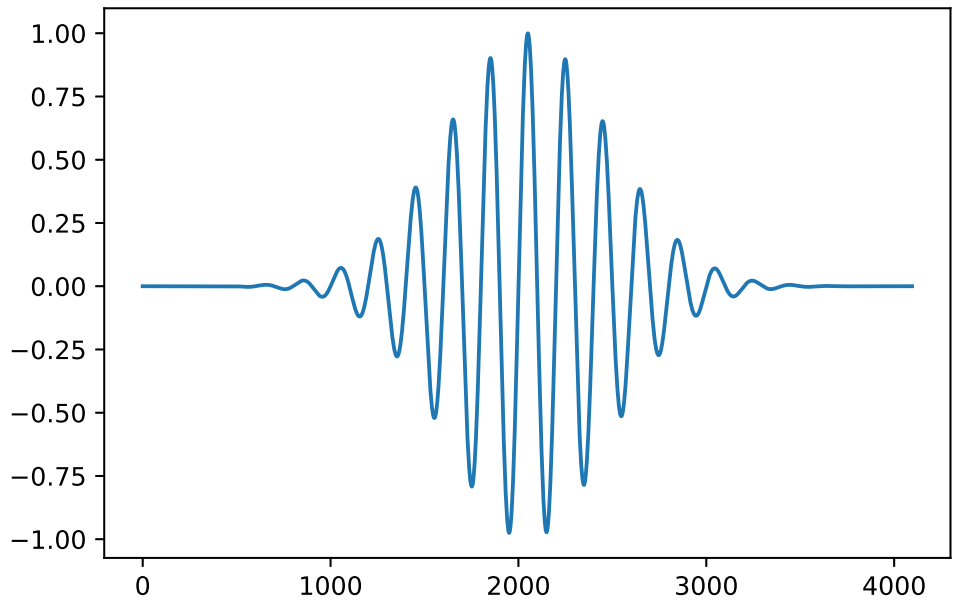

Fig. 5.8 Resulting signal from the gaussian window described above.

The importance of this process as mentioned on this section is relevant to the frequency retrieval performance. This kind of signal will produce parabolic peaks on the frequency domain after the application of the discrete Fourier transform algorithm which will enhance peak interpolation. We will analyze this on following sections.

5.2.2 Discrete Fourier Transform (DFT)

The Fourier Transform is a powerful tool widely employed to analyze the information contained on electrical signals by visualizing the power spectrum on the frequency domain. The mathematical definition for the Discrete Fourier Transform (DFT), F is:

$$F(\frac{n}{NT}) = \frac{1}{N}\sum_{k=0}^{N-1} m(kT)e^{-j\frac{2\pi nk}{N}} \tag{5.8}$$

Where T is the sampling period, N is the total sample number, n is the transform index and $m(kT)$ is the sampled signal value on time kT. Previously an ideal signal sampling process was presented on figure 5.2 to illustrate the acquisition process and understand the concepts of sampling and set of samples. The DFT algorithm input is the acquired set of samples obtained from the electrical signals. First value of the DFT would be computed as follows:

$$F(0) = \frac{1}{N}\sum_{k=0}^{N-1} m(kT) \tag{5.9}$$

This value represents the mean value of the sampling set which corresponds to the dc level of the signal under test; or lowest frequency value (0 Hz). Every single step we take on the algorithm will subsequently calculate additional steps on the frequency domain result. Next value would be:

$$F(\frac{1}{NT}) = \frac{1}{N}\sum_{k=0}^{N-1} m(kT)e^{-j\frac{2\pi k}{N}} \tag{5.10}$$

The result from above equation is the power associated to the frequency $\frac{1}{NT}$ or $\frac{f_s}{N}$. The value $\frac{f_s}{N}$ corresponds to the spectral resolution of the DFT process. The resulting values from the application of the algorithm conform the power spectrum of the signal over the frequency domain. Despite the fact that DFT calculates this spectrum, it is not the most efficient algorithm for computing the power spectrum from a sampled signal.

5.2.3 Fast Fourier Transform (FFT)

While the DFT can compute the frequency power spectrum from a sampled signal a different approach based on an optimized algorithm can produce similar outcomes, while reaching a higher level of computing performance. This algorithm is known as Fast Fourier Transform (FFT) and it improves the computation and memory performance. Furthermore it is suitable for real time applications and digital signal processing tasks.

Fast Fourier Transform (FFT) generates an output spectrum representing the signal components over the frequency domain, signal power is represented on the Y-axis, while X-axis represents the frequency range. To illustrate the algorithm an example output for a 1 kHz ideal signal is presented on figure 5.9. $F_s = 200\ kHz$, $n = 12$ which results in a sample number $N = 2^n = 4096$. Notice the peak around the 1 kHz frequency point. The frequency value of the most powerful component in any signal can be obtained by performing a valid estimation of the highest peak on the frequency spectrum. Using only the FFT output the maximum resolution is limited to $R = Fs/N = 48.8Hz$. In the following section we will analyze a method for increasing the frequency estimation resolution.

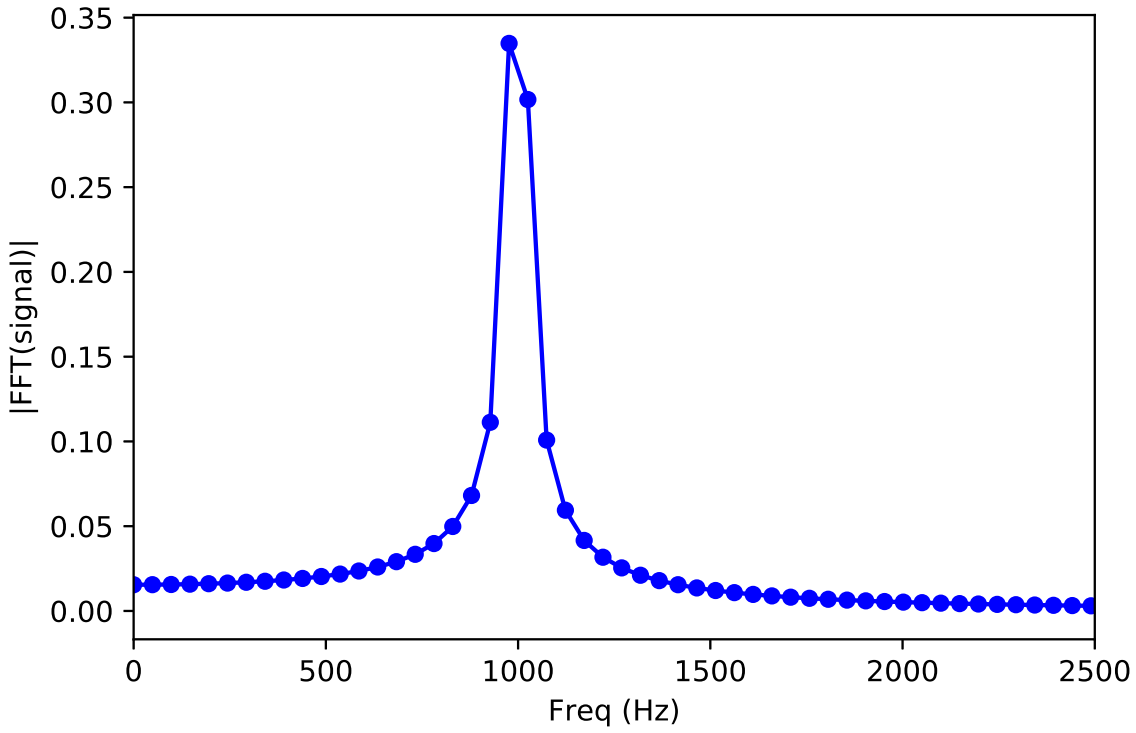

Fig. 5.9 Frequency spectrum for am ideal signal with a 1 kHz frequency value. $F_s = 200\ kHz$, $N = 2^n = 4096$.

The FFT is a popular topic on the signal processing field. It is widely described on books [132] and on the literature as a powwerful tool for performing several process associated to signal analysis. Among the many existing FFT-Implementation, the Cooley-Tukey FFT [136] algorithm has been selected for this project due to its great optimization in terms of memory efficiency and performance. According to the performance comparison presented in [137] the Cooley-Tukey algorithm is the appropriate choice for a micro-controller implementation, since it presents the lowest memory usage from the available FFT algorithms.

5.2.4 Signal parameters estimation

The power spectrum obtained from the FFT algorithm was illustrated on previous section. From the FFT output it is possible to estimate the amplitude and frequency parameters of the input signal. The process requires an accurate determination of the highest peak frequency and perform a small calibration step for the amplitude.

On figure 5.9 presented above, the power spectrum is provided as a set of discrete values over the frequency axes. The method depicted on [135] aims at finding the parabolic curve which contains the maximum value and its adjacent points. This curve is defined by:

$$y = ax^2 + bx + c \tag{5.11}$$

Since the gaussian window applied on a preliminary stage to the signal generates parabolic peaks over the frequency spectrum, the maximum value is obtainable through the recovery of the parabolic curve equations. A maximum value in such curve is required to meet the following condition:

$$y' = 2ax + b = 0 \tag{5.12}$$

$$X_f = \frac{-b}{2a} \tag{5.13}$$

Let i be the index for the maximum value of the FFT result array ($max(y) = y(i)$). The point Pm is defined as:

$$P_m = (i, y(i))$$

To simplify the calculations a translation is performed along the x axis, this displacement would be equal to i, and a parabolic curve having the point P_1 abscissa crossing point occurs. Such curve would have the following points:

$$P_0 = (x_0, y_0) = (-1, y(i-1))$$
$$P_1 = (x_1, y_1) = (0, y(i))$$
$$P_2 = (x_2, y_2) = (1, y(i+1))$$

On figure 5.10 all the points are illustrated.

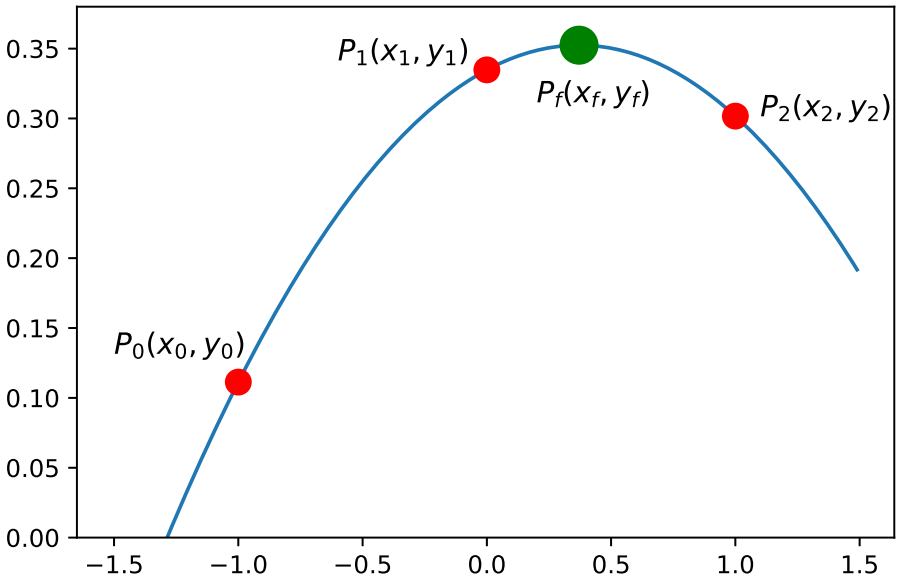

Fig. 5.10 FFT points and parabolic interpolation.

The following equation system is formed from the conditions expressed above:

$$\begin{aligned} y_0 &= ax_0^2 + bx_0 + c \\ y_1 &= ax_1^2 + bx_1 + c \\ y_2 &= ax_2^2 + bx_2 + c \end{aligned}$$

Simplifying:

$$\begin{aligned} y_0 &= a - b + c \\ y_1 &= c \\ y_2 &= a + b + c \end{aligned}$$

Solving:

$$\begin{aligned} y_0 &= a - b + y_1 \\ y_2 &= a + b + y_1 \end{aligned}$$

$$\begin{aligned} y_0 + y_2 &= 2a + 2y_1 \\ y_2 - y_0 &= 2b \end{aligned}$$

Which results in:

$$a = \frac{y_2 + y_0 - 2y_1}{2} \tag{5.14}$$

$$b = \frac{y_2 - y_0}{2} \tag{5.15}$$

$$c = y_1 \tag{5.16}$$

This allow us to calculate the parabolic peak, by applying equation 5.13

$$x_f = \frac{-b}{2a} = \frac{\frac{y_2 - y_0}{2}}{2\frac{y_2 + y_0 - 2y_1}{2}} = \frac{y_2 - y_0}{2(2y_1 - y_0 - y_2)} = \Delta x \tag{5.17}$$

And the frequency then is derived as:

$$F = (i + \Delta x)\frac{f_s}{N} \tag{5.18}$$

Where f_s represents the sampling frequency and N corresponds to the sample size.
The Amplitude is defined as:

$$A = k_F(ax_f^2 + bx_f + c) \tag{5.19}$$

Where k_F is a gain obtained from the calibration of the system using test signals within the operation range.

Total Harmonic Distortion (THD), Signal to Noise Ratio (SNR) and SNR+D parameters can also be estimated for a better analysis of the sensor signal behavior.

$$THD = \frac{\sqrt{V_2^2 + V_3^2 + V_4^2 + \ldots}}{V_1} \tag{5.20}$$

Being V_1 the fundamental component in the frequency domain, and V_2, V_3, V_4 subsequent components of the signal.

$$SNR = \frac{V_1}{V_r} \tag{5.21}$$

Where V_r corresponds to the noise amplitude in the signal.

$$SNR + D = \frac{V_1}{\sqrt{V_r^2 + THD^2}} \tag{5.22}$$

To analyze the signal quality the following metric was defined based on the FFT result; a Q Factor:

$$Q = \frac{a\sqrt[2]{\frac{c}{a}}}{b} \tag{5.23}$$

The calculation of all this parameters is implemented on a specific signal processing library which will be used to estimate the amplitude and frequencies of the signal as well as the signal quality, distortion and noise parameters.

5.3 Algorithm design and implementation

5.3.1 Algorithm design

The development system is a digital processing algorithm which parameters are fully configurable to adapt to any signal processing task, requiring the retrieval of signal parameters in a real time environment.

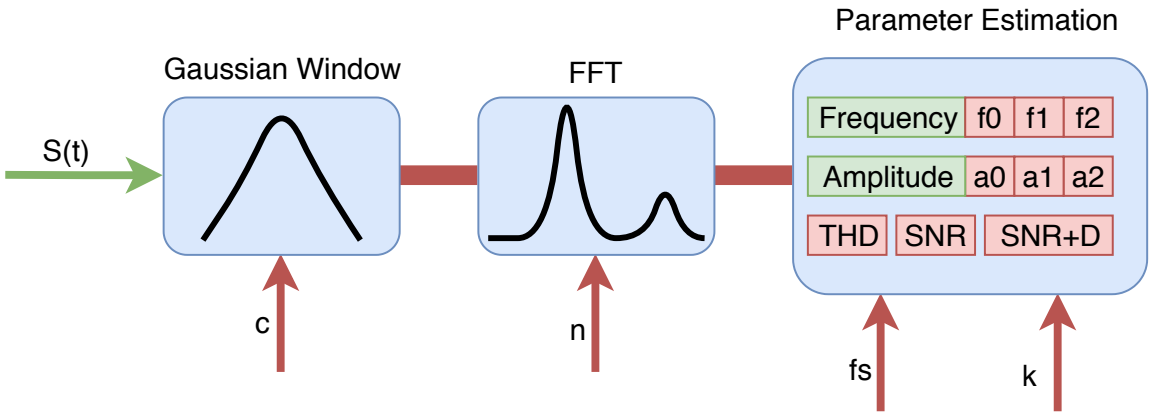

Fig. 5.11 Signal processing algorithm overview

On figure 5.11 a full schema depicting the processing system is presented. Configurable inputs to such system include:

- $n \rightarrow$ FFT size (order).
- $f_s \rightarrow$ Sampling frequency.
- $c \rightarrow$ Gaussian Window coefficient.
- $k \rightarrow$ Calibration factor for amplitude.

5.3.2 Processing algorithm calibration

The signal processing calibration will be illustrated. This system requires a set of sequential steps to provide accurate measurements.

1. Sampling frequency selection.
2. FFT Order selection.
3. c-value determination.
4. Amplitude gain determination.

Sampling Frequency

The initial step to implement this signal processing library is the sampling frequency definition. The microcontroller device included in the prototype and exposed on chapter 4 allows for custom configuration of the ADC peripheral at certain rates imposed by the microcontroller internal operation frequency. The default system frequency for the microcontroller generates a sampling frequency on the ADC $fs = 42.683\ kSPS$. This value is adequate for the target signal processing according to the Nyquist theorem since the signal ranges are located between $[500Hz - 1kHz]$.

FFT Order

The Fast Fourier Transform (FFT) algorithm is implemented for a signal of lenght 2^n, where n is denoted as the FFT order. This order will affect the memory requirements of the implemented algorithm. The following table 5.1 is provided to analyze its effect over frequency resolution, relative error generated using only the FFT output as the frequency estimator and memory usage associated to the frequency estimation process. The reference signal for error estimation is an ideal signal of $f = 1\ kHz$:

$$\delta e = \frac{Resolution}{2 \cdot 1000} \tag{5.24}$$

Table 5.1 Byte memory profiles for different FFT sizes.

FFT order (n)	7	8	9	10	11	12	13	14
Resolution (Hz)	340	170	85	43	22	11	5.4	2.7
Relative error (δe)	0.17	0.085	0.043	0.022	0.011	0.005	0.002	0.001
m (bytes)	1096	2120	4168	8264	16456	32840	65608	131144

n is the FFT order, **R** is the resolution, δe is the relative error and **m** is the memory size. The above table illustrates the differences in memory consumption and relative error on the frequency estimation process, to provide valuable information the algorithm must be capable

of performing an adequate signal parameters analysis, a value $n \geq 11$ implies $\delta e < 1e-4$ which is a valid value for this application.

C-value determination and Amplitude gain calibration

Final step on the signal processing algorithm configuration is the c-value selection and the amplitude gain (k) determination process. To analyze the influence of the C-value determination, a simulation is prepared generating a set of ideal signal in the range 500 Hz – 1 kHz with amplitudes varying from 100 mV to 1.65 V. The signal is further processed using the library ($n = 11$, $fs = 42.683$ $kSPS$) and the frequency/amplitude values are estimated. Analyzing the output of the maximum peak value and the input signal amplitude it is possible to map the results and provide a calibration value for this parameter.

C-value is a parameter related to the shape of the gaussian window implemented, For the project presented on this dissertation this value is set to $c = 4.5$.

Results

The calibration process is needed to perform the parameters estimation. Amplitude is computed from the gain value. This value correspond to the full algorithm attenuation effect over the amplitude value (window and FFT). Frequency is recovered from the peak estimation on the FFT output, using such approach improves relative error on the frequency recovery process as presented in table 5.2. A 1 kHz signal was employed for this example, as in the previous table 5.1.

Table 5.2 Relative error for different FFT orders.

FFT order (n)	7	8	9	10	11	12	13	14
Relative error (δe)	0.5+	0.5+	0.02	2.8e-4	2.5e-5	1.7e-5	7.2e-6	4.2e-6

The relative error difference is significant for the frequency ranges analyzed. These values not only provide good performance on the estimation results but also implies a reduction in power consumption and memory resources, since lowering the FFT order results in less machine operations and memory requirements per estimation.

Summary and conclusions

On this chapter, the signal processing tools applied to perform the frequency and amplitude estimation from the OBT sensor signals was exposed. The sensor system defined previously on this dissertation generates an oscillatory signal which physical properties are related to the biological sample under test. More specifically the frequency and amplitude of the OBT oscillation inherently represents the cell culture assay state. Hence, to further acquire cell culture information, determination of signal amplitude and frequency is mandatory.

- The Fast Fourier Transform (FFT) algorithm is the adequate mathematical tool to fill such purpose. There exist several implementations for this algorithm, the Cooley Tukey FFT algorithm features better suitability for the design exposed on this dissertation. Memory requirements are optimized with respect to other algorithms, to be implemented on the microcontroller.

- To improve the performance and accuracy of the process, an alternative solution based on a Gaussian window, FFT algorithm and a peak estimator is proposed. The final system implemented provides a significantly higher degree of accuracy to the signal parameter estimation process, reducing the total computational load at the microcontroller, and total power consumption in communication circuits, since the amount of data to be transmitted is reduced to a few bytes per measurement, corresponding to frequency and amplitude values resulting from the proposed signal processing.

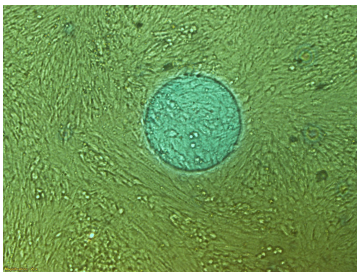

Chapter 6

Experimental results

6.1 Introduction

The design, development and implementation of a cell-culture assay sensor prototype was described through the previous chapters of the present dissertation. On this chapter many experimental data acquired from the aforementioned sensor are presented to illustrate the sensor behaviour under real cell-culture assays performed on biomedical laboratories.

On the final stage of this thesis several experiments were proposed and developed on various research group and facilities of different entities. Universidad de Sevilla (US), Instituto de Biomedicina de Sevilla (IBIS) and Virgen del Rocio Hospital (HUVR), helped us to develop these experiments. Additionally the Centro Andaluz de Biología Molecular y Medicina Regenerativa (CABIMER) helped us on prototype early testing stages. The experiments are summarized on table 6.1.

Table 6.1 Experiments performed

Institution	Cell line	Experiment type
IMSE-CNM (CSIC)	—	Preliminary tests (saline solution)
Cabimer (CSIC)	—	Preliminary tests (cell culture assays)
Faculty of Biology (US)	AA8	Growth
Faculty of Biology (US)	N2A	Growth
Faculty of Biology (US)	N2A APP	Growth
IBIS, HUVR	CRL-1458	Stem cell differentiation
Faculty of Biology (US)	N2A	Toxicity

The experiments performed on the different research facilities were planned, prepared and executed following a similar pattern. Initially the biomedical researchers prepare the

cells which will be later seed on the cell culture assay measuring device. There are four different cell lines reported, these cell lines are identified on table 6.1.

The biomedical researchers performed cell culture assays in parallel using the traditional approach to monitor the growth and acquired some pictures depicting the process evolution. At the same time, the cell culture sensor was locate into the cell culture reactor and performing regular measurements while the cells were growing over the substrate. This continuous monitoring of cell culture, produced a big amount of sensed data from the cell culture which will be analyzed through this chapter.

This chapter aims to validate the model cell-electrode model presented on chapter 2, the sensing principle exposed on chapter 3 and the sensor design and implementation exposed on chapter 4. To perform such validation experimental assays performed by the biomedical researchers are presented along the experimental data gathered from the cell culture sensor. The objective is to achieve real-time monitoring of cell culture growing process and matching the sensor values in an attempt to develop a accurate estimation of the number of adhered cells to the electrodes over substrate.

6.2 Growth experiments

On this section the results obtained from the cell culture sensor are presented to illustrate the system performance and present the relevant information which provides the device to the biomedical researchers performing cell culture assays. The experiment time period (T_s) between measurement was set at 1 hour in all cases, which is a parameter that can be adjusted by the biomedical researcher to meet the cell culture assay needs. Measurement evolution proves, that the predicted sensor behaviour is correct, the amplitude and frequency values are increasing with as a result time of the growing cells increasing the fill-factor over the electrodes.

6.2.1 AA8

The cell culture was carried out on a Chinese hamster ovary fibroblast cell line, AA8 (American Type Culture Collection). AA8 cells were cultured in McCoy's medium supplemented with 10% (v/v) foetal calf serum, 2 mM L-glutamine, 50 $\mu g/ml$ streptomycin, and 50 U/ml penicillin. Cells were routinely sub-cultured. The cell line was maintained at 37ºC in a humidified atmosphere with 5% CO_2. They were always in exponential growth phase during the experiments. The sensor recorded battery level information, along with temperature and

relative humidity from inside the cell culture reactor. The values obtained are presented on figure 6.1

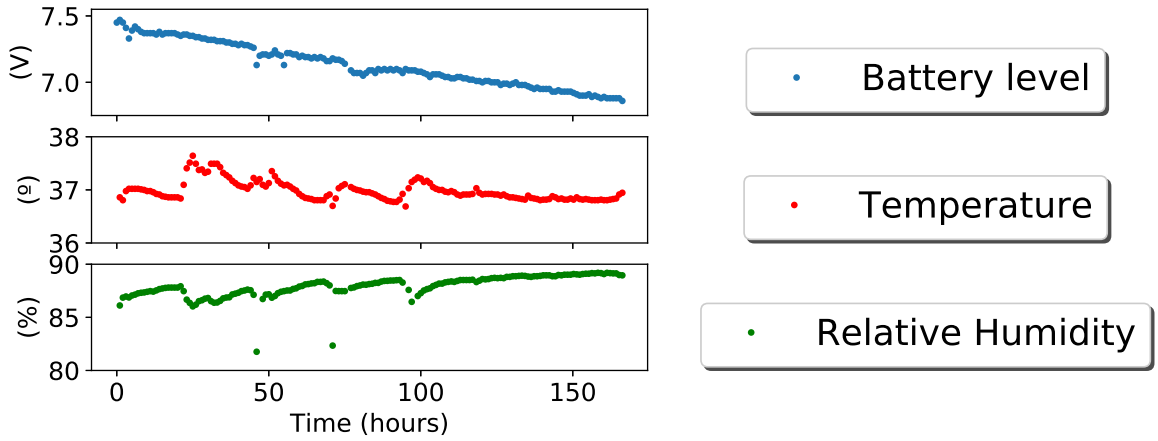

Fig. 6.1 Battery level and environment measurements captured from the sensor device during the AA8 growth experiment performed on the faculty of Biology (US).

The experiment consisted on the growth evolution analysis for the AA8 cell line over the 8W10E PET cultureware [98]. Using this substrate different cells were seeded over the eight wells. Every well was filled with medium and then three different cell densities were added in pairs; 2.5 *k* was added to wells 1 and 3; 5 *k* cells were seeded over wells 4 and 5 and finally 10 *k* cells were deposited over wells 7 and 8. Two wells (2,6), were only filled with medium so they can serve as a measurement control. Figure 6.2 and 6.3 present the sensor measurement acquired for seven days by the prototype.

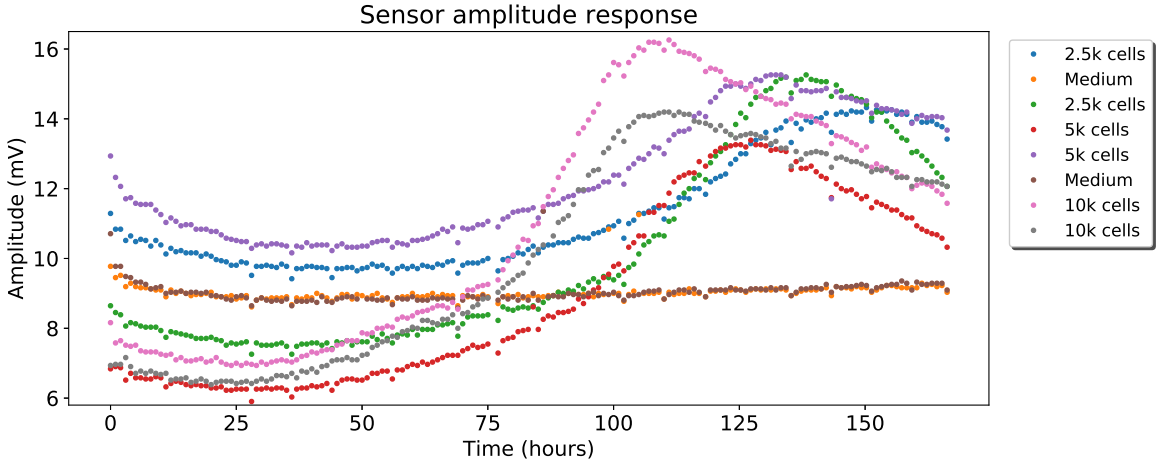

Fig. 6.2 Amplitude levels for the eight different wells captured from the sensor device during the AA8 growth experiment performed on the faculty of Biology (US).

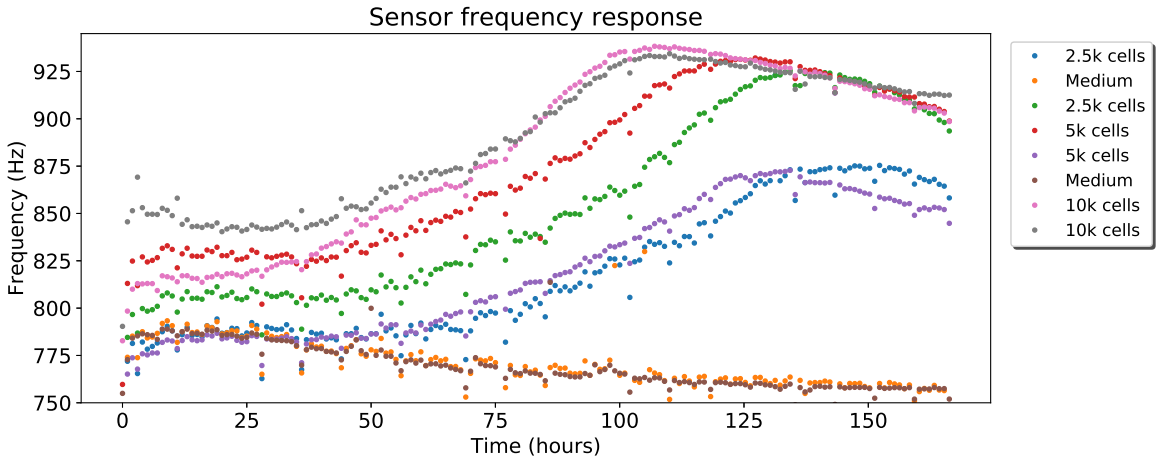

Fig. 6.3 Frequency measurements for the eight different wells captured from the sensor device during the AA8 growth experiment performed on the faculty of Biology (US).

The sampling period (T_s) between measurement was set at 1 hour. Measurement evolution proves that the predicted sensor behaviour is correct, the amplitude and frequency values are increasing with as a result time of the growing cells increasing the fill-factor over the electrodes.

Initially the cells require some time to adhere and start the proliferation process (approximately 24 hours), so, initial measurements on both magnitudes correspond to the empty sensing electrodes. This should lead to equal measurements in every single well in both amplitude and frequency, but that is not the case observed on these results. The initial amplitude and frequency (A_0, F_0) expose a certain dispersion ranging from 780-850 Hz (frequency) and 6-12 mV (amplitude). Moreover, dynamic ranges express a similar behaviour with different values over each well, values for them are presented on table 6.2 and are calculated applying the following equations:

$$ADR = A_{max} - A_{min} \tag{6.1}$$

$$FDR = F_{max} - F_{min} \tag{6.2}$$

Table 6.2 Dynamic ranges for amplitude and frequency

Well	**1**	**3**	**4**	**5**	**7**	**8**
FDR (Hz)	94	114	101	93	123	93
ADR (mV)	4.60	7.65	7.00	4.85	9.19	7.60

Measurement normalization

The frequency and amplitude values acquired by the sensor are proportional to the number of cells deposited over the sensing electrode and the fill-factor. However, to compare frequency and amplitude evolution and evaluate the sensor response over different wells it is necessary to normalize both responses with the normalization equations defined as:

$$A_{nor} = \frac{A(t) - A_{min}}{ADR} \tag{6.3}$$

$$F_{nor} = \frac{F(t) - F_{min}}{FDR} \tag{6.4}$$

The normalized response for both magnitudes is depicted on figures 6.4 and 6.5. On such plots it is possible to visualize the evolution over time of the different cell concentrations seeded over the sensing electrodes. 10 k cell density reach confluence phase ($ff = 1.0$) around 100 hours after seeding time, rest of the cells reach that level some hours later.

The AA8 cells form a circular shape of approximately 10 μm radius, using this value and the fact that the well area is $A_{total} = 0.8cm^2 = 0.8 \cdot 10^8\ \mu m^2$ it is possible to estimate the frequency and amplitude cell sensitivity, S_{Hz} and S_V from the normalized curves attending to the dynamic ranges exposed on table 6.2:

$$S_{Hz} = 0.4\ mHz/cell \tag{6.5}$$

$$S_V = 0.03\ \mu V/cell \tag{6.6}$$

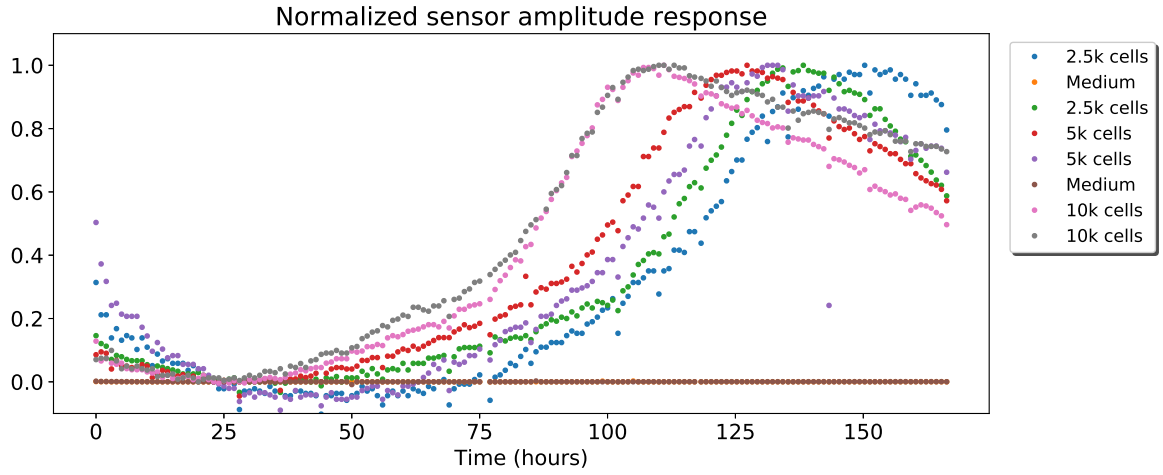

Fig. 6.4 Normalized amplitude levels for the eight different wells captured from the sensor device during the AA8 growth experiment performed on the faculty of Biology (US).

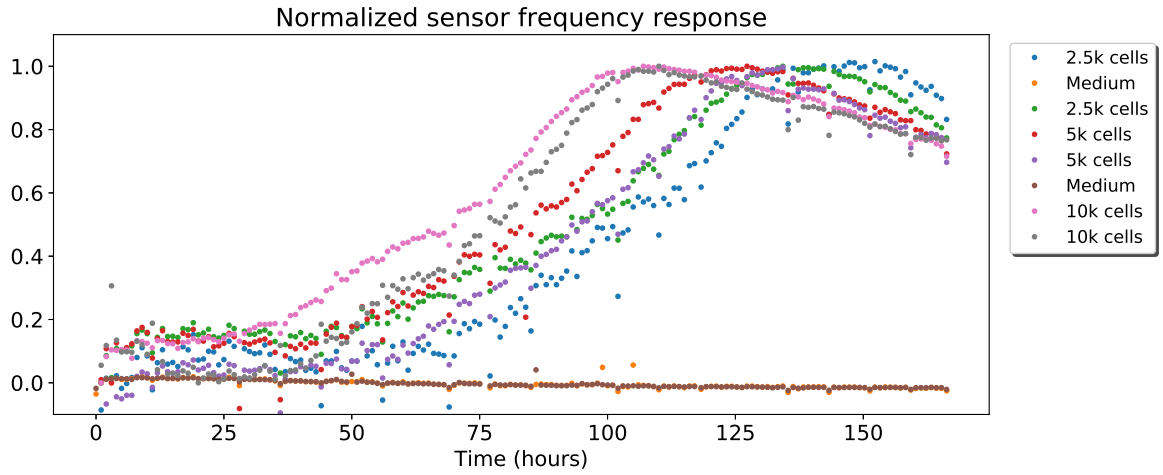

Fig. 6.5 Normalized frequency measurements for the eight different wells captured from the sensor device during the AA8 growth experiment performed on the faculty of Biology (US).

6.2.2 N2A

The second culture assay was performed over Mouse neuroblastoma (N2a) cell line. Cells were cultured in medium consisting of 50% DMEM High glucose (Biowest, Nuaillé, France) and 50% Opti-MEM (Gibco, Alcobendas, Spain) supplemented with 10% (v/v) foetal bovine serum (FBS) (Gibco, Alcobendas, Spain), 2 mM l-glutamine, 50 $\mu g/mL$ streptomycin and 50 U/mL penicillin (Sigma-Aldrich, Madrid, Spain). Cells were routinely sub-cultured. The cell line was maintained at 37ºC in a humidified atmosphere with 5% CO_2. They were always in exponential growth phase during the experiments. The sensor recorded battery level information, along with temperature and relative humidity from inside the cell culture reactor. The values acquired for this assay are presented on figure 6.6

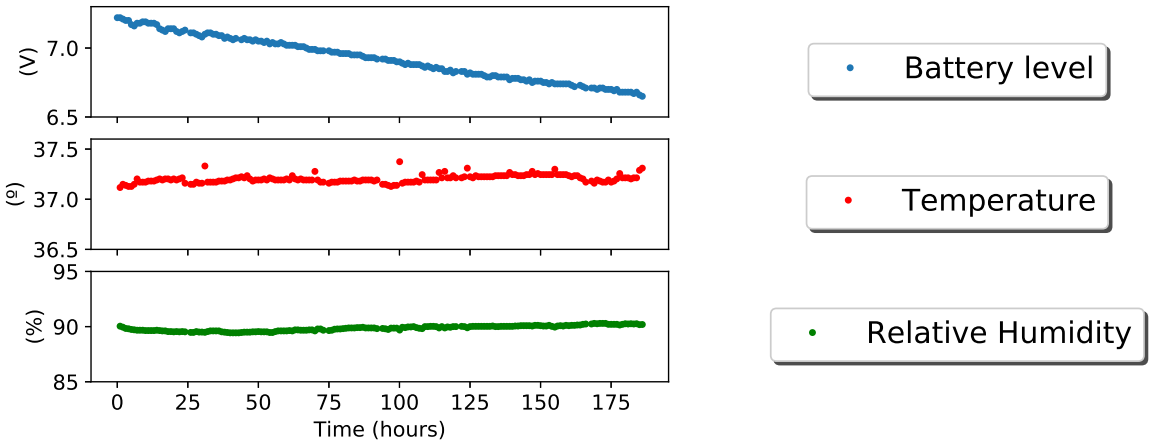

Fig. 6.6 Battery level and environment measurements captured from the sensor device during the N2A1 growth experiment performed on the faculty of Biology (US).

In a similar protocol to the one depicted over the first assay, this experiment consisted on the growth evolution analysis for the N2A cell line over the 8W10E PET cultureware. Different cell densities were seeded over the eight wells. Every well was filled with medium and then three different cell densities were added in pairs; 2.5 *k* was added to wells 2 and 6; 5 *k* cells were seeded over wells 3 and 7 and finally 10 *k* cells were deposited over wells 4 and 8. Two wells (1,5), were only filled with medium so they can serve as a measurement control. Figure 6.7 and 6.8 present the sensor measurement acquired for seven days by the prototype.

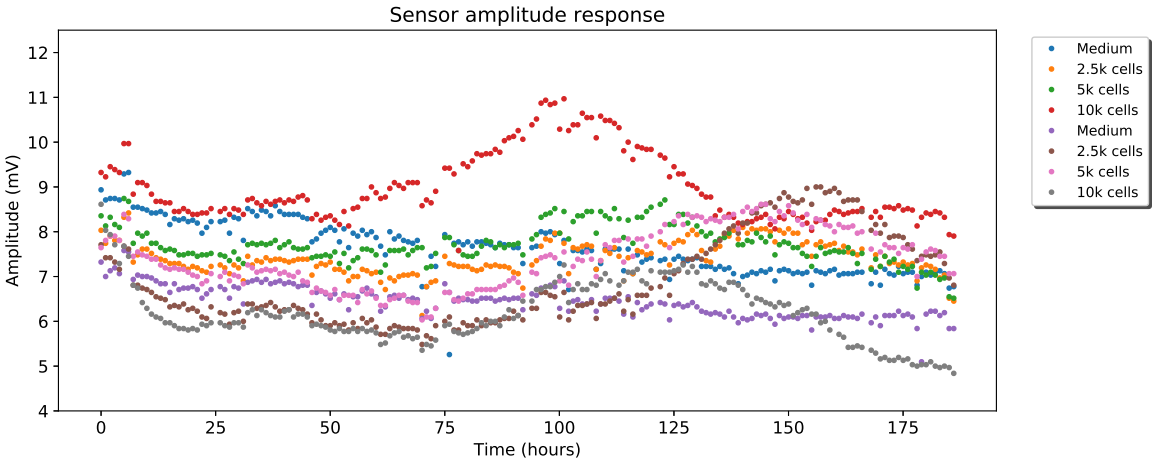

Fig. 6.7 Amplitude levels for the eight different wells captured from the sensor device during the N2A growth experiment performed on the faculty of Biology (US).

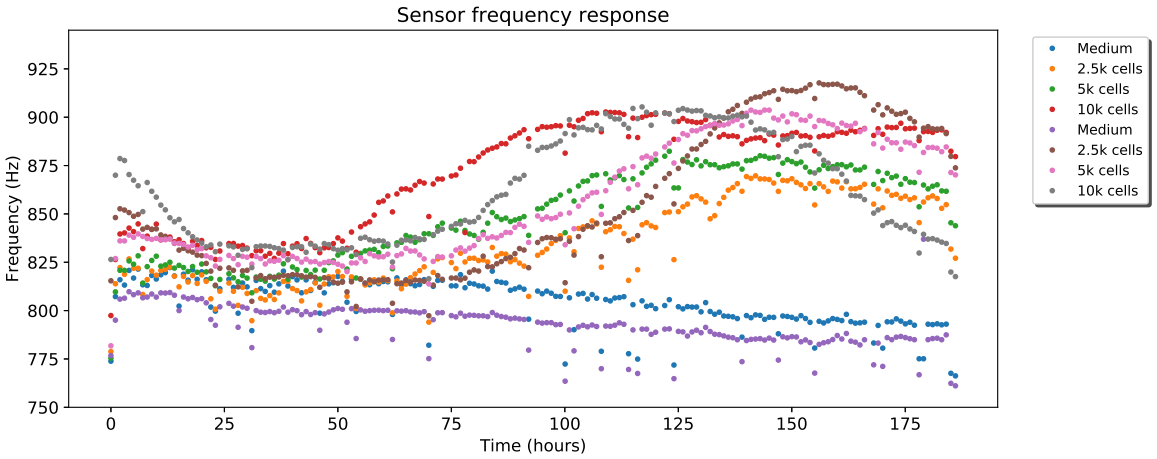

Fig. 6.8 Frequency measurements for the eight different wells captured from the sensor device during the N2A growth experiment performed on the faculty of Biology (US).

Again, the cells require some time to adhere and start the proliferation process. On these curves it is possible to observe identical dispersion effect as the one described on the previous assay. The initial amplitude and frequency (A_0, F_0) expose a dispersion ranging from 800-875 Hz (frequency) and 7-10 mV (amplitude). Moreover, dynamic ranges express a similar behaviour with different values over each well, values for them are presented on table 6.3 and are calculated applying the following equations (6.1) and (6.2).

Table 6.3 Dynamic ranges for amplitude and frequency

Well	**2**	**3**	**4**	**6**	**7**	**8**
FDR (Hz)	68.9	72.7	76.3	104.6	80.6	74.9
ADR (mV)	1.32	1.30	2.58	2.93	1.77	2.80

Measurement normalization

The frequency and amplitude values acquired by the sensor are proportional to the number of cells deposited over the sensing electrode and the fill-factor. However, to compare frequency and amplitude evolution and evaluate the sensor response over different wells it is necessary to normalize both responses with the normalization equations defined previously on (6.3) and (6.4).

Applying the calculations generates normalized response for both magnitudes which are illustrated on figures 6.9 and 6.10. On such plots it is possible to visualize the evolution over time of the different cell concentrations seeded over the sensing electrodes. 10 k cell density reach confluence phase ($ff = 1.0$) around 100 hours after seeding time, rest of the cells reach that level some hours later.

Using the dynamic ranges computed before and knowing the well area, again for this cell line it is possible to compute the sensitivity per cell of the implemented sensor. Considering a cell size of 300 μm^2, cell sensitivity for the N2A line would be:

$$S_{Hz} = 0.12\ mHz/cell \tag{6.7}$$

$$S_V = 0.003\ \mu V/cell \tag{6.8}$$

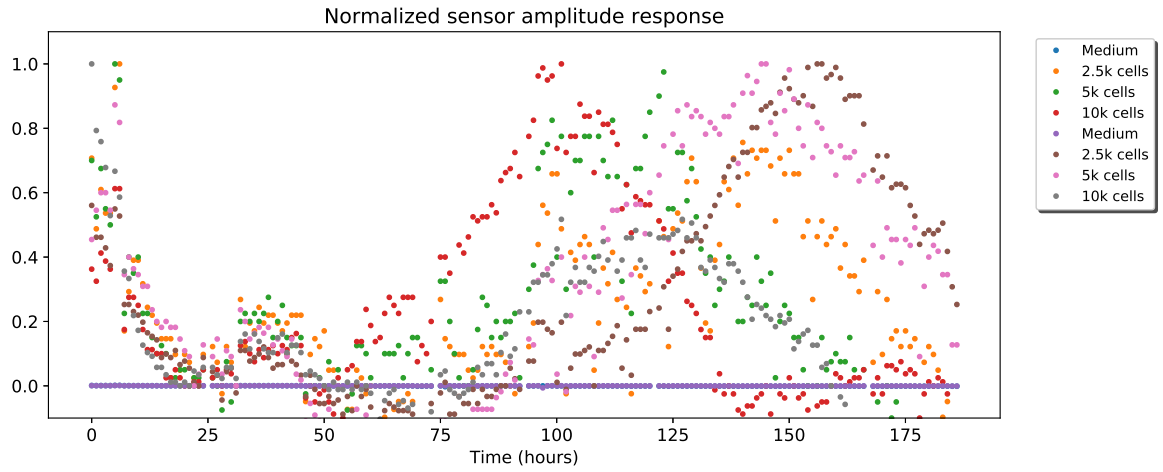

Fig. 6.9 Normalized amplitude levels for the eight different wells captured from the sensor device during the N2A growth experiment performed on the faculty of Biology (US).

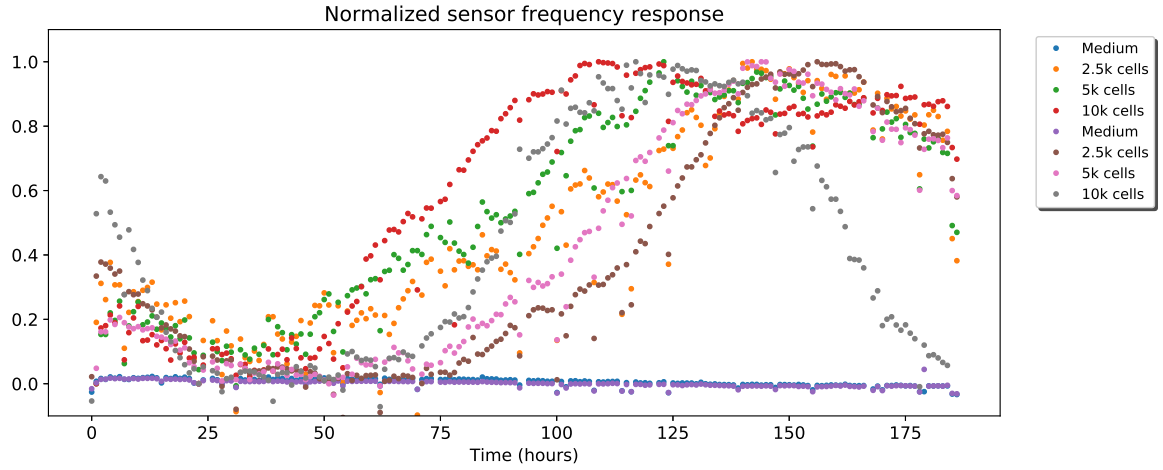

Fig. 6.10 Normalized frequency measurements for the eight different wells captured from the sensor device during the N2A growth experiment performed on the faculty of Biology (US).

6.2.3 N2A APP

Third culture assay was performed over Mouse neuroblastoma expressing wildtype human amyloid precursor protein (N2A-App) cell line. Cells were cultured in medium consisting of 50% DMEM High glucose (Biowest, Nuaillé, France) and 50% Opti-MEM (Gibco, Alcobendas, Spain) supplemented with 10% (v/v) foetal bovine serum (FBS) (Gibco, Alcobendas, Spain), 2 mM l-glutamine, 50 $\mu g/mL$ streptomycin, 50 U/mL penicillin (Sigma-Aldrich, Madrid, Spain) and 0.4% Geneticin (Gibco, Alcobendas, Spain). Cells were routinely subcultured. The cell line was maintained at 37ºC in a humidified atmosphere with 5% CO_2. They were always in exponential growth phase during the experiments. The sensor recorded

battery level information, along with temperature and relative humidity from inside the cell culture reactor. The values acquired for this assay are presented on figure 6.11

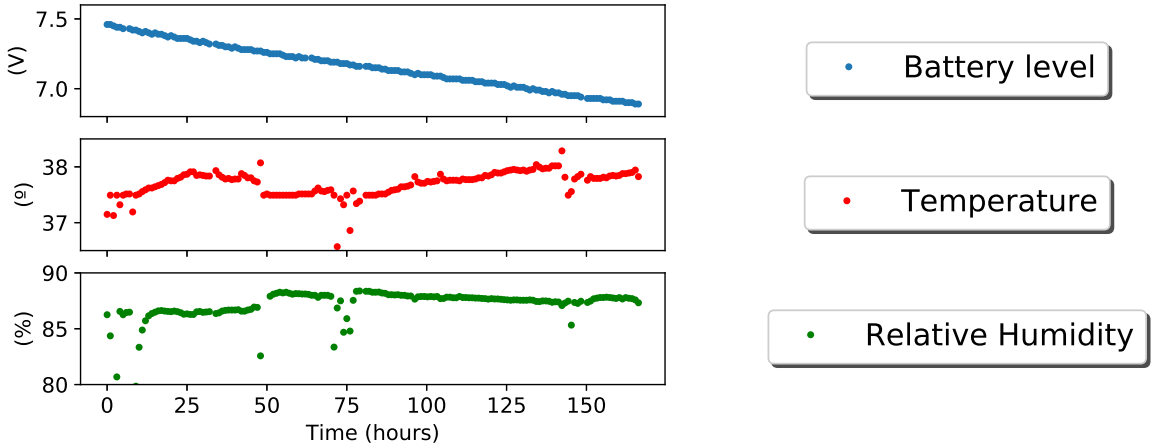

Fig. 6.11 Battery level and environment measurements captured from the sensor device during the N2A APP growth experiment performed on the faculty of Biology (US).

In a similar protocol to the one depicted over the first assay, this experiment consisted on the growth evolution analysis for the N2A cell line over the 8W10E PET cultureware. The seed pattern was identical to the second assay. Figure 6.12 and 6.13 present the sensor measurement acquired for seven days by the prototype.

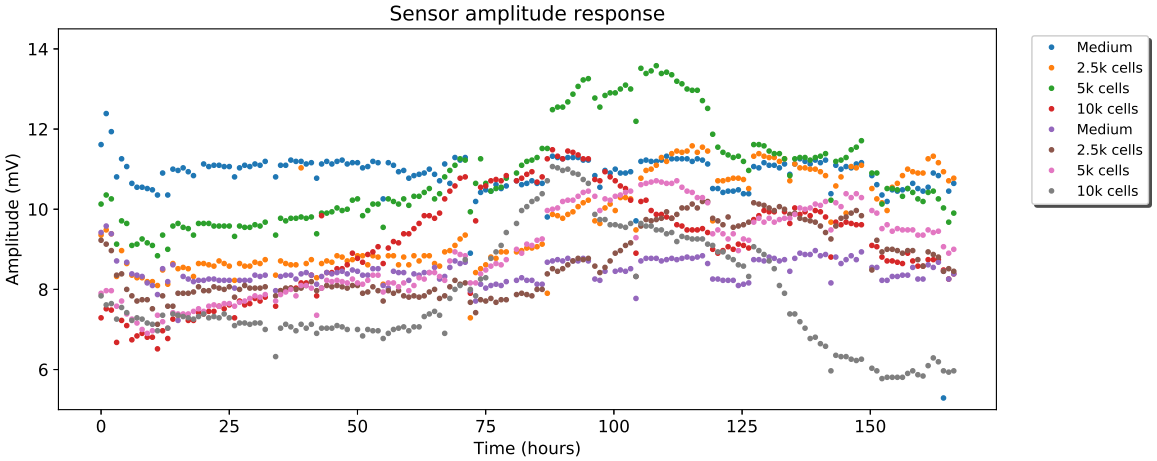

Fig. 6.12 Amplitude levels for the eight different wells captured from the sensor device during the N2A APP growth experiment performed on the faculty of Biology (US).

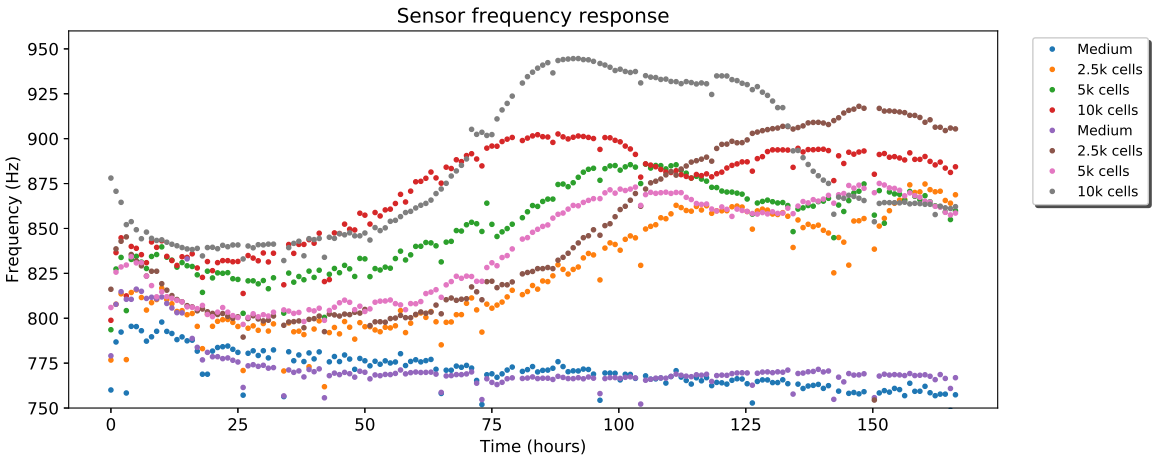

Fig. 6.13 Frequency measurements for the eight different wells captured from the sensor device during the N2A APP growth experiment performed on the faculty of Biology (US).

Again, the cells require some time to adhere and start the proliferation process. On these curves it is possible to observe identical dispersion effect as the one described on the previous assay. The initial amplitude and frequency (A_0, F_0) expose a dispersion ranging from 790-875 Hz (frequency) and 7-12 mV (amplitude). Moreover, dynamic ranges express a similar behaviour with different values over each well, values for them are presented on table 6.4 and are calculated applying the following equations (6.1) and (6.2).

Table 6.4 Dynamic ranges for amplitude and frequency

Well	**2**	**3**	**4**	**6**	**7**	**8**
FDR (Hz)	97.8	81.55	90.16	117.0	74.2	110.0
ADR (mV)	3.48	4.74	5.00	3.06	3.80	4.10

Measurement normalization

The frequency and amplitude values acquired by the sensor are proportional to the number of cells deposited over the sensing electrode and the fill-factor. However, to compare frequency and amplitude evolution and evaluate the sensor response over different wells it is necessary to normalize both responses with the normalization equations defined previously on (6.3) and (6.4).

Applying the calculations generates normalized response for both magnitudes which are illustrated on figures 6.14 and 6.15. On such plots it is possible to visualize the evolution over time of the different cell concentrations seeded over the sensing electrodes. 10 k cell density reach confluence phase ($ff = 1.0$) around 100 hours after seeding time, rest of the cells reach that level some hours later.

Using the dynamic ranges computed before and knowing the well area, again for this cell line it is possible to compute the sensitivity per cell of the implemented sensor. Considering a cell size of 184 μm^2 cell sensitivity for the N2A line would be:

$$S_{Hz} = 0.22\ mHz/cell \tag{6.9}$$

$$S_V = 0.0093\ \mu V/cell \tag{6.10}$$

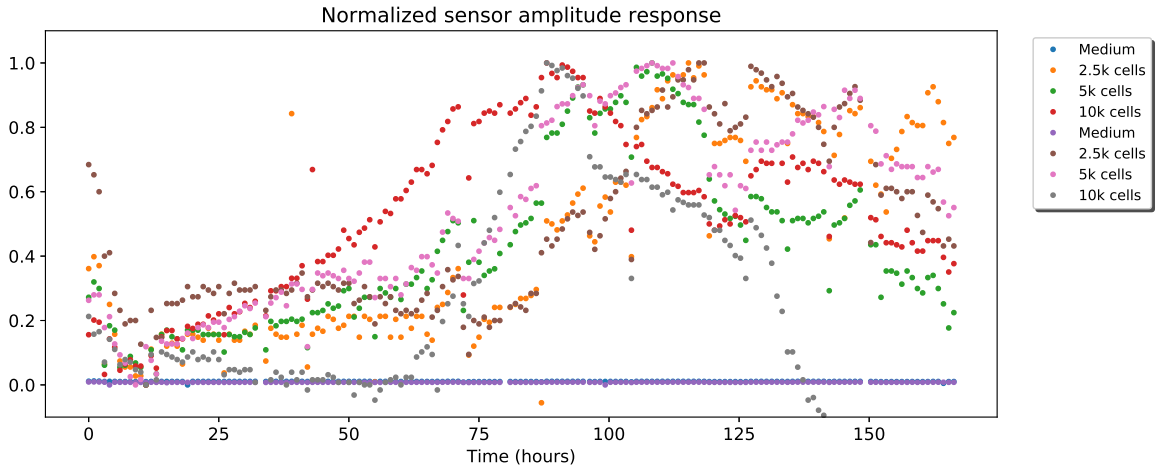

Fig. 6.14 Normalized amplitude levels for the eight different wells captured from the sensor device during the N2A APP growth experiment performed on the faculty of Biology (US).

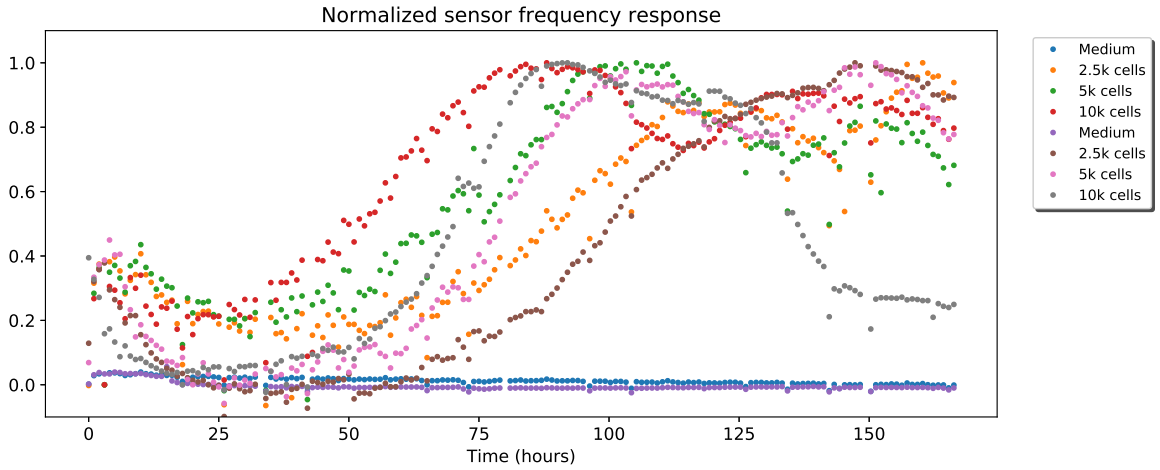

Fig. 6.15 Normalized frequency measurements for the eight different wells captured from the sensor device during the N2A APP growth experiment performed on the faculty of Biology (US).

6.2.4 Data analysis

The results presented on this chapter are consistent with the expected ranges predicted on chapter 3. Those predictions are dependant on the bio-OBT circuit design and mostly on the electrical interface developed on the electrode cell culture frontier. This model was validated by acquiring experimental measurements from a prototype interface and a cell culture assay prepared for this purpose. This measurements and the model matching process was exposed on the final part of chapter 2. derived from the models exposed on the same chapter.

The curves presented on this chapter, validate the sensor design and reports sensitivity over cellular evolution on top of the electrode as predicted by the models. The electrodes were seeded with different levels of cell density. These are expected to reach the confluent phase ordered in time by the cell amount deposited on the well. Despite this, similar densities not always describe similar sensor curves. Recalling from chapter 2, electrode geometry plays an important role in sensing the cells over the substrate, it is possible that cells are growing outside the electrode. Relevant information on these curves is the confluent phase event, which is perfectly correlated to the cell density in every single experiment reported.

Despite the sensor response to the cell culture evolution in time over the electrodes, there is a limitation spotted in the results presented. Initial frequencies, initial amplitudes, and both dynamic ranges suffer from a certain dispersion level. This dispersion may arise from the physical differences on the electrodes which affect the electrical behaviour and result on an impedance variation over the electrodes which are on the signal path, thus affecting the final measurement. This issue limits the system capability to predict the fill-factor ff from sensor curves with accuracy and hence estimate the cell number in real-time.

The electrode-interface contribution was modelled on chapter 2 using R_{ct}, C_{dl} and R_s passive values. Assuming the measurement dispersion is produced by electrode differences, this would translate on variations across the electrical model presented on chapter 2, this is:

$$R'_{ct} = R_{ct} + \Delta R \tag{6.11}$$

$$C'_{dl} = C_{dl} + \Delta C \tag{6.12}$$

$$R'_{s} = R_{s} + \Delta R_{s} \tag{6.13}$$

R_{ct}, C_{dl} and R_s are sufficient to describe the electrical model for an uncovered electrode immersed on an ionic solution. Precise determination of their is crucial to recover ff values since these parameters greatly affect the sensor curves. However not all of them affects the

electrical model (figure 1.10) and thus the measurement in the same way, R_{ct} value along with C_{dl} affect a low frequency pole on the electrical response of the electrode interface system. The operation point is located near a zero which value is governed by both C_{dl} and R_s. This zero value which will affect most the initial frequency and amplitude of the system since it is located near the operation point.

Estimation of such values can be performed by the application of a k-Nearest neighbors (KNN) algorithm over the bio-OBT model [138]. To create the training dataset, variations over R_{ct}, C_{dl} and R_s are performed, so that points are generated for both initial ($ff = 0.01$) frequency and amplitude over the whole parameter ranges. Reasonable ranges were established to such parameters according to the model described previously on chapter 2, and those are depicted on table 6.5. Resulting dataset are presented on figures 6.16 (a) and (b). Values for R_{ct} are considered too, but the influence over the operating point is not relevant so R_s and C_{dl} are illustrated over the plots presented.

Table 6.5 Ranges for passive elements on the electrode model.

$[R_{ct}]$ ($M\Omega$)	$[C_{dl}]$ (**nF**)	$[R_s]$ (Ω)
0.6-2.6	16-64	250-1000

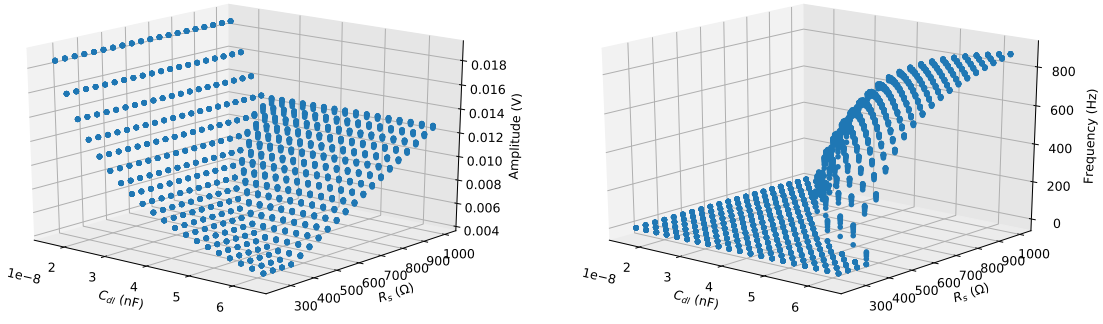

(a) (b)

Fig. 6.16 (a) Amplitude (b) frequency datasets for the variation across the electrical parameters (C_{dl} and R_s).

The system is then trained using the generated dataset and electrical response can be adapted to every single well by estimating the initial passive values for the electrical model. To evaluate this approach the experiment results will be analyzed using this algorithm.

AA8 growth assay

The output of the system for the AA8 cells is described on table 6.6, where the best fitting values for R_ct, C_dl and R_s are obtained for the eight wells. Selected $R_{gap} = 600\ \Omega$ for this cell line.

Table 6.6 Electrical model values obtained from the KNN classifier for the AA8 cells.

Well	R_{ct} $(M\Omega)$	C_{dl} **(nF)**	R_s (Ω)
1	0.82	46.3	1000
2	1.71	51.3	920
3	1.04	64.0	760
4	0.6	58.9	880
5	0.6	58.9	800
6	1.04	48.8	1000
7	2.6	58.9	880
8	0.6	58.9	1000

On figure 6.17 the predicted values over the sensor frequency evolution curves are plotted as red lines identifying predicted maximum and minimum values. Frequency values are reasonably contained within the predicted ranges in most of the wells. The values along with the dynamic ranges are presented on table 6.7. The relative error in the frequency dynamic range (δ FDR (%)) is under 10% for all cases except for well 1 which value is 12.5 %.

Along with the frequency results, the curves depicted on figure 6.18 illustrates the amplitude sensor response with the predicted ranges as red lines over the plot. The amplitude values are totally out of range with respect to the prediction, however ranges seem to be correct. There is a certain offset value which separates prediction and experimental values. If such offset is compensated the resulting ranges fit much better the amplitude ranges as is illustrated on figure 6.19. The actual values are presented on table 6.8, the relative error in the amplitude dynamic range is significantly higher, which might be due to the offset factor along with a gain factor derived from the circuit implementation.

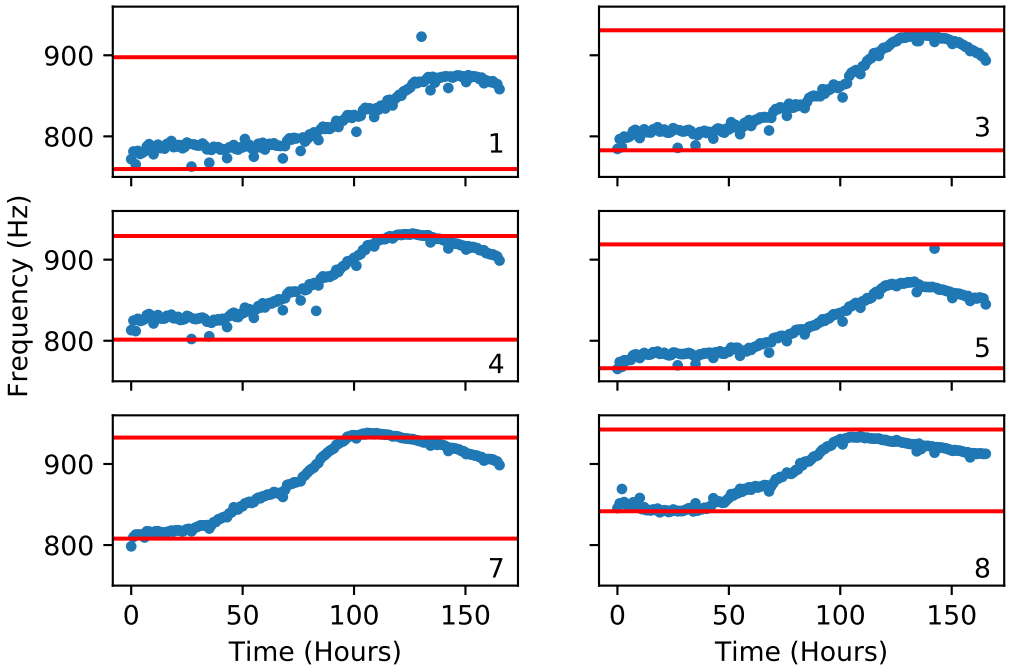

Fig. 6.17 Frequency predicted ranges for each of the seeded well. Range prediction is depicted as a red line. AA8 cell line.

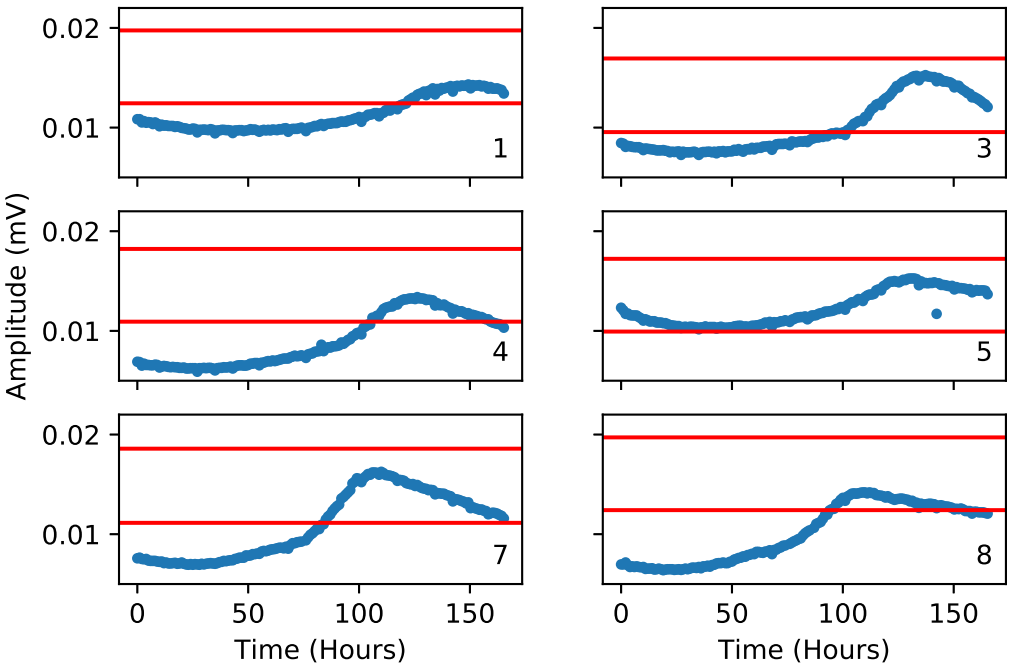

Fig. 6.18 Amplitude predicted ranges for each of the seeded well. Range prediction is depicted as a red line. AA8 cell line.

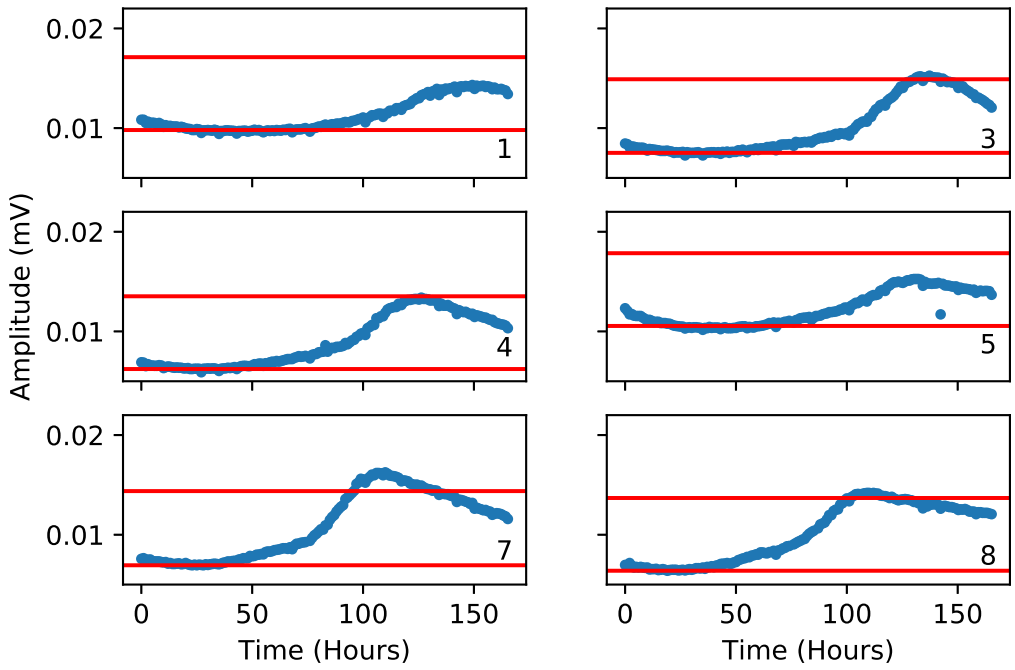

Fig. 6.19 Amplitude corrected ranges for each of the seeded well. Range prediction is depicted as a red line. AA8 cell line.

Table 6.7 AA8 cell line. Frequency prediction vs experimental and dynamic ranges over the wells. δFDR represents the relative error between the experimental range and the model predicted range.

	Theoretical			**Experimental**			
Well	f_{min} (Hz)	f_{max} (Hz)	FDR	f_{min} (Hz)	f_{max} (Hz)	FDR	δFDR (%)
1	759.7	897.6	137.9	765.4	923.0	157.6	12.5
2	772.6	911.0	138.4	773.8	829.9	56.1	empty
3	782.8	930.8	148.0	786.8	925.4	138.6	6.8
4	801.3	929.1	127.8	811.9	932.1	120.2	6.3
5	766.1	918.8	152.7	767.8	913.6	145.8	4.7
6	782.5	909.8	127.3	783.5	813.6	30.1	empty
7	808.0	932.6	124.6	809.3	938.3	129.0	3.4
8	841.7	942.5	100.8	840.4	934.4	94.0	7.2

N2A growth assay

A second study was conducted using cells from the N2A cell line. The algorithm returned the values presented on table 6.9 for the N2A cell line using the initial frequency from the experimental measurements. Selected $R_{gap} = 400\ \Omega$ for this cell line.

Table 6.8 AA8 cell line. Amplitude prediction vs experimental and dynamic ranges over the wells. δADR represents the relative error between the experimental range and the model predicted range.

	Theoretical			**Experimental**			
Well	a_{min} (mV)	a_{max} (mV)	ADR	a_{min} (mV)	a_{max} (mV)	ADR	δADR (%)
1	12.4	19.7	7.3	9.8	14.3	4.5	62.2
2	11.6	19.0	7.4	8.9	11.3	2.4	empty
3	9.5	16.9	7.4	7.5	15.3	7.8	5.1
4	10.9	18.2	7.3	6.2	13.4	7.2	1.4
5	9.9	17.2	7.3	10.5	15.3	4.8	52.1
6	12.5	19.9	7.5	8.8	11.4	2.6	empty
7	11.1	18.6	7.5	6.9	16.3	9.4	20.2
8	12.4	19.7	7.3	6.4	14.2	7.8	6.4

Prediction results for this cell line are less significant on both magnitudes frequency (table 6.10) and amplitude (table 6.11). The relative error in the frequency dynamic range (δ FDR (%)) is under 15% for all cases except for well 6 which value is 22.2 %. Amplitude results (after an offset correction similar to the one applied to AA8 cell line) show a relative error over the amplitude dynamic range significantly higher.Selected $R_{gap} = 400\ \Omega$ for this cell line.Selected $R_{gap} = 300\ \Omega$ for this cell line.

Table 6.9 Electrical model values obtained from the KNN classifier for the N2A cells.

Well	R_{ct} $(M\Omega)$	C_{dl} **(nF)**	R_s (Ω)
1	1.9	51.3	960
2	2.6	56.4	880
3	2.6	58.9	880
4	0.6	58.9	920
5	0.6	64.0	760
6	1.0	64.0	800
7	2.6	58.9	920
8	2.4	56.4	960

N2A APP growth assay

Final growth study was performed using cells from the N2A APP cell line. The algorithm returned the values presented on table 6.12 for the N2A APP cell line using the initial frequency from the experimental measurements. Selected $R_{gap} = 300\ \Omega$ for this cell line.

Table 6.10 N2A cell line. Frequency prediction vs experimental and dynamic ranges over the wells. δFDR represents the relative error between the experimental range and the model predicted range.

	Theoretical			**Experimental**			
Well	f_{min} (Hz)	f_{max} (Hz)	FDR	f_{min} (Hz)	f_{max} (Hz)	FDR	δFDR (%)
1	789.0	869.8	80.8	789.6	822.3	32.7	empty
2	792.8	877.7	84.9	794.8	869.7	74.9	13.4
3	807.9	887.9	80.0	809.2	882.4	73.2	9.3
4	816.2	891.1	74.9	826.4	902.7	76.3	1.8
5	779.1	878.0	98.9	780.8	836.9	56.1	empty
6	801.2	889.0	87.8	804.8	917.7	112.9	22.2
7	822.4	895.4	73.0	823.0	903.7	80.7	9.5
8	821.9	892.8	70.9	822.2	905.3	83.1	14.7

Table 6.11 N2A cell line. Amplitude prediction vs experimental and dynamic ranges over the wells. δADR represents the relative error between the experimental range and the model predicted range.

	Theoretical			**Experimental**			
Well	a_{min} (mV)	a_{max} (mV)	ADR	a_{min} (mV)	a_{max} (mV)	ADR	δADR (%)
1	12.1	15.8	3.7	7.8	9.3	1.5	empty
2	11.1	14.9	3.8	6.9	8.4	1.5	153.3
3	11.1	14.9	3.8	7.3	8.7	1.4	171.4
4	11.4	15.1	3.7	8.4	11.0	2.6	42.3
5	9.5	13.1	3.6	6.4	7.6	1.2	empty
6	10.0	13.7	3.7	5.9	9.0	3.1	19.4
7	11.6	15.4	3.8	6.8	8.6	1.8	111.1
8	12.1	15.9	3.8	5.8	8.0	2.2	72.7

Prediction results for this cell line are less significant on both magnitudes frequency (table 6.13) and amplitude (table 6.14). The relative error in the frequency dynamic range (δ FDR (%)) is under 20% for all cases except for well 8 which value is 25.8 %. Despite amplitude results (after an offset correction similar to the one applied to AA8 and N2A cell line) show a relative error over the amplitude dynamic range significantly higher some of the well perform under 5% (3, 4, and 8),

Table 6.12 Electrical model values obtained from the KNN classifier for the N2A APP cells.

Well	R_{ct} ($M\Omega$)	C_{dl} **(nF)**	R_s (Ω)
1	0.6	46.3	1000
2	1.9	48.8	960
3	0.8	53.8	960
4	0.6	53.8	1000
5	1.9	51.3	880
6	1.5	61.4	800
7	0.6	51.3	1000
8	0.8	58.9	960

Table 6.13 N2A APP cell line. Frequency prediction vs experimental and dynamic ranges over the wells. δFDR represents the relative error between the experimental range and the model predicted range.

	Theoretical			**Experimental**			
Well	f_{min} (Hz)	f_{max} (Hz)	FDR	f_{min} (Hz)	f_{max} (Hz)	FDR	δFDR (%)
1	756.2	864.4	108.2	756.4	797.9	41.5	empty
2	770.0	876.0	106.0	770.6	874.8	104.2	1.7
3	801.8	896.0	94.2	802.7	885.8	83.1	13.4
4	813.1	900.7	87.6	812.4	902.6	90.2	2.9
5	755.3	873.4	118.1	756.8	833.1	76.3	empty
6	787.8	899.6	111.8	789.5	918.0	128.5	13.0
7	796.4	890.0	93.6	796.6	875.1	78.5	19.2
8	831.6	915.1	83.5	832.1	944.6	112.5	25.8

6.2.5 Biological measurements

The cell culture assays performed to evaluate the performance of the system were associated in parallel with a set of assays which the biomedical researcher team processed and counted on the microscope. This section will illustrate and compare traditional counting method with the real-time estimation performed by the prototype system developed on this project.

The sensor output as depicted on previous section is a fill-factor estimation, however since the biomedical researchers do operate on petri dishes and the quantization process returns a number of cell per square centimeter, it is mandatory to estimate the cell number from the sensor system. Assuming area of culture cell is A_{cell}, the total number of cells with respect to fill factor (ff) is defined as:

Table 6.14 N2A APP cell line. Amplitude prediction vs experimental and dynamic ranges over the wells. δADR represents the relative error between the experimental range and the model predicted range.

	Theoretical			**Experimental**			
Well	a_{min} (mV)	a_{max} (mV)	ADR	a_{min} (mV)	a_{max} (mV)	ADR	δADR (%)
1	12.3	17.2	4.9	0.3	12.4	12.1	empty
2	12.1	17.1	5.0	8.1	11.6	3.5	42.9
3	12.0	16.9	4.9	8.8	13.6	4.8	2.1
4	12.4	17.2	4.8	6.5	11.5	5.0	4.0
5	11.1	16.0	4.9	0.3	9.6	9.3	empty
6	10.1	15.0	4.9	7.1	10.2	3.1	58.1
7	12.4	17.2	4.8	6.9	10.7	3.8	26.3
8	12.0	16.9	4.9	6.3	11.1	4.8	2.1

$$n = ff * \frac{a_{sensor}}{a_{cell}} \tag{6.14}$$

where $a_{sensor} = 0.8\ cm^2$ corresponds to the well area. The value n represent the total number of cells over the sensing area. From there, the following equation leads to cell number per unit area:

$$n_{cells} = \frac{n}{a_{sensor}} cells/cm^2 \tag{6.15}$$

Three different cell densities corresponding to $2.5\ k/0.8\ cm^2$, $5\ k/0.8\ cm^2$ and $10\ k/0.8\ cm^2$ were seeded in the different assays (AA8, N2A and N2A APP). Following pages illustrates the comparison between biomedical researchers traditional counting and sensor values. Cell areas employed were presented on table 6.1. Methodology is exactly the same from previous section (electrical parameters estimation and R_{gap} values).

AA8 cell line

Figure 6.20 presents the resulting values from both, the sensor and traditional counting method for the lowest, mid, and higher initial density values respectively.

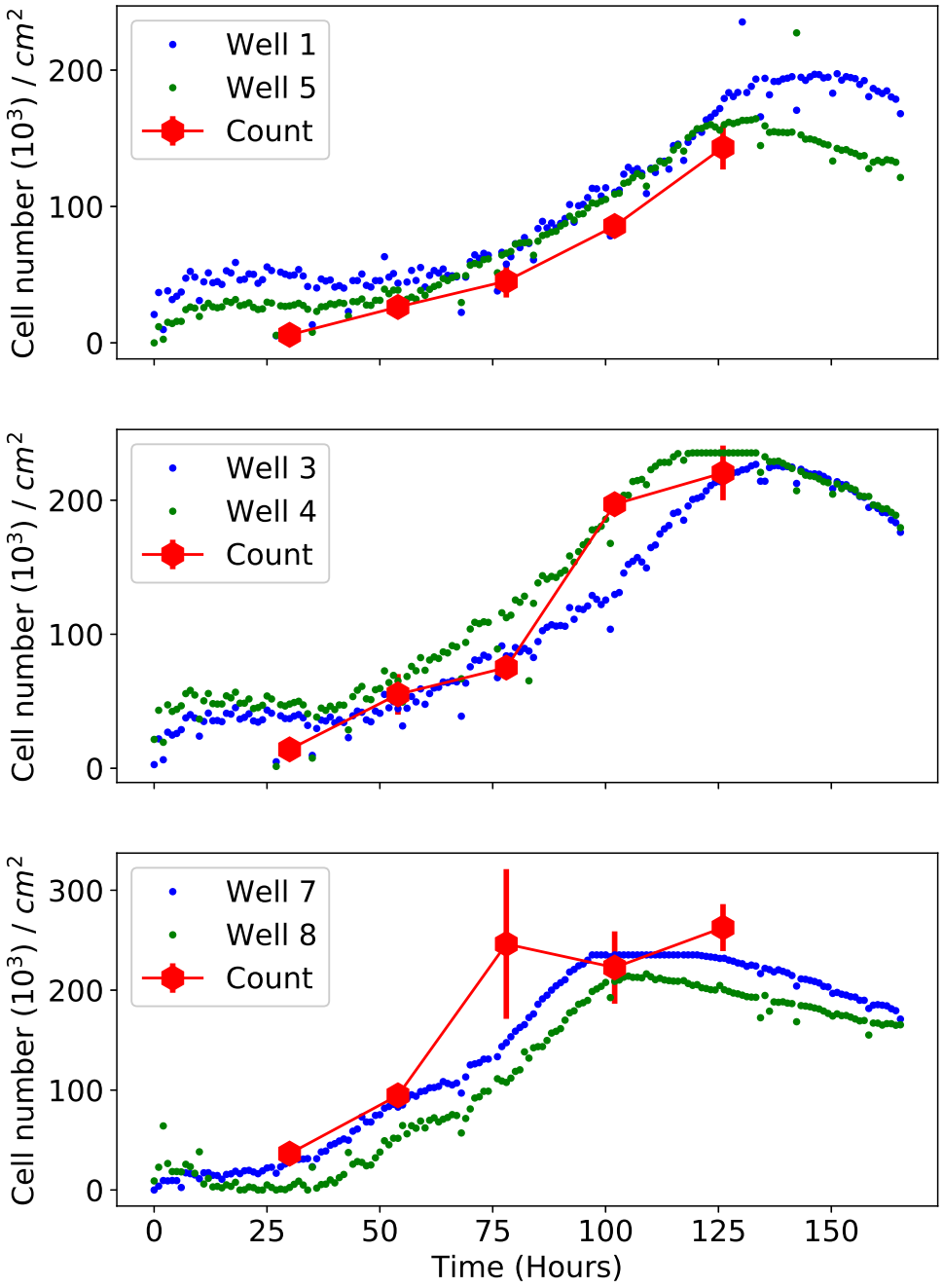

Fig. 6.20 Predicted cell density (cells/cm^2) evolution over time. Cell amount seeded was 2.5 k on wells 1 and 5, 5 k on wells 3 and 4 and 10 k on wells 7 and 8. Comparable cell densities was seeded over the control substrates.

N2A cell line

Figure 6.21 presents the resulting values from both, the sensor and traditional counting method for the lowest, mid, and higher initial density values respectively.

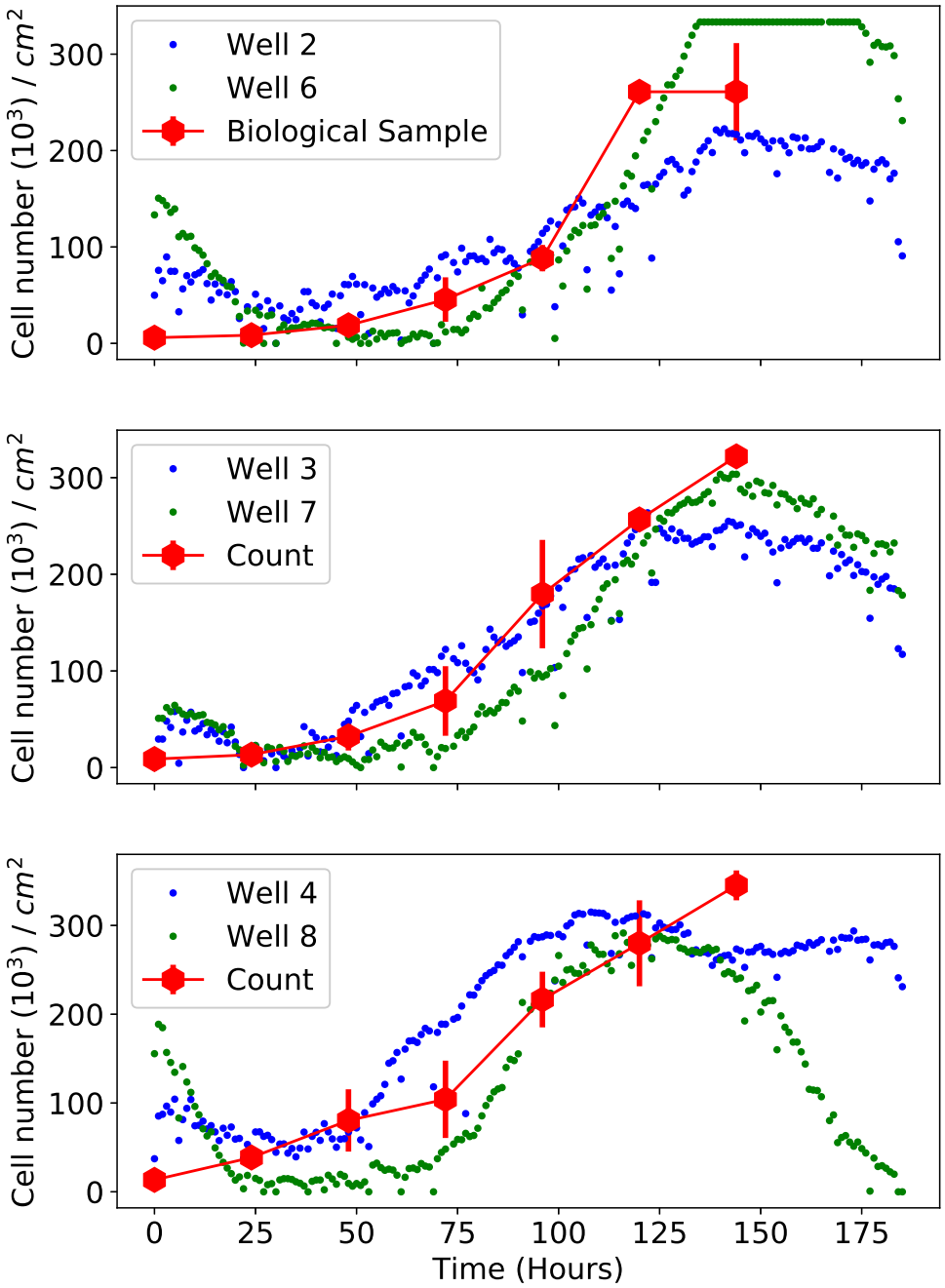

Fig. 6.21 Predicted cell density (cells/cm^2) evolution over time. Cell amount seeded was 2.5 k on wells 2 and 6, 5 k on wells 3 and 7 and 10 k on wells 4 and 8. Comparable cell densities was seeded over the control substrates.

N2A APP cell line

Figure 6.22 presents the resulting values from both, the sensor and traditional counting method for the lowest, mid, and higher initial density values respectively.

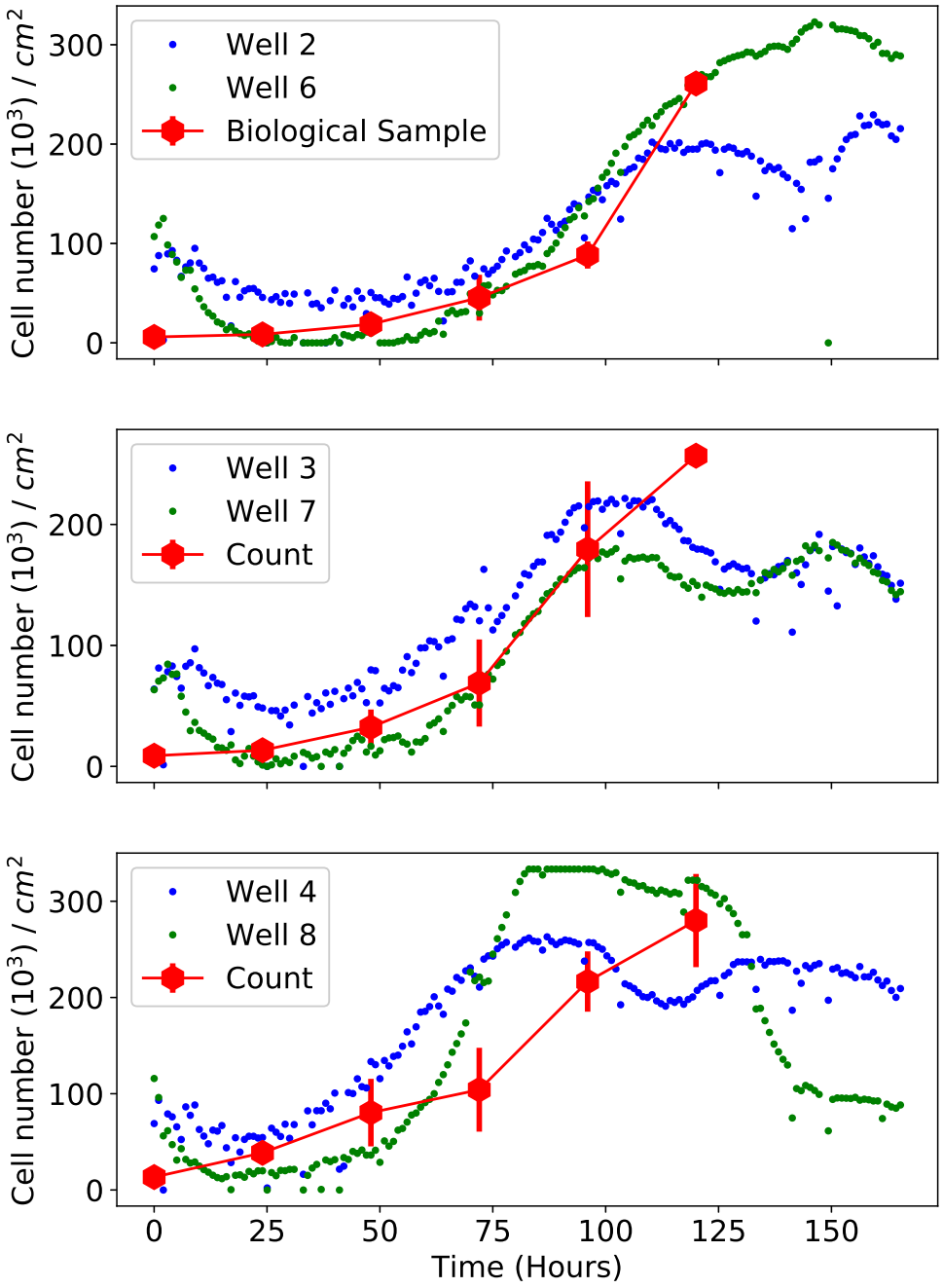

Fig. 6.22 Predicted cell density (cells/cm^2) evolution over time. Cell amount seeded was 2.5 k on wells 2 and 6, 5 k on wells 3 and 7 and 10 k on wells 4 and 8. Comparable cell densities was seeded over the control substrates.

6.3 Cell differentiation

Previous section presented the results obtained from three different cell growth experiments using different cell lines (AA8, N2A and N2A APP). These experiments illustrated the sensitivity of the sensor developed to growth over the cell culture substrate and fill factor estimation performance applying a simple algorithmic approach based on a big dataset of simulated responses and machine learning processing to estimate the values that correspond to the initial frequency and amplitude.

In this section, a different experiment was planned to analyze the sensor response while performing a cell culture assay over Rat skeletal myoblasts. The cells were obtained from Rattus Norvegicus L6 cell line (American Type Cell Culture CRL-1458) and were cultured at 37ºC in a CO_2 incubator at 5% on the Seville Bio-medicine Institute (IBIS). The growth medium used was Minimum Essential Medium α (12571-063, Gibco) supplemented with 10% fetal bovine serum (F7524, Sigma) and 1% penicillin-streptomycin (15140-122, Gibco). The cells were routinely sub-cultured using trypsin-EDTA at 0.05% (25300-062, Gibco). A cell amount of 10^4 was seeded in the appropriate wells of the 8W10E cultureware with growth medium. On approximate 70% of occupation level cells were rinsed with phosphate buffered saline (L0615, Linus) and the medium was changed to differentiation medium in some of them, MEMα supplemented with 2% horse serum (S0910, Biowest) and 17.8 mM NaHCO3 (S6297, Sigma-Aldrich). Figure 6.23 represents (a) non-differentiated cells (b) differentiated cells. Figures 6.24 and 6.25 illustrate sensor response on this experiment.

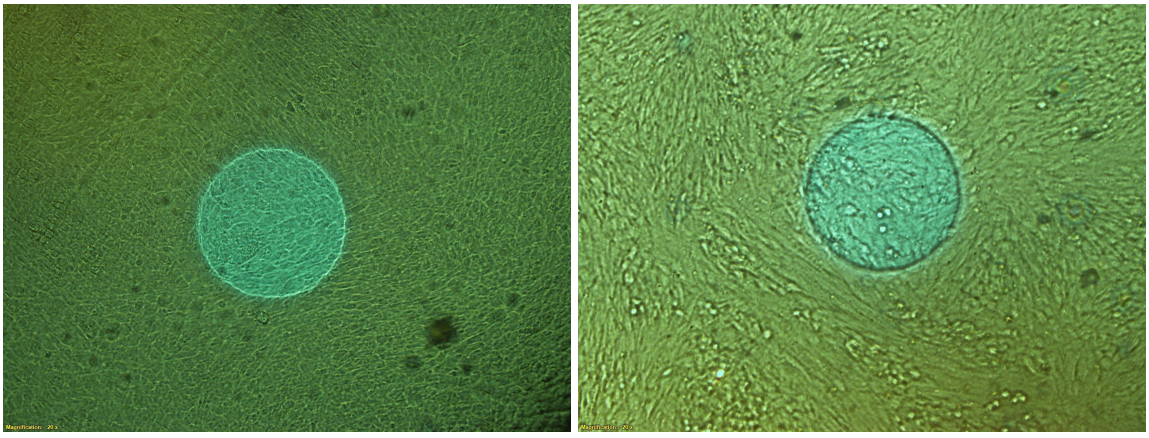

(a) (b)

Fig. 6.23 Time = 156 hours. Electrodes under the microscope. 20x optical magnification for (a) control cells and (b) differentiated cells.

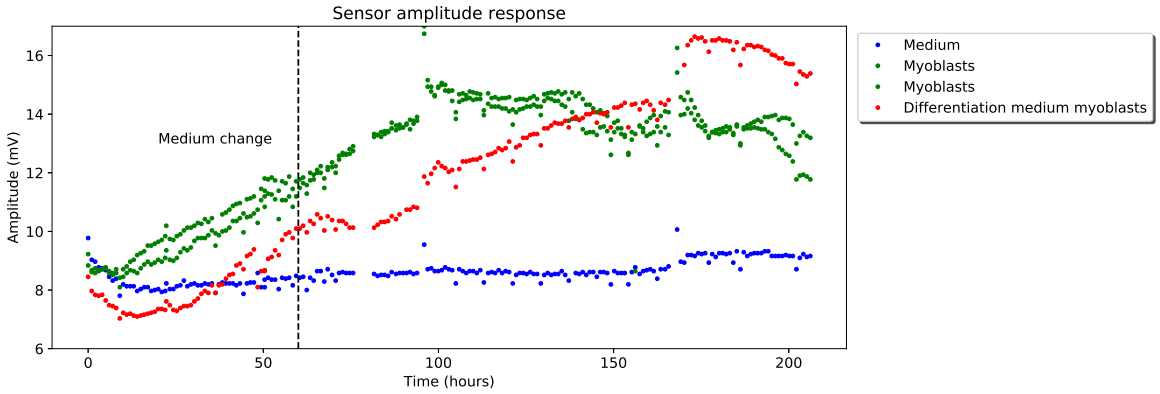

Fig. 6.24 Amplitude levels for wells captured from the sensor device during the AA8 growth experiment performed on the Seville Bio-medicine Institute (IBIS).

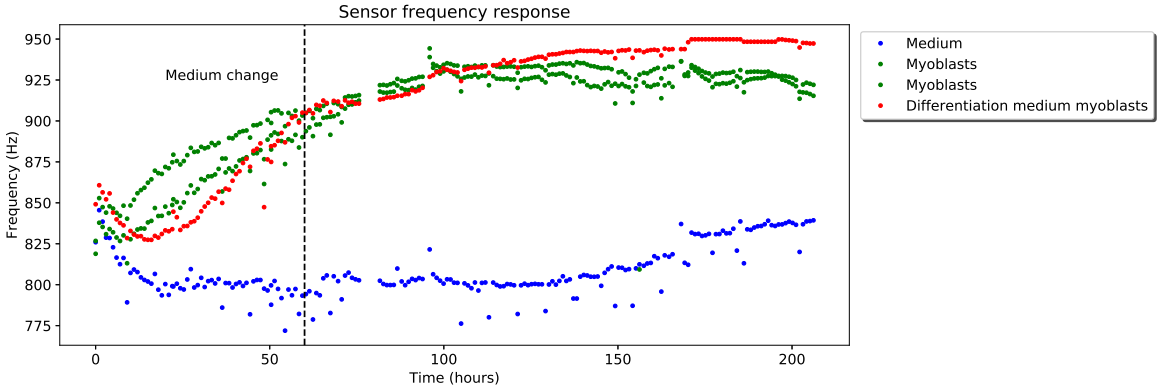

Fig. 6.25 Frequency measurements for wells captured from the sensor device during the AA8 growth experiment performed on the Seville Bio-medicine Institute (IBIS).

6.3.1 Data analysis

To analyze the results obtained from the myoblast experiment a similar approach to the followed on the growth experiments is performed. Results from the KNN estimation algorithm are presented on table 6.15. Figures 6.26 and 6.27 illustrate the predicted ranges for frequencies and the corrected amplitude ranges (following same offset correction approach performed on previous sections). The absolute values are presented on tables 6.16 and 6.17. The relative error in the frequency dynamic range (δ FDR (%)) is under 4% for the control cases and rises up to 12.9% for the differentiation case. Despite amplitude results (after an offset correction similar to the one applied to AA8 and N2A cell line) show a relative error over the amplitude dynamic range significantly higher than the frequency value, the control wells perform at 10.3 and 12.3 % and the differentiation well is performing at 24%.

Table 6.15 Electrical model values obtained from the KNN classifier for the CRL-1458 cells.

Well	R_{ct} $(M\Omega)$	C_{dl} **(nF)**	R_s (Ω)
1	1.7	51.3	960
2	0.6	53.8	1000
3	0.6	58.9	1000
4	2.6	16.0	250
5	0.8	64.0	840
6	2.6	64.0	1000
7	0.6	56.4	1000
8	2.6	16.0	250

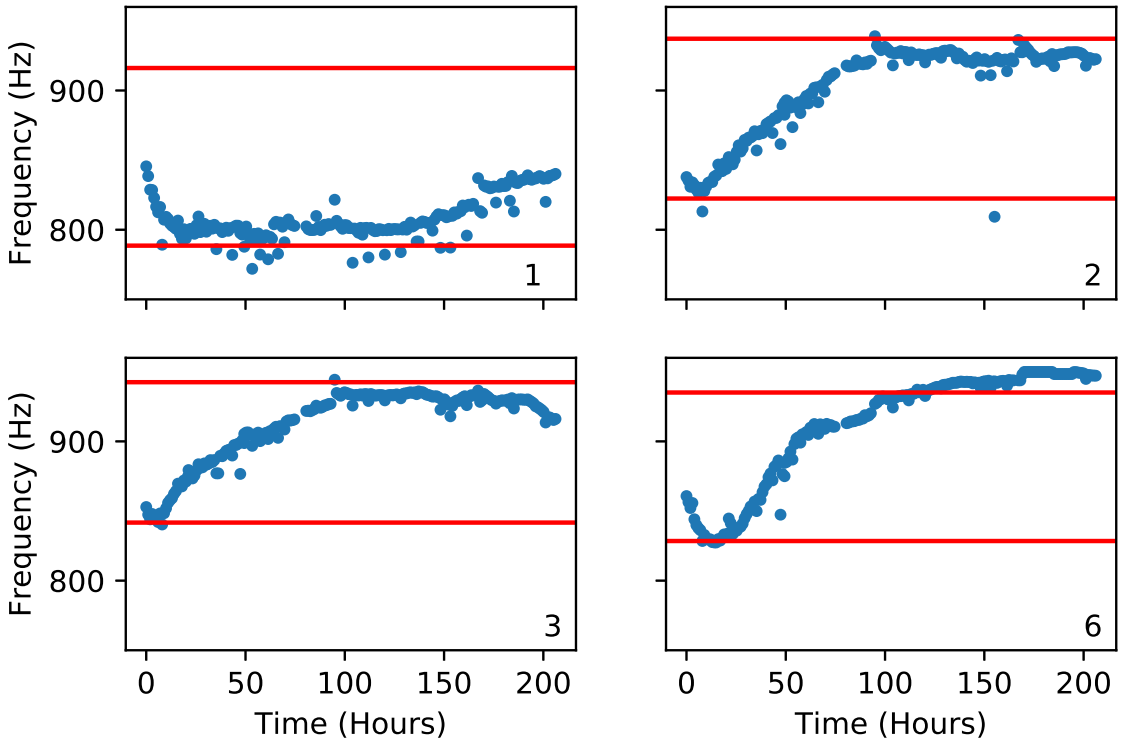

Fig. 6.26 Frequency predicted ranges for each of the seeded well. Range prediction is depicted as a red line. CRL-1458 cell line.

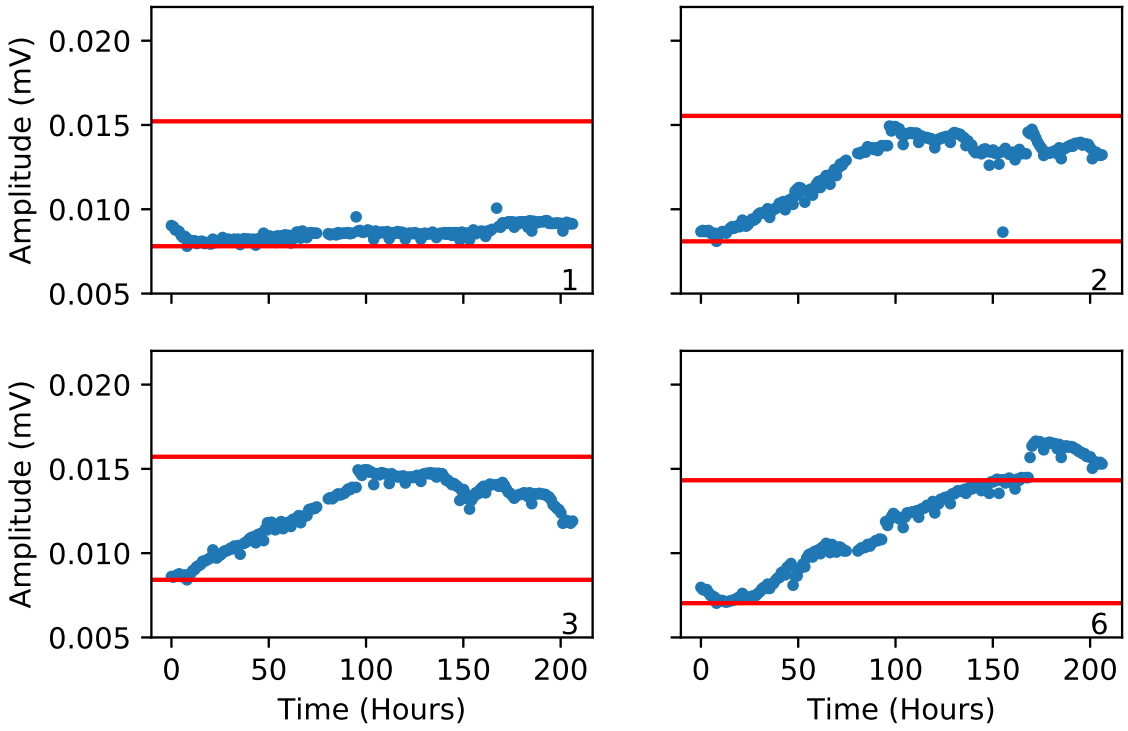

Fig. 6.27 Amplitude corrected ranges for each of the seeded well. Range prediction is depicted as a red line. CRL-1458 cell line.

Table 6.16 AA8 cell line. Frequency prediction vs experimental and dynamic ranges over the wells. δFDR represents the relative error between the experimental range and the model predicted range.

	Theoretical			**Experimental**			
Well	f_{min} (Hz)	f_{max} (Hz)	FDR	f_{min} (Hz)	f_{max} (Hz)	FDR	δFDR (%)
1	788.6	916.1	127.5	789.2	845.5	56.3	126.5
2	822.4	937.2	114.8	825.0	939.0	114.0	0.7
3	841.7	942.5	100.8	840.3	944.3	104.0	3.1
7	828.4	935.1	106.7	827.4	949.9	122.5	12.9

The result presented might suggest a potential variation over the R_{gap} parameter as a result of the differentiation process, as already introduced on previous section modelling R_{gap} value has an enormous potential as a bio-metric marker for cell culture assays. For this experiment, a generic $R_{gap} = 600\ \Omega$ value was applied. Considering the above statement as a valid hypothesis the a different R_{gap} value might improve the results over the differentiated cells. Following figure 6.28 illustrates the predicted fill-factor for the non-differentiated cells applying the $R_{gap} = 600\ \Omega$. Figure 6.29 depicts again prediction for fill-factor but

Table 6.17 CRL-1458 cell line. Amplitude prediction vs experimental and dynamic ranges over the wells. δADR represents the relative error between the experimental range and the model predicted range.

	Theoretical			**Experimental**			
Well	a_{min} (mV)	a_{max} (mV)	ADR	a_{min} (mV)	a_{max} (mV)	ADR	δADR (%)
1	12.1	19.5	7.4	7.8	10.1	2.3	221.7
2	11.6	19.1	7.5	8.1	14.9	6.8	10.3
3	12.4	19.7	7.3	8.4	14.9	6.5	12.3
7	12.4	19.7	7.3	7.0	16.6	9.6	24.0

with a $R_{gap} = 700\ \Omega$. Under this configuration the differentiation cell prediction reports δ FDR = 4.8% and δ ADR = 11.5% which are similar to the control results. Despite the study performed, further analysis is required to validate the R_{gap} variation effect over differentiating cell under bi-dimensional cell culture assays. As a secondary conclusion for this experiment no effect was observed due to the real-time measurement over the cell culture growth evolution compared to a control assay and the wells which were never measured (so they could be used as a control for the measurement process too.

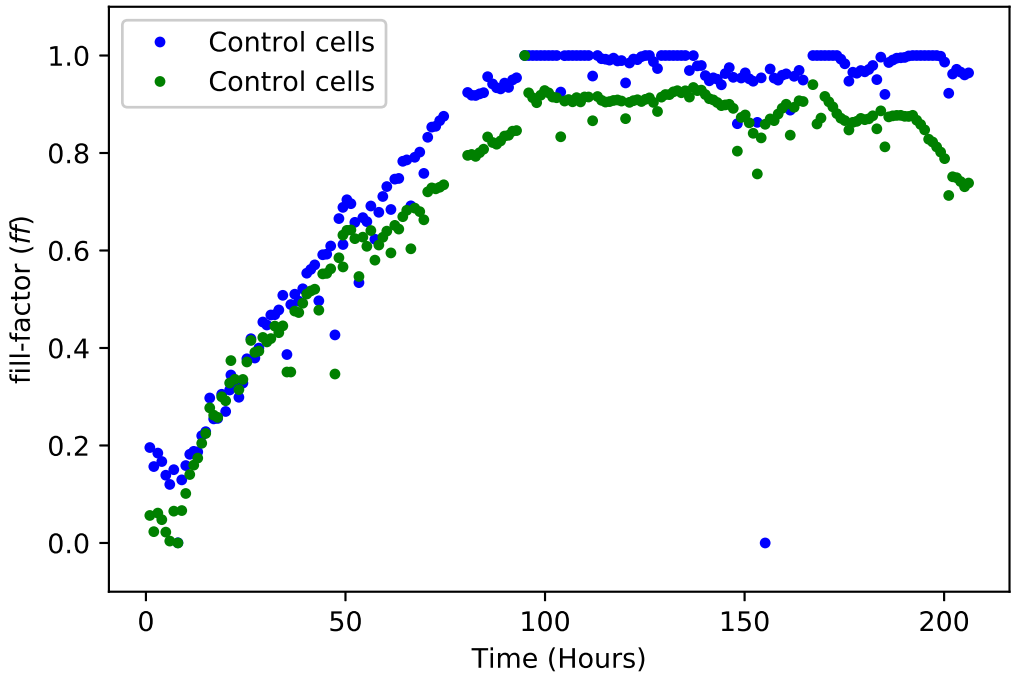

Fig. 6.28 Predicted fill-factor (ff) evolution over time for the control cells.

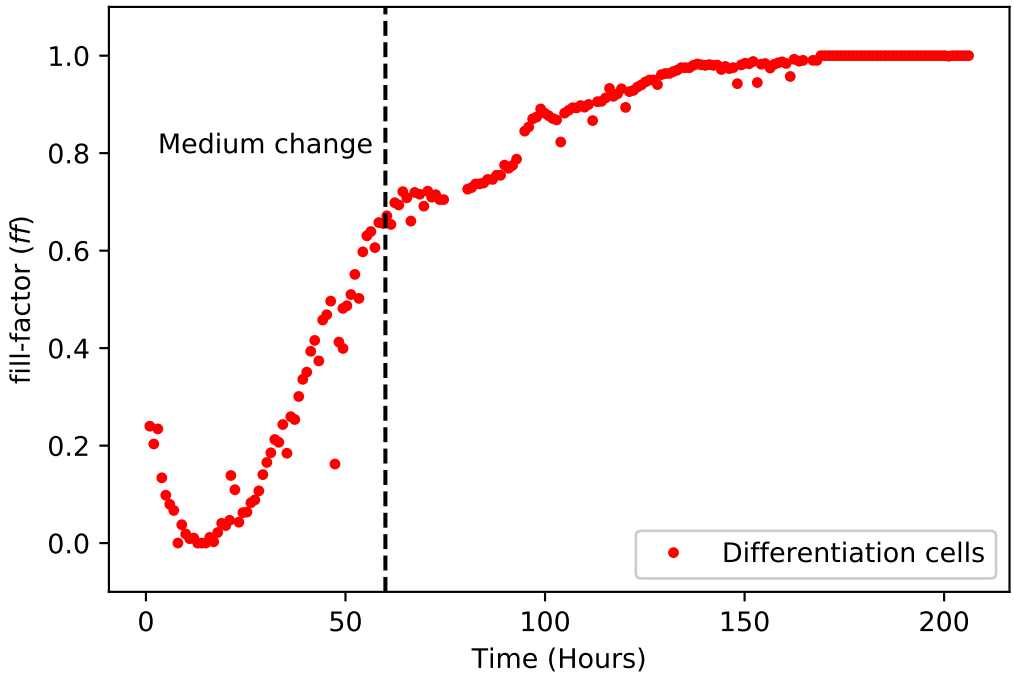

Fig. 6.29 Predicted fill-factor (ff) evolution over time for the differentiated cells.

An alternative approach to sensor information could be derived from a simple offset correction process to the raw amplitude signals acquired from the sensor. This result is presented in figure 6.30. However, this is only a qualitative analysis, since the dispersion presented on previous section imposes caution on the result analysis based only on raw data from the sensor due to the variation spotted on amplitude dynamic ranges.

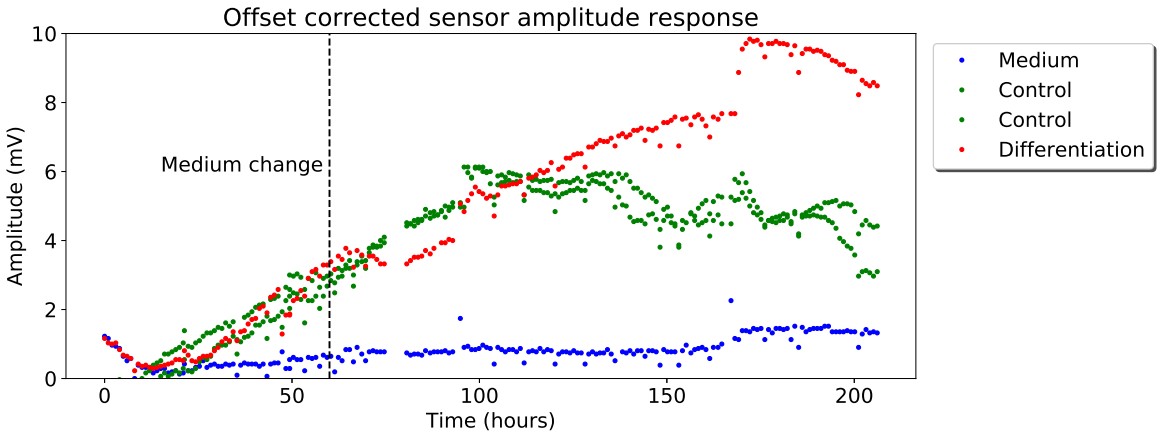

Fig. 6.30 Offset corrected amplitude measurement for the cell culture assay.

6.4 Cyto-toxicity analysis

Final assay to perform using the prototype is a drug response analysis over the N2A APP cells. Cell assay was prepared following the same protocol depicted on previous growth analysis for this cell line but every well is seeded with 3.5 k cells, except for two which are left only with medium. On the second day, the MG132 proteasome inhibitor (Sigma Aldrich) drug is added to the cell culture assay, applying different dosage to the wells; two control wells)(1 and 8), MG 200 nM (well 2), MG 500 nM (well 4), MG 1 μM (well 5) and MG 5 μM (well 7). Wells 3 and 7 were left unseeded. Raw curves acquired from the sensor are presented on figures 6.31 and 6.32.

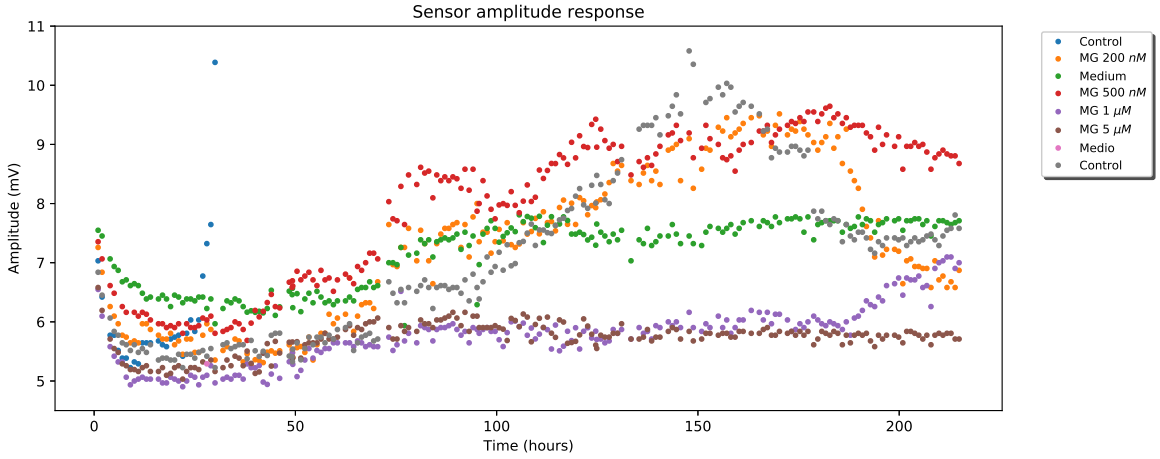

Fig. 6.31 Amplitude levels for the eight different wells captured from the sensor device during the cytotoxicity experiment performed on the faculty of Biology (US).

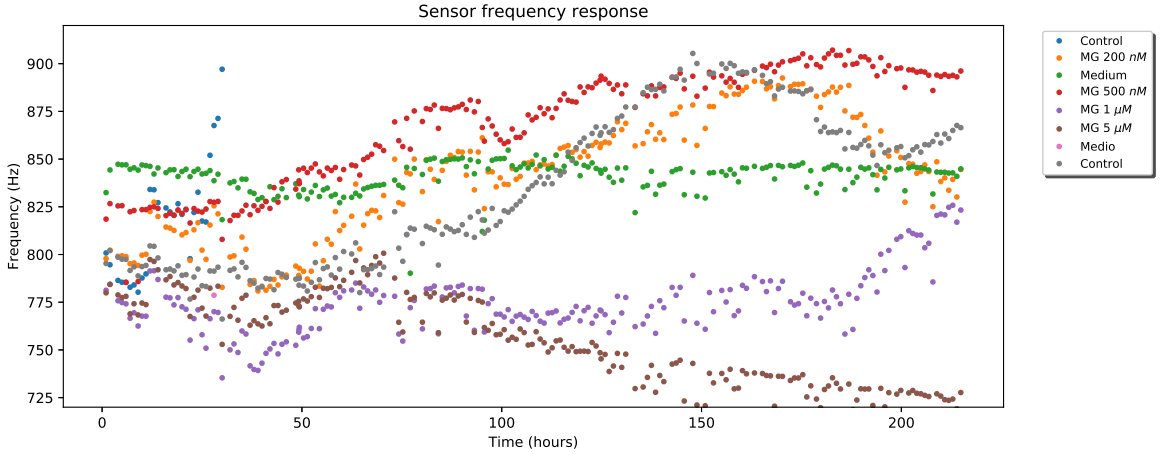

Fig. 6.32 Frequency measurements for the eight different wells captured from the sensor device during the cytotoxicity experiment performed on the faculty of Biology (US).

6.4.1 Data analysis

To analyze the results obtained from the cytotoxicity experiment again the algorithmic approach already applied to the rest of the experiments is performed. Results from the KNN estimation algorithm are presented on table 6.18. The fill-factor estimation is provided on figure 6.33, this curve was obtained using a $R_{gap} = 300\ \Omega$.

Table 6.18 Electrical model values obtained from the KNN classifier for the N2A APP under the MG drug.

Well	R_{ct} $(M\Omega)$	C_{dl} **(nF)**	R_s (Ω)
1	0.6	64.0	760
2	0.8	48.8	1000
3	1.0	64.0	840
4	1.7	64.0	840
5	1.9	56.4	760
6	0.8	53.8	840
7	0.6	48.8	1000
8	0.6	51.3	920

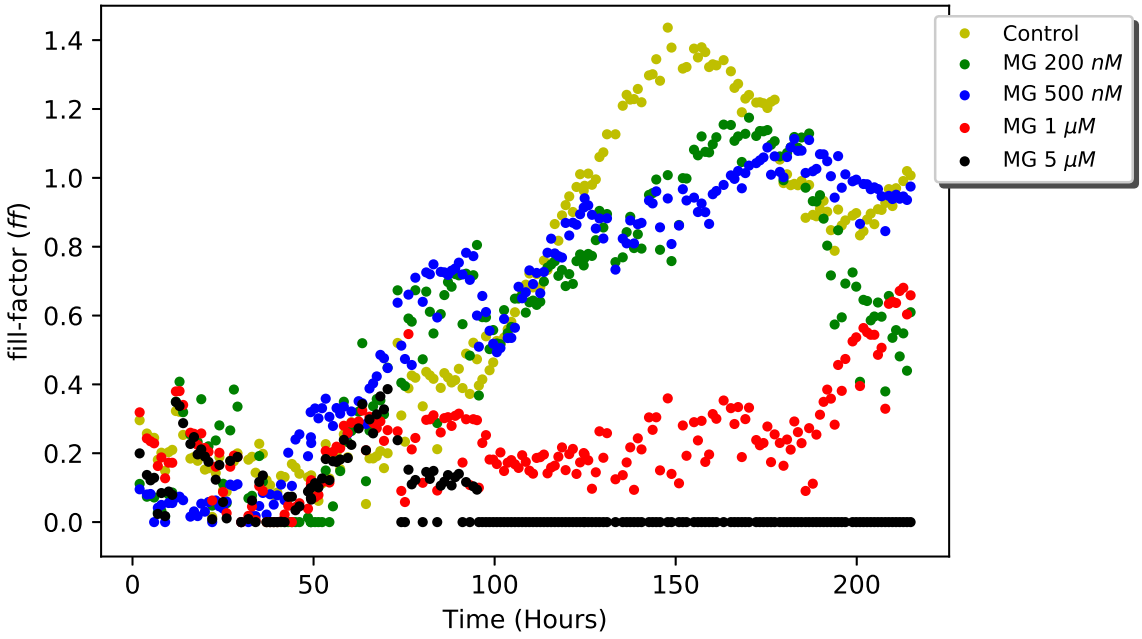

Fig. 6.33

Again, as in the cell differentiation experiment, an alternative approach to sensor information could be derived from a simple offset correction process to the raw amplitude signals

acquired from the sensor. This result is presented in figure 6.34. However, this is only a qualitative analysis, since the dispersion presented on previous section imposes caution on the result analysis based only on raw data from the sensor due to the variation spotted on amplitude dynamic ranges.

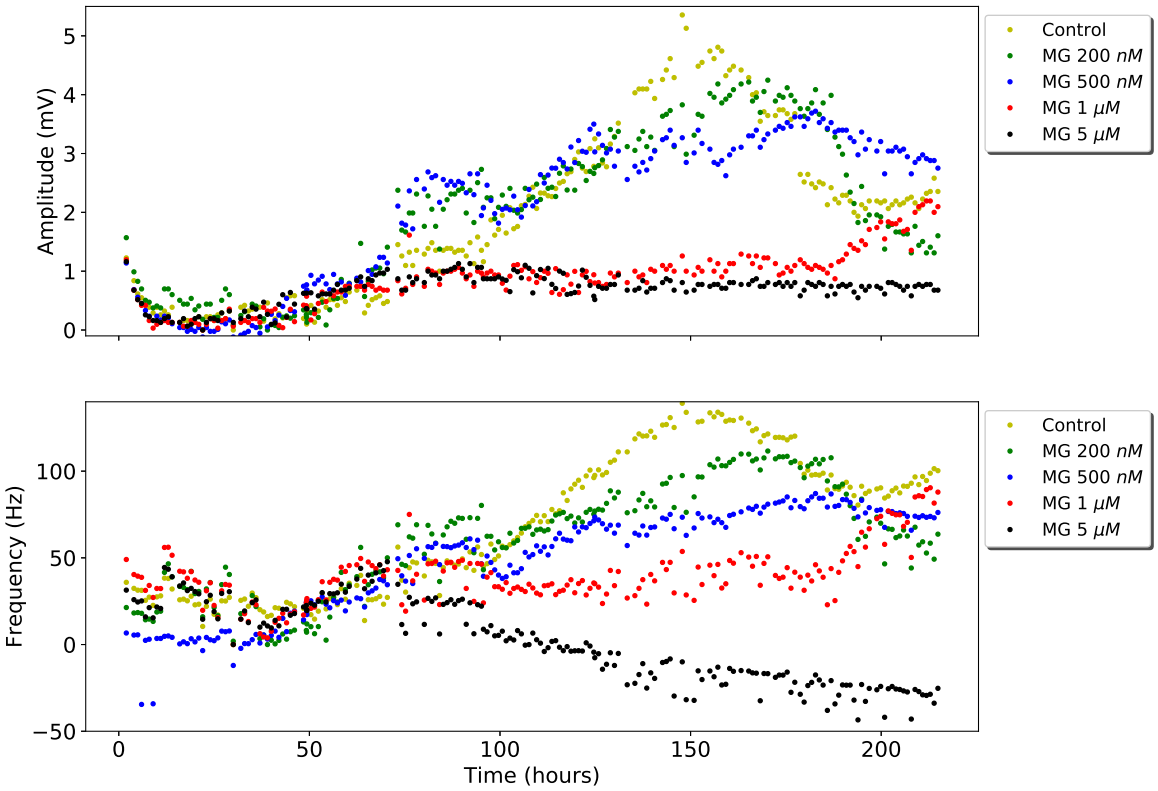

Fig. 6.34 Offset corrected amplitude (TOP) and frequency (BOTTOM) measurement for the cell culture assay.

Both graphs illustrate the fact that sensor response curves correspond to the expected (and experimentally observed) result. Greater cell densities are observed over the lower doses of MG drug, whereas lower cell densities arise from the higher doses. The drug is known for having a cyto-toxicity effect over cell cultures which matches the experimental result depicted on this section.

Summary and conclusions

Experimental results from the proposed prototype are presented in this chapter for five cell culture assays. In these experiments, four different cell lines were employed: AA8, N2A, N2APP and CRL-1458.

- In all cases, growth curves are recovered as expected. Both; frequency and amplitude, correlate with cell culture dynamics, and estimate correctly the location in time of the confluence phase of cell-cultures. This information is of great value in this kind of experiments.

- Growth experiment results illustrates the sensitivity of the prototype designed and implemented in this thesis. The device is sensitive to the number of initial cells seeded, arriving to a confluent phase those with larger initial cell density (10 k) than those with lower densities (2.5 k).

- Frequency and amplitude ranges match with the expected design ranges described in chapter 3. Defining $f_0 = 1.09\ kHz$ and $Q_f = 6.23$ as the band-pass parameters, and considering the electrode and cell models results in a similar response prediction for the system.

- Frequency and amplitude curves show some dispersion over initial values on different well, both in offset levels and dynamic ranges. This is true even for identical test circuits and experiments conditions. The reason for this is an existing mismatch of electrical parameters associated to the electrode model. A solution proposed involves a k-Neighbour Classifier machine learning algorithm which estimates the electrical model parameters to approximate a solution: R_{ct}, C_{dl} and R_s values. This estimation provides a tool to predict dynamic ranges and perform the fill-factor (ff) estimation. The electrical parameters values estimated are within expected ranges of 100% from their nominal values.

- The R_{gap} resistance is different for each cell line. This value is a potential candidate to serve as a bio-metric marker, associated to cell line identification.

- Cell densities have been estimated from electrical model and the predicted fill factors, considering for each cell line an approximated size. Values obtained are, in general, better for lower initial cell densities. However, it is possible to make a good cell density (or number of cell / cm^2) estimation from experimental measurements.

- Additionally, the experiment with the CRL-1458 myoblast cell line, illustrated an additional potential for this prototype to evaluate cell differentiation in cell cultures. In this case, final stem cell differentiation derived on new biological structures (myotubes) that should be correctly modelled in the future.
- The final assay involved a drug cell culture analysis with the N2A cell line. The fill-factor was computed using the estimation method applied on the growth assays. The results show the cells response to MG drug. Cell death is higher in those wells with larger MG doses, which is the expected result and is achieved by the full system proposed system on this dissertation.

Final conclusions

- The objectives for this thesis are the design, fabrication and test of circuits and systems required for real-time monitoring and characterization of cell culture assays, useful in many biomedical environments and disciplines. The selected sensing parameter is the biological impedance (Bio-impedance) of cells due to the electrical properties of the biology matter.
- The electrical Bio-Impedance (BI) is identified as an excellent parameter for real-time monitoring in cell culture applications. This is due to the fact that live matter is BI dependent, and considering that the physical sensing approach can benefit directly from electronic as an enabling technology.
- Electrical Cell-substrate Impedance Spectroscopy (ECIS) denotes the selected electrical technique for cell culture sensing in two-dimensions, due to the wide range of possible assays and maturity. In ECIS environments, electrode-solution electrical model and cell-medium electrical model was described and their influence analyzed over the ECIS technique. Design equations for the electrode-medium-cell system were developed, considering the parameter introduced by the electrode fabrication technology and solution medium, and geometry constrains imposed by electrode and cell sizes. The fill-factor parameter was defined to measure the sensing area percentage referred to area covered by cells in a culture. This serve as the main indicator of assay dynamics. The electrical model was experimentally validated over individual electrodes (8W10E) along with cell cultures.
- Oscillation Based Test (OBT) was the selected circuit technique for bioimpedance sensing due to several advantages over different solutions: OBT does not require external *AC* stimulation; does not need a precise instrumentation amplifier; and does not need synchronization circuitry to acquire impedance information.
- OBT operation principle was applied to ECIS technique, including parametric electrical models for cells and electrodes. Design curves are obtained for OBT output signals: oscillation frequency and amplitude of the oscillations. These curves allow

the estimation of the predicted circuit performance specifications. The optimal values for the BPF parameters which govern the OBT sensor are $f_0 = 1\ kHz$ and Q_f in the [5-10] range.

- A low-cost sensor device is implemented based on off-the-shelf components. The device includes analog and digital blocks. The analog part is formed by a band-pass filter, a comparator, a current source, a noise filter, a start-up circuit, channel multiplexing circuit and voltage level shifters. All of them were designed into a PCB prototype. Main digital blocks are the micro-controller STM32F7, which is capable of managing the whole sensing process, performs the signal acquisition and processes the OBT signal.

- As the final elements on any Internet of Things (IoT) architecture the gateway and service layers are defined. The gateway is located on the biomedical laboratory with a direct link to the remote web server, which provides the service layer. The gateway device is formed by a commercial Linux based system on a chip; Intel Edison. This device includes a Yocto Linux version as the Operating System and implements both WiFi and Bluetooth communication.

- The service layer provides secure access, storage and real-time visualization for the potential users of the system; biomedical researchers. All the information gathered is stored on a MySQL database. The database is designed to provide scalability and comply to the functional requirements of the system. The remote control and real time visualization of the system is performed via a custom web application prototype developed for this purpose.

- A FFT algorithm was implemented on the micro-controller to estimate the OBT signal frequency and amplitude. However, the computational costs in terms of memory and workload to achieve high resolution (higher FFT orders) is high. To overcome this issue an alternative solution based on a Gaussian window, FFT and a peak estimator is presented. The final system implemented provides a significantly higher degree of accuracy to the signal parameter estimation process, reducing the total computational load at the micro-controller. This contributes to low power consumption, especially during the data transfer process since the amount of data to be transmitted corresponds only to frequency and amplitude results.

- Experimental data obtained with the proposed prototype have been exposed in the final chapter for five cell culture experiments. In summary, more than 60 assays were performed during this thesis. In these assays, have been employed four cell lines: AA8,

N2A, N2APP and CRL-1458. From the data obtained, results illustrate the following: In all cases, growth curves fit the traditional counting method curves, as expected. Both; frequency and amplitude, allows the prediction of the cell culture dynamics, and estimate correctly the location in time of the confluent phase of cell cultures. This is valuable information for the biomedical researchers performing cell culture assays.

- Growth experiment results demonstrate that the prototype is sensitive to the initial cells number Those with larger initial cell density (10 k) reach first the confluent phase than the lower density (2.5 k) ones. Frequency and amplitude ranges match with the expected design ranges in chapter 3, for BP parameters of $f_0 = 1.096\ kHz$ and $Q_f = 6.23$.

- Frequency and amplitude curves show some initial values dispersion over different wells, both in offset levels and dynamic ranges. This occurs even when test circuits and experiments conditions are equal. This must be due to the electrical parameters mismatch of electrode model. A solution proposed involves a k-Neighbour Classifier machine learning algorithm which estimates the electrical model parameters to approximate sensor curve solution on every particular case: R_{ct}, C_{dl} and R_s, which fits frequency and amplitude dinamycs ranges to those experimentally measured .

- The R_{gap} resistance value is a parameter specific to every cell line. This could be proposed as a bio-metrical parameter which enables characterization of cell culture under tests in this kind of assays.

- From electrical model fill-factor values are predicted and cell densities estimated. This is performed by considering an approximate size for each cell line. Values are in general, better for lower initial cell densities, but still permit to perform cell density (or number of cell / cm2) estimation from experimental measurements on all of them.

- Additionally, the experiment involving CRL-1458 myoblast cell line, illustrated an additional potential for the prototype to evaluate cell differentiation in cell cultures. In this case, final stem cell differentiation derive on new biological structures (myotubes) which alters the measurement from the sensor, however, further analysis would be required for characterization of this process.

- Finally, a drug cell culture analysis for the N2A cell line was performed, and the fill-factor was computed using the estimation method applied on the growth assays. The result illustrates the cells response to MG drug. Cell death is higher in those wells

with larger MG doses, a proposal matched with the cell densities predicted by the system created in this thesis.

Future work

The most important future work associated to the development exposed on this dissertation would be implementing a full integrated system capable of sensing cell culture assays and forming part of a Lab-On-A-Chip device. The integration is highly interesting since the precision and power consumption specifications would be greatly improved from this process.

Additionally, several proposals arise from this work:

- The design and implementation of a frequency configurable OBT. Capable of tuning the sensor over different central frequencies (f_0) thus enabling to perform impedance spectroscopy using the OBT approach.
- The electrical cell parameter estimation can also be an interesting follow-up work. Cell line characterization would be a valuable asset to improve cell count estimation.
- The design and fabrication of different electrode layout. The insight gained over the electrodes immersed on ionic solution and the ECIS technique, will allow the design of new electrode structures, simulate them and apply them along with an OBT sensor to analyze the impedance under test.
- Migrate of the Bluetooth communication system to Bluetooth 5.0 which would greatly improve the power consumption of the overall system.
- Explore machine learning algorithms which may be useful to estimate cell number from the amplitude and frequency values measured with the sensor. An example of this could be the Unscented Kalman Filter algorithm.

References

[1] D. J. Harrison, K. Fluri, K. Seiler, Z. Fan, C. S. Effenhauser, and A. Manz, "Micromachining a Miniaturized Capillary Electrophoresis-Based Chemical Analysis System on a Chip," *Science*, vol. 261, pp. 895–897, 8 1993.

[2] R. E. Oosterbroek and A. v. d. A. Berg, *Lab-on-a-chip : miniaturized systems for (bio)chemical analysis and synthesis*. Elsevier, 2003.

[3] Y. H. Ghallab and Y. Ismail, "CMOS Based Lab-on-a-Chip: Applications, Challenges and Future Trends," *IEEE Circuits and Systems Magazine*, vol. 14, pp. 27–47, 22 2014.

[4] R. I. Freshney and Wiley InterScience (Online service), *Culture of animal cells : a manual of basic technique and specialized applications*. Wiley-Blackwell, 2010.

[5] J. G. Webster and J. W. J. W. Clark, *Medical instrumentation : application and design*. John Wiley & Sons, 2010.

[6] J.-Y. Yoon, *Introduction to Biosensors*. Springer, 2002.

[7] A. A. Turner, I. Karube, G. S. G. Wilson, and P. Worsfold, *Biosensors: Fundamentals and Applications*. 1987.

[8] A. Romani, N. Manaresi, G. Medoro, A. Leonardi, M. Tartagni, and R. Guerrieri, "Capacitive sensor array for localization of bioparticles in CMOS lab-on-a-chip," in *Solid-State Circuits Conference, 2004. Digest of Technical Papers. ISSCC. 2004 IEEE International*, pp. 224–225, 2004.

[9] N. Manaresi, A. Romani, G. Medoro, L. Altomare, A. Leonardi, M. Tartagni, and R. Guerrieri, "A CMOS Chip for Individual Cell Manipulation and Detection," in *IEEE Journal of Solid-State Circuits*, vol. 38, pp. 2297–2305, 12 2003.

[10] N. Nelson, D. Sander, M. Dandin, S. B. Prakash, A. Sarje, and P. Abshire, "Handheld fluorometers for lab-on-a-chip applications," in *IEEE Transactions on Biomedical Circuits and Systems*, vol. 3, pp. 97–107, 4 2009.

[11] F. Sekli Belaïdi, L. Farouil, L. Salvagnac, P. Temple-Boyer, I. Séguy, J. Heully, F. Alary, E. Bedel-Pereira, and J. Launay, "Towards integrated multi-sensor platform using dual electrochemical and optical detection for on-site pollutant detection in water," *Biosensors and Bioelectronics*, vol. 132, pp. 90–96, 5 2019.

[12] P. A. Kyriacou, M. Hickey, and J. P. Phillips, "Pulse oximetry of body cavities and organs," in *2013 35th Annual International Conference of the IEEE Engineering in Medicine and Biology Society (EMBC)*, pp. 2664–2667, IEEE, 7 2013.

[13] J. P. Phillips, P. A. Kyriacou, K. J. George, J. V. Priestley, and R. M. Langford, "An Optical Fiber Photoplethysmographic System for Central Nervous System Tissue," in *2006 International Conference of the IEEE Engineering in Medicine and Biology Society*, pp. 803–806, IEEE, 8 2006.

[14] E. Boulanger, M. Dempsey, T. Jarobski, E. Lurier, M. Kural, and K. Billiar, "A device for dynamic modulation of cell-generated tension in 3D biopolymer gels," in *2014 40th Annual Northeast Bioengineering Conference (NEBEC)*, pp. 1–2, IEEE, 4 2014.

[15] Yu-Jie Huang, Che-Wei Huang, Tsung-Hsien Lin, Chih-Ting Lin, Li-Guang Chen, Po-Yun Hsiao, Bi-Ru Wu, Hsiao-Ting Hsueh, Bing-Jye Kuo, Hann-Huei Tsai, Hsin-Hao Liao, Ying-Zong Juang, Chorng-Kuang Wang, and Shey-Shi Lu, "A CMOS Cantilever-Based Label-Free DNA SoC With Improved Sensitivity for Hepatitis B Virus Detection," *IEEE Transactions on Biomedical Circuits and Systems*, vol. 7, pp. 820–831, 12 2013.

[16] R. Doldán, E. Peralías, A. Yúfera, and A. Rueda, "A CMOS optical PSD with submicrometer resolution," *Analog Integrated Circuits and Signal Processing*, vol. 53, pp. 109–118, 10 2007.

[17] Y. C. Yang Choon Lim, A. Z. Kouzani, W. Wei Duan, X. J. Dai, A. Kaynak, and D. Mair, "A Surface-Stress-Based Microcantilever Aptasensor," *IEEE Transactions on Biomedical Circuits and Systems*, vol. 8, pp. 15–24, 2 2014.

[18] J. A. Miguel, Y. Lechuga, R. Mozuelos, and M. Martínez, "Modeling of an implantable device for remote arterial pressure measurement," vol. 8765, p. 876508, International Society for Optics and Photonics, 5 2013.

[19] E. Rodríguez-Villegas, G. Chen, J. Radcliffe, and J. Duncan, "A pilot study of a wearable apnoea detection device.," *BMJ open*, vol. 4, p. e005299, 10 2014.

[20] M. Arakawa, J. Shikama, K. Yoshida, R. Nagaoka, K. Kobayashi, and Y. Saijo, "Development of an ultrasound microscope combined with optical microscope for multiparametric characterization of a single cell," *IEEE Transactions on Ultrasonics, Ferroelectrics, and Frequency Control*, vol. 62, pp. 1615–1622, 9 2015.

[21] G. Papadakis, P. Murasova, A. Hamiot, K. Tsougeni, G. Kaprou, M. Eck, D. Rabus, Z. Bilkova, B. Dupuy, G. Jobst, A. Tserepi, E. Gogolides, and E. Gizeli, "Micro-nano-bio acoustic system for the detection of foodborne pathogens in real samples," *Biosensors and Bioelectronics*, vol. 111, pp. 52–58, 7 2018.

[22] Z. Djinović, R. Pavelka, M. Tomić, G. Sprinzl, H. Plenk, U. Losert, H. Bergmeister, and R. Plasenzotti, "In-vitro and in-vivo measurement of the animal's middle ear acoustical response by partially implantable fiber-optic sensing system," *Biosensors and Bioelectronics*, vol. 103, pp. 176–181, 4 2018.

[23] M. J. Milgrew and D. R. S. Cumming, "A proton camera array technology for direct extracellular ion imaging," in *2008 IEEE International Symposium on Industrial Electronics*, pp. 2051–2055, IEEE, 6 2008.

[24] X. Huang, H. Yu, X. Liu, Y. Jiang, M. Yan, and D. Wu, "A Dual-Mode Large-Arrayed CMOS ISFET Sensor for Accurate and High-Throughput pH Sensing in Biomedical Diagnosis," *IEEE Transactions on Biomedical Engineering*, vol. 62, pp. 2224–2233, 9 2015.

[25] Y. Jiang, X. Liu, T. C. Dang, X. Huang, H. Feng, Q. Zhang, and H. Yu, "A High-Sensitivity Potentiometric 65-nm CMOS ISFET Sensor for Rapid E. coli Screening," *IEEE Transactions on Biomedical Circuits and Systems*, vol. 12, pp. 402–415, 4 2018.

[26] J. Y. Lucisano, T. L. Routh, J. T. Lin, and D. A. Gough, "Glucose Monitoring in Individuals With Diabetes Using a Long-Term Implanted Sensor/Telemetry System and Model," *IEEE Transactions on Biomedical Engineering*, vol. 64, pp. 1982–1993, 9 2017.

[27] C. Russell, A. C. Ward, V. Vezza, P. Hoskisson, D. Alcorn, D. P. Steenson, and D. K. Corrigan, "Development of a needle shaped microelectrode for electrochemical detection of the sepsis biomarker interleukin-6 (IL-6) in real time," *Biosensors and Bioelectronics*, vol. 126, pp. 806–814, 2 2019.

[28] D. Satake, H. Ebi, N. Oku, K. Matsuda, H. Takao, M. Ashiki, and M. Ishida, "A sensor for blood cell counter using MEMS technology," in *Sensors and Actuators, B: Chemical*, vol. 83, pp. 77–81, Elsevier, 3 2002.

[29] N. Piacentini, D. Demarchi, P. Civera, and M. Knaflitz, "MEMS-based blood cell counting system," in *2008 15th IEEE International Conference on Electronics, Circuits and Systems*, pp. 198–201, IEEE, 8 2008.

[30] G. Medoro, N. Manaresi, A. Leonardi, L. Altomare, M. Tartagni, and R. Guerrieri, "A lab-on-a-chip for cell detection and manipulation," *IEEE Sensors Journal*, vol. 3, pp. 317–325, 6 2003.

[31] A. Yúfera, A. Rueda, J. M. Muñoz, R. Doldán, G. Leger, and E. O. Rodríguez-Villegas, "A tissue impedance measurement chip for myocardial ischemia detection," *IEEE Transactions on Circuits and Systems I: Regular Papers*, vol. 52, pp. 2620–2628, 12 2005.

[32] S. A. Imtiaz, Z. Jiang, and E. Rodriguez-Villegas, "An Ultralow Power System on Chip for Automatic Sleep Staging," *IEEE Journal of Solid-State Circuits*, vol. 52, pp. 822–833, 3 2017.

[33] A. Yúfera and A. Rueda, "A CMOS bio-impedance measurement system," in *2009 12th International Symposium on Design and Diagnostics of Electronic Circuits & Systems*, pp. 252–257, IEEE, 2009.

[34] Y. Pan, N. Hu, X. Wei, L. Gong, B. Zhang, H. Wan, and P. Wang, "3D cell-based biosensor for cell viability and drug assessment by 3D electric cell/matrigel-substrate impedance sensing," *Biosensors and Bioelectronics*, vol. 130, pp. 344–351, 4 2019.

[35] S. Radke, E. Alocilja, S. Radke, and E. Alocilja, "Design and Fabrication of a Microimpedance Biosensor for Bacterial Detection," *IEEE Sensors Journal*, vol. 4, pp. 434–440, 8 2004.

[36] G. M. Xiong, A. T. Do, J. K. Wang, C. L. Yeoh, K. S. Yeo, and C. Choong, "Development of a miniaturized stimulation device for electrical stimulation of cells," *Journal of Biological Engineering*, vol. 9, p. 14, 12 2015.

[37] L. Majer, V. Stopjaková, and E. Vavrinsk, "Wireless Measurement System for Non–Invasive Biomedical Monitoring of Psycho–Physiological Processes," *Journal of ELECTRICAL ENGINEERING*, vol. 60, no. 2, pp. 57–68, 2009.

[38] H. Gensler, R. Sheybani, P.-Y. Li, R. Lo, S. Zhu, K.-T. Yong, I. Roy, P. N. Prasad, R. Masood, U. K. Sinha, and E. Meng, "Implantable MEMS drug delivery device for cancer radiation reduction," in *2010 IEEE 23rd International Conference on Micro Electro Mechanical Systems (MEMS)*, pp. 23–26, IEEE, 1 2010.

[39] J. Scott and P. Single, "Compact Nonlinear Model of an Implantable Electrode Array for Spinal Cord Stimulation (SCS)," *IEEE Transactions on Biomedical Circuits and Systems*, vol. 8, pp. 382–390, 6 2014.

[40] S. Grimnes and G. Martinsen, *Bioimpedance and bioelectricity basics*. Academic, 2008.

[41] P. Horowitz, W. Hill, and H. Winfield, *The art of electronics*. Cambridge University Press, 1989.

[42] H. P. Schwan, "Electrical properties of tissue and cell suspensions.," *Advances in Biological and Medical Physics*, vol. 5, pp. 147–209, 1 1957.

[43] A. Ivorra, "Bioimpedance monitoring for physicians : an overview," *Medicine for non physicians*, vol. 2002, no. October 2001, pp. 131–178, 2002.

[44] D. Borkholder, *Cell Based Biosensors Using Microelectrodes*. PhD thesis, Stanford University, 11 1998.

[45] A. Mercanzini, P. Colin, J. C. Bensadoun, A. Bertsch, and P. Renaud, "In vivo electrical impedance spectroscopy of tissue reaction to microelectrode arrays," *IEEE Transactions on Biomedical Engineering*, vol. 56, pp. 1909–1918, 7 2009.

[46] J. O. Bockris, A. K. N. Reddy, and M. E. Gamboa-Aldeco, *Modern electrochemistry*. Plenum Press, 1998.

[47] Sohmyung Ha, Chul Kim, Y. M. Chi, A. Akinin, C. Maier, A. Ueno, and G. Cauwenberghs, "Integrated Circuits and Electrode Interfaces for Noninvasive Physiological Monitoring," *IEEE Transactions on Biomedical Engineering*, vol. 61, pp. 1522–1537, 5 2014.

[48] J. J. Ackmann, "Complex bioelectric impedance measurement system for the frequency range from 5 Hz to 1 MHz.," *Annals of biomedical engineering*, vol. 21, no. 2, pp. 135–46.

[49] D. Allegri, A. Donida, P. Malcovati, and D. Barrettino, "CMOS-Based Multifrequency Impedance Analyzer for Biomedical Applications," in *2018 IEEE International Symposium on Circuits and Systems (ISCAS)*, pp. 1–5, IEEE, 5 2018.

[50] F. Mellert, K. Winkler, C. Schneider, T. Dudykevych, A. Welz, M. Osypka, E. Gersing, and C. J. Preusse, "Detection of (Reversible) Myocardial Ischemic Injury by Means of Electrical Bioimpedance," *IEEE Transactions on Biomedical Engineering*, vol. 58, pp. 1511–1518, 6 2011.

[51] O. I. Al-Surkhi and R. Y. Naser, "Detection of Cell Morphological Changes of Ischemic Rabbit Liver Tissue Using Bioimpedance Spectroscopy," *IEEE Transactions on NanoBioscience*, vol. 17, pp. 402–408, 10 2018.

[52] P. Daza, A. Olmo, D. Cañete, and A. Yúfera, "Monitoring living cell assays with bio-impedance sensors," *Sensors and Actuators B: Chemical*, vol. 176, pp. 605–610, 1 2013.

[53] I. Giaever and C. R. Keese, "Use of Electric Fields to Monitor the Dynamical Aspect of Cell Behavior in Tissue Culture," *IEEE Transactions on Biomedical Engineering*, vol. BME-33, pp. 242–247, 2 1986.

[54] X. Huang, D. Nguyen, D. Greve, and M. Domach, "Simulation of Microelectrode Impedance Changes Due to Cell Growth," *IEEE Sensors Journal*, vol. 4, pp. 576–583, 10 2004.

[55] D. Das, F. A. Kamil, S. Agrawal, K. Biswas, and S. Das, "Fragmental Frequency Analysis Method to Estimate Electrical Cell Parameters From Bioimpedance Study," *IEEE Transactions on Instrumentation and Measurement*, vol. 63, pp. 1991–2000, 8 2014.

[56] Guofeng Qiao, Wei Wang, Wei Duan, Fan Zheng, A. J. Sinclair, and C. R. Chatwin, "Bioimpedance Analysis for the Characterization of Breast Cancer Cells in Suspension," *IEEE Transactions on Biomedical Engineering*, vol. 59, pp. 2321–2329, 8 2012.

[57] P. Aberg, I. Nicander, J. Hansson, P. Geladi, U. Holmgren, and S. Ollmar, "Skin Cancer Identification Using Multifrequency Electrical Impedance—A Potential Screening Tool," *IEEE Transactions on Biomedical Engineering*, vol. 51, pp. 2097–2102, 12 2004.

[58] I. Giaever and C. R. Keese, "Micromotion of mammalian cells measured electrically.," *Proceedings of the National Academy of Sciences of the United States of America*, vol. 88, pp. 7896–900, 9 1991.

[59] P. Linderholm, T. Braschler, J. Vannod, Y. Barrandon, M. Brouard, and P. Renaud, "Two-dimensional impedance imaging of cell migration and epithelial stratification," *Lab on a Chip*, vol. 6, p. 1155, 9 2006.

[60] C. R. Keese, J. Wegener, S. R. Walker, and I. Giaever, "Electrical wound-healing assay for cells in vitro.," *Proceedings of the National Academy of Sciences of the United States of America*, vol. 101, pp. 1554–9, 2 2004.

[61] R. Beach, R. Conlan, M. Godwin, and F. Moussy, "Towards a Miniature Implantable In Vivo Telemetry Monitoring System Dynamically Configurable as a Potentiostat or Galvanostat for Two- and Three-Electrode Biosensors," *IEEE Transactions on Instrumentation and Measurement*, vol. 54, pp. 61–72, 2 2005.

[62] A. Manickam, A. Chevalier, M. McDermott, A. D. Ellington, and A. Hassibi, "A CMOS Electrochemical Impedance Spectroscopy (EIS) Biosensor Array," *IEEE Transactions on Biomedical Circuits and Systems*, vol. 4, pp. 379–390, 12 2010.

[63] A. Hassibi and T. H. Lee, "A programmable 0.18-μm CMOS electrochemical sen-Hassibi, A., & Lee, T. H. (2006). A programmable 0.18-μm CMOS electrochemical sensor microarray for biomolecular detection. IEEE Sensors Journal, 6(6), 1380–1388. https://doi.org/10.1109/JSEN.2006.883904sor m," *IEEE Sensors Journal*, vol. 6, pp. 1380–1388, 12 2006.

[64] C.-L. Hsu, A. Sun, Y. Zhao, E. Aronoff-Spencer, and D. A. Hall, "A 16×20 electrochemical CMOS biosensor array with in-pixel averaging using polar modulation," in *2018 IEEE Custom Integrated Circuits Conference (CICC)*, pp. 1–4, IEEE, 4 2018.

[65] J. Ramos, J. L. Ausín, G. Torelli, and J. F. Duque-Carrillo, "A wireless sensor network for fat and hydration monitoring by bioimpedance analysis," in *Proceedings of the 6th International Workshop on Wearable, Micro, and Nano Technologies for Personalized Health*, pp. 49–52, IEEE, 6 2009.

[66] Long Yan, J. Pettine, S. Mitra, Sunyoung Kim, Dong-Woo Jee, Hyejung Kim, M. Osawa, Y. Harada, K. Tamiya, C. Van Hoof, and R. F. Yazicioglu, "A 13 μA Analog Signal Processing IC for Accurate Recognition of Multiple Intra-Cardiac Signals," *IEEE Transactions on Biomedical Circuits and Systems*, vol. 7, pp. 785–795, 12 2014.

[67] M. Guermandi, R. Cardu, E. Franchi Scarselli, and R. Guerrieri, "Active Electrode IC for EEG and Electrical Impedance Tomography With Continuous Monitoring of Contact Impedance," *IEEE Transactions on Biomedical Circuits and Systems*, vol. 9, pp. 21–33, 2 2015.

[68] O. G. Martinsen, B. Nordbotten, S. Grimnes, H. Fossan, and J. Eilevstjnn, "Bioimpedance-Based Respiration Monitoring With a Defibrillator," *IEEE Transactions on Biomedical Engineering*, vol. 61, pp. 1858–1862, 6 2014.

[69] W. Lee and S. Cho, "Integrated All Electrical Pulse Wave Velocity and Respiration Sensors Using Bio-Impedance," *IEEE Journal of Solid-State Circuits*, vol. 50, pp. 776–785, 3 2015.

[70] R. Kusche, P. Klimach, and M. Ryschka, "A Multichannel Real-Time Bioimpedance Measurement Device for Pulse Wave Analysis," *IEEE Transactions on Biomedical Circuits and Systems*, vol. 12, pp. 614–622, 6 2018.

[71] R. Pallàs-Areny and J. Webster, "Bioelectric impedance measurements using synchronous sampling," *IEEE Transactions on Biomedical Engineering*, vol. 40, no. 8, pp. 824–829, 1993.

[72] P. M. Ramos, "How signal processing is changing impedance spectroscopy," in *2018 IEEE International Instrumentation and Measurement Technology Conference (I2MTC)*, pp. 1–6, IEEE, 5 2018.

[73] A. Sánchez-González, N. Medrano, B. Calvo, P. A. Martínez, A. Sanchez-Gonzalez, N. Medrano, B. Calvo, and P. A. Martínez, "A Multichannel FRA-Based Impedance Spectrometry Analyzer Based on a Low-Cost Multicore Microcontroller," *Electronics*, vol. 8, p. 38, 1 2019.

[74] A. Hafid, S. Benouar, M. Kedir-Talha, F. Abtahi, M. Attari, and F. Seoane, "Full Impedance Cardiography Measurement Device Using Raspberry PI3 and System-on-Chip Biomedical Instrumentation Solutions," *IEEE Journal of Biomedical and Health Informatics*, vol. 22, no. 6, pp. 1883–1894, 2018.

[75] J. Ferreira, I. Pau, K. Lindecrantz, and F. Seoane, "A Handheld and Textile-Enabled Bioimpedance System for Ubiquitous Body Composition Analysis. An Initial Functional Validation," *IEEE Journal of Biomedical and Health Informatics*, vol. 21, pp. 1224–1232, 9 2017.

[76] M. Zamani, Y. Rezaeiyan, O. Shoaei, and W. A. Serdijn, "A 1.55 μW Bio-Impedance Measurement System for Implantable Cardiac Pacemakers in 0.18 μm CMOS," *IEEE Transactions on Biomedical Circuits and Systems*, vol. 12, pp. 211–221, 2 2018.

[77] G. Huertas, A. Maldonado, A. Yúfera, A. Rueda, and J. L. Huertas, "The Bio-Oscillator: A Circuit for Cell-Culture Assays," *IEEE Transactions on Circuits and Systems II: Express Briefs*, vol. 62, pp. 164–168, 2 2015.

[78] R. Onet, A. Rusu, and S. Rodriguez, "High-Purity and Wide-Range Signal Generator for Bioimpedance Spectroscopy," *IEEE Transactions on Circuits and Systems II: Express Briefs*, vol. 65, pp. 1884–1888, 12 2018.

[79] Yi-Qiang Zhao, A. Demosthenous, and R. Bayford, "A CMOS Instrumentation Amplifier for Wideband Bioimpedance Spectroscopy Systems," in *2006 IEEE International Symposium on Circuits and Systems*, pp. 5079–5082, IEEE.

[80] F. A. Alexander, D. T. Price, and S. Bhansali, "From Cellular Cultures to Cellular Spheroids: Is Impedance Spectroscopy a Viable Tool for Monitoring Multicellular Spheroid (MCS) Drug Models?," *IEEE Reviews in Biomedical Engineering*, vol. 6, pp. 63–76, 2013.

[81] I. Giaever and C. R. Keese, "Micromotion of mammalian cells measured electrically (cell motility/fibroblast behavior/nanometer motions/electrical measurements)," *Cell Biology*, vol. 88, pp. 78–7900, 1991.

[82] D. Holder and Institute of Physics (Great Britain), *Electrical impedance tomography : methods, history, and applications*. Institute of Physics Pub, 2005.

[83] B. Taji, S. Shirmohammadi, V. Groza, and I. Batkin, "Impact of Skin–Electrode Interface on Electrocardiogram Measurements Using Conductive Textile Electrodes," *IEEE Transactions on Instrumentation and Measurement*, vol. 63, pp. 1412–1422, 6 2014.

[84] D. Robinson, "The electrical properties of metal microelectrodes," *Proceedings of the IEEE*, vol. 56, no. 6, pp. 1065–1071, 1968.

[85] R. Bragós, E. Sarro, A. Fontova, A. Soley, J. Cairo, A. Bayes-Genis, and J. Rosell, "Four Versus Two-Electrode Measurement Strategies for Cell Growing and Differentiation Monitoring Using Electrical Impedance Spectroscopy," in *2006 International Conference of the IEEE Engineering in Medicine and Biology Society*, pp. 2106–2109, 8 2006.

[86] L. Avery, D. Raizen, and S. Lockery, *Electrophysiological Methods*, vol. 48. NIH Public Access, 1995.

[87] R. W. Simpson, J. G. Berberian, and H. P. Schwan, "Nonlinear AC and DC Polarization of Platinum Electrodes," *IEEE Transactions on Biomedical Engineering*, vol. BME-27, pp. 166–171, 3 1980.

[88] H. P. Schwan, "Linear and nonlinear electrode polarization and biological materials," *Annals of Biomedical Engineering*, vol. 20, pp. 269–288, 5 1992.

[89] W. Franks, I. Schenker, P. Schmutz, and A. Hierlemann, "Impedance Characterization and Modeling of Electrodes for Biomedical Applications," *IEEE Transactions on Biomedical Engineering*, vol. 52, pp. 1295–1302, 7 2005.

[90] Y. Xu, X. Xie, Y. Duan, L. Wang, Z. Cheng, and J. Cheng, "A review of impedance measurements of whole cells," 3 2016.

[91] K. Asami, "Characterization of biological cells by dielectric spectroscopy," *Journal of Non-Crystalline Solids*, vol. 305, pp. 268–277, 7 2002.

[92] J. Wang, C. Wu, N. Hu, J. Zhou, L. Du, and P. Wang, "Microfabricated electrochemical cell-based biosensors for analysis of living cells in vitro.," *Biosensors*, vol. 2, pp. 127–70, 4 2012.

[93] A. Susloparova, D. Koppenhöfer, X. Vu, M. Weil, and S. Ingebrandt, "Impedance spectroscopy with field-effect transistor arrays for the analysis of anti-cancer drug action on individual cells," *Biosensors and Bioelectronics*, vol. 40, pp. 50–56, 2 2013.

[94] B. P. Senevirathna, S. Lu, M. P. Dandin, J. Basile, E. Smela, and P. A. Abshire, "Real-Time Measurements of Cell Proliferation Using a Lab-on-CMOS Capacitance Sensor Array," *IEEE Transactions on Biomedical Circuits and Systems*, vol. 12, pp. 510–520, 6 2018.

[95] J. S. Park, M. K. Aziz, S. Li, T. Chi, S. I. Grijalva, J. H. Sung, H. C. Cho, and H. Wang, "1024-Pixel CMOS Multimodality Joint Cellular Sensor/Stimulator Array for Real-Time Holistic Cellular Characterization and Cell-Based Drug Screening," *IEEE Transactions on Biomedical Circuits and Systems*, vol. 12, pp. 80–94, 2 2018.

[96] I. Holland, C. McCormick, and P. Connolly, "Towards non-invasive characterisation of coronary stent re-endothelialisation – An in-vitro, electrical impedance study," *PLOS ONE*, vol. 13, p. e0206758, 11 2018.

[97] S. Arndt, J. Seebach, K. Psathaki, H.-J. Galla, and J. Wegener, "Bioelectrical impedance assay to monitor changes in cell shape during apoptosis.," *Biosensors & bioelectronics*, vol. 19, pp. 583–94, 1 2004.

[98] "ECIS Cell-based Assays from Applied BioPhysics." http://www.biophysics.com/.

[99] E. Zudaire, N. Cuesta, V. Murty, K. Woodson, L. Adams, N. Gonzalez, A. Martínez, G. Narayan, I. Kirsch, W. Franklin, F. Hirsch, M. Birrer, and F. Cuttitta, "The aryl hydrocarbon receptor repressor is a putative tumor suppressor gene in multiple human cancers," *Journal of Clinical Investigation*, vol. 118, pp. 640–50, 1 2008.

[100] N. Yu, J. M. Atienza, J. Bernard, S. Blanc, J. Zhu, X. Wang, X. Xu, and Y. A. Abassi, "Real-Time Monitoring of Morphological Changes in Living Cells by Electronic Cell Sensor Arrays: An Approach To Study G Protein-Coupled Receptors," *Analytical Chemistry*, vol. 78, pp. 35–43, 1 2006.

[101] J. Hong, K. Kandasamy, M. Marimuthu, C. S. Choi, and S. Kim, "Electrical cell-substrate impedance sensing as a non-invasive tool for cancer cell study," *The Analyst*, vol. 136, no. 2, 2011.

[102] G. H. Williams and K. Stoeber, "The cell cycle and cancer," *The Journal of Pathology*, vol. 226, pp. 352–364, 1 2012.

[103] I. H. Heijink, S. M. Brandenburg, J. A. Noordhoek, D. S. Postma, D.-J. Slebos, and A. J. M. van Oosterhout, "Characterisation of cell adhesion in airway epithelial cell types using electric cell-substrate impedance sensing.," *The European respiratory journal*, vol. 35, pp. 894–903, 4 2010.

[104] P. O. Bagnaninchi and N. Drummond, "Real-time label-free monitoring of adipose-derived stem cell differentiation with electric cell-substrate impedance sensing," *Proceedings of the National Academy of Sciences*, vol. 108, pp. 6462–6467, 4 2011.

[105] G. Nabovati, E. Ghafar-Zadeh, A. Letourneau, and M. Sawan, "Towards High Throughput Cell Growth Screening: A New CMOS 8 8 Biosensor Array for Life Science Applications," *IEEE Transactions on Biomedical Circuits and Systems*, vol. 11, pp. 380–391, 4 2017.

[106] R. Buyya and A. V. Dastjerdi, *Internet of things : principles and paradigms*.

[107] T. Pan, Y. Ding, L. Wu, L. Liang, X. He, Q. Li, C. Bai, and H. Zhang, "Design and synthesis of aminothiazole based Hepatitis B Virus (HBV) capsid inhibitors," *European Journal of Medicinal Chemistry*, vol. 166, pp. 480–501, 3 2019.

[108] M. Jedrzejczak-Silicka, "History of Cell Culture," in *New Insights into Cell Culture Technology*, InTech, 5 2017.

[109] R. I. Freshney, *Culture of Animal Cells*. Hoboken, NJ, USA: John Wiley & Sons, Inc., 9 2010.

[110] J. Wegener, C. R. Keese, and I. Giaever, "Electric Cell–Substrate Impedance Sensing (ECIS) as a Noninvasive Means to Monitor the Kinetics of Cell Spreading to Artificial Surfaces," *Experimental Cell Research*, vol. 259, pp. 158–166, 8 2000.

[111] P. Wang and Q. Liu, *Cell-based biosensors : principles and applications*. Artech House, 2010.

[112] R. Pradhan, A. Mitra, and S. Das, "Characterization of Electrode/Electrolyte Interface of ECIS Devices," *Electroanalysis*, vol. 24, pp. 2405–2414, 12 2012.

[113] A. J. Bard and L. R. Faulkner, *Electrochemical methods : fundamentals and applications*. Wiley, 2001.

[114] H. Helmholtz, "Studien über electrische Grenzschichten," *Annalen der Physik und Chemie*, vol. 243, pp. 337–382, 1 1879.

[115] H. J. Lewerenz, "On the Structure of the Helmholtz Layer and its Implications on Electrode Kinetics," *ECS Transactions*, vol. 50, pp. 3–20, 4 2013.

[116] "Minimum Essential Medium Eagle (MEM) Formulation | Sigma-Aldrich."

[117] A. Yúfera, P. Daza, and D. Canete, "Using microelectrode models for real time cell-culture monitoring," in *2011 Annual International Conference of the IEEE Engineering in Medicine and Biology Society*, vol. 2011, pp. 3983–3986, IEEE, 8 2011.

[118] J. A. Serrano, G. Huertas, A. Maldonado-Jacobi, A. Olmo, P. Pérez, M. E. Martín, P. Daza, and A. Yúfera, "An Empirical-Mathematical Approach for Calibration and Fitting Cell-Electrode Electrical Models in Bioimpedance Tests," *Sensors*, vol. 18, p. 2354, 7 2018.

[119] B. O. Arredondo Vega, D. Voltolina, T. Zenteno Savín, M. Arce Montoya, and G. A. Gómez Anduro, *Métodos y Herramientas Analíticas en la Evaluación de la Biomasa Microalgal*. 2017.

[120] J. R. Stein-Taylor, *Handbook of phycological methods : culture methods and growth measurements*. University Press, 1979.

[121] G. A. Harris, J. Coombs, D. D. Hall, S. P. Long, and J. M. O. Scurlock, *Techniques in Bioproductivity and Photosynthesis*, vol. 40. 2007.

[122] "Analog Discovery - USB Oscilloscope, Logic Analyzer And More." https://analogdiscovery.com/.

[123] G. H. Sanchez, *Oscillation-based test in mixed-signal circuits*. Springer, 2006.

[124] P. Fleischer, A. Ganesan, and K. Laker, "A switched capacitor oscillator with precision amplitude control and guaranteed start-up," *IEEE Journal of Solid-State Circuits*, vol. 20, pp. 641–647, 4 1985.

[125] "Documentation for the Intel® Edison Module | IoT | Intel® Software." https://software.intel.com/en-us/iot/hardware/edison/documentation.

[126] "Microprocessor Cores and Technology – Arm." https://www.arm.com/products/silicon-ip-cpu.

[127] "Extending Python with C or C++ — Python 2.7.16 documentation." https://docs.python.org/2/extending/extending.html.

[128] "STM32F7 - ARM Cortex-M7 Microcontrollers - STMicroelectronics." http://www.st.com/en/microcontrollers/stm32f7-series.html.

[129] "SHT2x (RH/T) - Digital Humidity Sensor | Sensirion." https://www.sensirion.com/en/environmental-sensors/humidity-sensors/humidity-temperature-sensor-sht2x-digital-i2c-accurate/.

[130] "Autodesk Inventor,"

[131] "Prusa i3 MK3S." https://www.prusa3d.com/original-prusa-i3-mk3/.

[132] W. v. Drongelen, *Signal processing for neuroscientists : introduction to the analysis of physiological signals*. Elsevier/Academic Press, 2007.

[133] K. Rao, D. Kim, and J. Hwang, *Fast Fourier transform : algorithms and applications*. Signals and Communication Technology, Dordrecht: Springer, 2010.

[134] F. J. Harris, "On the use of Windows for Harmonic Analysis with the Discrete Fourier Transform,"

[135] M. Gasior and J. L. Gonzalez, "Improving FFT Frequency Measurement Resolution by Parabolic and Gaussian Spectrum Interpolation," 2004.

[136] J. W. Cooley and J. W. Tukey, "An Algorithm for the Machine Calculation of Complex Fourier Series," *Mathematics of Computation*, vol. 19, p. 297, 4 1965.

[137] A. Ganapathiraju, J. Hamaker, J. Picone, and A. Skjellum, "Contemporary view of FFT algorithms,"

[138] M. Parsian, *Data Algorithms*. O'Reilly Media, Inc, 2015.

[139] P. Villanueva, S. Pereira, A. Olmo, P. Pérez, Y. Yuste, A. Yúfera, and F. Portilla, "Electrical pulse stimulation of skeletal myoblasts cell cultures with simulated action potentials," *Journal of Tissue Engineering and Regenerative Medicine*, p. term.2869, 5 2019.

[140] P. Pérez, G. Huertas, A. Maldonado-Jacobi, M. Martín, J. Serrano, A. Olmo, P. Daza, and A. Yúfera, "Sensing Cell-Culture Assays with Low-Cost Circuitry," *Nature Scientific Reports*, vol. 8, no. 1, 2018.

[141] P. Pérez, G. Huertas, A. Olmo, A. Maldonado-Jacobi, J. Serrano, M. Martín, P. Daza, and A. Yúfera, "Remote cell growth sensing using self-sustained bio-oscillations," *Sensors (Switzerland)*, vol. 18, no. 8, 2018.

[142] J. A. Serrano, P. Pérez, A. Maldonado, M. Martín, A. Olmo, P. Daza, G. Huertas, and A. Yúfera, "Practical Characterization of Cell-Electrode Electrical Models in Bio-Impedance Assays," in *Proceedings of the 11th International Joint Conference on Biomedical Engineering Systems and Technologies*, pp. 100–108, SCITEPRESS - Science and Technology Publications, 2018.

[143] Y. Yuste, J. Serrano, A. Olmo, A. Maldonado-Jacobi, P. Pérez, G. Huertas, S. Pereira, F. de la Portilla, and A. Yúfera, "Monitoring muscle stem cell cultures with impedance spectroscopy," in *BIODEVICES 2018 - 11th International Conference on Biomedical Electronics and Devices, Proceedings; Part of 11th International Joint Conference on Biomedical Engineering Systems and Technologies, BIOSTEC 2018*, vol. 1, 2018.

[144] A. Maldonado, G. Huertas, A. Rueda, J. Huertas, P. Perez, and A. Yúfera, "Cell-culture measurements using voltage oscillations," in *LASCAS 2016 - 7th IEEE Latin American Symposium on Circuits and Systems, R9 IEEE CASS Flagship Conference*, 2016.

[145] A. Maldonado, P. Pérez, G. Huertas, A. Yúfera, A. Rueda, and J. Huertas, "Monitoring tissue evolution on electrodes with bio-impedance test," in *2016 Conference on Design of Circuits and Integrated Systems, DCIS 2016 - Proceedings*, 2017.

[146] P. Pérez-Garcia, A. Maldonado, A. Yúfera, G. Huertas, A. Rueda, and J. L. Huertas, "Towards Bio-Impedance Based Labs: A Review," *2015 Conference on Design of Circuits and Integrated Systems, DCIS 2015*, pp. 1–11, 11 2016.

[147] A. Maldonado, P. Pérez, G. Huertas, A. Yúfera, A. Rueda, and J. Huertas, "From voltage oscillations to tissue-impedance measurements," in *IEEE Biomedical Circuits and Systems Conference: Engineering for Healthy Minds and Able Bodies, BioCAS 2015 - Proceedings*, 2015.

Scientific publications

The dissertation exposed on this document contributed in the production of valuable scientific contributions in the form of journal articles (**Nature Scientific Reports, Journal of Tissue Engineering and Regenerative Medicine, MDPI Sensors**) and international conferences (**Biodevices, LASCAS, DCIS, EMBC and BioCAS**). Main contributions are summarized on the following table A.1.

Table A.1 Scientific contributions

Reference	**Journal**	**Year**	**Quartile**
[139]	Tissue Eng. and Regenerative Medicine	2019	Q1
[140]	Nature Scientific Reports	2018	Q1
[141]	MDPI Sensors	2018	Q2
[118]	MDPI Sensors	2018	Q2
Reference	**Conference**	**Year**	**City**
[142]	11th BioDevices	2018	Madeira (Portugal)
[143]	11th BioDevices	2018	Madeira (Portugal)
[144]	7th LASCAS	2016	Florianopolis (Brasil)
[145]	31st DCIS	2016	Granada (Spain)
[146]	30th DCIS	2015	Estoril (Portugal)
[147]	BioCAS	2015	Atlanta (USA)